Calibration of DEM models for granular materials using bulk physical tests

Mical William Johnstone

Doctor of Philosophy

The University of Edinburgh

June 2010

Declaration

This thesis entitled “Calibration of DEM models for granular materials using bulk physical test” is submitted to the University of Edinburgh for the degree of Doctor of Philosophy. The research work described and reported in this thesis has been completed solely by Mical Johnstone under the supervision of Professor Jin Y. Ooi. Where other sources are quoted full references are given.

Publications based on this thesis:

Johnstone, M. W. and Ooi, J. Y. (2007) Development of bulk laboratory devices used for DEM model calibration. Industrial sponsor technical report, University of Edinburgh, Scotland. 65pp.

Johnstone, M. W. and Ooi, J. Y. (2008) Experiment and DEM modelling of rotating drum with spherical and non-spherical particle. Poster presentation, Runners up award. *International Conference on Structures and Granular Solids, Royal Society of Edinburgh, 1-2 July 2008*. Edinburgh Scotland.

Johnstone, M. W. and Ooi, J. Y. (2008) Numerical modelling of bulk experimental devices used for DEM model calibration. Industrial sponsor technical report, University of Edinburgh, Scotland. 90pp.

Johnstone, M. W. and Ooi, J. Y. (2009) Experiment and DEM modelling of laboratory devices with spherical and non-spherical particle. Poster presentation. *EDEM User Conference 13-14 August 2009*. Edinburgh, Scotland.

Johnstone, M. W. and Ooi, J. Y. (2010) Calibration of DEM models using rotating drum and confined compression measurements. *Proceedings for the World Conference on Particle Technology IV*. Nuremberg, Germany.

Mical Johnstone
June 2010

Abstract

From pharmaceutical powders to agricultural grains, a great proportion of the materials handled in industrial situations are granular or particulate in nature. The variety of stresses that the materials may experience and the resulting bulk behaviours may be complex. In agricultural engineering, a better understanding into agricultural processes such as seeding, harvesting, transporting and storing will help to improve the handling of agricultural grains with optimised solutions. A detailed understanding of a granular system is crucial when attempting to model a system, whether it is on a micro (particle) or macro (bulk) scale.

As numerical capabilities are ever increasing, the Discrete Element Method (DEM) is becoming an increasingly popular numerical technique for computing the behaviour of discrete particles for both industrial and scientific applications. A look into the literature shows a lack of validation of what DEM can predict, specifically with respect to bulk behaviour. In addition, when validation studies are conducted, discrepancies between bulk responses in physical tests and numerical predictions using measured particle properties may arise.

The aim of this research is to develop a methodology to calibrate DEM models for agricultural grains using data measured in bulk physical tests. The methodology will have a wider application to granular solids in general and will advance understanding in the area of DEM model calibration. A contrasting set of granular materials were used to develop the methodology including 3 inorganic solids (single and paired glass beads, and polyethylene terephthalate pellets) and two organic materials (black eyed beans and black kidney beans). The developed methodology consists of three steps:

1. The development of bulk physical tests to measure the bulk responses that will be used to calibrate the DEM models,
2. The creation of the numerical dataset that will describe how the DEM input parameters influence the bulk responses, and
3. The optimisation of the DEM parameters using a searching algorithm and the results from Step 1 and 2.

Two laboratory devices were developed to provide calibration data for the proposed methodology: a rotating drum and a confined compression test. These devices were chosen as they can produce bulk responses that are repeatable and easy to quantify, as well as generate discriminating results in numerical simulations when DEM parameters are varied.

The bulk response determined from the rotating drum device was the dynamic angle of repose ϕ_r formed when the granular material in a 40% filled drum is rotating at a speed of 7 *rpm*. The confined compression apparatus was used to determine the bulk stiffness of a system by monitoring the change in void ratio from the stress applied during a loading and unloading cycle. The gradient of the loading and unloading curves termed λ and κ respectively were chosen as the bulk responses to calibrate the DEM models. The experimental results revealed that the dynamic ϕ_r was significantly influenced by the particle aspect ratio and boundary conditions. The stiffness parameters were found to be predominantly influenced by the initial packing arrangement.

The numerical dataset describing how the DEM input parameters influence the numerical bulk responses was created by simulating the bulk physical tests, varying selected DEM parameters and monitoring the effects on bulk parameters. To limit the number of simulations required, design of experiment (DOE) methods were used to determine a reduced factorial matrix of simulations. In addition, an extensive parametric investigation on the non-optimised parameters as well as a scaling sensitivity study was carried out.

The final step in determining the optimised parameters is to use a searching algorithm to infer the DEM parameters based on the numerical dataset and use the experimental results as calibration data. To perform a comparative study, two searching algorithms were explored: the first was a simple method based on Microsoft Excel's Solver algorithm coupled with a weighted inverse distance method. The second made use of the statistical analysis program Statistica. It was shown that the Excel Solver algorithm is simpler and quicker to use but for the present first implementation, could only perform an optimisation based on two bulk responses. Statistica required the creation of a statistical model based on the numerical dataset before using the *profiling and desirability* searching technique, but was able to optimise the parameter using all three bulk responses.

A verification and validation of the optimisation methodology was conducted using the optimised parameters for the black eyed beans. A verification was conducted by simulating the

two calibration experiments using the optimised parameters and comparing these with the experiments. In addition, a validation was performed by predicting the response of a shallow footing penetration on a bed of black eyed beans. It was found that DEM simulations using optimised parameters predicted vertical stress on the footing during penetration to an acceptable degree of accuracy for industrial application (<10%) at penetration depths up to 30 *mm*.

Acknowledgements

The author would like to thank his supervisor Professor Jin Ooi for his excellent supervision, expert guidance, friendship and support in this research endeavour not to mention his motivational enthusiasm and unconditional help.

The author would also like to thank the all the members of the Silos and Granular Solids research group at the University of Edinburgh for their academic and emotional support. In addition, the author would like to acknowledge DEM Solutions Ltd. and School of Engineering and Electronics at the University of Edinburgh for funding this research.

Finally, the author would like to thank his family for their amazing patience, encouragement and support without which this study would not be possible. To them I dedicate this thesis.

Contents

List of figures

List of tables

Nomenclature

Roman characters

a_r	Aspect ratio
c	Apparent cohesion
C_B, k_B	Beverloo constants
C, n	Bulk stiffness parameter constants
D	Diameter of the cylinder and rotating drum
d	Diameter of particles
D_0	Diameter of outlet orifice
D_κ	load dependant parameter relating to the stress path during unloading
D_λ	load dependant parameter relating to the stress path during loading
E	Particle Young's modulus
e	Void ratio
e_0	Initial void ratio
e_r	Particle to particle coefficient of restitution
$e_{r,pw}$	Particle to wall coefficient of restitution
E_w	Young's modulus of the cylinder
f	Rotating drum filling degree
$\vec{F}$	Resultant force vector, the sum of all the contact forces
F_B	Measured force on the bottom platen
F_{CN}	Normal component of the contact force
$F_{CN,D}$	Normal damping force
$F_{CN,S}$	Normal spring force
F_{CT}	Tangential component of the contact force
$F_{CT,D}$	Tangential damping force
$F_{CT,S}$	Tangential spring force
$F_{CT,S,(n-1)}$	Spring force at previous time step
F_n	Normal force
F_r	Radial force
F_s	Shear forces
F_T	Applied load at the top platen

F_t	Tangential force
F_w	wall frictional force
Fr	Non dimensional rotational Froude number
G	Shear modulus of the particle
g	Gravity constant
$\vec{g}$	Gravity acceleration vector
h	Height of the granular material
$\dot{\vec{H}}$	Time rate of change of the angular momentum
K	Lateral pressure ratio
K_c	Geometric constant
K_n	Hertz contact constant
k_n	Normal contact stiffness
k_t	Tangential contact stiffness
m	total mass of the particle
m^*	Equivalent mass
$\vec{M}_G$	Resultant moment vector taken about the mass centre
M_s	Mass of solids
N_c, N_q, N_γ	Bearing capacity factors
P	Normal pressure
p	Inverse distance weighting factor
R	Confined compression cylinder radius
r	Radius of sphere
r^*	Equivalent radius
R_i	Distance of the contact point from the centre of mass
T_R	Rayleigh time step
t	Thickness of the cylinder
t_c	Computational time
t_s	Simulation time
$t_{s,a}$	Adjusted simulation time
V_R	Rayleigh wave velocity
$V_{relative,n}$	Relative normal velocity
$V_{relative,t}$	Relative tangential velocity
V_s	Volume of the solids

$\vec{x}_G$	Position vector of mass centre
$\dot{\vec{x}}_G$	Velocity vector of mass centre
$\ddot{\vec{x}}_G$	Acceleration vector of mass centre
W	Flow rate

Greek characters

α	Inclination angle in a rotating drum
α_n	Normal contact displacement (overlap)
α_s	Statistical significance parameter
β_d	Damping ratio
γ	Bulk of total unit weight (c.f. ρ)
$\Delta\alpha_t$	Incremental tangential displacement
$\Delta F_{CT,S}$	Increment of the tangential spring force
ε_θ	Hoop strain of the cylinder at the measuring points
ε_a	Axial strain of sample of the cylinder at the measuring points
ε_v	Mean vertical strain
λ	Bulk loading parameter
μ_{mob}	Mobilised friction coefficient
μ_{pp}	Particle to particle coefficient of sliding friction
μ_{pw}	Particle to wall coefficient of sliding friction
$\mu_{pw,c}$	Critical particle to wall friction for transition from slipping to avalanching motion
$\mu_{pp,bulk}$	Bulk particle to particle coefficient of sliding friction
$\mu_{pw,bulk}$	Bulk particle to wall coefficient of sliding friction
$\mu_{r,pp}$	Particle to particle coefficient of rolling friction
$\mu_{r,pw}$	Particle to wall coefficient of rolling friction
ζ	Characteristic range of the influence on the drum end plate
κ	Bulk unloading parameter
ξ	Dimensional scaling factor with respect to confined compression sample height
ρ	Bulk density
ρ_s	Density of solids
$\bar{\sigma}_h$	Mean horizontal stress
σ'_h	Effective horizontal pressure

σ_n	Normal stress on failure plane
$\bar{\sigma}_v$	Mean vertical stress
σ'_v	Effective vertical pressure
$\bar{\tau}$	Mean shear stress
τ_f	Limiting shear stress on failure plane
τ_w	Wall shear stress
υ	Poisson's ratio
υ_b	Bulk Poisson's ratio
υ_w	Poisson's ratio of the cylinder
$\phi_{pp,bulk}$	Bulk particle friction angle
$\phi_{pw,bulk}$	Bulk particle to wall friction angle
χ	Poisson's ratio depended parameter
ϕ_r	Angle of repose
Ω^2	Dimensional rotation rate
ω	Drum angular rotational speed
$\vec{\omega}$	Angular velocity vector of the particle
$\dot{\vec{\omega}}$	Angular velocity vector of the mass centre
ω_i	Angular velocity vector

Acronyms

AC	Ascending cone filling method
AFM	Atomic force microscope
ANOVA	Analysis of variance
AVG	Average
BEB	Black eyed beans
BKB	Black kidney beans
BSI	British Standard Institute
CAD	Computer aided design
CAE	Computer aided engineering
CFD	Computational fluid dynamics
COV	Coefficient of variance
DACE	Design and analysis of computer experiments
DEDS	Discrete-event dynamic systems

DEM	Discrete element method
GB	Glass beads
GFO	General function optimisation
GLM	Generalised linear model
GRSM	Generalised response surface methodology
GUI	Graphical user interface
INT	Intermediate
LVDT	Linear variable differential transformer
MAJ	Major
MIN	Minor
MES	Microsoft Excel Solver algorithm
NFD	Normal force-displacement
NMRI	Nuclear magnetic resonance imaging
ODEG	Optimum desirability at exact grid points
PEPT	Positron emission particle tracking
PET	Polyethylene terephthalate
PIV	Particle image velocimetry
PP	Polyethylene terephthalate pellets
RDP	Response Desirability Profiling
RF	Rainfall filling method through a sieve
RSM	Response surface methodology

Chapter 1

Introduction

1.1 General background

From pharmaceutical powders to agricultural grains, a great proportion of the materials handled in industrial situations are of granular or particulate nature. The variety of stresses and deformation regimes that granular materials may experience in industrial scenarios are complex and these have been the centre of a great deal of research over the last century. In agricultural engineering, a better understanding of agricultural processes such as seeding, harvesting, transporting and storing will help to improve the handling of agricultural grains and provide optimised solutions.

In recent years, the discrete element method (DEM), developed by Cundall and Strack (1979) has been used extensively to investigate the behaviour of granular solids subjected to a variety of loading conditions with the goal of understanding and predicting quantitative results. As numerical capabilities are rising, DEM is becoming an increasingly popular numerical technique for computing the behaviour of discrete particles for both industrial and scientific applications.

Although DEM has been shown to be a very promising tool, a look into the literature shows a lack of careful validation of the predictive capabilities of DEM as input parameters were often assumed and not measured. In addition, validation studies comparing experimental results and simulations based on measured particle properties have shown some discrepancies (Chung 2006). This has led to the question of whether DEM is capable of producing quantitative predictions rather than only a qualitative representation of a particulate assembly.

1.2 Objectives and scope of this research

The aim of this research was to develop a methodology to calibrate DEM models for agricultural grains using data measured in bulk physical tests. The methodology will have a wider application to granular solids in general and should advance the understanding in the area of DEM model calibration. Secondary objectives were to explore the differences in bulk physical behaviour for a range of contrasting grains in several bulk tests. In addition, a detailed investigation of DEM input parameters on numerical bulk behaviour should provide a useful insight into the development of the parametric optimisation procedure. The work presented in this thesis includes:

I. The development of two bulk calibration tests that will provide the test data necessary to calibrate the DEM models as well as identify contrasting characteristics from a range of granular materials. The chosen physical tests were a rotating drum and a confined compression test.

II. A comprehensive parametric study to investigate the influence of particle (micro) scale parameters on the chosen bulk (macro) response parameters, specifically the dynamic angle of repose in the rotating drum and the bulk loading and unloading stiffness in the confined compression test.

III. Producing a numerical dataset of the bulk tests that will describe how the DEM parameters influence the numerical bulk responses. The matrix of simulations will provide a set of data that will be used in the development of a parametric optimisation procedure.

IV. Finally, a verification and validation of the parametric optimisation procedure in a large scale experiment was carried out on a set of optimised parameters.

1.3 Structure of thesis

The thesis is divided into eight chapters. A brief outline of each chapter is described below.

Chapter 1 presents the background, objectives and scope of this research

Chapter 2 reviews the literature relevant to this thesis. It focuses on the various flow regimes that may exists in a rotating drum, loading conditions in granular materials, previous research with regards to experimental validation of DEM simulations, experimental design methods and optimisation techniques.

Chapter 3 describes the selection of the two laboratory devices and the measured bulk response parameters that were used to calibrate the DEM models in the optimisation procedure. These include the dynamic angle of repose in a rotating drum and the bulk stiffness parameters in a confined compression test. Furthermore, a summary of the particle and bulk material properties of the five various materials used in this thesis are presented.

Chapter 4 summarises the results obtained from the two laboratory tests for each granular material whilst highlighting and discussing the key findings. Focus was placed on the bulk response parameters used to calibrate the DEM models.

Chapter 5 focuses on the numerical DEM implementation used to simulate the rotating drum apparatus and the confined compression test. Furthermore a detailed parametric investigation is described focusing on the non-optimised parameters and their influence on the bulk response parameters. Three further sensitivity analyses to explore the effect of geometric scaling, compression rate and particle stiffness on the confined compression simulation are described.

Chapter 6 describes the development of the parametric optimisation procedure by assembling the outcomes in the previous chapters of the thesis in a series of steps. To conduct a comparative study, two searching techniques were used in the optimisation procedure; the first was based on the Microsoft Excel's Solver algorithm coupled with a weighted inverse distance

method and the second used the statistical analysis program Statistica. Finally, a set of optimised parameters for each granular material is determined.

Chapter 7 investigates the verification and validation of the optimisation procedure using the optimised parameters for black eyed beans. The parameters are verified using the same system as the numerical dataset and validated in an industrial scenario. The validation was conducted by comparing the experimental results of a footing penetration test with the numerical results simulated using the optimised parameters.

Chapter 8 summarises the general conclusions of the whole thesis and makes recommendations for further work.

Chapter 2

Literature review

2.1 Introduction

A great proportion of the materials handled in industrial situations are granular in form. The loading conditions of granular materials can be complex in nature and has been the centre of a great deal of research over the last century. In recent years, DEM developed by Cundall and Strack (1979) has been used extensively to investigate the behaviour of granular solids subjected to a variety of loading conditions in the goal of understanding and predicting quantitative results.

The intention of this chapter is not to present an exhaustive and comprehensive review of granular solids research, but to focus on the main topics which are directly related to the work discussed in this thesis. This review consists of five main parts:

- A brief review of DEM
- A review of granular loading experiments and numerical simulations
- A review of the rotating drum, covering physical experiments and numerical simulations

- Experimental validations of DEM simulations
- Experimental design and optimisation techniques

2.2 A brief review of discrete element method

The literature on DEM has been covered extensively in the past (Kremmer and Favier 2001; Chung 2006; Härtl 2008). This literature review on DEM will therefore be concise and focus only on the key aspects related to this study.

2.2.1 Overview

DEM is an increasingly popular numerical technique for computing the behaviour of discrete particles. This method was originally applied by Cundall (1971) to problems in rock mechanics. The method is based on the use of an explicit numerical scheme in which the interactions between a finite number of particles are monitored contact by contact and the motion of the particles is modelled particle by particle. Each contact follows a soft contact approach where an overlap of particles is accepted. This overlap is not a real phenomenon but instead intends to model the deformation of the interacting bodies at a contact point in an indirect way. The parties are treated as rigid bodies and the overlap during a contact is assumed to be relatively small compared to the particle size.

In contrast to static continuum analysis, Newton's equations of motion for each particle effectively replace the equilibrium equations used in continuum mechanics, and the model of inter-particle contacts replaces the constitutive model. The main difference to this approach is that each particle is modelled separately so that the integrated behaviour of the mass should be accurately represented, without the need for control tests to establish constitutive models for the bulk behaviour.

The DEM scheme relies upon the assumption that a small enough time step should be chosen to ensure that, during a single time step, others disturbances do not propagate from any particle further than its immediate neighbours. DEM has the capacity of modelling materials at microscopic levels and analysing multiple interacting bodies undergoing large displacements and rotations, thus capturing all the phenomena that relates to the particulate nature of granular mediums. Following the pioneering work of Cundall and Strack in 1979, research into DEM has

increased dramatically in light of its potential. The last 25 years has seen DEM being researched and utilised in many industries and for various purposes, a few of which are listed below.

- Fundamental investigation and application of DEM in granular soils, rocks, pharmaceutical powders, chemical pellets, agricultural grains, coals and other minerals;
- Development of improved contact force models;
- Development of representation for non-spherical particles and complex boundary geometry;
- Experimental validation of the DEM;
- Development of coupled modelling methods. For example, DEM and finite element method as well as DEM and computational fluid dynamics (CFD);
- Large-scale industrial applications of DEM.

The equations given in this section are primarily for completeness and are largely from the manuals of the DEM simulation software EDEM (DEM Solutions Ltd 2009) and PFC3D (Itasca 2003), and the work of Chung (2006) and Härtl (2008).

2.2.2 Contact Model

The overall behaviour of a material is simulated by attributing a simple constitutive model with each contact. Essentially, the contact model describes how elements will behave when they come into contact with each other. Several contact models have been developed over the years and can be categorised into three groups:

- Contact stiffness models
- Slip models, and
- Bonding models

Contact stiffness models provide an elastic relation between the contact force and the relative displacement. Examples of the contact stiffness model include the *linear* and *Hertz-Mindlin* models. The bonding model serves to limit the total normal and shear forces that the contact can carry by enforcing bond strength limits.

2.2.2.1 Hertz-Mindlin no slip contact model

Due to its efficient and accurate force calculations, the most commonly used contact model is the Hertz-Mindlin no slip contact model. The Hertz-Mindlin no-slip contact model with damping and a frictional slider in the tangential direction (Tsuji et al. 1992), shown schematically in Figure 2.1, is briefly reviewed in this section.

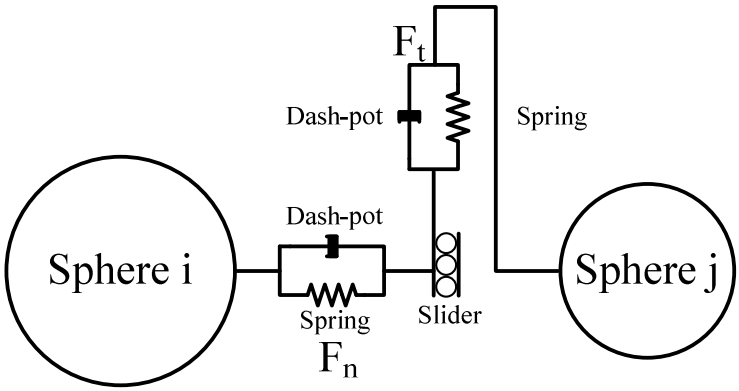

Figure 2.1 Spring dash-pot contact model

In Figure 2.1, sphere *i* is in contact with sphere *j*, the normal component of the contact force, F_{CN}, acting on sphere *i*, is given by the sum of the normal spring force $F_{CN,S}$ and normal damping force $F_{CN,D}$ as

$$F_{CN} = F_{CN,S} + F_{CN,D} \quad \text{Equation 2.1}$$

where,

$$F_{CN,S} = -K_n \propto_n{}^{1.5} \quad \text{Equation 2.2}$$

$$F_{CN,D} = -2 \cdot \sqrt{\frac{5}{6}} \cdot \beta_d \cdot \sqrt{m^* \cdot k_n \cdot V_{relative,n}} \quad \text{Equation 2.3}$$

where α_n is the normal contact displacement (overlap), $V_{relative,n}$ is the relative normal velocity (from sphere *i* to sphere *j*), β_d is a damping ratio and k_n is the normal contact stiffness. Equation 2.2 and Equation 2.3 are based on the Hertz contact theory (Johnson 1987) and give a non-linear elastic relationship between the normal contact force and normal contact displacement. The Hertz contact constant K_n is given by

$$K_n = \frac{4G \cdot \sqrt{r^*}}{3(1-\upsilon)} \qquad \text{Equation 2.4}$$

where G is the shear modulus, υ is the Poisson's ratio and the terms m^* and r^* are the equivalent mass and radius.

The tangential component of the contact force, F_{CT}, is similarly given by the sums of the tangential spring force $F_{CT,S}$ and the tangential damping force $F_{CT,D}$ as

$$F_{CT} = F_{CT,S} + F_{CT,D} \qquad \text{Equation 2.5}$$

$F_{CT,S}$ is normally expressed in incremental form as

$$F_{CT,S} = F_{CT,S,(n-1)} + \Delta F_{CT,S} \qquad \text{Equation 2.6}$$

where $F_{CT,S,(n-1)}$ is the spring force at the previous time step and $\Delta F_{CT,S}$ is the increment of the tangential spring force. The increment $\Delta F_{CT,S}$ is given by

$$\Delta F_{CT,S} = k_t \cdot \Delta \alpha_t \qquad \text{Equation 2.7}$$

where k_t is the tangential contact stiffness and $\Delta \alpha_t$ is the incremental tangential displacement.

The tangential damping force $F_{CT,D}$ is given by

$$F_{CT,D} = -2 \cdot \sqrt{\frac{5}{6}} \cdot \beta_d \sqrt{m^* \cdot k_t \cdot V_{relative,t}} \qquad \text{Equation 2.8}$$

where $V_{relative,t}$ is the relative tangential velocity. Throughout this thesis, unless explicitly stated, the non-linear elastic Hertz-Mindlin contact was used.

2.2.2.2 Elasto-plastic contact model

During the loading of granular materials in a confined compression test, the plastic deformation in the solids is a result of two phenomena:

1. The relative displacement of particles through rolling or sliding, and
2. Plastic deformation of the particles at the points of contact.

In DEM simulations, relative displacement occurs naturally. However, plastic deformation at the points of contact is often ignored in the numerical contact, including EDEM (DEM Solutions Ltd 2009), the DEM program used in this thesis. EDEM uses a non-linear elastic contact model. Therefore for soft agricultural grains, EDEM is expected to underestimate the total plastic deformation of the system.

Previous attempts to account for the effects of plasticity in the contact model have been conducted (Vu-Quoc et al. 2000; Vu-Quoc and Zhang 1999). Vu-Quoc and Zhang (1999) accounted for plastic deformation using a simple and accurate model for the normal force-displacement (NFD) relation for contacting spherical particles based on the formalism of the continuum theory of elasto-plasticity.

2.2.3 Non-spherical particles

Three dimensional simulations carried out using DEM software have more often than not used spherical particles as they have the advantage of computational simplicity, where every sphere can be described by a centre point and a radius. Spherical particles roll and rotate within an assembly to a greater degree than non-spherical particles due to the lack of interlocking forces

between them. Several methods of representing non-spherical particles have been developed to overcome this problem. The most commonly used method is to create non-spherical particles with a number of primitive elements (three dimensional spheres) that are mutually connected in a rigid way, as these elements require the simplest contact detection algorithm (Kremmer and Favier 2000; Favier et al. 2001; Matsushima 2004). Using this multi-spherical method it is possible to create a clump of spheres with varying sizes and positions which may be overlapped to create a desired shape. Contacts found within a clump are skipped during calculations, reducing the simulation time. The multi-spherical shapes act as a rigid indestructible body regardless of the forces acting upon it.

The motion path of the non-spherical particle is determined by the resultant force and the moment vector acting upon it. As the particle is treated as a rigid body, its trajectory can be described in terms of the translational motion taken from a point in the particle and the rotational motion of the entire particle. The translational motion of the centre of mass is described in terms of its position $\vec{x}_G$, velocity $\dot{\vec{x}}_G$ and it acceleration $\ddot{\vec{x}}_G$, whilst the rotational motion of the particle is described in terms of the angular velocity $\vec{\omega}$ and the angular acceleration $\dot{\vec{\omega}}$. The translational and rotational motions can be described by the vectors in Equation 2.9 and Equation 2.10 respectively, where $\vec{F}$ is the resultant force vector which includes the sum of all externally applied forces acting on the clump, m_p is the total mass of the particles and $\vec{g}$ is the gravity acceleration vector. $\vec{M}_G$ is the resultant moment vector taken about the mass centre and $\dot{\vec{H}}$ is the time rate of change of the angular momentum about the centre of the mass.

$$\vec{F} = m \cdot \left(\ddot{\vec{x}}_G - \vec{g}\right) \qquad \text{Equation 2.9}$$

$$\vec{M}_G = \dot{\vec{H}} \qquad \text{Equation 2.10}$$

2.2.4 Damping

Energy may be dissipated in two ways in DEM; frictional sliding and damping. Frictional sliding is a real phenomenon, whereas damping is artificially introduced to dissipate energy to achieve a steady state packing within a reasonable time frame. In EDEM this is done by

specifying a coefficient of restitution. DEM software, such as PFC3D, support two forms of damping; viscous and global damping (sometimes referred to as local damping). Global non-viscous damping dissipates energy in the whole system through damping of the equations of motions by including a damping force term to the equations of motion. The advantages of using this form of damping include:

- No erroneous damping forces arise from steady-state motion as the accelerating motion is the only term that is damped,
- The damping term is dimensionless, and
- Regions of the assembly with different natural periods are damped equally using the same damping constant as damping is frequency independent.

Viscous damping approximates plastic straining of surfaces asperities (Munjiza 2004). When using viscous damping, normal and shear dash-pots are added to each contact as illustrated in Figure 2.1. These dash-pots act in parallel to the existing contact model and the contact force is attenuated with a damping force. Viscous damping is characterised by the critical damping ratio β_d. The damping ratio is related to the coefficient of restitution e_r and this relationship is given by (Tsuji et al. 1993)

$$\beta_d = -\frac{\ln e_r}{\sqrt{(\ln e_r)^2 + \pi^2}} \qquad \text{Equation 2.11}$$

When $\beta_d = 1$, the system is said to be critically damped and the response will decay to zero at the fastest rate. Furthermore, $\beta_d = 1$ represents the transition from an oscillatory response, when $\beta_d < 1$, to an exponentially decaying response when $\beta_d > 1$. When $\beta_d < 1$, the system is said to be under damped, or slightly damped. When $\beta_d > 1$ is said to be overdamped of heavily damped (Ginsberg and Genin 1984).

2.2.5 Rolling friction model

Conventional DEM models use springs and dampers in the normal and tangential directions to describe particle to particle and particle to boundary interactions. However, this does not account for the rotation of particles. Research using experimental and numerical studies

has highlighted the importance of incorporating a torque in the rotational direction to account for the rolling resistance or rolling friction.

The concept of rolling friction was probably first introduced into DEM modelling by Sakaguchi et al. (1993) when conducting a comparison study of experimental and numerical modelling of plugging of granular flow during silo discharge. Zhou et al. (1999) proposed a rolling friction model based on experimental and theoretical analyses of Beer and Johnson (1976) and Brilliantov and Pöschel (1998). In their model, the rolling frictional torque is proportional to the normal contact force with its direction always opposite to the relative rotation. Using this model, they managed to produce stable piles with coarse spheres. This is the basis of the model termed by Ai et al. (2010) as model A.

The coefficient of rolling friction μ_r is a scalar value used to determine how much torque is needed to be applied to an object of a given material at rest on a flat surface to put it into motion. The rolling friction model used throughout this thesis is based on model A. In this model, the direction of the torque is always against the relative rotation between the two contact entities. The torque is applied on each pair of particles in contact and can be expressed as

$$\tau_i = -\mu_r F_n R_i \omega_i \qquad \text{Equation 2.12}$$

where R_i the distance of the contact point from the center of mass and ω_i the unit angular velocity vector of the object at the contact point. The main disadvantage of using this model is its simplistic approach to rolling friction estimation.

Ai et al. (2010) developed a more detailed rolling friction model, termed the *elastic-plastic spring-dashpot* model, which is based on the previous works of Iwashita and Oda (2000) and Jiang et al. (2005). The torque in the models consists of two components: a mechanical spring torque (dependent on the relative rotation between the two contacting entities) and a viscous damping torque.

2.2.6 Time-step

The time step referred to in DEM simulations is the duration between two consecutive iterations. DEM usually uses an explicit and central time-finite-difference scheme. Although this explicit numerical scheme is more computationally efficient than the implicit numerical scheme,

there is a limitation that it is only conditionally stable; so small time steps must be used. If the used time step is greater than a critical time step, the scheme is unstable and the simulation outcomes are unreliable. Within a group of particles, the force transmission between individual particles is through the Rayleigh wave that travels around the surface of the elastic bodies. The time step that should be used in a DEM simulation is chosen so that the time step for calculating the incremental forces and displacements must be less than the time it takes for the wave to transverse the minimum size particle within the group of particles. The Rayleigh wave velocity of force transmission between individual particles is given by Li et al. (2005) as

$$V_R = \chi \cdot \sqrt{\frac{G}{\rho_s}} \qquad \text{Equation 2.13}$$

where ρ_s is the particle solid density and G is the particle shear modulus in the system. χ is a Poisson's ratio depended parameter that can be obtained from (Li et al. 2005)

$$(2-\chi^2)^4 = 16 \cdot (1-\chi^2) \cdot \left(1-\chi^2\left(\frac{1-2\cdot v}{2\cdot(1-v)}\right)\right) \qquad \text{Equation 2.14}$$

This can be approximated by (Ning and Ghadiri 1996)

$$\chi = 0.1613 \cdot v + 0.8766 \qquad \text{Equation 2.15}$$

For a granular assembly consisting of particles with the same properties, the critical time step can be described by (DEM Solutions Ltd 2009)

$$T_R = \pi r^2 \left(\frac{\rho}{G}\right)^{\frac{1}{2}} \Big/ (0.1631\upsilon + 0.8766) \qquad \text{Equation 2.16}$$

where r is the radius of the smallest particle in the system, ρ_s is the particle density, G the shear modulus and υ the Poisson's ratio. For a system with material of different properties, the smallest critical time step for the various materials should be chosen.

Selecting a suitable time step for running the numerical simulation is crucial to increase the computational efficiency. Itasca (2003) suggests that when running simulations with a Hertz-Mindlin contact model, a time step which is 80% of the critical time step for general simulations and 25% for dynamic systems is sufficient. DEM Solutions recommend a 20% for densely packed systems and 40% for looser assemblies when using their DEM code in EDEM. Chung (2006) found that 20% of the critical time step was sufficient for the majority of systems which were predominantly quasi-static. Contact force distributions and particle velocities will be investigated in this thesis to determine which time step is the most appropriate.

2.2.7 Shape representation accuracy

Particle shape representation is an important aspect in DEM simulation. Creating a more accurate representation of irregular shapes such as agricultural grains (Kremmer & Favier 2000; Tijskens et al. 2003; Chung & Ooi 2006; Härtl & Ooi 2008) requires more spheres per particle and will increase the computational time. It has been suggested (Chung 2006; Härtl 2008) that an accurate geometrical representation of a granular material does not necessarily lead to a more accurate prediction of the bulk behaviour and that often quite crude representations with fewer numbers of spheres can produce similar results, thereby reducing the computational time.

This thesis aims to investigate the relative effect of the level of shape representation required for a satisfactory prediction and will provide guidance on how to approach the question of particle shape in DEM simulation.

2.3 Loading condition in granular materials

The loading conditions of granular materials may produce complex and unpredictable bulk behaviour but are present in many industries, and as a result have been a centre of research for the better part of a century. In recent years, DEM (Cundall and Strack 1979) has been used extensively to investigate the behaviour of granular solids subjected to a variety of loading conditions, with the goal of understanding and predicting quantitative results. This section will review some of the concepts of soil mechanics with respect to granular materials.

2.3.1 Phase relationships, void ratios and porosity analysis

A typical multi phase granular solid is comprised of two phases; a solid skeleton and a void (liquid and/or air) as demonstrated by the phase diagrams in Figure 2.2 (Craig 2004).

(a) Phase diagram (b) Arranged phase diagram

Figure 2.2 The various phases of a typical soil represented in a phase diagram

The granular systems described in this thesis are comprised entirely of solids (the material being tested) and air voids between the particles, therefore, the phase relationship diagram can be expressed using air and solid as shown in Figure 2.3. The void fraction is often described in two ways:

- Void ratio *e* is the volume of voids per unit volume of solid and
- Porosity *n* is the volume of void per unit volume of soil

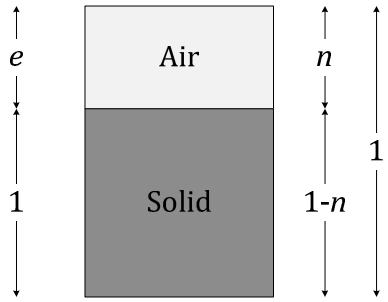

Figure 2.3 The definition of void ratio and porosity in soils (Craig 2004)

The void ratio, e is a ratio of the volume of void to the volume of solid and can be described as

$$e = \frac{V_v}{V_s} \qquad \text{Equation 2.17}$$

where,

$$V_s = \frac{M_s}{\rho_s}, \qquad V_v = V - V_s \qquad \text{Equation 2.18}$$

where V_v and V_s are the volumes of void and solids respectively, V is the total volume of the system and M_s is the mass of solids.

2.3.1.1 Compression, consolidation and bulk stiffness parameters

Applying a load to a soil will cause the soil to compress. This time dependent process is known as consolidation, whereas the relationship between the volume of the soil and the effective stress is termed compression. As a sample is loaded during compression, the volume of voids will decrease in turn reducing e, and vice versa during unloading. When e is plotted against the vertical stress, σ_v the curve is non-linear over a small range of stresses. When e is plotted against $log_{10}\sigma$ the relationship is found to be linear over a wide range of stresses. This semi-logarithmic plot (Figure 2.4) is in line with the classical concept of normal consolidation and overconsolidation in soil mechanics (Craig 2004). The gradient of the loading and unloading lines are used to describe the stiffness of the sample, and are termed the bulk loading λ and unloading κ stiffness parameters.

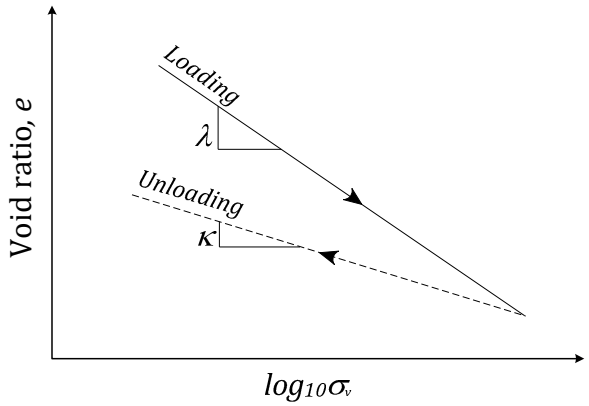

Figure 2.4 Classical concept of normal consolidation and overconsolidation in soil mechanics using semi-logarithmic plot of void ratio versus vertical stress

Based on the assumption that the loading and unloading trends in the semi-log plot are linear, the trendlines can be described as

$$\frac{de}{d(\ln \sigma)} = -\lambda \qquad \text{Equation 2.19}$$

$$\frac{de}{d(\ln \sigma)} = -\kappa \qquad \text{Equation 2.20}$$

2.3.2 Numerical modelling of granular systems

The past few decades has seen a large growth of Computer Aided Engineering (CAE) programs that model industrial applications. In recent years, the numerical modelling of granular materials using DEM has been used extensively to investigate the behaviour of granular solids subjected to a variety of loading conditions. However, the majority of the numerical computations were often assumed and not validated with experimental results. There is a question as to whether DEM is capable of producing quantitative predictions rather than only qualitative representations of a particulate assembly. Chung (2006) highlighted the necessity to verify DEM calculations and to investigate the relative importance of the DEM input parameters to produce satisfactory predictions. He investigated the DEM computations of a densely packed granular medium subjected to compression and penetration. He observed the mechanical

response of the granular system and the load transfer to the containing using glass beads (GB) and agricultural materials. A comparative study between the physical experiments and closely simulated numerical experiments was conducted. Chung (2006) found that DEM could produce quantitative predictions of the confined compression and rod penetration systems, and whilst it is important to use the correct particle stiffness parameter when attempting to predict the deformation response of a granular assembly, this may not be so important for producing satisfactory prediction of the force transmission in a dense quasi-static system.

2.4 Rotating drums and tumbling mills

Understanding the behaviour of granular materials is of great technological interest and has been an area of research for over 200 years. A special interest has been placed on granular materials in tumbling mills and rotating drums as its usage is present in a wide range of industrial sectors from agricultural to mineral mining and they are used in size reduction, mixers, dryers, granulators and reactors for processing granular materials. As a result, the material behaviour in rotating drums has attracted numerous research efforts from both engineering and physics communities over the past few decades that have attempted to analyse and describe the granular behaviour using experimental and numerical techniques. The majority of research carried out on rotating drums has focused on flow regimes at lower rotational speeds as this is the most common speed range found in industrial situations.

2.4.1 Flow regimes and drum terminology

The flow regimes that exist within a rotating drum have been linked to many parameters including the end plate sliding friction, fill volume, drum depth, particle shape and size, the Froude number and rotational speed to name a few (Rutgers 1965; Metcalfe et al. 1995; Dury et al. 1998; Ding et al. 2001; Santomaso et al. 2003; Yang et al. 2008). These will be covered in more detail in this section. Although the flow description for the various flow regimes is consistent, the terminology adopted may vary. The terminology used in this thesis is predominantly based on Henein et al. (1983) and Mellmann (2001). The drum terminology used in this thesis is shown in Figure 2.5.

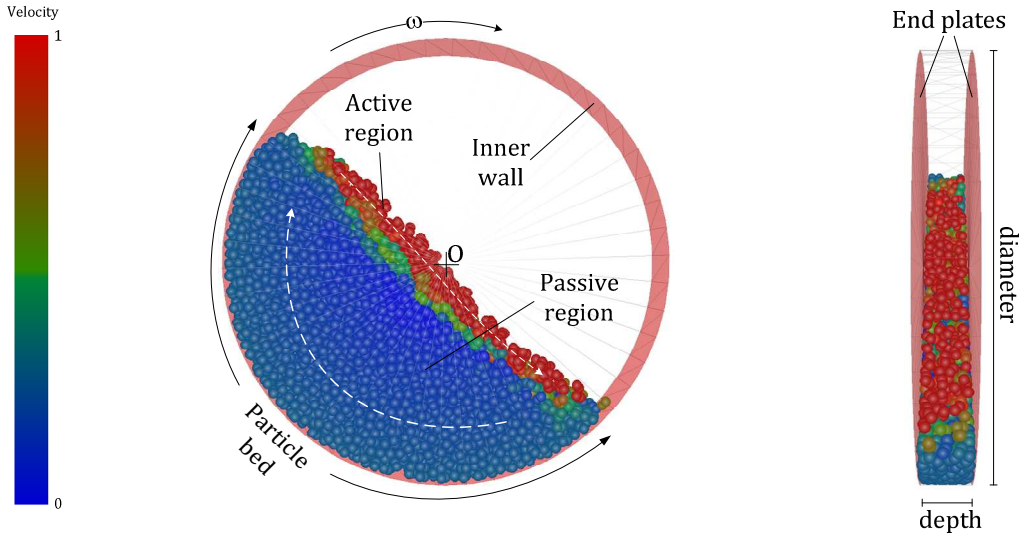

(a) Transverse view (b) Side view

Figure 2.5 Rotating drum terminology adopted in the thesis

where,

- The *inner drum wall* is the section lining the inside of the drum and should not be confused with the e*nd plates* which are the circular plates on either side of the drum, confining the granular materials.
- The *Diameter* of the drum is defined as the diameter of the transverse section and the *depth* of the drum is defined as the distance between end plates.
- The *passive region* is where the particles are carried up the inner drum wall and the *active region*, referred to as the fluidised region by Ristow (1996), is the region where the particles cascade down the surface.
- The *surface profile* is defined as the top layer of particles which are exposed and used to determine the surface inclination angle.
- The *particle bed* is the circumferential distance where the granular material lines the inner drum wall, and the *bed overturn time* is the time required to turn the whole particle bed over once (Ding et al. 2002).
- The *drum filling degree f* is the percentage of the granular material volume to total volume.

The various flow regimes that may exist within a drum have been covered extensively, notably by Mellmann (2001) who identified 3 main groups of flow regimes within a drum;

1. Slipping motion
2. Avalanching (referred to cascading by Mellmann 2001), and
3. Cataracting

Mellmann (2001) used the rotational Froude number Fr, drum filling degree f, the particle to wall μ_{pw} and the critical particle to wall $\mu_{pw,c}$ coefficient of friction to delimit the various flow regimes. Where Fr is defined as the ratio of centrifugal to gravitational forces and $\mu_{pw,c}$ is there critical wall friction fort the transition from a slipping to avalanching regime.

The various motions of granular material in a rotating drum are shown in Figure 2.6 and described below.

Slipping regime

The slipping motion in a rotating drum can manifest itself through *sliding* and *surging*. Sliding may occur as a result of low rotational speeds, ω (according to Rutgers (1965) at very high ω as well), high degrees of filling or when the drum material is smooth, and is characterised by the particle bed constantly sliding along the inner drum wall. A low surface profile inclination angle is generally observed and the granular material does not appear to move position in a "standing state". As the drum speed or μ_{pw} increases, sliding turns into *surging*, where intermittent slip-stick behaviour is observed along the material bed. During surging, the material goes through periodic cycles of adhering to the inner drum wall until a certain inclination is reached and the material subsequently slides down. Throughout the slipping regime, no mixing of the particles occurs as the granular materials effectively act as one solid mass.

Basic Form	Slipping regime		Avalanching regime			Cataracting regime	
Subtype	Sliding	Surging	Slumping	Avalanching	Cascading	Cataracting	Centrifuging
Schematic	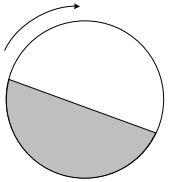	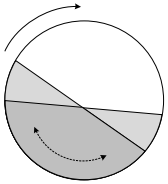	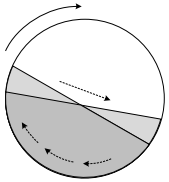	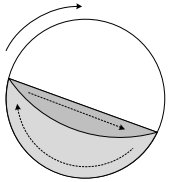	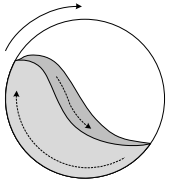	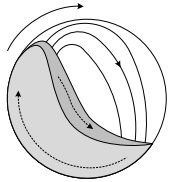	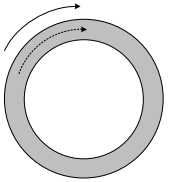
Physical process	Slipping		Mixing			Crushing	Centrifuging
Rotational Froude number [Fr]	$0 < Fr < 10\text{-}4$		$10\text{-}5 < Fr < 10\text{-}3$	$10\text{-}4 < Fr < 10\text{-}2$	$10\text{-}3 < Fr < 10\text{-}1$	$0.1 < Fr < 1$	$Fr \geq 1$
Wall friction	$\mu_{pw} < \mu_{pw,c}$	$\mu_{pw} \geq \mu_{pw,c}$	$\mu_{pw} > \mu_{pw,c}$			$\mu_{pw} > \mu_{pw,c}$	
Industrial application	No use		Rotary kilns and reactors, rotary dryers and coolers, mixing drums			Ball mills	No use

Figure 2.6 Transverse flow regimes of solids in rotating drum (after Mellmann 2001)

Avalanching regime

Also referred to as the cascading or tumbling regime, during the avalanching regime there is a continuous circulation of granular material and is generally a result of sufficient μ_{pw} and ω to avoid slipping. The avalanching can be subdivided into *slumping*, *avalanching* and *cascading*.

During *slumping*, the material bed is carried along the inner drum wall and continuously levelled, as the highest particles intermittently roll along the surface profile. Metcalfe et al. (1995) investigated the effects of the drum fill level on the particle intermixing and demonstrated that the effects were greatly reduced when fill volumes exceeded 50%.

As ω increases, the regime transitions to an *avalanching* motion, where a uniform static flow develops as particles are carried up the inner wall and a constant flow of particles avalanche along the surface. During this regime, a flat surface profile with a constant inclination forms the dynamic angle of repose ϕ_r of the particles. In addition, no more slippage along the inner wall is visible as $\mu_{pw} > \mu_{pw,c}$. Increasing ω further will see the transition to a *cascading* regime, where the surface profile arches slightly and an S-shape develops. The height of the S-shape is dependent on ω, μ_{pw} and particles size (Mellmann 2001).

Due to the consistent flowing of particles and mixing patterns observed in the drum without particle bed slippage, the avalanching regime is the most widely used for industrial applications. For similar reasons, including a stable dynamic ϕ_r, rotating drum experiments conducted in this thesis have focused on the avalanching regime.

Cataracting regime

At very high ω, the flow pattern within a drum will transition from cascading to cataracting, where particles will detach from the top of the surface profile and are thrown into the unfilled drum space. There are two main forms of cataracting; *cataracting* and *centrifuging*.

During *cataracting* particles are thrown into unfilled drum space, and as the ω increases, the height and distance of the particles' trajectory increases. Increasing ω further will cause the particles to line the inner drum wall with a uniform layer of particles in a regime known as *centrifuging*, similar to a washing machine's drying cycle. There are very little industrial applications for this regime and a result is rarely studied.

2.4.2 Rotating drum experiments

The wide range of flow regimes that may exist within a rotating drum have been discussed in the previous section (2.4.1). This section will focus on the research that has been carried out on the rotating drums and tumbling mills. The majority of research carried out on rotating drums has focused on flow regimes at lower speeds such as slumping and avalanching as their industrial significance and application stretch further than research of cataracting and centrifuging.

The dynamics, mixing and separation of granular materials in partially filled rotating drums has been the centre of a larger range of experimental and theoretical investigations (Khakhar et al. 1997; Boateng and Barr 1997; Rao et al. 1991). However, these studies did not attempt to describe a continuous granular flow in a transverse plane of a rotating drum or the boundary value approximation which is used to describe a two dimensional granular flow. Elperin and Vikhansky (1998) developed an approach that considers the transition from slumping to avalching (referred to by Elperin and Vikhansky (1998) as the transition from solid to liquid-like behaviour) as a key process for specifying the granular dynamics. Their experiments included analysing the flow of granular material in a partially filled rotating cylinder using a boundary layer approach which involved deriving simple equations to describe the granular dynamics in a transverse plane; a small parameter was recognised, then a derived equation was solved analytically in the first-order approximation of the small parameter. They were able to establish in a close analytical form, the cascading layer thickness, mean velocity along the layer and profile of the free surface. Similar research was carried out by Ding et al. (2002) who investigated the motion of the particles during the flow regimes at low rotational speeds. They determined the flow regimes transition in terms of bed turnover time, building on their earlier work (Ding et al. 2001; Forster et al. 2001), where they investigated the particle motion in the transverse plane of a three-dimensional rotating drum operated at low to medium rotational speeds. The earlier work of Ding et al. (2002) focused on the particle exchange between the active and passive regions of the drum flow as their interests were in the mixing process within a drum. Mixing and segregation in rotating drums has been covered extensively (Rao et al. 1991; Metcalfe et al. 1995; Boateng and Barr 1997; Laurent et al. 2002; Sherritt et al. 2003; Kuo et al. 2006; Zuriguel et al. 2006; Chou and Lee 2009) as it is especially important

when dealing with finer granular solids such as powders or when a variety of different granular solids exists within the drum.

Santomaso et al (2003) conducted comprehensive experiments to investigate granular behaviour in a drum operated over a wide range of rotational speed, with granular solid motions covering the avalanching, cascading and cataracting regimes. They described the granular materials bed behaviour as a function of rotational speed, drum fill level and particle size. This eventually led to the description of the surface profile expressed in terms of various characteristic lengths, operating condition and sliding friction properties. Their findings had the advantage of being applicable to a wide range of rotational speeds and flow regimes.

Yang et al. (2008) investigated the granular flow dynamics in a rotating drum for different regimes using DEM, by varying the rotation speed. They found that the dynamic angle of repose, ϕ_r formed by the particle surface had a weak dependence on the rotation speed during the slumping and avalanching regimes, whereas during the cascading, cataracting and centrifuging regimes the influence increased significantly.

Rotational Froude number

The rotational Froude number, Fr (referred to by Walton and Braun 1993 as the non dimensional rotation rate Ω^2) expresses the ratio of centrifugal to gravitational forces within a rotating drum and is a dimensionless coefficient. It is commonly used in the analysis of flow regimes within a rotating drum (Henein et al. 1983; Elperin and Vikhansky 1998; Ding et al. 2001; Mellmann 2001; Orpe and Khakhar 2001). The Froude number can also be used to scale the rotating drum (as the centrifugal forces are proportional to the diameter); however, Bell (2005) noted that particulate processes scaling should be done with extreme caution as the granular materials behave differently at different scales, unlike gases and liquids. When $Fr = 1$, the gravitational forces are equal to the centrifugal forces and results in the granular material adhering to the inner drum wall as the centrifuging flow regime occurs. Mellmann (2001) linked the various flow regimes in a rotating drum to Fr and showed that avalanching typically occurs for Fr between 10^{-4} and 10^{-2} (assuming a filing degree $> 10\%$) and also found that centrifuging occurs when $Fr > 1$ (See section 2.4.3 for more details).

Non-invasive methods of extracting data from the rotating drum

The microscopic and macroscopic data extraction from DEM simulations is relatively simple compared to similar physical experiments. Many researchers have developed or used non-invasive techniques to extract data from rotating drum in an effort to describe flow regimes and granular behaviour in more detail. Several methods are described in this section.

The simplest method for tracking a particle is to label a particle by colouring it; which aids visual tracking with the use of video recording equipment. Some researchers are able to acquire accurate three dimensional experimental particles trajectory data from a tumbling mill using a Bi-planar angiographic x-ray (McBride et al. 2004; Powell and McBride 2004; Govender et al. 2004). Nuclear Magnetic Resonance Imaging (NMRI) has been used to determine the dynamic angle of repose, ϕ_r formed in a deep drum (Dury et al. 1998) and monitoring the velocity profiles at various locations within the drum (Nakagawa et al. 1993; Nakagawa et al. 1997). Another method that is often used is Positron Emission Particle Tracking (PEPT) and enables a single radioactive tracer particle moving inside a piece of equipment to be tracked accurately at speeds up to 2 *m*/*s*. It is a popular techniques to trace particles in a rotating drum (McBride et al. 2004; Ding et al. 2001; Santomaso et al. 2003; Lim et al. 2003) as it non invasive, accurate and allows position data to be extracted from deeper drums where visibility is restricted. Particle Image Velocimetry (PIV) techniques have been used to determine the velocity profiles that exist within rotating drum (Zhang et al. 2006), however, PIV techniques have been shown to be less accurate than MRI, PEPT and Bi-planar angiographic x-ray at tracking single particles within a drum.

Many of the methods mentioned here are very expensive and time consuming to use. As the drum setup used in the thesis was relatively thin (drum diameter/depth=9.2) and made from clear acrylic (which allowed the granular material flow to be clearly visible) non-invasive data extraction techniques were not required.

2.4.3 Theoretical analysis of rotating drums

Walton and Braun (1993) investigated centrifuging a drum using dynamic particle simulations. They defined the ratio of the centrifugal force, F_c to gravitational forces F_g of a particle along the inner drum wall as the rotational Froude number (Equation 2.21) which is irrespective of particle mass.

$$Fr = \frac{r \cdot \omega^2}{g}$$ Equation 2.21

where r is the inner drum radius, g the gravitational constant and ω the angular velocity of the drum. At $Fr = 1$, the centrifugal forces at the top of the drum just cancels gravity on a particle moving along with the outer wall. However, at this rate the particles do no stay along the inner drum wall, instead a cataracting flow regimes develops. To produce a centrifuging flow regime, an Fr considerably higher than 1 is required. Walton and Braun (1993) conducted a simple two-body frictional contact analysis to understand the motion of particles on the inner drum wall in a centrifuging drum. They compared the stability of a particles located at the top of an inclined granular surface in a drum to the stability of a frictional block on an inclined surface. Therefore the block will accelerate down the inclined surface if the tangent of the angle of inclination is greater than the coefficient of sliding friction between the frictional block and the surface. Within a drum, this translates to the flow being stable as long as

$$\tan\alpha < \tan\phi_r$$ Equation 2.22

where α is the inclination angle, ϕ_r is the dynamic angle of repose and $\tan\alpha$ corresponds to the ratio of tangential to normal body forces due to gravity acting on a particle on a plane inclined at the angle α. The stability of a particle can further be determined by examining the ratio of tangential to normal forces acting on it. Consider the two-dimensional view of a particle along the inner drum wall as shown in Figure 2.7, with the origin at the centre of the drum and the polar angle θ measured from the horizontal.

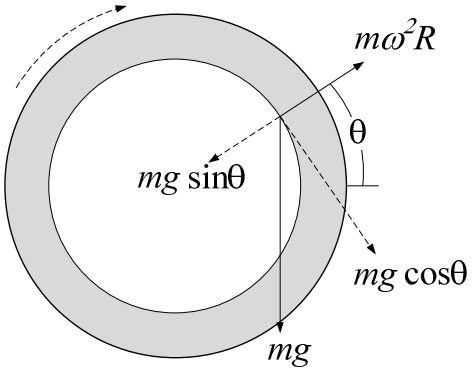

Figure 2.7 Two-dimensional view of a particle on the inner drum wall of a centrifuging granular bed in a drum with a high rotational speed

The tangential force F_t acting on the particles is given by

$$F_t = mg\cos\theta \qquad \text{Equation 2.23}$$

The force in the radial direction F_r is given by

$$F_r = m\omega^2 \mathrm{r} - mg\sin\theta \qquad \text{Equation 2.24}$$

where m is the particle mass. The ratio of tangential to normal force for $Fr > 1$ can be therefore be written as

$$\frac{F_t}{F_r} = \frac{\cos\theta}{Fr - \sin\theta} \qquad \text{Equation 2.25}$$

2.4.4 Numerical modelling of rotating drum

In recent years, there has been a rapid advancement in the understanding of rotating drums and tumbling mills through computer simulations, attributed mainly to the possibility of simulating granular particles in DEM software. Numerical simulations have been able to qualitatively capture the various flow regimes that may exist within a drum. Quantitatively, it

also allows accurate predictions of individual particle trajectories for improved plant operation, power draw prediction, liner and lifter design and micro scale modelling for calculation of size distribution, distribution of contact forces and energies between collisions, and wear. DEM software has helped the design and optimisation of rotating drums and tumbling mills and the challenge is to effectively use the simulation tool to improve industrial practice further. With regards to this thesis, the focus is not to optimise the rotating drum but to produce accurate predictions of granular flow in drums using DEM models.

Particle shape representation

Walton and Braun (1993) investigated the effect of particle shape on the dynamic angle of repose, ϕ_r and on the bulk flow behaviour in rotating horizontal cylinders using particle dynamic simulations. They performed simulations to determine the dynamic (using rotating drums) and static ϕ_r using single spheres and a cluster of spheres (tetrahedral and eight sphere cube). They concluded that dynamic and static ϕ_r increases greatly between the spheres and tetrahedral, as the particle interlocking is much larger. However, the discrepancies between the dynamic and static ϕ_r formed from a tetrahedral and eight sphere cube is significantly less.

Two and three dimensional representation of a rotating drum

Two-dimensional DEM representation of granular flow in rotating drums are often used for analytical simplicity and computational efficiency, however, the complexity of the flow regimes and granular behaviour may be oversimplified.

Using three-dimensional DEM simulations, Walton and Braun (1993) determined the effect of the drum rotational speed and the inter-particle friction on the bulk flow behaviour. Dury et al. (1998) was able to determine the effect on particle to boundary interaction on the dynamic ϕ_r. Mishra (2003a) critically evaluated the understanding of the three important areas of the simulation aspect: the inter-particle force laws, significance and choice of contact parameters, and the implementation of the numerical scheme using DEM in tumbling mills.

Drum end plate influence on the flow regime and bulk behaviour

The particle to wall friction μ_{pw} between the granular material and the drum end plates has been shown to significantly influence the flow regime within a drum containing granular

material (Dury et al. 1998; Taberlet et al. 2006). Dury et al. (1998) examined the variance in dynamic angle of repose, ϕ_r experimentally and numerically for a deep drum (diameter/depth=0.14). By fitting the numerical results to an exponentially decaying function, he was able to calculate the characteristic range ζ of the influence on the drum end plate which was found to scale with the drum radius, but was not dependent on either the density or the gravitational constant. Dury et al. (1998) measured the discrepancies in dynamic ϕ_r between the mid-section and the drum end-plate and noted as much as 8° difference. In addition, Taberlet et al. (2006) conducted a numerical study to demonstrate that the "S-shape" of the surface profile in a rotating drum obtained during the cascading flow regime at higher speeds is heavily influenced by the friction of the end plates. This study involved a series of drum simulations (drum diameter/depth=16) with high friction and frictionless end plate.

Periodic boundaries

In DEM simulations, periodic boundaries may be added to one or more planes. When periodic boundaries are included in a particular direction, any particle leaving the domain in that direction will instantly re-enter it on the opposite side (DEM Solutions Ltd 2009). Periodic boundaries have several advantages when simulating flow in rotating drums and as a consequence, are frequently used in numerical simulations (Dury et al. 1998; Walton and Braun 1993):

- Deep drum may be very time consuming to simulate. A thinner slice can be used to simulate the flow of particles around the mid-section of the drum using periodic boundaries instead of end plates.
- The particle to boundary (end plates) interactions may be eliminated by using periodic boundaries. In this case, the bulk behaviour will be predominantly influenced by inter-particle parameters.

2.5 Experimental validation using DEM simulations

Until recently, researchers have validated their three-dimensional DEM results by conducting corresponding physical experiments. The benefit of performing validation study is to highlight any discrepancies between numerical and experimental responses, providing the basis

for creating a more accurate numerical model. A review of the various experimental validation studies of DEM simulations are presented below.

Zhang and Vu-Quoc (2000) simulated soybeans flowing down a bumpy inclined chute and the corresponding physical experiments were conducted. DEM simulations revealed that the soybeans flow transitioned from an unsteady to steady state of flow. During the steady state flow, the average velocity of the granular flow calculated from the DEM simulations was found to match the corresponding physical experiments. In addition, along the boundary, the numerical velocity profile was found to match the experimental results qualitatively as well as quantitatively.

The compaction of powders in a cylindrical die is a typical method to produce moulded products of powders and is widely used in industries ranging from chemical to pharmaceutical. Odagi et al. (2002) performed DEM simulations of a compression test on zirconiaceramic particles in a cylindrical die and compared the results with corresponding experiments. They determined that the particle surface roughness was one of the main factors to affect the properties of compression and therefore, an accurate measurement was conducted using an atomic force microscope (AFM), before introducing the parameter into DEM simulations. The study showed that the numerical results matched the experimental results well, specifically between the normalised pressure and the axial strain.

A direct grain-shape modelling method has been proposed by Matsushima and Saomoto (2002) in order to quantitatively simulate shear behaviour of engineering granular materials composed of irregularly-shaped grains by DEM. Matsushima et al. (2003) validated this model using simple shear tests of glass grains made by crushing blocks with DEM simulations, under constant confining pressure and constant volume. Using a special visualisation technique known as laser-aided tomography, three-dimensional images of the irregular grain shapes were detected and the multiple sphere method was used to represent the irregular shapes of the glass grains in the DEM simulations. In addition, the particle size distribution was also taken into account in the simulations. The study revealed several discrepancies between the numerical and experimental results including higher void ratios (10% and 5% higher than dense and loose filling physical experiments respectively) and higher shear strengths.

O'Sullivan et al. (2004a) examined the triaxial and plane strain laboratory compression tests of steel spheres using face-centred-cubic and rhombic packing arrangements. DEM

simulations and experimental validation tests were conducted. The results of the study showed that the DEM simulations managed to capture the observed laboratory response well if the particle configuration, particle size, and boundary conditions were accurately represented, specifically with regards to the peak strength values in the triaxial and plane strain test. However, the post-peak response was found be more difficult to capture and was shown to be sensitive to the coefficient of friction assumed along the specimen boundaries. O'Sullivan et al. (2004b) conducted an experimental validation of DEM simulations using the direct shear tests of stainless steel spheres. The study revealed that the response from the DEM simulations was found to be significantly stiffer than that measured in the physical tests. In addition, the angle of internal friction was found to be 4.8° lower in the DEM simulations than that observed in the experimental tests (24.4°).

Chung and Ooi (2006) conducted a careful validation study where DEM was used to model the confined compression and rod penetration test of spherical (glass beads) and non-spherical (corn grains) particles. The confined compression test was designed to investigate the mechanical response of a granular material under vertical loading and the load transfer to the containing walls (Masroor et al. 1987). The penetration test was designed to evaluate the resistance of granular bulk to penetration of a moving object and the dynamic force transmission to a contact surface. The key properties of the particles were independently measured using various laboratory experiments. The experimental data on the bulk compressibility and the corresponding load transfer to the cylindrical wall and the bottom platen provide quantitative information for direct comparison with the DEM results. They determined that the initial particle packing arrangement influenced the bulk behaviour of the assembly and therefore, several methods of particle generation were used to investigate the sensitivity of particle generation in DEM. As part of the study, an investigation into the influence of inter-particle friction and particle stiffness in DEM simulations provided an insight into granular materials behaviour under confined compression. The study revealed that the DEM prediction match the experimental results for all cases except the force-displacement responses with respect to the corn grains, but were not always in quantitative agreement with respect to the glass beads.

Härtl and Ooi (2008) conducted a validation study comparing the experimental results with DEM simulations of the Jenike shear tester using single and paired glass beads. Numerous laboratory experiments were conducted to study the influence of the particle shape, stress level

and packing density on the bulk friction at the limiting shear. In an attempt to verify the predictive capabilities of DEM, closely matching three-dimensional DEM simulations of the shear tests were performed. The measured bulk friction showed significant dependency on the initial packing porosity for both single and paired particles with a stronger dependency observed for the paired particles. Comparative studies showed the single spheres had a good quantitative agreement for the limiting bulk friction when there is a good match in the sample porosity. In addition, Härtl and Ooi (2008) illustrated through the simulations that DEM always produces looser packing in a shear box than the corresponding experiments when the measured properties are used.

The various experimental validation of DEM simulations studies have demonstrated DEM's capabilities of producing quantitative predictions of bulk granular behaviour using particles properties measured from laboratory tests. However, the discrepancies seen in certain cases highlights the need for a more robust method of producing systematically accurate predictions of bulk behaviour.

2.6 Experimental design and optimisation methods

There is a gap in the literature of how DEM parameters should be determined to produce accurate quantitative DEM predictions. The aim of this thesis is to develop a robust methodology that will generate a set of optimised parameters able to produce accurate predictions of bulk physical behaviour. This section will cover various relevant concepts and review experimental designs and optimisation methods that are used to develop the methodology.

2.6.1 Experimental design

Design of experiments (DOE) is an efficient method of planning experiments to provide essential data for analysis and has been an integral procedure to achieve many innovations in quality and process efficiency. DOE is especially useful for conducting analysis on multiple variables simultaneously and efficiently. DOE can determine the best possible independent variables and combination of independent variables by studying the response on the dependent variable. In an industrial context, DOE can help to identify the best parameters to yield the desired results. Experimental design is especially useful for experiments with;

1. Real life (physical) systems;
2. Deterministic simulation models; and
3. Random (stochastic) simulations models.

The modern development of statistical experimental design for *real-life* systems started with the pioneering work by Sir Ronald A. Fisher in the 1920s. He carried out agricultural experiments and systematically introduced statistical thinking and principles into designing experimental investigations. This included the factorial design concept and the Analysis of Variance (ANOVA). In the 1950s, DOE was developed further by George Box who applied experimental design methods for chemical experiments. DOE is now applied to social systems such as educational and service systems (Myers et al. 2009).

Deterministic simulations have become increasingly popular following the increase in the use of computer code for design in engineering applications using computer aided engineering (CAE) and computer aided design (CAD) tools. In this domain, DOE is often referred to as design and analysis of computer experiments (DACE).

Random simulations include discrete-event dynamic systems (DEDS) such as queuing and inventory models, but also stochastic difference and differential equation models.

2.6.1.1 Experimental design analysis methods

There are three main methods of analysis used in experimental designs; the factorial design, the Taguchian robust approach and the response surface methodology. A brief review of each is presented in this section.

Factorial Design

An efficient designed experiment can significantly reduce time and costs. DOE essentially organises methods of conducting experiments in a manner that will allow the greatest and most relevant amount of information to be extracted from the least amount of experiments. For experiments with a single independent variable, experimental procedures are simpler which involves altering the independent variable and monitoring the dependant response. As the number of independent variables increase, the number of experiments that is needed to investigate every possible combination of variables will increase exponentially. For example, in

an experiment with 4 independent variables, each having three levels (a high, mid and low level) and two measured responses, the number of experiments required to run a full factorial matrix of simulations is 3^4 x 2 = 162. In this case, the one-factor-at-a-time approach is no longer feasible and the *factorial design* approach would be more efficient. The *factorial design* method was adopted in this thesis and is discussed in detail in section 6.3.

Taguchian robust approach

Taguchi (1987) advocates the use of DOE to aid improvements of quality, primarily throughout the parameter design and tolerance design stages of industrial designs. Whereas many simulation-optimisation methods assume know environments, Taguchi used methodologies based on uncertain environments, where factors are difficult to control. His approach was originally developed to help Toyota design 'robust' cars that would perform adequately in a wide range of circumstances (Taguchi 1987; Wu and Hamada 2000). A key aspect to the Taguchi approach involved the reduction of variability by focusing on mean of response variance. The objective was to reduce the variability of quality around a target or nominal value. Taguchi is responsible for renewing the interest of experimental design and statistical design and introducing the concept in an industrial context in the last few decades.

Response surface methodology

The response surface methodology (RSM) was developed by Box and Wilson (1951) who originally applied the methods to real-life systems. RSM is an optimisation heuristic that tries to estimate the input combination that minimises a given univariate goal function in a stepwise (multistage) method. In these steps, RSM uses local first-order and second-order polynomial response surface. Although RSM is an approximation, its popularity stems from its simplicity of modelling and application, especially when little is known about the process.

A brief review of DOE is presented in this section for completeness. A detailed review of design and analysis of experimental methods are described by Taguchi (1987), Kleijnen (2008), Wu and Hamada (2000) and Myers et al. (2009).

2.6.1.2 Statistical analysis packages

There are many statistical analysis packages available and may be commercial or open source programs. The statistical analysis package used in thesis is Statistica v9.0 (StatSoft 2009) unless stated otherwise. One of the main advantages of using Statistica is that an experimental design and statistical analysis software are incorporated into one package.

DOE: $3^{(k-p)}$ Box-Behnken factorial design overview

In some instances, the effects of a variable on a response cannot be adequately described using 2 levels (high and low) specifically when responses are expected to be non linear. In these cases, 3 levels (high, mid and low) are necessary in order to test for the linear and quadratic effects for those factors. Box and Behnken (1960) determined a class of incomplete three level factorial designs useful for estimating the coefficients in a second degree graduating polynomial. The experimental design module in Statistica contains a complete implementation of the standard $3^{(k-p)}$ designs enumerated by Connor and Young (1961) and McLean and Anderson (1984) for the National Bureau of Standards of the U.S. Department of Commerce.

In the case of a $2^{(k-p)}$ design, Plackett and Burman (1946) developed highly fractionalised designs to screen the maximum number of main effects in the least number of experimental runs. The equivalent of a $3^{(k-p)}$ design is referred to as Box-Behnken designs (Box and Behnken 1960; Box and Draper 1987). These designs do not follow a simple design generating algorithm, but are constructed by combining two-level factorial design with incomplete block designs and have complex confounding of interactions. The general mechanism of generating fractional factorial designs with 3 levels ($3^{(k-p)}$ designs) starts with a full factorial design, and then uses the interactions of the full design to construct new factors by making their factor levels identical to those for the respective interaction terms (StatSoft 2009).

2.7 Single and multivariate regression

Karl Pearson first used the term of multiple regression back in 1908 and it has been extensively used in many industrial and scientific applications since then. Multiple regression shares all the assumptions of correlation, including the linearity of relationships and the same finite variance throughout the range of the independent variables. In a scatter plot where a linear

relationship is desired between an independent variable *x* and a dependent variable *y*, computation based on least squares fits a straight line to the set of points so that the deviations of the observed points from the best-fit line are minimised. The regression line in the two dimensional space is defined by the standard equation $y = a + bx$, where the variable y is expressed in terms of the intercept a and the regression coefficient b.

In multivariate cases, the regression line can no longer be visualised in a two dimensional manner. Multiple regression procedures may generally be expressed in the form

$$y = a + b_1 x_1 + b_2 x_2 + \cdots + b_p x_p \qquad \text{Equation 2.26}$$

It should be noted that it is important to correctly specify the model, the exclusion of important causal variables or the inclusion of extraneous variables can drastically change the weight and hence the interpretation of the importance of the independent variables. The implementation of the multiple regression analysis can be found in spreadsheet programs and in many engineering tool packages. The methodology behind multiple linear regressions is briefly explained below.

Predicted or fitted values are in each case found by using the regression equation for all the cases in the analysis. Residuals are the difference between the values predicted by the regression equation and the observed values. The coefficient of determination R^2 indicates how good the fit is to the measured data and is given by

$$R^2 = 1 - \frac{sum(y_i - y_{est,i})}{sum(y_i - y_{mean})} \qquad \text{Equation 2.27}$$

where y_i is the actual value of $y_{est,i}$ for the i^{th} case, y is the regression prediction for the i^{th} case and y_{mean} is average of the y_i values. The coefficient of determination R^2 ranges between 0.0 and 1.0 and is a statistical measure of how well the regression equation describes the real data. A value close to 1 indicates a very good fit to the data.

2.7.1.1 Assumptions, limitations and practical considerations

In multiple linear regression, it is assumed that the relationships between the variables are linear but in most cases this cannot be confirmed. Whilst multiple regression procedures are not generally affected by minor deviations from this assumption, it is still prudent to look at the scatter plot and determine whether or not other regression procedures are necessary. The major conceptual limitation in regression procedures is that relationships may be obtained without considering alternative causal explanations. Increasing the number of independent variables will increase the chances of producing significant results. Problems occur when there are too few predictive results to produce a suitable regression line. It is generally advised to have 10 to 20 times as many cases as variables.

2.7.1.2 Interpolation methods

A key aspect of the optimisation procedure involves an inverse searching technique to determine the optimal DEM input parameters. A detailed review of various interpolation methods as described by Yang et al. (2004) and two methods relevant to this thesis are briefly described below.

The *inverse distance to a power method* is a weighted average interpolator, which can be either exact or smoothing. With the inverse distance to a power, data are weighted during interpolation, so that the influence of one point, relative to another, declines with distance from the specified point. Weighting is assigned to data through the use of a weighting power, which controls how the weighting factors drop off as distance from the data point increases. The greater the weighting power, the less effect the points have during interpolation. As the power increases, the data value approaches the value of the nearest point. For a smaller power, the weights are more evenly distributed among the neighbouring data points. Normally, inverse distance to a power behaves as an exact interpolator.

Kriging is a geostatistical gridding method that has proven useful and popular in many fields and attempts to express trends suggested in the data and can either be an exact or a smoothing interpolator. Kriging interpolation incorporates anisotropy and underlying trends.

2.7.1.3 Responses desirability function

Derringer and Suich (1980) highlighted the problem facing the product development community in selecting independent parameters which will result in a product with a desirable response. This problem had previously been addressed by Harrington (1965) who presented a desirability function approach. However, Derringer and Suich (1980) modified his approach by transforming several response variables into a desirability function which can then be optimised by univariate techniques. Their method was validated in the development of a rubber compound for tire treads. The Derringer and Suich (1980) modified desirability function for the optimisation of multiple independent variables is one of the searching methods used in the parametric optimisation procedure described in this thesis.

2.7.1.4 Microsoft Excel Solver optimisation algorithm

One of the searching methods used in the optimisation procedure uses the Microsoft Excel Solver (MES) algorithm. A detailed review of the design and use of Solver is presented by Fylstra et al. (1998); however only a brief review of the algorithm is presented below and is based primarily from Fylstra et al. (1998) and Microsoft Office (2007). MES uses the generalised reduced gradient algorithm for optimising non-linear problems and was developed by Leon Lasdon of the University of Texas at Austin and Allan Waren of Cleveland State University. MES uses iterative numerical methods that involve "plugging in" trial values for the adjustable cells and observing the response calculated by the constraint cells and the optimum cell. One advantage of MES is that it performs extensive analyses of the observed outputs and their rates of change as the inputs are varied, to guide the selection of new trial values as opposed to the traditional time consuming trial and error approach.

In a typical problem, the constraints and the optimum cells are functions of the adjustable cells and the first derivative of a function measures its rate of change as the input is varied. When there are several values entered, the function has several partial derivatives measuring its rate of change with respect to each of the input values forming a vector called the gradient of the function. Derivatives (and gradients) play a crucial role in the iterative methods of MES as they provide indications as to how the adjustable cells should be varied. For example, if MES determines that the partial derivative for an optimum cell with respect to one adjustable cell is a large positive number, while another partial derivative is near negligible, the next iteration will

see the first adjustable cell's value increase. However, a negative partial derivative suggests that the related adjustable cell's value should be varied in the opposite direction.

The derivatives are numerically approximated by slightly altering each adjustable cell value and monitoring the rate of change of each constraint cell and the optimum cell in a process known as a finite difference estimate of the derivative. Two possible differencing methods are available in MES, forward or central. In forward differencing, a single point slightly different from the current point is used to compute the derivative. Alternatively, central differencing uses two points in opposite directions. Central differencing is more accurate than forward differencing when the derivative changes rapidly, however requires more recalculations.

In certain cases, many locally optimum points may exits where the partial derivatives of the optimum cell are zero. A graph of the optimum cell function in such cases would show many hills and valleys of varying heights and depths. One possible limitation of MES is that, when starting at a given set of adjustable cell values, the iterative methods will tend to converge on a single hilltop or valley floor close to the starting point and MES will not assume there is a taller hilltop or deeper value further away. Therefore, the best way to find the global optimum is to apply external knowledge of the problem through common sense reasoning or through experimentation.

2.8 Summary

The related literature regarding this thesis has been reviewed in this chapter. The literature review includes a brief review of DEM, loading conditions in granular materials, the various flow regimes that may exists in a rotating drum, a review of the experimental validation of DEM simulations, experimental design methods and optimisation techniques. There is a clear gap in the literature of how DEM parameters should be determined to produce quantitative DEM predictions and forms the basis of the research conducted in this thesis: The development of a robust parametric optimisation methodology.

Chapter 3

Development of bulk experiments and material characterisation for DEM calibration

3.1 Introduction

The aim of this study is to develop a DEM parametric optimisation procedure. The DEM models will be calibrated using bulk experimental results. Choosing the appropriate bulk responses to calibrate the DEM models is of paramount importance and should replicate the industrial strains and stresses that the granular material will experience in a full scale system. In addition, suitable measurements should produce sufficiently discriminating values from variations in material properties so that the optimisation procedure is well posed to infer the DEM model parameters from these measurements. The measurements should also be highly repeatable and preferably ones that are relatively easy to measure from simple laboratory tests. This chapter describes various physical experiments and bulk responses, concentrating on the rotating drum and the uniaxial confined compression test which were used in the optimisation procedure. The reasons for including and excluding the various tests from this project are described in detail in the following chapter.

Before attempting to model a granular material, it is important to describe the material's physical and mechanical properties as well as each material's characterisation. The optimisation procedure described in this thesis was designed to be generic and applicable to a wide range of different materials. A range of materials were therefore selected with varying properties to demonstrate the optimisation procedure's versatility. This chapter will describe the physical and mechanical properties of the five different granular materials.

3.2 Selection of the laboratory bulk experiments

3.2.1 Rotating drum

Rotating drums have been extensively investigated in the past as they are an integral part of many industrial processes. The great majority of the published work on drums has focused on the various flow regimes and phenomena that exist within the drum (Khakhar, McCarthy et al. 1997; Kuo, Shih et al. 2006; Zuriguel, Gray et al. 2006). The thesis will focus on using the rotating drum as a bulk calibration instrument and attempt to understand how DEM input parameters may affect granular flow behaviour in numerical simulations. The rotating drum as a bulk response calibrator was chosen by request of the industrial sponsor due to its wide use in literature and presence in industrial applications. However, the thesis will highlight some of the drum's limitations and explain methods of exploiting the test to produce usable results.

3.2.1.1 Experimental setup

The drum was designed based on the thesis requirements as well as run experiments carried out in the literature (Dury et al. 1998; Ristow et al. 1998; Powell and McBride 2004).The experimental setup of the rotating drum can be seen in Figure 3.1.

(a) Transverse view

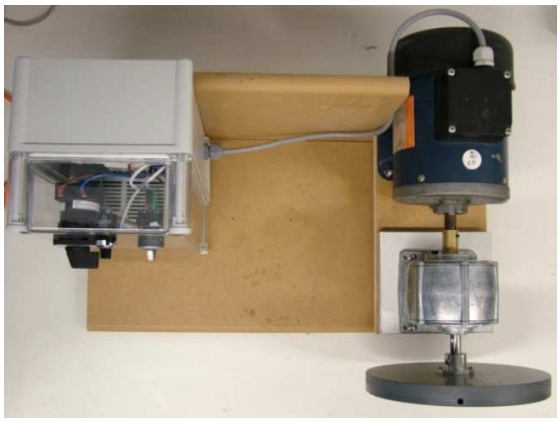

(b) Top view

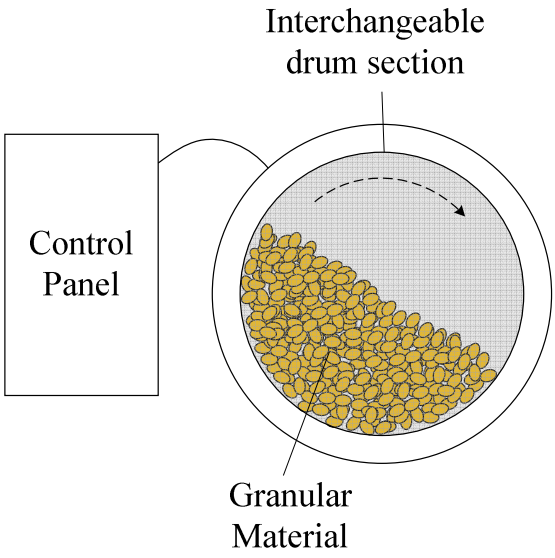

(c) Transverse view schematic

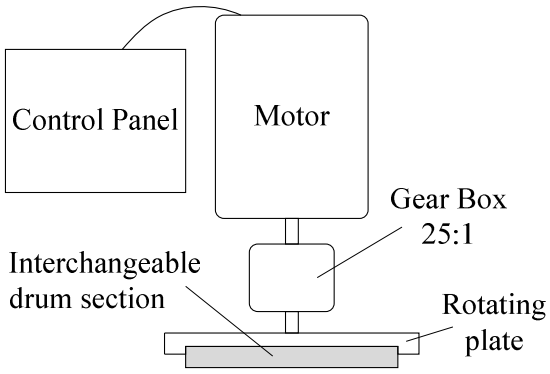

(d) Top view schematic

Figure 3.1 Experimental setup of the rotating drum device

The main specifications of the drum and the reasoning behind the choices made are listed below.

- *Drum diameter 184 mm*: using the major dimensions of the five materials (Table 3.4), 184 *mm* is between 15 and 45 particles across the surface profile (depending on the particle size of the various granular materials). An adequate number of particles along the surface profile are important to determine the dynamic angle of repose. If there are too few particles across, the results may be compromised. If there are too many particles within the drum, DEM computational times will increase significantly.
- *Thickness 20 mm*: The thickness is between 2 and 5 particles thick (depending on the average dimensions of the various granular materials) and was chosen to manage the computational effort required. This creates a pseudo two-dimensional setup. The particle to wall friction is expected to play a significant role (Dury et al. 1998; Ristow et al. 1998).
- *Drum rotational speed range 1 to 14 rpm*: The speed range that the drum offered was too high for this study and a 25:1 step down gear box was installed to produce the desired range of 1 to 14 *rpm*. The study focused on this speed range as it produced slumping and avalanching flow regimes where rotational speeds have weaker influences on the bulk behaviour (Santomaso et al. 2003; Yang et al. 2008). The gear box was designed to be interchangeable and may be adjusted at any time. Another benefit of including a gear box is the increased torque in the rotation and as a result, the rotational speed will not be affected by the mass of the granular material.
- *Acrylic wall material*: The drum was made from see-through acrylic material. Acrylic was chosen as the material properties are well documented and is readily available.
- *Filling degree,* $f = 40\%$: This fill volume was chosen as it was deemed the most suitable to allow visual clarity of the flow phenomenon in the drum which will enable a more accurate dynamic angle of repose determination.

3.2.1.2 Rotating drum device bulk response

Several flow regimes exist in a rotating drum and are commonly divided into 3 distinct regimes; slipping (low speeds), avalanching (mid speeds) and cataracting (high speeds) as described in section 2.4.1. Throughout the various regimes, the dynamic angle of repose ϕ_r

varies. The dynamic ϕ_r has been used extensively in literature (Dury et al. 1998; Ristow 1998; Ding et al. 2001; Mellmann 2001; Mishra 2003b; Powell and McBride 2004; Yang et al. 2008;) as it is an effective and simple method of quantifying flow behaviour in a rotating drum.

It was chosen to fix certain parameters of the rotating drum during the bulk response measurement tests to limit the number of variables in the analysis. These include the drum material, the fill volume and the rotational speed. The rotational speed remained constant at 7 *rpm* as this produced an avalanching regime with a steady inclination. During this regime, the dynamic ϕ_r is easier to measure and less susceptible to fluctuation.

Dynamic angle of repose determination

The drum rotational speed was verified with a cadence meter. The effect of granular mass on the rotational speed was investigated using an empty drum and a 40 % filled drum. Due to sufficient torque, the effect was negligible.

The dynamic ϕ_r, which was measured from the horizontal, was obtained from images taken using a typical commercial digital camera. To increase the clarity and reduce overexposure of the pictures, the camera was adjusted to have a shutter speed of 1/1500s. With such a high shutter seed a great deal of light is needed. Two halogen lights were used to produce enough light to produce a clear picture. The setup of the experiment is shown in Figure 3.2. A total of 10 separate images of the drum at each *rpm* between 1 and 14 were taken to check for repeatability. In each case, the dynamic ϕ_r was determined manually. For cases where the solid surface is not flat (e.g. cascading or S-shape) the slope at the mid-section of the surface profile was chosen to be the representative angle, as shown in Figure 3.3 (a). Determining the dynamic ϕ_r numerically was done by extracting images from the simulation using the software's image extraction function (an example of an image in Figure 3.3, b) and the dynamic ϕ_r determination was conducted in the same manner as the physical experiments.

There were some initial concerns over the unsystematic nature of the manual dynamic ϕ_r determination, however simple standardised procedures were investigated but these often produced less accurate results as stray particles along the surface would significantly affect the angle determination.

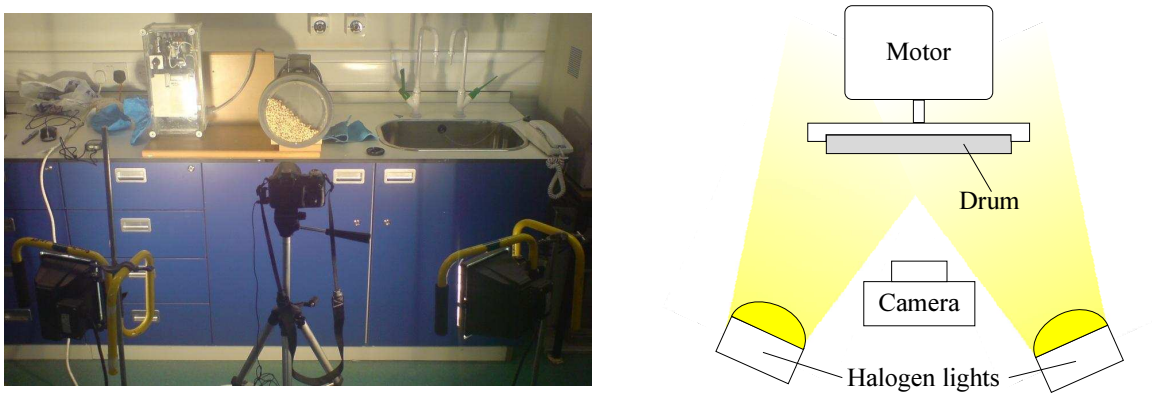

(a) Laboratory setup (b) Laboratory setup schematic

Figure 3.2 Experimental setup of the rotating drum apparatus

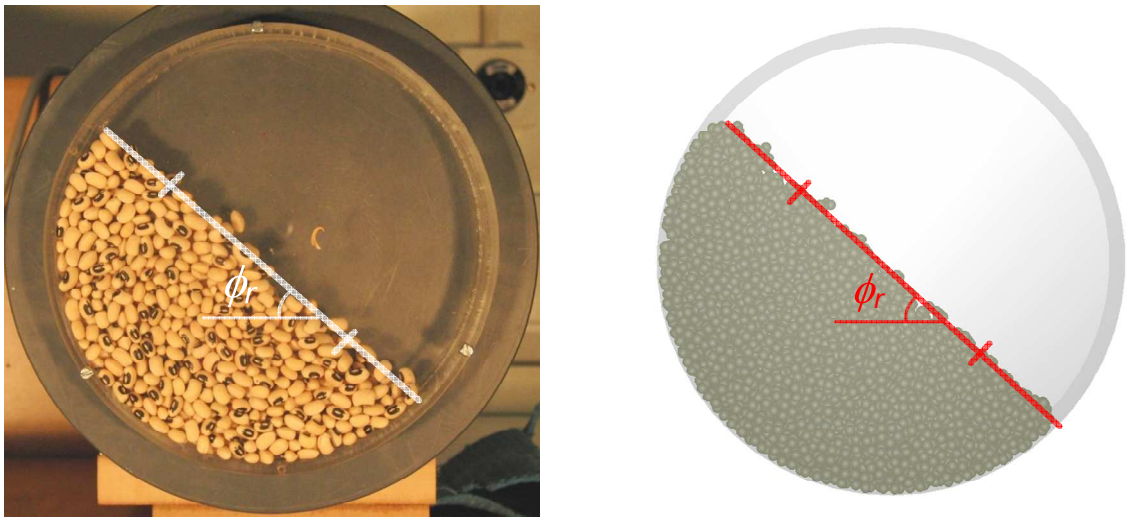

(a) Experimental dynamic angle of repose determination using black eyed beans

(b) Numerical dynamic angle of repose determination using particles with 2 equal sphere [1]

Figure 3.3 Example of the dynamic angle of repose determination from images

[1] Particle radius = 2 *mm*, aspect ratio = 1.50

3.2.2 Confined compression test

The confined compression test (also referred to as the K_0 test) is used to investigate the mechanical response of a granular bulk material under vertical loading with lateral confinement. The K_0 tester used in this thesis is a modification of the Masroor et al. (1987) apparatus and is similar to the test apparatus proposed by the European standards for measuring the lateral pressure ratio for silo design (EN 1991-4 1995). The vertical load applied to the bulk solid is applied by a top platen driven by an Instron machine (Inston 2009). The Instron control centre records the applied load and the vertical displacement. The resultant strain is measured by four strain gauges equally spaced around the cylinder wall measuring vertical and horizontal strains. The lateral pressure ratio K and the bulk friction coefficient μ_{bulk} may be determined using Equation 3.1 and Equation 3.2.

$$K = \frac{\bar{\sigma}_h}{\bar{\sigma}_v} \qquad \text{Equation 3.1}$$

$$\mu_{bulk} = \frac{\bar{\tau}}{\bar{\sigma}_h} \qquad \text{Equation 3.2}$$

where $\bar{\sigma}_v$ is the average vertical stress determined from the average of the top and bottom load cell readings on the apparatus, $\bar{\sigma}_h$ is the mean horizontal stress at the strain gauge level, determined from the strain gauge readings and $\bar{\tau}$ is the average shear stress calculated from the difference between the top and bottom load cell readings. These stresses can be expressed as

$$\bar{\sigma}_v = \frac{2(F_T + F_B)}{\pi D^2 (1 + \varepsilon_\theta)^2} \qquad \text{Equation 3.3}$$

$$\bar{\sigma}_h = \frac{2tE_w(\varepsilon_\theta + \nu_w \varepsilon_a)}{D(1 - \nu_w^2)} \qquad \text{Equation 3.4}$$

$$\bar{\tau} = \frac{F_T - F_B}{\pi D h(1 - \bar{\varepsilon}_v)}$$ Equation 3.5

where, *D*, *t*, E_w, and υ_w are the diameter, thickness, Young's modulus and Poisson's ratio of the cylinder respectively; ε_θ is the hoop and ε_a is the axial strain of the cylinder at the measuring points. F_T and F_B are the applied load at the top platen and the measured force at the bottom platen respectively, $\bar{\varepsilon}_V$ is the mean vertical strain and *h* is the height of the granular material in the system.

3.2.2.1 Experimental setup

The confined compression calibration work carried out in this thesis builds on the previous work carried out by Chung (2006), however the apparatus and experimental procedure was altered to suit the aims and objectives of the study.

Chung (2006) previously carried out confined compression experiments on glass beads and corn grains using a squat setup centred around one set of strain gauges of the confined compression apparatus. In addition, during his experiments the acrylic silo was restrained at the base. This setup effectively resulted in a one-way compression during loading. The apparatus used by Chung (2006) is shown in Figure 3.4.

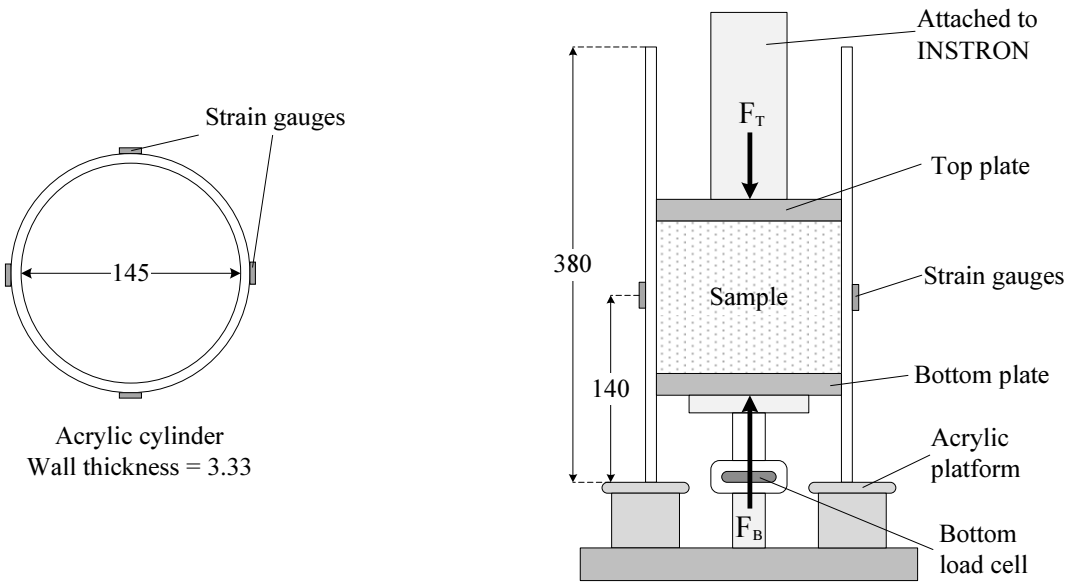

(a) Cross sectional diagram (b) Side view diagram

Figure 3.4 Confined compression apparatus used by Chung (2006)

(All dimensions in *mm*)

The diameter, thickness and height of the cylinder are 145 *mm*, 3.33 *mm* and 380 *mm* respectively. In addition, four rosettes of strain gauges can be found equally spaced around the circumference at two levels as shown in Figure 3.4 (a). The main adjustments between Chung's (2006) setup for the confined compression test and the one used in this study were:

- The bottom edge of the cylinder was free to move and not restrained, allowing significant compression from the bottom platen as well as the top platen;
- The sample went through one loading and unloading cycle;
- The speed of the loading and unloading remained constant throughout the experiment and was logged at 0.5 *Hz*. The glass beads were loaded at 0.1 *mm*/*min* whilst the other materials were compressed at 1 *mm*/*min*.
- A taller sample and aspect ratio was used, when sufficient material was available.

The confined compression test was carried out on the single and paired glass beads, polyethylene terephthalate pellets, black eyed beans and black kidney beans (see section 3.3.2). Each test was carried out 3 times to check for repeatability using a different batch each time (excluding the glass beads) and the initial packing conditions were recorded.

Sufficient material was available to fill the entire compression cylinder; therefore, the experimental setup for the PET pellets, black eyed beans and black kidney beans was as shown in Figure 3.5. To fill the entire acrylic cylinder with 6 *mm* glass beads would require ±30,000 single and ±15,000 paired particles. However, only 2000 paired spheres were available, so a squatter sample was tested; localised around a set of strain gauges as seen in Figure 3.6. The average sample heights for the various materials using the ascending cone and rainfall filling methods are shown in Table 3.1.

Table 3.1 Average sample heights in *mm* for various materials during the confined compression test

Filling method	Ascending cone	Rainfall
Single glass beads	59	57
Paired glass beads	64	58
Black eyed beans	328	328
Black kidney beans	327	331
PET pellets	328	329

Average sample height based on 3 tests

The loading rate for the PET pellets, black eyed beans and black kidneys beans was 1 *mm*/*min*. As the glass beads have a higher particle stiffness than the other materials tested (Chung 2006; Härtl 2008) the average sample strain will be relatively less for similar stresses compared to the other materials, therefore the Instron speed was reduced to 0.1 *mm*/*min*.

For the experiments on the PET pellets, black eyed beans and black kidney beans, a single loading and unloading cycle to 65 *kPa* was carried out for each test (this maximum pressure includes the self weight of the sample and top plates, therefore 65 *kPa* is the effective stress experienced by the sample). To preserve the integrity of the glass beads, it was chosen to limit the maximum loading on the material to 35 *kPa*.

(a) Setup using black eyed beans

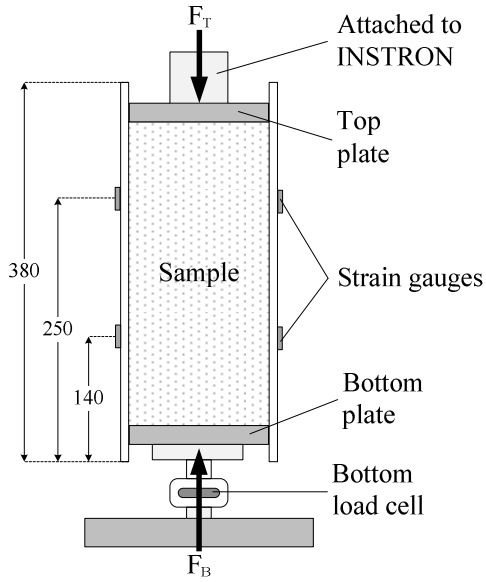

(b) Experimental setup schematic

Figure 3.5 Experimental setup of the confined compression apparatus

(All dimensions in *mm*)

(a) Setup using single glass beads

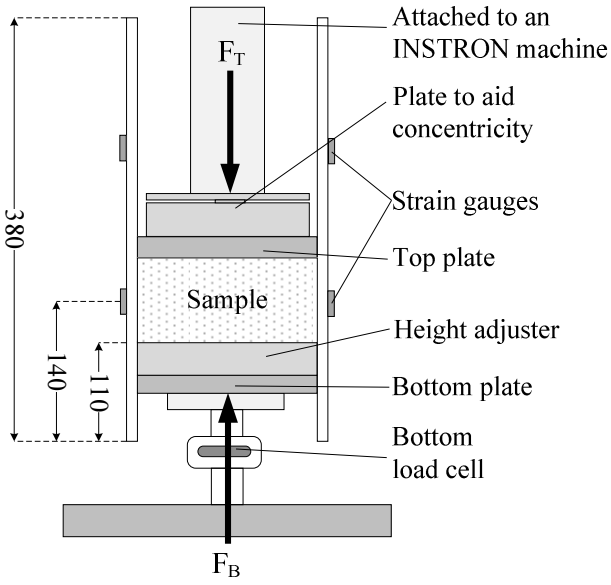

(b) Experimental setup schematic

Figure 3.6 Experimental setup for the confined compression of single and paired glass beads

(All dimensions in *mm*)

3.2.2.2 Confined compression bulk response

As for the rotating drum, a suitable bulk response measurement to calibrate the DEM models should be selected from the confined compression test.

This section will analyse a set of confined compression results and highlight the best bulk responses parameter to use in the optimisation procedure. The example used in this section is the confined compression of black eyed beans with a loose filling.

3.2.2.3 Lateral pressure ratio, *K*

Lateral pressure ratio *K* describes the resultant horizontal pressure in granular material that would occur from a vertical pressure application and is therefore a widely used parameter in Eurocodes for the design of containment structures and geotechnical systems. However, due to the inherent variability of particulate material properties, Eurocodes (EN 1991-4 1995) suggest altering K to represent extreme values when designing silos and tanks.

The lateral pressure ratio *K* can be described as

$$K = \frac{\sigma_h'}{\sigma_v'} \qquad \text{Equation 3.6}$$

where σ_h' and σ_v' are the effective horizontal and vertical pressure respectively. Therefore the horizontal pressure is assumed to be directly proportional to the vertical pressure at any given point in the granular system. The lateral pressure ratio is affected by several factors including material properties and the stress history of the solid.

Figure 3.7 shows the relationship between the mean applied vertical pressure (average of top and bottom platens) and the mean radial pressure (calculated using 8 circumferential strain gauges). The gradient of the data points gives the ratio of horizontal to vertical pressure, known as the lateral pressure ratio *K*.

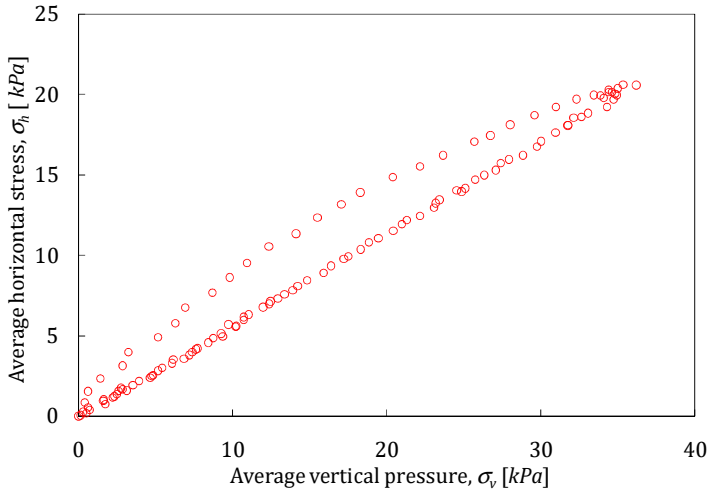

Figure 3.7 Resultant horizontal pressure due to vertical pressure of loosely packed black eyed beans in a confined compression test

3.2.2.4 Vertical stress-strain response

Understanding the mechanical response of a system is important to be able to predict a system's response to various loading conditions. Using the average vertical forces measured on the top and bottom platens of the confined compression apparatus, the average stress experience by the granular material can be determined. The average sample vertical strain ε_v is determined using the initial height and subsequent displacements of the top and bottom platen. As the acrylic cylinder is not fully rigid, a small amount of radial deformation will occur as the horizontal stress increases and ε_v will be overestimated. A sensitivity analysis was carried out and determined the difference in ε_v due to small radial deformations and was found to have minimal effects on the overall ε_v for the stress levels used in this study. Therefore the radial deformation was excluded from the analysis and the cylinder was assumed to be fully rigid.

An example of a stress-strain response curve for black eyed beans is plotted in Figure 3.8 (a). The plot shows the loading and unloading experienced by the sample. As it can be seen, the top and bottom platen stresses were very similar, so for convenience an average of the top and bottom stresses is used throughout the analysis (Figure 3.8, b). The higher stresses seen on the top plate are a result of the Instron machine applying the vertical load on the top plate. A small amount of force is lost as in the transfer to the bottom plate, possibly through wall friction. Further discussion and the implications of this are discussed in section 5.3.5.

The components of plastic and elastic deformation during loading and unloading are highlighted in the plots. The plastic deformation of the system can be seen when unloading occurs and approaches the x-axis at 0.6% strain when the load drops to zero. During loading, the plastic deformation in granular solids is a result of two phenomena:

1. The relative displacement of particles through rolling or sliding,
2. Plastic deformation of the particles at the points of contact.

In DEM simulations, relative displacement occurs naturally. However, plastic deformation at the points of contact is often ignored in the numerical contact, including EDEM (DEM Solutions Ltd 2009), the DEM program used in this thesis. EDEM uses a non-linear elastic contact model. Therefore for soft agricultural grains, EDEM is expected to underestimate the total plastic deformation of the system.

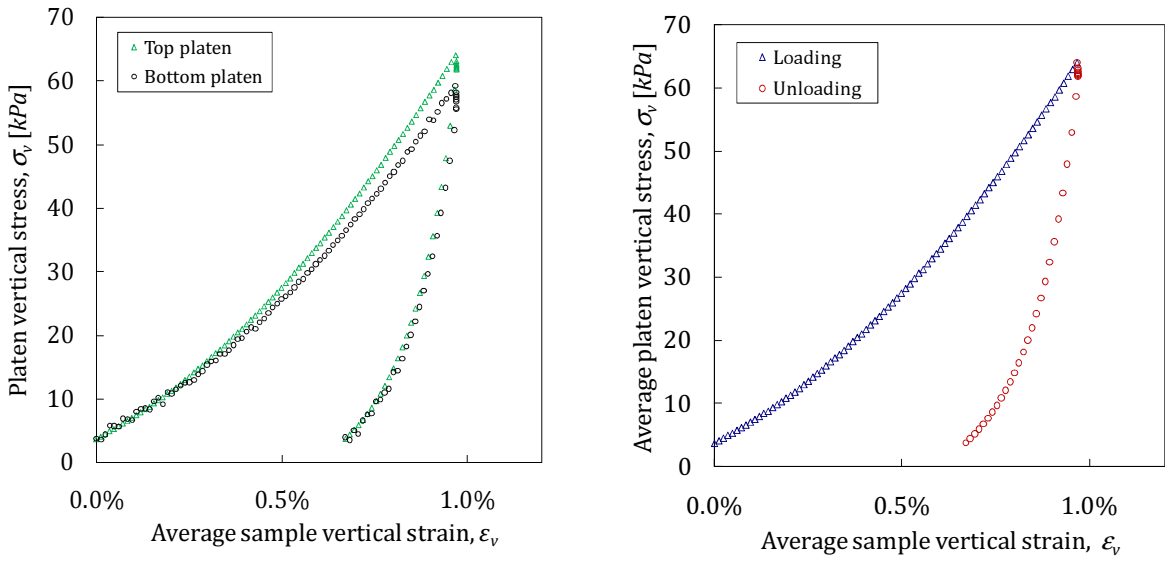

(a) Top and bottom platens (b) Average of top and bottom platens

Figure 3.8 Vertical stress-strain response for black eyed beans under confined compression

The gradients from a stress-strain plot give a measure of the loading and unloading bulk stiffness. To establish an accurate method of determining the loading and unloading gradients, a regression trendline was fitted to the virgin loading using the trendline function in Microsoft

Excel (Microsoft Office 2007). As the loading path was found to be non-linear (illustrating an increasing stiffness as vertical stress increases) a linear trendline (Figure 3.9, a) would produce a less accurate description of the loading curve than a second order polynomial (Figure 3.9, b). This is highlighted by the lower coefficient of determination R^2.

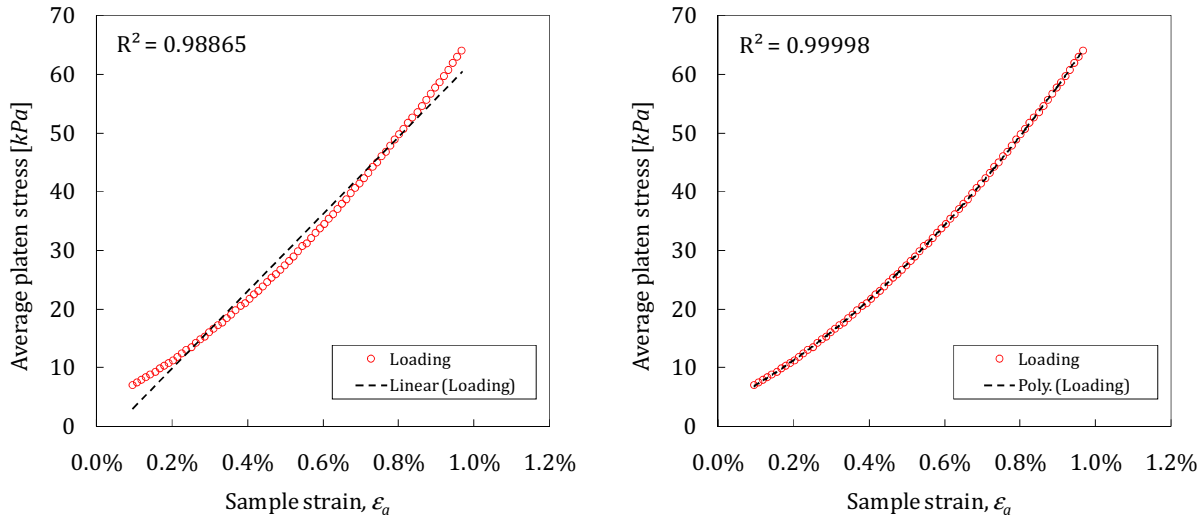

(a) Linear trendline (b) Polynomial trendline

Figure 3.9 Linear and polynomial trendline curve fitting comparison for the loading of black eyed beans

Using a polynomial trendline, the loading path may be described as an empirical polynomial in the form

$$y = Ax^2 + Bx \qquad \text{Equation 3.7}$$

The drawback of using polynomial regression trendline is that there are two coefficients (A and B) to describe the bulk stiffness. A comparison of the trendline coefficients for the test materials can be found in section 4.3.1.

3.2.2.5 Bulk stiffness parameters

The void ratio *e* is a ratio of the volume of void to the volume of solid as described in Equation 2.17 (see section 2.3.1 for more information on phase relationship diagrams). As a sample is consolidated, the volume of voids will decrease, reducing the void ratio.

Figure 3.10 illustrates how the void ratio varies with the vertical pressure plotted on a logarithmic scale.

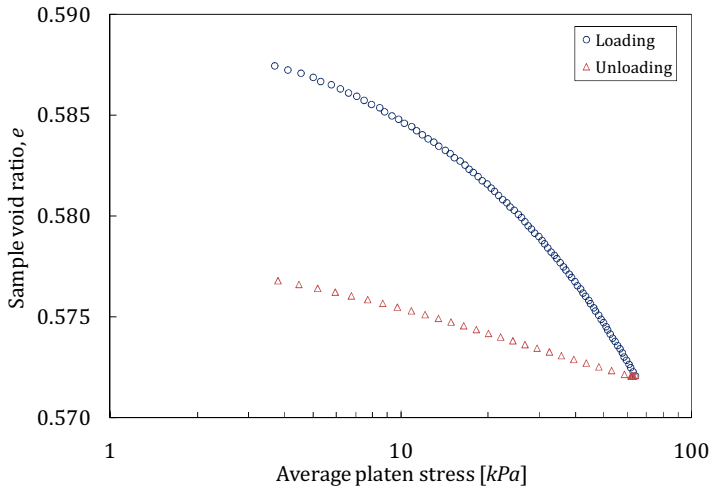

Figure 3.10 Semi-log plot for the void ratio against mean platen vertical pressure for loosely packed black eyed beans

This semi-logarithmic plot is in line with the classical concept of normal consolidation and overconsolidation in soil mechanics. The advantage of using a semi-log plot is that the unloading curve is straightened and a logarithmic trendline can be added to the loading and unloading lines as shown in Figure 3.11 (a). However, the loading line (Figure 3.11, b) still remains non linear and a logarithmic curve fitting is not accurate enough to describe the line.

Granular material behaviour at lower stresses can be less unpredictable and more sensitive to initial packing structure; therefore to increase the accuracy of the loading curve fitting, lower stresses were ignored. These cases are explicitly expressed in the thesis.

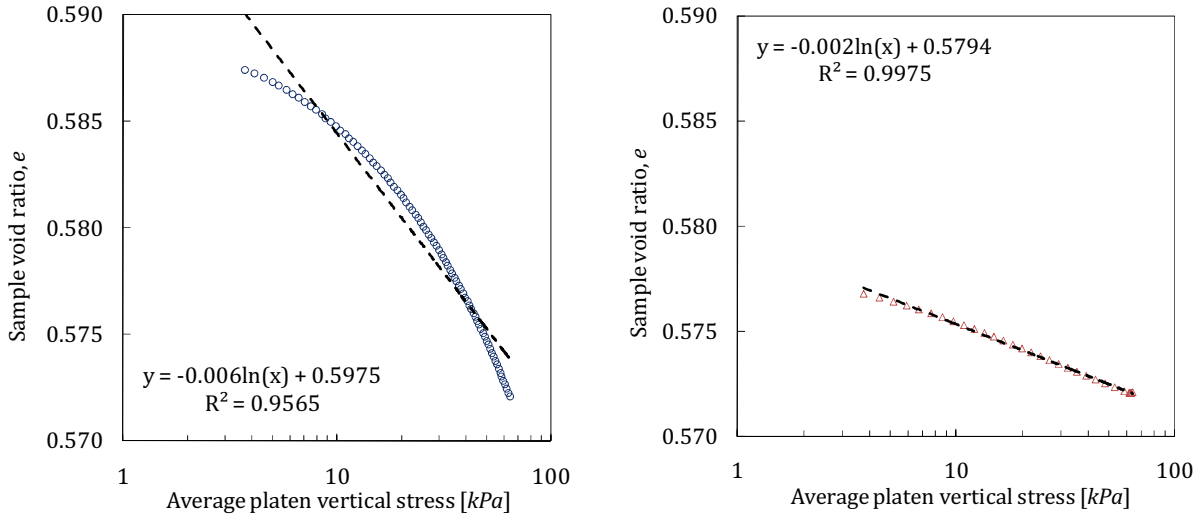

(a) Loading (b) Unloading

Figure 3.11 logarithmic trendline fitting to the void ratio against vertical pressure semi-log plot

As it can be seen from Figure 3.11(a), the loading trend on the semi-log plot has a small degree of curvature, whereas the unloading curve is much more linear. Assuming that the loading and unloading trends in the semi-log plot are linear, the trendlines may be described as a single parameter in the form

$$\text{Loading}, -\lambda = \frac{de}{d(\ln \sigma)} \qquad \text{Equation 3.8}$$

$$\text{Unloading}, -\kappa = \frac{de}{d(\ln \sigma)} \qquad \text{Equation 3.9}$$

λ and κ are often used in geotechnics and are the gradients of the loading and unloading curves in the semi-log plot, also known as the bulk *loading* and *unloading* parameters respectively. Whereas λ is a parameter dependent on the plastic first loading response of a granular system, κ is dependent on the elastic unloading properties.

Using the stiffness parameters as calibration data in the optimisation procedure has the advantage of a single parameter description as seen in Equation 3.10 and Equation 3.11.

$$e_\lambda = D_\lambda - \lambda \ln(\sigma)$$ Equation 3.10

$$e_\kappa = D_\kappa - \kappa \ln(\sigma)$$ Equation 3.11

where D_λ and D_κ are constants which depends on the point of loading and unloading. When $\sigma = 1$ (intersect on y-axis), D_λ and D_κ are equal to the void ratio e. Therefore the void ratio is equal to D_λ and D_κ for a unit stress. D_λ and D_κ are not material properties, they are in fact a load dependant parameter relating to the stress path. Due to the simplicity of this semi-log gradient description it is an appropriate and efficient bulk parameter for the model calibration and optimisation procedure.

3.2.3 Investigation of additional laboratory experiments

Several other laboratory devices were investigated in addition to the rotating drum and the confined compression tests, however their bulk responses were considered to be less suitable for the optimisation procedure after preliminary investigations. These tests are listed below and the reasons for their exclusion from this study are highlighted. This section is included for completeness to demonstrate alternative devices, however as this was a preliminary study, only initial results are presented.

3.2.3.1 Silo filling

The particle packing structure in a bulk solid is generally understood to significantly influence its bulk behaviour (Chung 2006; Härtl 2008) and understanding the parameters that affects the system's packing arrangement and ultimately bulk properties is important. Chung (2006) investigated a dense filling method which involved rainfalling particle deposition through a sieve and Härtl (2008) investigated a loose filling method using an ascending cone filled with particle.

This study investigated the effects of these two filling methods on the bulk properties of various different granular materials using an acrylic cylinder with an internal diameter of 145 *mm* and the sample which had an average height of 340 *mm*.

Loose filling using an ascending funnel method

With the use of a funnel, the cylinder was centrally filled. The funnel is filled with grains and raised slowly so that there is no impact from the grains as they are introduced into the silo. The only movement that occurs is avalanching along the angle of repose formed from the grain pile as shown in Figure 3.12 (d). This method was used to produce a loose arrangement and a higher void ratio.

(a) Filling the funnel

(b) Before cylinder filling

(c) During cylinder filling (top view)

(d) During cylinder filling (side view)

Figure 3.12 Central Silo filling method with the use of a funnel

Dense filling using rainfall through a sieve method

To study a range of filling arrangements, a dense packing method was investigated. Initially, this was achieved by filing the acrylic cylinder in layers which were subsequently packed compacted. Eventually, with the use of a 14 *mm* aperture sieve, a rainfall distributed filling was tried. The particles experienced significant impact as they settled within the silo which encouraged a denser packing arrangement. It was chosen to use this method as it was more time efficient and produced similar results to the compacted layers (within 10%) as well as being easier to simulate in a numerical model using random particle generation techniques. An example of filling using the rainfall through a sieve method is shown in Figure 3.13.

(a) Before filling (b) During filling

Figure 3.13 Dense filling using the rainfall through a 14 *mm* sieve with black eyed beans

3.2.3.2 Silo discharge

Another possible laboratory experiment investigated the use of silo discharge flow rate as a bulk response for the optimisation procedure. Chung (2006) conducted a silo discharge experiments by releasing grains through a circular orifice of a flat-bottomed model silo onto a flat surface as shown in Figure 3.14. The flow rates and the static angles of repose during discharged were measured using various outlet sizes.

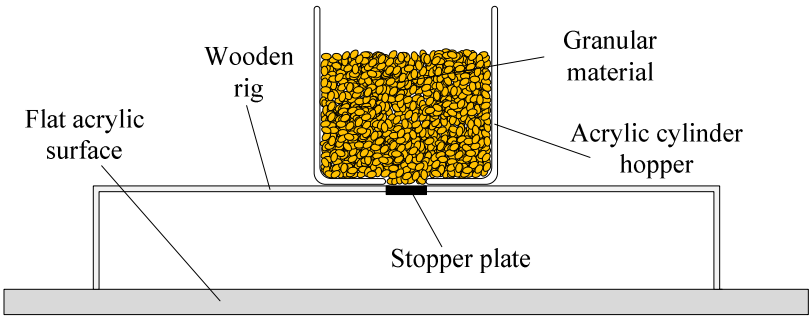

(a) Silo discharge setup schematic

(b) Test on single glass beads

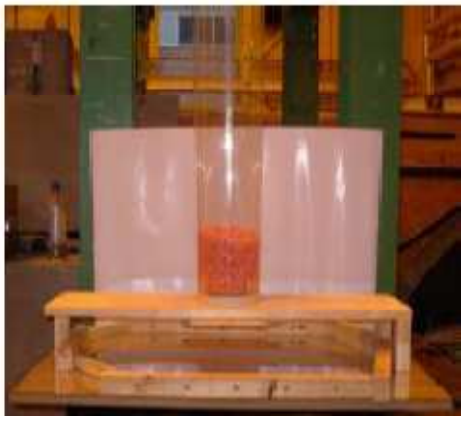

(c) Test on corn grains

Figure 3.14 Silo discharge experiment conducted by Chung (2006)

The discharge flow rates were then compared with the Beverloo formula (Beverloo, Leniger et al. 1961).

$$W = C_B \cdot \rho\sqrt{g}(D_0 - k_B \cdot d)^{2.5} \qquad \text{Equation 3.12}$$

where W is the mass flow rate, ρ is the bulk density of the solid, g the gravity term, D_0 the diameter of the orifice, and d the mean size of the particles. According to Nedderman (1992), the Beverloo constant C_B has been found to be in the range of 0.58 to 0.64 and the adjustment factor k_B should be around 1.5 for spherical particles and larger for non-spherical particles.

Chung (2006) noted that the predicted flow rates compared well with Beverloo formula, with the constant *C* being closer to 0.64 for glass beads and closer to 0.58 for corn grains, as expected.

If we take *C*, and *k* as empirical constants for a given granular material, the difference lies in *d*, the diameter of the particles.

Härtl (2008) conducted a set of DEM simulations using 30,000 (60,000 spheres) particles with an aspect ratio of 1.5 to determine the discharge rate from a silo for a range of bulk frictions to produce the graph seen in Figure 3.15. The bulk frictions of the various granular materials used in this thesis range from 0.35 to 0.7 (Table 3.6). It can be seen that the change in discharge rate when the bulk friction parameter is changed between 0.35 and 0.7 is relatively small (10%). As the flow rate does not produce a measurable effect from changes in the input parameter, it was decided not to include the silo discharge flow rate as a bulk response in the optimisation procedure.

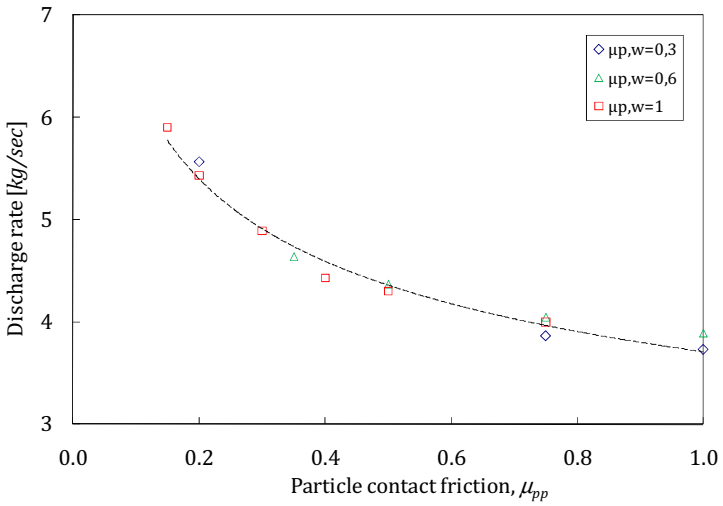

Figure 3.15 Influence of particle friction on silo discharge rate: DEM predictions conducted by Härtl (2008)

3.2.3.3 Bulk collision dissipation experiment

The rotating drum device and confined compression test were used to measure the dynamic angle of repose and bulk stiffness parameter respectively and are the bulk response parameters that will be used to calibrate the numerical models. The dynamic angle of repose is predominantly influenced by the frictional properties of the granular material, whereas the bulk unloading stiffness will be influenced by the particles stiffness (Dury et al. 1998; McBride et al. 2004; Chung 2006; Härtl 2008). A preliminary study was conducted to explore simple tests that would be heavily dependent on the coefficient of restitution e_r which gives a measure of the energy dissipated during collision.

An attempt was made to devise a bulk experiment in which the effect of the in-elastic collisions in a sample of grains is measured. Before a physical device was developed, a numerical trial was conducted to see if a bulk dissipation measurement could be observed accurately. In an effort to find a suitable and simple manner to measure the "bulk restitution", a drop test similar to the one conducted by Chung (2006) was carried out, however a layer of granular material was used instead of single particle.

There are various ways to calculate e_r which include the use of velocities, forces, energies and distances (height) to name a few, however many of these are not practical or feasible methods to measure experimentally. One method that was tried investigated the particle impact forces along a base plate as shown in Figure 3.16. To measure the bulk particle to wall e_r a layer of particles is held at a known height and dropped within a confining cylinder onto a flat base plate where impact forces would be measured. To determine the particle to particle e_r, a layer of particles was dropped onto a stationary layer of particles already located on the base plate.

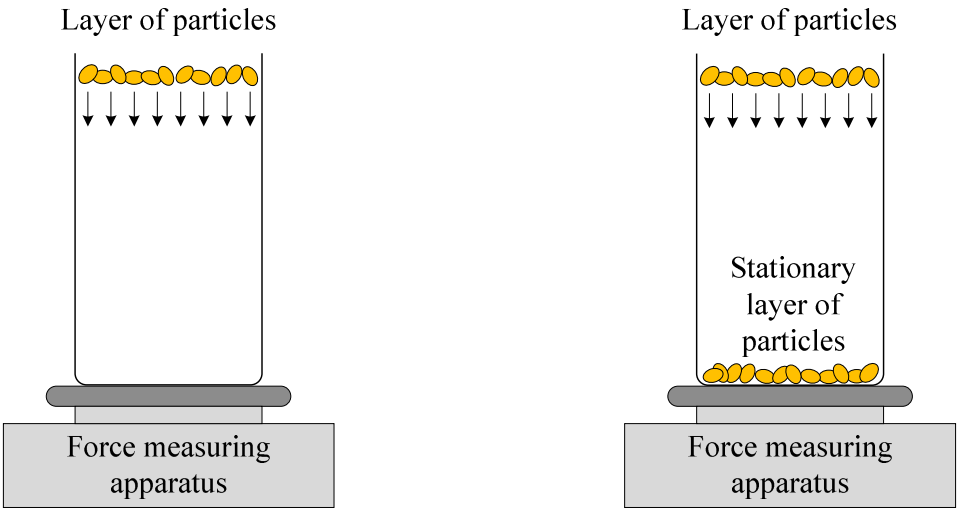

(a) Particle to boundary (b) Particle to particle

Figure 3.16 Schematic of a bulk experimental device concept for measuring the bulk collision dissipation granular material

Preliminary studies proved to be inconclusive over the potential and validity of this experiment for the optimisation procedure and no further development of this device was conducted in this study. Further research could investigate the bulk collision dissipation using a similar or variation of this setup.

3.3 Material Properties

3.3.1 Introduction

A detailed understanding of a granular system is crucial when attempting to model the system, whether it is on a micro (particle) or macro (bulk) scale. One aspect that is particularly important is correctly identifying the granular materials properties. The material properties for a typical granular solid may be grouped into two categories; physical and mechanical.

Physical properties refer to properties of a material that can be determined without altering its shape or density. Examples of physical properties include mass, density and geometric shape descriptors.

Mechanical properties refer to the properties of a material that reveal its elastic and plastic behaviour when a force is applied. Typical mechanical properties include contact stiffness, contact friction, coefficient of restitution, Poisson's ratio and Young's modulus.

Chung (2006) used individually measured material properties to predict bulk behaviour in DEM simulations; however granular materials in industrial systems are rarely found individually and are typically found in bulk form. Therefore, as well as individual material properties this section will investigate bulk physical and mechanical material properties.

The optimisation procedure developed to calibrate DEM models described in this thesis was developed to be applicable to a wide range of materials, and thus contrasting granular materials were chosen, three inorganic and two organic materials. Microscopic enhanced pictures of the test materials are shown in Figure 3.17.

An initial investigation using the microscopic enhanced images shows contrasting surface conditions. The black eyed beans appear to have a rougher surface than the black kidney beans, and the microscopic images reveal a roughness of the glass beads surface.

The rest of this chapter describes and summarises the laboratory measurements of the material properties for the five contrasting materials used in this thesis. The material properties were either determined through a set of laboratory tests or taken from literature. The optimisation procedure will eventually alter the DEM material parameters and therefore having a complete set of accurate measurements is not essential. The material properties included in this chapter are for completeness.

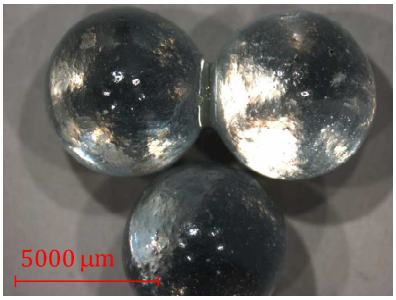

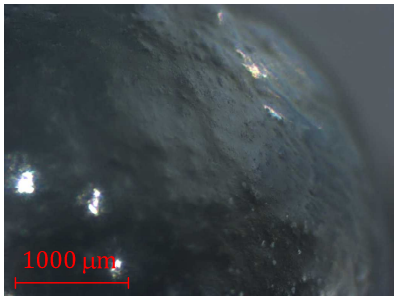

(a) Single and paired 6 *mm* glass beads

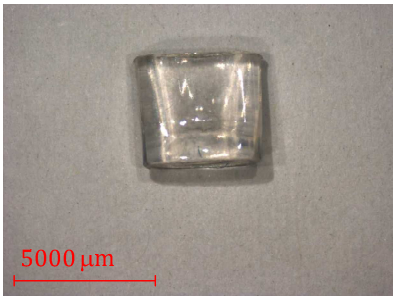

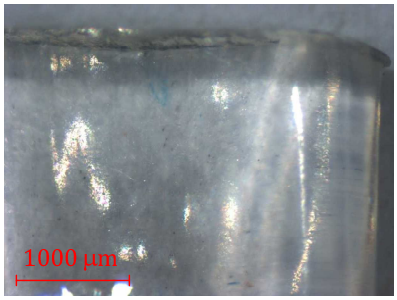

(b) Polyethylene terephthalate (PET) pellet

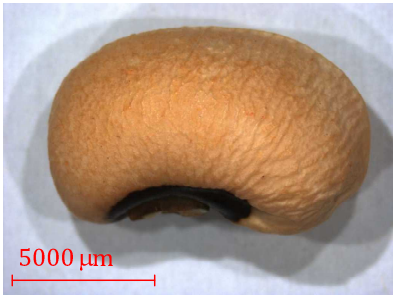

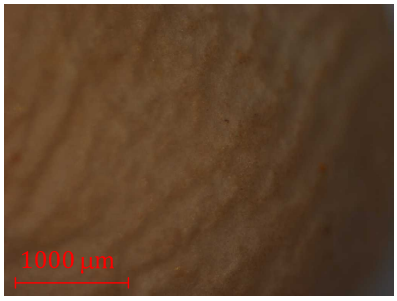

(c) Black eyed bean

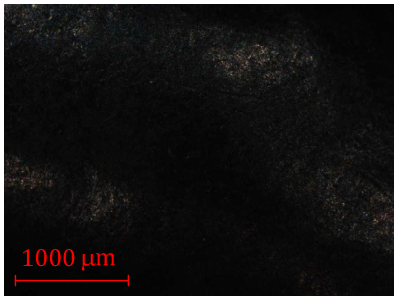

(d) Black kidney bean

Figure 3.17 Microscope enlarged images of various granular materials

3.3.2 Background on test materials

Glass beads

Glass beads (GB) are widely used in DEM research (Dury et al. 1998; Chung 2006; Härtl 2008) as they are easier to accurately model in DEM simulations which use spheres to represent particles. The glass beads used in this thesis were 6 *mm* glass beads Type M manufactured by Sigmund Lindner GmbH (Lindner). The glass beads are manufactured to have an excellent roundness with a low proportion of air-bubbles and a high degree of purity. Härtl (2008) manually glued pairs of glass beads together as part of a study to compared experiments and numerical simulations of single and paired glass beads. As the paired glass beads are simply two single glass beads, their contact properties are identical (Except when explicitly mentioned). Most of the material properties for the single and paired glass beads are taken from Chung (2006) and Härtl (2008).

Polyethylene Terephthalate pellets

Polyethylene terephthalate (PET) pellets are an intermediate good used to produce final plastic products. They are produced in granular form to facilitate transportation and storage.

Black eyed beans

The black eyed beans (BEB) (also referred to as the black eyed pea, ChawaLie, Lobia) is a subspecies of the cowpea. It is pale-coloured with a prominent black spot and the currently accepted botanical name is *Vigna unguiculata* subspecies *Unguiculata*. Originally native to India, the cowpea is now grown around the world for its medium-sized edible bean. The sample used in the project originated from Madagascar.

Black kidney beans

Originating from Peru, black kidney beans (BKB) eventually spread through South and Central America thanks to Indian traders and are said to have been brought to Europe by Spanish explorers returning home from the New World in the fifteenth century. Spanish and Portuguese traders eventually spread the kidney beans through Africa and Asia. The black kidney bean owes

its name due to its strong resemblance to a kidney. The BKB used for the thesis originated from China.

3.3.3 Particle physical properties

25 kilograms of BEB, BKB and PET pellets (PP) were available for conducting the experiments. To homogenise the samples, each material was put through a sample riffler. The glass beads were obtained from Härtl's (2008) research project and consisted of approximately 4000 single and 2000 paired glass beads.

Individual particle weight

A total of 70 BEB, BKB and PP were randomly selected and weighed using a scale with an accuracy of ±0.0001g. The average weights and coefficient of variance of the materials used in this thesis are summarised in Table 3.2. The glass beads (GB) measurements were taken from Härtl (2008).

Table 3.2 Average individual particle weight of various granular materials

Material	AVG [*g*]	COV	*n*
Single glass beads [1]	0.2860	1.3%	20
Paired glass beads [2]	0.5720	1.3%	20
PET pellets	0.0329	9.5%	70
Black eyed beans	0.2107	16.4%	70
Black kidney beans	0.3921	22.4%	70

AVG: Average, COV: coefficient of variance, *n*: sample size
[1] Glass beads measurements from Härtl, 2008
[2] Not measured, calculated as twice the individual weight of a single glass bead

The individual weight distributions of the materials are presented as histograms in Figure 3.18. The individual weights for the BEB and the BKB appear to follow a normal distribution, whereas the PP and GB do not. This is possibly due to the various methods in which the grains are produced. The BEB and BKB are organic and produced naturally, whereas the PP and GB are manufactured to a specific size.

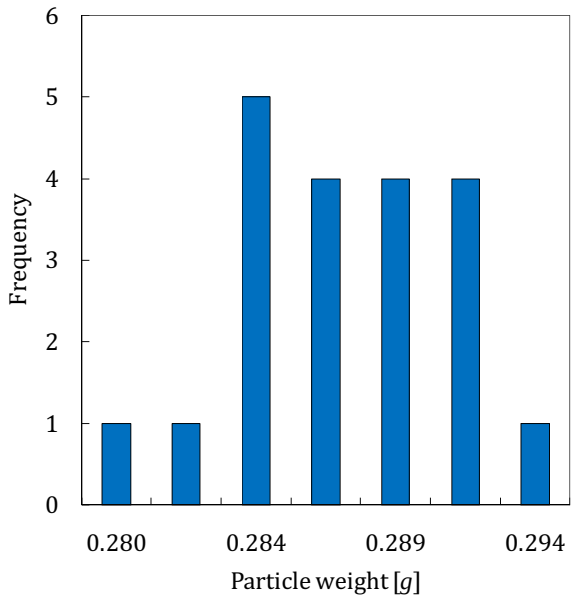

(a) Single glass beads (*n*=20)

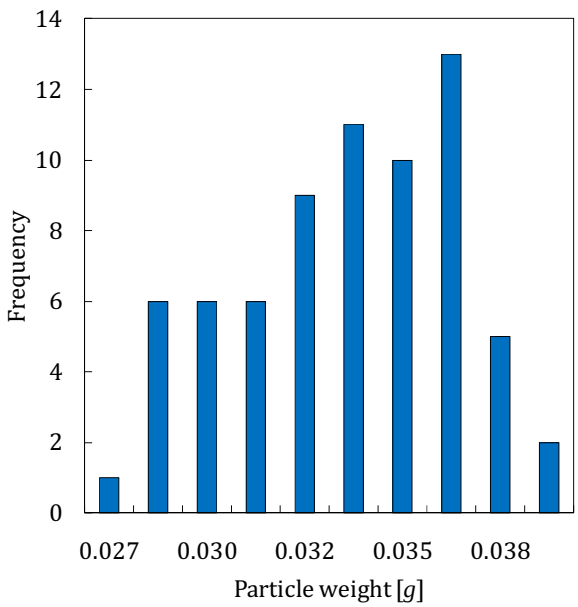

(b) PET pellets (*n*=70)

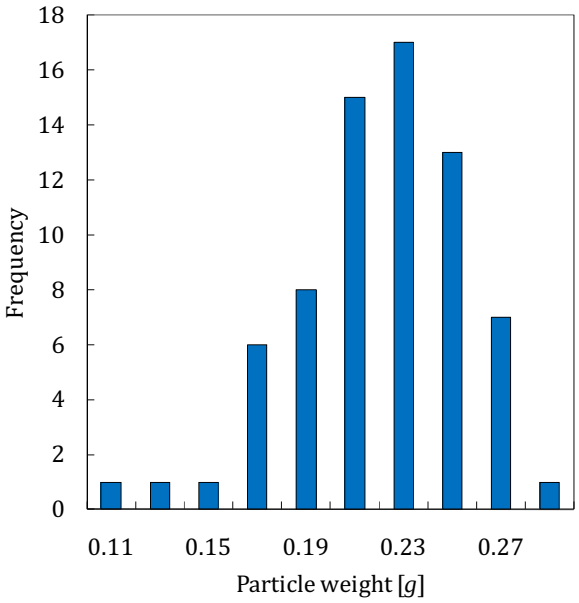

(c) Black eyed beans (*n*=70)

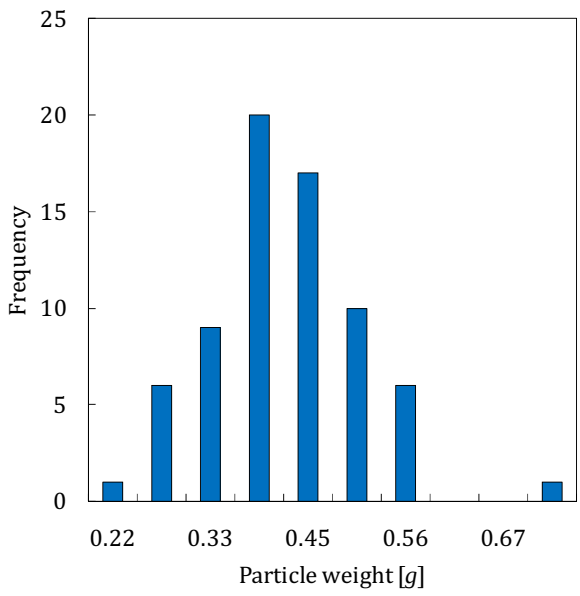

(a) Black kidney beans (*n*=70)

Figure 3.18 Individual weight distribution of various granular materials

n: sample size

Particle solid density

The particle density or density of solids ρ_s is defined as the mass of solids M_s divided by the volume of solids V_s. Solid densities do not take into account the voids present in bulk systems. Experimentally the densities of solids were determined by placing a known mass of granular material into a measuring cylinder with a known volume of water. The volume of solids is then determined using the volume change. The densities of solids are summarised in Table 3.3.

Table 3.3 Various granular material density of solids

Material	AVG ρ_s [kg/m^3]	COV	n
Single glass beads [1]	2550		
PET pellets	1247	1.5%	3
Black eyed beans	1186	0.5%	3
Black kidney beans	1277	1.5%	3

ρ_s:solid density, AVG: Average, COV: coefficient of variance, n: sample size
[1] Härtl (2008) calculated from average dimensions and mass of glass beads

Particle shape descriptors

Agricultural materials are generally quite irregular and do not match any of the geometric primitives easily. A significant number of shape parameters may be required to describe them accurately. Practical measurements show that the various shapes may broadly be characterised by specifying selected orthogonal axes. For example, BEB can be characterised by using the linear dimensions along the three orthogonal axes; length, width and thickness. Theses dimensions almost always range in size from the largest to the smallest. Therefore, it is proposed to refer to the length, width and thickness as the major (MAJ), intermediate (INT) and minor (MIN) dimensions respectively. An example using BEB is illustrated in Figure 3.19.

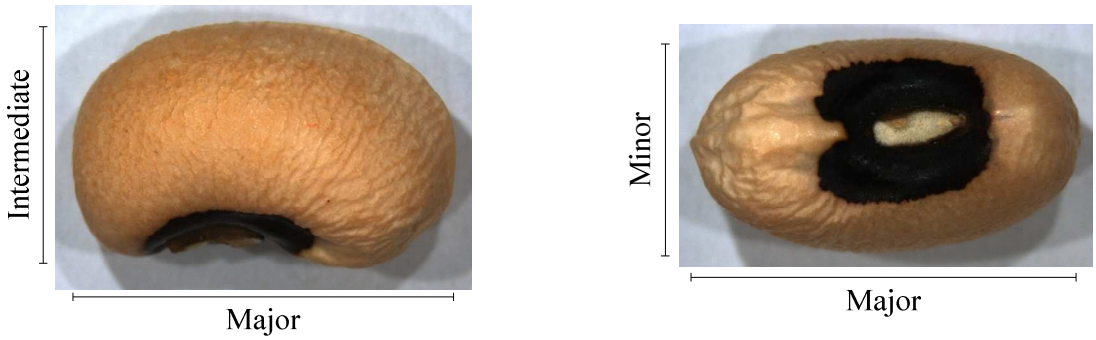

Figure 3.19 Definition of particle major, intermediate and minor dimensions using a black eyed bean

The particle dimensions for the various materials were measured with a digital calliper (accuracy ±0.01 *mm*) and are summarised in Table 3.4. The aspect ratio a_r of a particle is defined as the ratio between the major and intermediate dimensions in this study.

Table 3.4 Particle shape dimensions for various granular materials

		MAJ	INT	MIN	a_r
Single glass beads (*n*=120) [1]	AVG	6.0	6.0	6.0	1.00
	COV	1.4%	1.4%	1.4%	
Paired glass beads (*n*=120) [2]	AVG	12.0	6.0	6.0	2.00
	COV	1.4%	1.4%	1.4%	
PET pellets (*n*=70)	AVG	4.20	3.85	1.85	1.10
	COV	3.0%	5.7%	11.7%	
Black eyed beans (*n*=70)	AVG	9.19	6.54	5.41	1.40
	COV	11.1%	6.3%	7.6%	
Black kidney beans (*n*=70)	AVG	14.73	6.73	5.24	2.20
	COV	11.1%	8.9%	11.1%	

AVG: Average, COV: coefficient of variance, *n*: sample size, MIN: minor, INT: intermediate, MAJ: major, a_r: aspect ratio
[1] Measurements from Härtl (2008)
[2] Based on single glass bead measurements

3.3.4 Particle mechanical Properties

Mechanical properties refer to the properties of a material that reveal its elastic and plastic behaviour when a force is applied. The mechanical properties of the glass beads have been investigated extensively by Chung (2006) and Härtl (2008) and will be summarised in this

section. As the paired glass beads are simply a formation of two single glass beads, their material properties are identical to single glass beads. The mechanical properties for the PP, BEB and BKB were acquired through a combination of laboratory tests and from literature. The mechanical properties of the materials were determined as follows:

- The *Young's modulus* was measured using the ASAE method with a spherical indenter and a rigid platen compression method.
- The *coefficient of sliding friction* was measured with a sliding friction tester developed by Chung (2006).
- The particle to wall *coefficient of restitution* was measured using the restitution drop test apparatus.

Other relevant mechanical properties include the coefficient of rolling friction; however, it is not a property that can be measured easily (Ai 2010). Therefore, no attempts were been made to quantify the coefficient of rolling friction.

3.3.4.1 Particle stiffness

To determine the Young's modulus of the glass beads, Chung (2006) initially used the ASAE Standard single particle compression test using a spherical indenter (Figure 3.20, a) to determine the particle stiffness. He discovered that the spherical indenter was accurate on agricultural grains with a flat surface; however, he observed that when the granular material being tested was rounder, the indenter slipped and was subsequently bent. In these cases, the contact area was no longer circular or elliptical and the line of the applied load was also no longer vertical. Consequently, the formula in the ASAE Standard (ASAE 1996) would not be valid and therefore, the indenter method is not suitable for granular material that do not have sufficiently flat surface. To overcome this issue, Chung (2006) used a vertical compression of the particle between two rigid platens. A 3D laser scanner (3D Scanners Ltd 1998) was used to capture the three-dimensional surface geometry of individual grains. The scanned data were processed to more accurately measure the radii of curvature.

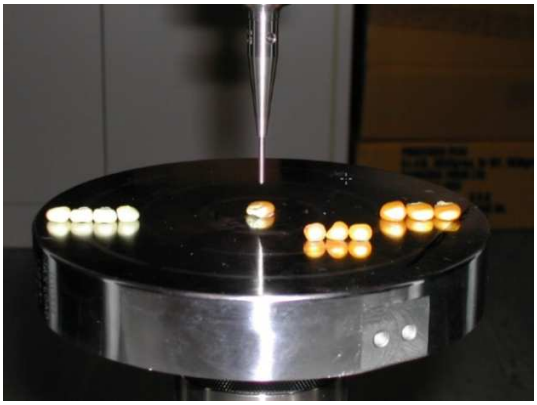

(a) ASAE method with a spherical indenter

(b) Rigid compression platen combined with 3D laser scan of surface profile

Figure 3.20 Experimental setup to determine particle stiffness after Chung (2006)

According to the ASAE standard (1996), the modulus of elasticity for a granular material may be determined using the spherical indenter and the formula given by Shelef and Mohsenin (1969).

$$E = \frac{0.338K_c^{3/2} \cdot P(1-v^2)}{\alpha^{3/2}}\left(\frac{4}{d}\right)^{1/2} \qquad \text{Equation 3.13}$$

where E is the modulus of elasticity of a single corn grain; P is the load applied; α is the deformation of the grain; υ is the Poisson's ratio of the grain; d is the diameter of the indenter and K_c is a geometric constant depending on the principal radii of curvature of the contacting bodies. Equation 3.13 is based on a Hertzian contact with the assumption that the radii of curvature of the corn grains are infinite. Based on this assumption, K_c = 1.351. For an indenter with a diameter of 2 *mm* and an assumed Poisson's ratio of 0.3, Equation 3.13 can be rewritten as

$$E = \frac{0.68 \cdot P}{\alpha^{3/2}} \qquad \text{Equation 3.14}$$

Chung (2006) proposed a method to derive an appropriate approach to interpret this; the rigid platen compression methods based on the more general Hertzian contact theory

(Timoshenko and Goodier 1970). The shear modulus *G* for a particle can be determined using Equation 3.15.

$$G = \frac{E}{2(1+v)} \qquad \text{Equation 3.15}$$

The shear modulus for the glass beads was 1.67E10 *Pa* (Chung 2006) and the shear moduli for the other materials were not measured as they were not required in the parametric optimisation procedure.

3.3.4.2 Coefficient of sliding friction

Many researchers have attempted to measure the friction coefficient, both particle-particle and particle-boundary friction (Lorenz et al. 1997; O'Sullivan et al. 2004b). However, previous research is almost all limited to spherical or nearly spherical particles and may not be suitable for irregularly shaped particles such as typical organic materials. Therefore the literature on the measurement of friction coefficient for irregularly shaped particles is scarce. In this study, the sliding friction angle between the granular material and boundary was determined using a sliding friction tester (Figure 3.21) devised by Chung (2006).

In this test, three particles of a granular material are glued to the base plate and a test plate is placed over them. A spirit level is used to ensure that the test plate is horizontal. During the test, the inclination of the base plate is gradually increased around the hinge using an Instron machine at constant speed, until relative sliding between the grains and the test plate occurs. The inclination of the base plate θ can then be determined using height measurements from the rulers. The static particle to wall coefficient of friction, μ_{pw} can then be determined using

$$\mu_{pw} = \tan(\theta) \qquad \text{Equation 3.16}$$

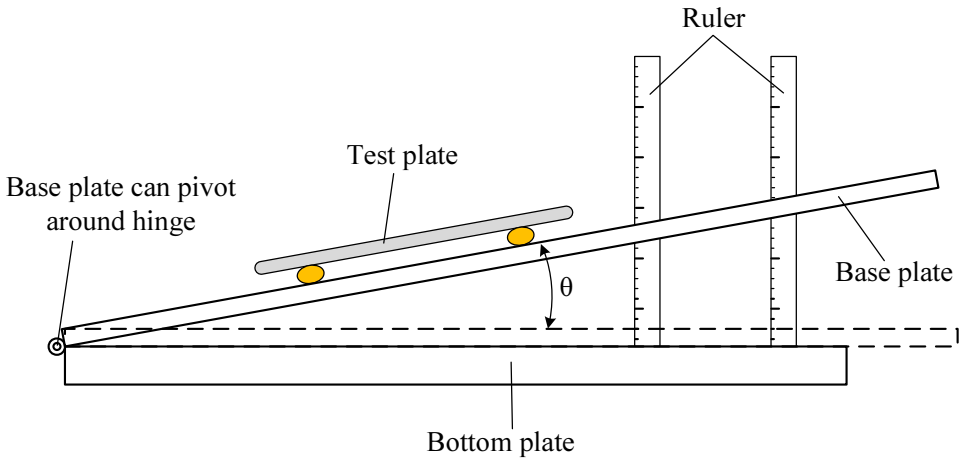

(a) Side view

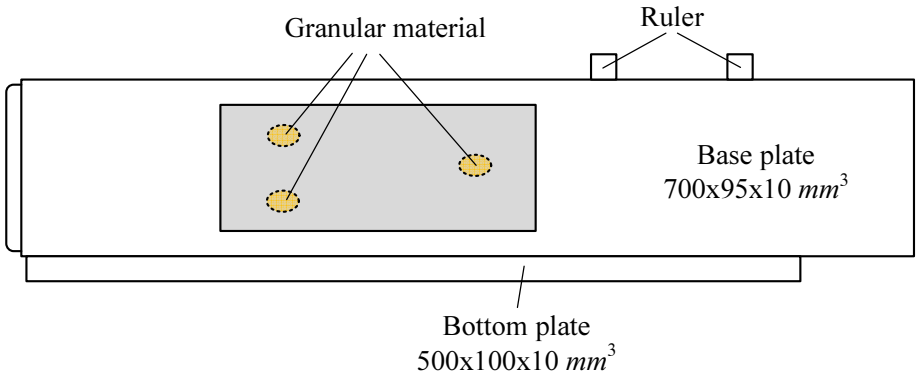

(b) Top view

Figure 3.21 Experimental setup for sliding friction tester developed by Chung (2006)

The particle to particle coefficient sliding friction for organic materials is harder to measure than industrial materials as a flat surface is required. Chung (2006) measured the particle to wall (steel) μ_{pw} and particle to particle μ_{pp} coefficient of sliding friction of glass beads to be 0.13 and 0.18 respectively.

3.3.4.3 Coefficient of restitution

The coefficient of restitution e_r gives a measure of the energy dissipated during a contact. The coefficient of restitution between a granular material and a boundary can be determined using a drop tester as shown in Figure 3.22 and is described in detail by Chung (2006).

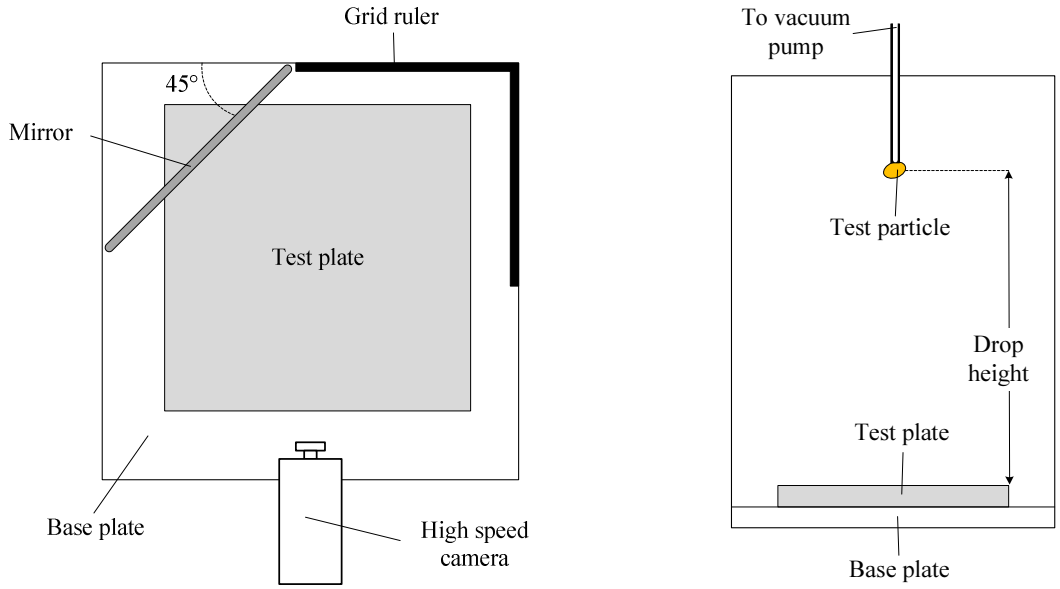

(a) Top view (b) Transverse view

Figure 3.22 Experimental setup for the drop tester as described by Chung (2006)

Using the impact and rebound velocity of a particle e_r may be determined. To determine e_r for the 6 *mm* single glass bead, a single bead was dropped from a height of 294 *mm* onto a stainless steel plate resulting in an impact velocity of 2.4 *m/s*. The results were extracted from images taken during the experiment using a high speed camera (1000 frames/sec). An example of consecutive images of a drop test using a 6 *mm* single glass bead is shown in Figure 3.23.

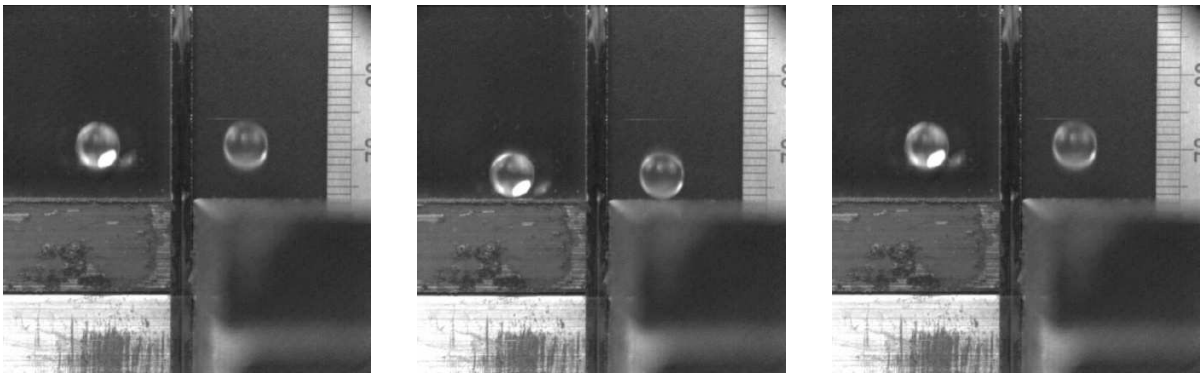

(a) Before impact (b) During impact (c) After impact

Figure 3.23 Consecutive images of a drop test using a 6 *mm* single glass bead (after Chung, 2006)

The particle to wall e_r is easier to measure experimentally than the particle to particle e_r as dropping a spherical particle directly onto another spherical particle with perfect precision is difficult. For this reason, the particle to particle e_r is generally taken to be the same as the particle to wall e_r (Chung 2006; Härtl 2008). Härtl (2008) measured the particle to wall e_r between glass beads and steel to be 0.87.

3.3.5 Bulk physical properties

Bulk densities and void ratios

The volume of voids between the particles in a system is subject the packing arrangement, therefore a range of bulk densities can exist for a single granular material. To establish the range of possible densities that a material may experience, the bulk densities were determined for a system with an artificially induced loose and dense packing arrangement. The densest packing arrangement is obtained using a British Standard Institute 1 litre mould for compaction (BS 1377-4: 1990) with an internal diameter of 105 *mm* mould and shaker shown in Figure 3.24 (a) and (b). The loosest packing arrangement was determined using the same 1 *l* mould but filled using the ascending cone with no impact method (section 3.2.3.1) as illustrated in Figure 3.24 (c).

(a) BSI 1 *l* compaction mould with top ring for aiding filling

(b) Vibrating 'shaker' device to produce denser packing

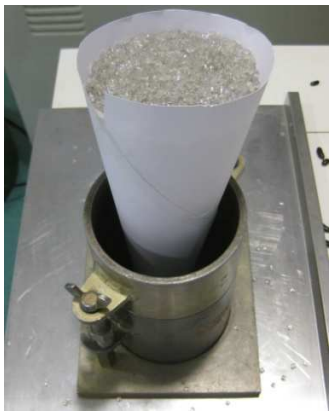

(c) Ascending cone with no impact filling method

Figure 3.24 Laboratory apparatus used to determine bulk densities and void ratios of granular materials

As granular material behaviour is heavily dependent the initial packing conditions (Chung 2006; Härtl 2008), determining a range of possible densities has the advantage of helping to determine how the various granular materials are affected by the contrasting packing arrangements. The average loose and dense bulk densities and void ratios for the five materials are summarised in Table 3.5. The low coefficient of variance highlights the test's repeatability, however the limited sample size (n=3) in some case should be considered.

Table 3.5 Bulk densities and void ratios for various granular materials

(a) Loose bulk densities using the ascending cone with no impact filling method

Material	AVG ρ [kg/m^3]	COV	e	n
Single glass beads [1]	1500	4.9%	0.70	15
Paired glass beads [1]	1401	2.1%	0.82	15
PET pellets	747	0.8%	0.67	3
Black eyed beans	732	0.8%	0.62	3
Black kidney beans	769	0.9%	0.66	3

(b) Dense bulk densities using the rainfall through a sieve filling method

Material	AVG ρ [kg/m^3]	COV	e	n
Single glass beads [1]	1574	0.5%	0.62	15
Paired glass beads [1]	1483	0.4%	0.72	15
PET pellets	815	1.0%	0.67	3
Black eyed beans	777	0.8%	0.62	3
Black kidney beans	819	0.1%	0.66	3

AVG: average, COV: coefficient of variance, n: sample size, e: void ratio, ρ: bulk density
[1] Härtl (2008)

3.3.6 Bulk mechanical properties

Bulk coefficient of sliding friction

The bulk mechanical properties of friction, including the particle to wall $\mu_{pw,bulk}$ and the internal friction $\mu_{pp,bulk}$ were measured using a Jenike shear tester. The experimental setup is shown in Figure 3.25.

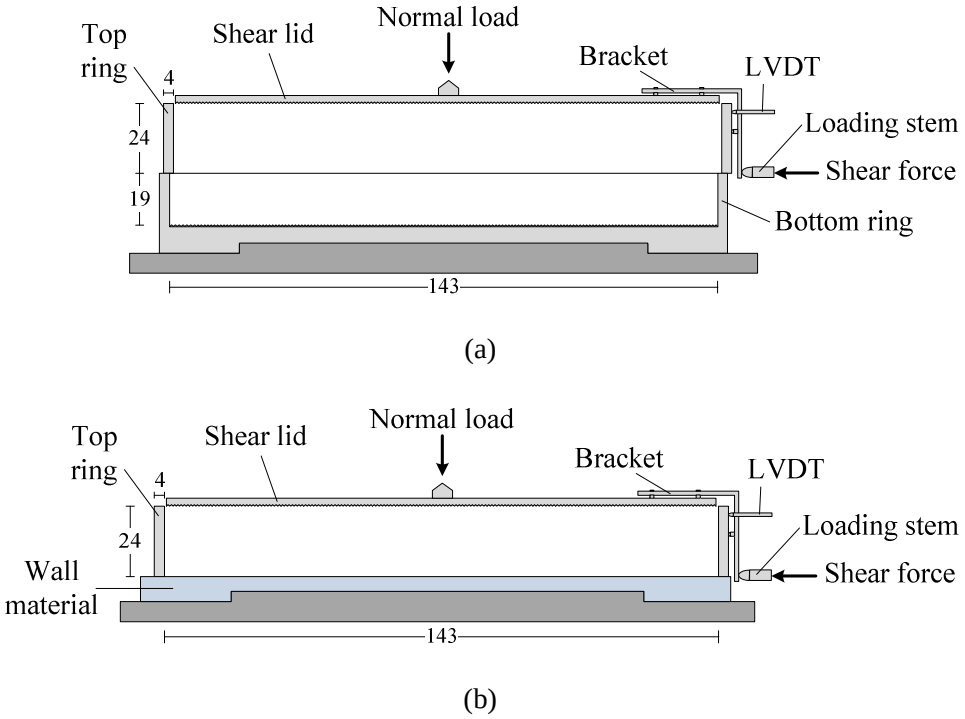

Figure 3.25 Jenike shear tester used to measured (a) the internal and (b) the bulk particle to wall friction (All dimensions in *mm*)

The Jenike shear tester is one of the most widely used instruments to measure the flow properties of particulate solids (Schwedes 2003). The internal friction is measured by filling a squat metal cylinder (internal diameter 143 *mm*, height 43 *mm*) with granular materials (Figure 3.25, a). The cylinder consists of a top and bottom ring. During the test, the sample is sheared laterally by moving the top ring relative to the bottom. The bulk particle to wall coefficient of friction was measured in a similar manner (Figure 3.25, b); however, instead of having a bottom ring, a flat surface of wall material is used and is constraint from movement. Again, the sample is sheared laterally by moving the top ring. The Jenike shear testing was conducted in the following stages (as described by Härtl, 2008):

1. Filling the shear cell and mould ring
2. Levelling
3. Pre-consolidating
4. Removing the mound ring, and levelling
5. Applying vertical stress and
6. Shearing under constant normal load

The lid and bottom of the shear cell were roughened with 1 *mm* grooves as recommended in the standards (IChE 1989). The top ring was sheared for 6 *mm* at a nominal rate of 1 *mm*/*min* (the displacement rate actually varied from 0.8 to 1.4 *mm*/*min*). The force was measured using a load cell with an accuracy of 0.14 *N* (equivalent to 9 *Pa* average shear stress for the 143 *mm* diameter shear ring used) at log rate of 4 *Hz*. The linear horizontal displacement of the upper shear ring was measured using spring loaded linear variable differential transformer (LVDT).

For each material, a dense (rainfall through a sieve method) and a loose filling (ascending cone with no impact) were tested under 4 different normal loads, each of which were conducted three times for repeatability.

The Mohr-Coulomb criterion (Lambe and Whitman 1979) can generally be used to adequately described the failure properties of a granular mass using

$$\tau_f = c + \sigma_n \cdot \tan(\varphi_{bulk}) \qquad \text{Equation 3.17}$$

Where τ_f and σ_n are the limiting shear stress and normal stress on the failure plane respectively, c and φ_{bulk} are the material constants known as the cohesion and the internal friction angle respectively. The granular material used in this study were all treated as cohesionless materials (c=0). Based on this assumption, the bulk coefficient of friction can be determined by fitting a linear regression line to the test series over the normal stress range μ_{bulk}. Another method of describing the bulk friction is by using the secant friction coefficient μ_s, which is a ratio of the shear to normal stress at failure (τ_f/σ_n).

An example of the shearing response during a Jenike shear test Figure 3.26. The maximum or limiting shear stress is determined using the average stress over 2 *mm* of the plateau region of each curve. The shearing responses curves for internal friction $\mu_{pp,bulk}$ and particle to wall (acrylic) friction $\mu_{pw,bulk}$ can be found in Appendix A.

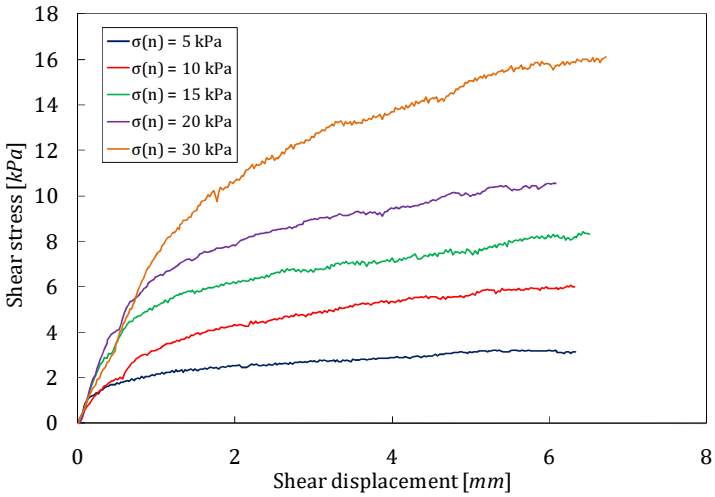

(a) Internal friction of black eyed beans

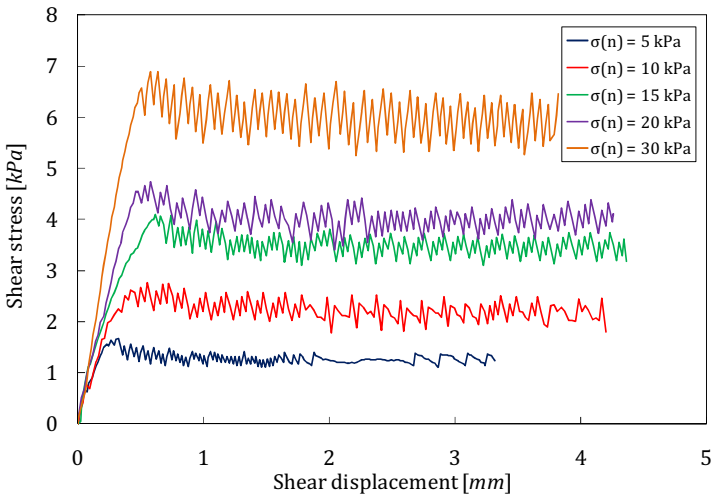

(b) Bulk particle to wall friction using PET pellets against an acylic wall

Figure 3.26 Shearing response during a Jenike shear test with central filling

Figure 3.27 shows the best line fit for each test series consisting of five different normal stress levels. A linear regression line was added to the set of results for each material, with an acceptable fit ($R^2 > 0.95$).

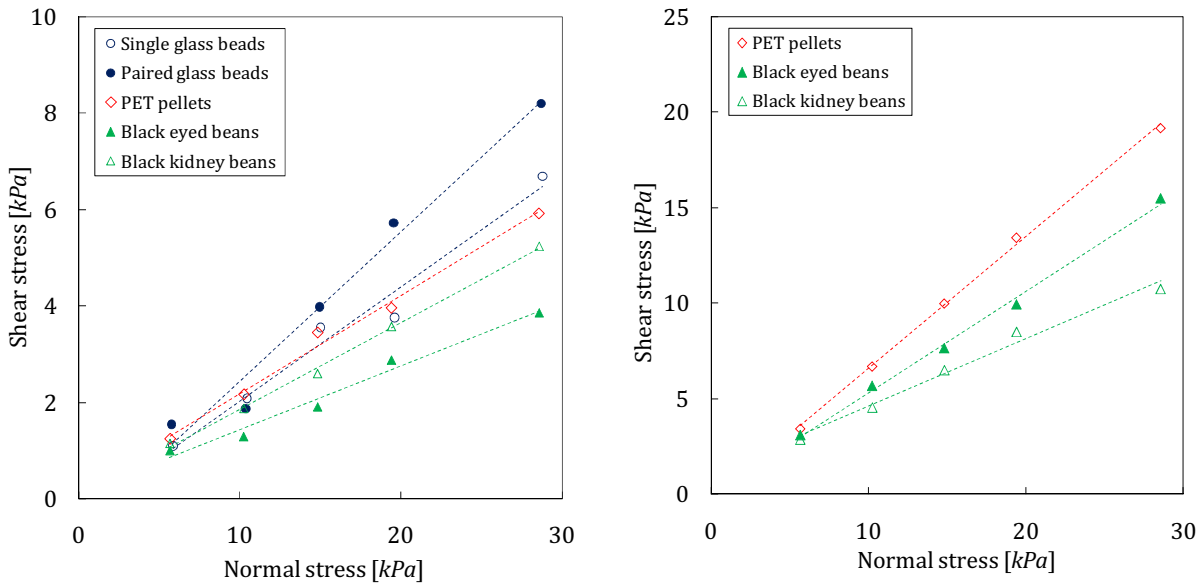

(a) Bulk particle to acrylic friction, $\mu_{pw,bulk}$

(b) Internal friction, $\mu_{pp,bulk}$

Figure 3.27 Shearing stress versus normal stress for various granular materials

From Figure 3.27, positive and negative cohesion is observed from the various materials, neither of which are physical phenomenon. As the material tested is cohesionless, positive cohesion is unlikely, and negative cohesion is physically impossible. One possible explanation is the overestimation of the normal stresses as a result of wall friction. The plotted normal stresses are calculated based on the applied stresses on the top surface ($\sigma_{n,T}$) of the sample; however a portion is absorbed by the wall friction along the shear ring wall and a lower stress will exist at the plane of shear. The vertical stress at the shear plane ($\sigma_{n,B}$) is given by Equation 3.18, the derivation of which is presented in Appendix A.

$$\sigma_{n,B} = \sigma_{n,T} - \left[1 - \frac{2H \cdot \mu_{pp} \cdot K}{R}\right] \qquad \text{Equation 3.18}$$

Where H is the height of the sample, K is the lateral pressure ratio and R is the Jenike shear cell radius. This equation illustrates that particles with higher values of K will experience greater overestimations of $\sigma_{v,T}$. It cannot be said what the direct influence on the gradient of the curve is, as many others factors will affect the system (μ_{pp}, stress level, porosity, etc). For these

reason, it was not chosen to fix the linear regression curves to a cohesion of 0 (through the origin). The coefficients of frictions $\mu_{pp,bulk}$ and $\mu_{pw,bulk}$, and their respective bulk friction angles are summarised in Table 3.6.

Table 3.6 The bulk particle to particle and particle to wall coefficients of frictions for various granular materials, using a central filling method

(a) Bulk particle to particle coefficients of friction, $\mu_{pp,bulk}$

Particle material	e_0	$\mu_{pp,bulk}$	$\varphi_{pp,bulk}$
Single glass beads [1]	0.70	0.48	26 °
Paired glass beads [1]	0.82	0.45	24 °
Plastic pellets	0.57	0.69	35 °
Black eyed beans	0.51	0.53	28 °
Black kidney beans	0.54	0.35	19 °

(b) Bulk particle to acrylic coefficients of friction, $\mu_{pw,bulk}$

Particle material	e_0	$\mu_{pw,bulk}$	$\varphi_{pw,bulk}$
Single glass beads	0.55	0.24	13 °
Paired glass beads	0.89	0.31	17 °
Plastic pellets	0.49	0.20	12 °
Black eyed beans	0.49	0.13	8 °
Black kidney beans	0.58	0.18	10 °

[1] After Härtl (2008)
e_o: initial void ratio

The initial void ratio e_0 is relatively similar in all cases, except for paired glass beads, as the particle shape inhibits a naturally denser formation during filling. A larger friction force would be expected for a denser arrangement using the same material.

Particles with larger aspect ratio are expected to produce higher $\varphi_{pp,bulk}$ as particle interlocking will be greater. However, the lowest internal angle of friction $\varphi_{pp,bulk}$ is observed in the BEB which have the highest aspect ratio of in the various grains and the PP which has the highest $\varphi_{pp,bulk}$ have the smallest aspect ratio.

A closer inspection of the particles reveals that the PP is very angular and the small particle size allowed for a denser packing arrangement. The BKB have a very smooth surface and the large aspect ratio encouraged a looser packing. This is echoed in the difference in initial void ratio between the two grains.

It can be seen that the paired GB have a higher $\mu_{pw,bulk}$ than the single GB. This could be attributed to the greater particle interlocking of the paired particles. In addition, the single GB will be more susceptible to rolling. The other materials have similar values for $\mu_{pw,bulk}$. The shearing response curves for the particle to wall friction (Figure 3.26, b) show slip-slip stick behaviour which are typically seen when sheared along acrylic boundaries and have been linked to honking and quaking in silos (Buick et al. 2005).

3.4 Summary

3.4.1 Laboratory devices and measurement of the bulk response parameters

Two laboratory devices for measuring the bulk responses that will be used to calibrate the DEM models in this study were selected; the rotating drum and the confined compression test. These devices were chosen as they can produce bulk responses that are repeatable and easy to quantify, as well as generate discriminating results in numerical simulations when DEM parameters are varied.

The bulk response measured from the rotating drum is the dynamic angle of repose formed by the granular material in a drum rotating at a speed of $7rpm$ at. The confined compression apparatus can be used to determine the bulk stiffness of system by monitoring the change in void ratio from the stress applied during a loading and unloading cycle. The gradients of the loading and unloading curve λ and κ will be the bulk response parameters used to calibrate the DEM models.

3.4.2 Summary of material properties

The optimisation procedure developed in this thesis was designed to be applicable to a wide range of materials. Therefore, a contrasting set of granular materials were chosen for this study and consisted of:

- Single glass beads
- Paired glass beads
- PET pellets
- Black eyed beans
- Black kidney beans

Granular material in industrial handling scenarios rarely involve single particles and are often found in bulk assemblies. It is therefore important to distinguish between particle and bulk properties. The material properties for a typical granular solid may be grouped into two categories; physical and mechanical and can either be a particle or a bulk property.

This chapter described and summarised the laboratory tests used to determine the material properties for the five granular materials. The material properties were either determined through a set of laboratory tests when required or taken from literature.

This chapter has demonstrated the contrasting and complex nature of the material properties that are present in granular materials.

Chapter 4

Experimental results and analysis of bulk tests

4.1 Introduction

Chapter 3 described the selection of the experimental devices and granular material used in this study. This chapter will summarise the bulk experimental results obtained from the tests for each granular material and discuss the salient results. The focus will be placed on the two main devices that were used to calibrate DEM models; the rotating drum and the confined compression apparatus. The granular materials that were tested include the single and paired glass beads (GB), Polyethylene Terephthalate pellets (PP), black eyed beans (BEB) and black kidney beans (BKB).

4.2 Rotating drum device

The flow regimes that exist within a rotating drum have been linked to many parameters including the end plate sliding friction, fill volume, drum depth, particle shape and size, the

Froude number and rotational speed to name a few (Rutgers 1965; Metcalfe et al. 1995; Dury et al. 1998; Ding et al. 2001; Santomaso et al. 2003; Yang et al. 2008).

The rotating drum device was used determine the dynamic angle of repose ϕ_r produced by the granular material at a given rotational speed. This study focused on a relatively low speed range (1 to 14 *rpm*).

4.2.1 The influence of rotational drum speed on the dynamic angle of repose

The five granular materials were tested in the rotating drum to determine the dynamic ϕ_r as described in section 3.2.1.1. The rotational speed of the rotating drum was increased incrementally from 1 to 14 *rpm* to investigate the effects of angular velocity on the dynamic ϕ_r. The results are shown in Figure 4.1. The rotational speed at which the flow regime was observed to change from slumping to avalanching is delineated by a dashed line.

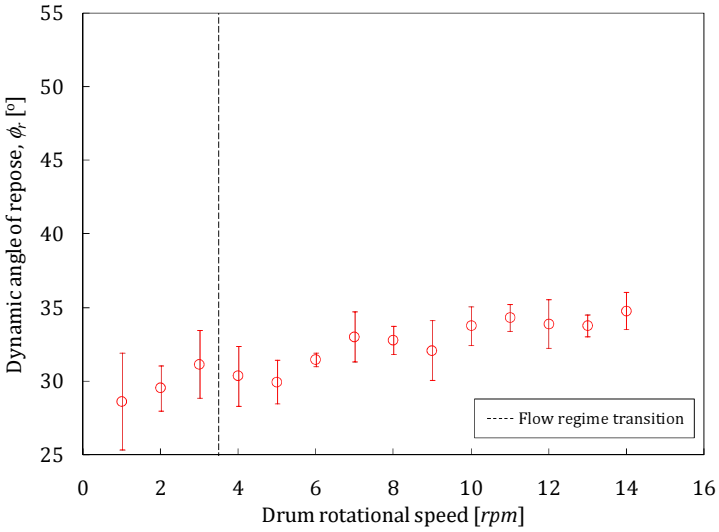

(a) Single glass beads

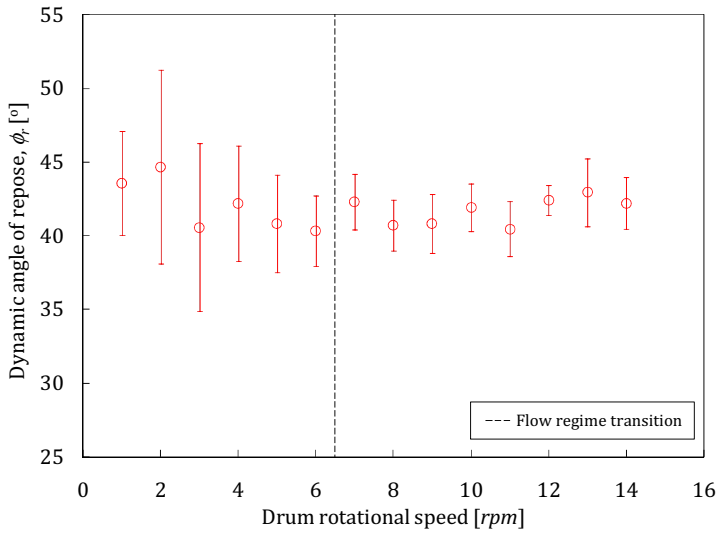

(b) Paired glass beads

Figure 4.1 Influence of drum rotational speed on the dynamic angle of repose in a rotating drum for various materials

Each data point is an average of 10 images and the error bar represents the standard deviation
The flow regime transition line represents the transition from a slumping to avalanching flow regime

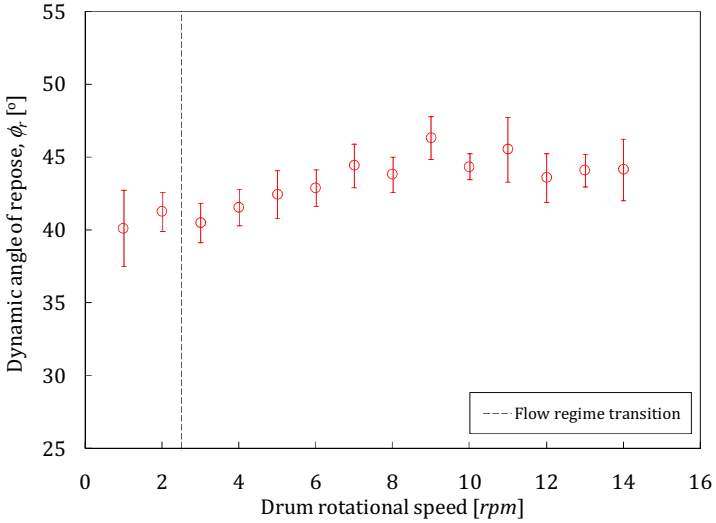

(c) PET pellets

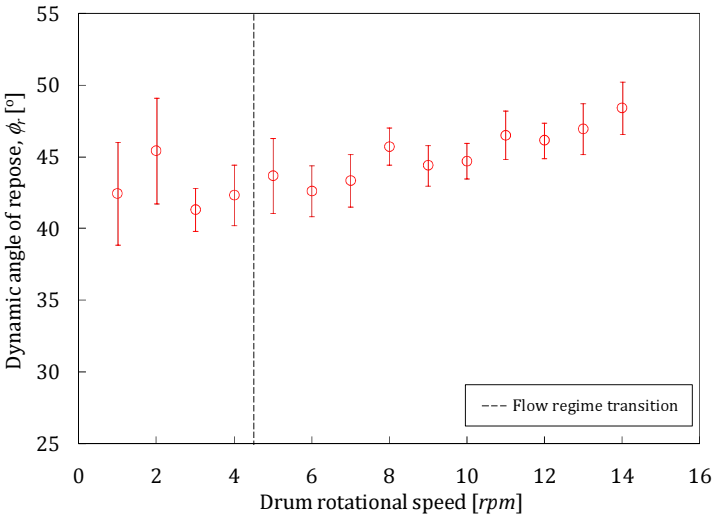

(d) Black eyed beans

Figure 4.1 Influence of drum rotational speed on the dynamic angle of repose in a rotating drum for various materials

Each data point is an average of 10 images and the error bar represents the standard deviation
The flow regime transition line represents the transition from a slumping to avalanching flow regime

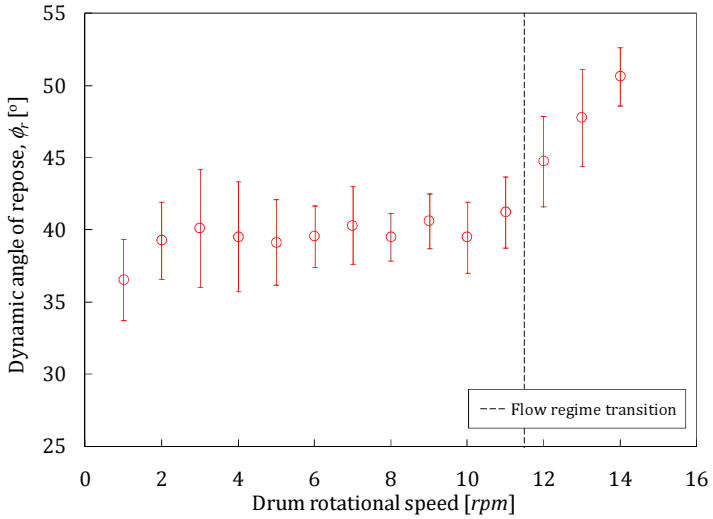

(e) Black kidney beans

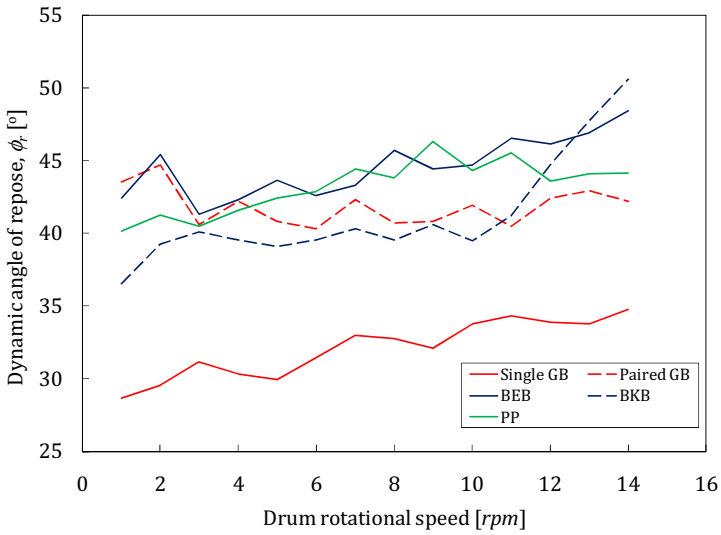

(f) Trend comparison using all the granular materials

Figure 4.1 Influence of drum rotational speed on the dynamic angle of repose in a rotating drum for various materials

Each data point is an average of 10 images and the error bar represents the standard deviation
The flow regime transition line represents the transition from a slumping to avalanching flow regime
GB: glass beads, PP: PET pellets, BEB: black eye bens, BKB: black kidney beans

4.2.1.1 Centrifugal forces

Yang (2008) investigated the granular flow dynamics in a rotating drum for different regimes using DEM by varying the rotation speed. He found that the dynamic ϕ_r formed by the particle surface had a weak dependence on the rotation speed during the slumping and avalanching regimes, whereas during the cascading, cataracting and centrifuging regimes the influence increased significantly. This study focused on the inter-particle behaviour by studying slow shearing systems and additional forces were reduced or eliminated from the analysis where possible.

The ratio of the centrifugal force, F_c to gravitational forces F_g of a particle along the inner drum wall (the most critical value) is defined as the non dimensional rotation Froude number *Fr* that may be described as Equation 2.21 and is irrespective of particle mass.

$$Fr = \frac{r \cdot \omega^2}{g} \qquad \text{Equation 4.1}$$

where *r* is the inner drum radius, *g* the gravitational constant and ω the angular velocity of the drum. As *r* and *g* are constants in the drum experiments, *Fr* will be affected by the angular velocity at a quadratic rate. This is illustrated in Figure 4.2 for a 184 *mm* drum and speed range of 1 to 14 *rpm*s. The bulk measurements used to calibrate the DEM models was the dynamic ϕ_r at 7 *rpm* which has an *Fr*=5E-3 and can be considered negligible in the analysis. Mellmann (2001) predicted an avalanching flow regime for a *Fr*=5E-3 which is correct for all materials excluding the BKB.

4.2.2 Observations and discussion

The salient experimental results from the rotating drum device laboratory experiments on the five granular materials are summarised in Table 4.1.

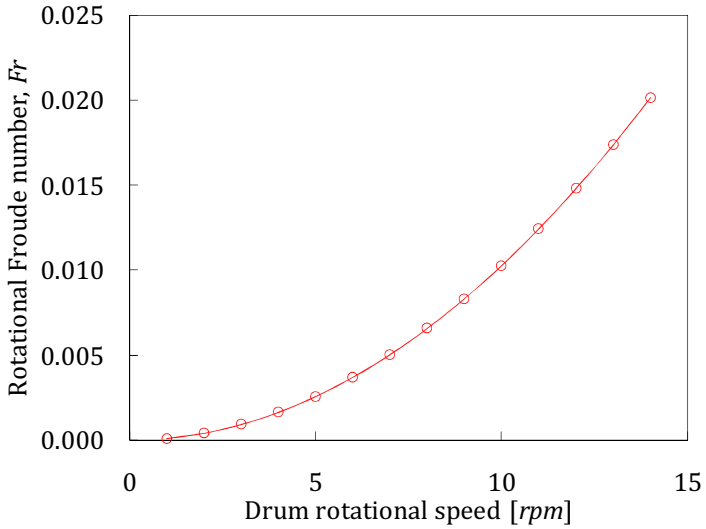

Figure 4.2 The effect of rotational speed on the centrifugal forces in a rotating drum with an inner drum diameter 184 *mm*

Table 4.1 Summary of experimental results using the rotating drum

	Single GB	Paired GB	PP	BEB	BKB
Minimum dynamic ϕ_r [°]	28.6	40.3	40.1	41.3	36.5
Maximum dynamic ϕ_r [°]	34.8	44.7	46.3	48.4	50.6
Difference between min and max ϕ_r [%]	21.7%	10.9%	15.5%	17.1%	38.5%
AVG dynamic ϕ_r at 7 *rpm*	33.0	42.3	44.4	43.3	40.3
COV at 7 *rpm*	5.2%	4.5%	3.4%	4.2%	6.6%
n at 7 *rpm*	10	10	10	10	10
Regime transition speed [*rpm*] [1]	3-4	6-7	2-3	4-5	11-12
Rotational Froude number at 7 *rpm*, *Fr*	5E-03	5E-03	5E-03	5E-03	5E-03
Aspect ratio of material, a_r	1.00	2.00	1.10	1.40	2.20
Drum fill degree, *f*	40%	40%	40%	40%	40%
Number of particles in drum [2]	1210	590	5505	805	460
Drum diameter/major particle dimension	30.7	15.3	43.8	20.0	12.5
Drum depth/major particle dimension	3.3	1.7	4.8	2.2	1.4

AVG: Average, COV: coefficient of variance, *n*: sample size, ϕ_r: angle of repose
GB: glass beads, PP: PET pellets, BEB: black eyed beans, BKB: black kidney beans
[1] Transition from a slumping to avalanching flow regime
[2] Determined using average particle and sample weights

The main observations that were made from the results obtained from the rotating drum experiments on the single and paired GB, PP, BEB and BKB are summarised below:

I. As the literature would suggest (Santomaso et al. 2003; Ding et al. 2001; Yang et al. 2008), the general trend for all of the granular materials (less visible with paired GB) is an increase in dynamic ϕ_r as the drum rotational speed increases (Figure 4.1).

II. The difference between the maximum and the minimum dynamic ϕ_r over the rotational speed range varies significantly for the five granular materials. This difference is an indicator of the influence of rotational speed on the dynamic ϕ_r. Paired GB and PP appear to be less influenced by rotational speed than BKB.

III. The number of particles to achieve a 40% fill volume varies considerable for the five granular materials (460-5500). This is important as DEM computational times are directly affected by the number of particles in the system.

IV. For all the granular material (Figure 4.1), the standard deviation is greater before the flow regime transition than after. The higher standard deviation coincides with the slumping regime where the dynamic ϕ_r is more likely to vary. After the regime transition, the avalanching flow regime and the dynamic ϕ_r is more consistent. This is reflected in the lower standard deviation.

V. Systems with larger particles (paired GB and BKB) have greater dynamic ϕ_r variance (i.e. higher standard deviations) as the number of particles along the surface profile decreases (Table 4.1, drum diameter/major particle dimension) and the dynamic ϕ_r determination is more susceptible to experimental error. This phenomenon is illustrated in Figure 5.16 and described in detail using a parametric study in section 5.3.9.

VI. The flow regime transition occurs at a range of rotational speeds for the various granular materials (2.5 to 11.5 *rpm*). The rotational speed of the flow regime transitions appears to be influenced by the particle aspect ratio a_r (defined as the major to intermediate dimension ratio). As a_r increases, the inter-particle locking will increase accordingly. As a result, a higher rotational speed is required to achieve a constant avalanching flow. This is illustrated by the BKB having the largest a_r (2.20) and highest flow regime transition speed (11-12 *rpm*). Due to the high coefficient of variance of the dynamic ϕ_r during the slumping regime, this study will focus on the avalanching regime.

VII. The BKB (Figure 4.1, e) see a significant increase in dynamic ϕ_r following the flow regime transition (25%). After a macroscopic investigation of the experimental videos, slipping was observed along the inner drum wall before the regime transition. This is a result of the high a_r and inter-particle locking, forcing the particles in the system to behave as a single solid. When the system behaves in this manner, a lower dynamic ϕ_r is observed. As the rotational speed increase, the particles in the system loosen and develop a more fluid like motion, the avalanching regime develops and the dynamic ϕ_r increases.

VIII. At lower *rpm*, the paired GB displayed a significantly larger dynamic ϕ_r than the single GB (53% difference at 1*rpm*). This is attributed to the greater inter-locking forces found in the paired GB. As angular velocities increase, the two lines converge demonstrating that individual particle properties may not have much influence at greater *rpm*s and the flow regimes is influence primarily by the centrifugal forces and boundary conditions. This was confirmed in preliminary studies that used a speed range of 1 to 49 *rpm*, the results of which can be found in Appendix A.

IX. Although the two organic materials (BEB and BKB) have contrasting a_r, their dynamic ϕ_r are similar in magnitude. A closer look at the grain surface (Figure 3.17) show contrasting surface roughness which translates to a higher bulk sliding friction observed in the material characterisation using the Jenike shear cell (Table 3.6).Therefore, although the BKB have a higher a_r than the BEB, the grain surface is smoother and the results is similar dynamic ϕ_r.

X. Dury et al. (1998) conducted a similar experiment using a rotating drum filled with single glass beads. A comparative study with their results for similar rotational speeds found that their dynamic ϕ_r were consistently lower. However, their experimental setup included a significantly deeper drum, where there influence of the drum end plates is reduced and the result is a lower dynamic ϕ_r.

XI. DEM simulations of granular materials have previously been represented using single spheres (Walton and Braun 1993; Dury et al. 1998; Zhou et al. 1999). However, the comparative plot in Figure 4.1 (f) illustrates that using single GB to represent the granular materials will underestimate the dynamic ϕ_r, whereas paired GB display a more representative angle.

The various granular materials have displayed an interesting set of results in the rotating drum device. It can be seen from the results that the bulk behaviour is complex in nature and predicting bulk responses using numerical simulations will require an in depth understanding of the experimental device and material properties.

4.2.3 Sources of errors

The main potential source of error in the rotating drum experiments comes from a manual determination of the dynamic ϕ_r during the slumping regime as the number of particles along the surface profile decreases. To limit the potential for error, ten separate pictures were taken at random intervals for each rotational speed and the method of manually estimating ϕ_r was systematic throughout the study.

The end plates have a significant influence on the dynamic ϕ_r (Dury et al. 1998) and the experimental setup of the rotating drum had a high diameter to depth ratio (9.2), therefore the end plate friction is expected to have a greater influence on the results than in a deeper drum.

At higher rotational speeds, a minor amount of static electricity was produced between the PP and the acrylic drum wall and manifested itself through particles adhering to the drum wall. However, the magnitude of the static electric charges did not appear to affect the dynamic ϕ_r significantly, so was ignored. At greater rotational speeds, if the dynamic ϕ_r is seen to be affected by the static attraction, a static electrical or cohesion model may need to be included in the numerical simulations when modelling the system.

4.3 Confined compression

The confined compression test (also referred to as the K_0 test) is used to investigate the mechanical response of a granular bulk material under vertical loading and the subsequent load transfer to the containing walls.

The confined compression test is the second experimental device used in the parametric optimisation developed in this study. More specifically, the bulk measurement used to calibrate the DEM models was the bulk loading λ and unloading κ stiffnesses of the system under a compression stress of 65 kPa. The test was carried out on five granular materials and each material was tested using a dense filling method which involved rainfalling (RF) particle

deposition through a sieve (after Chung 2006) and a loose filling method using an ascending cone (AC) filled with particles (after Härtl 2008). The granular materials were tested in the confined compression test as described in section 3.2.2.1. The results were all analysed in a systematic manner and each test was repeated three times to check for repeatability.

4.3.1 Stress-strain responses

The strains incurred from applied stresses in the confined compression vary throughout the sample. In this study, the strain is defined as the average sample strain determined using the confined compression platen heights, and the stress is defined as the average stress applied by the top and bottom platens.

The virgin loading of the confined compression tests on the granular materials were analysed by fitting a regression trendline. As the loading path was found to be non-linear, a linear trendline would produce a less accurate description of the loading curve than a second order polynomial (see section 3.2.2.4). Using a polynomial trendline will enable the loading path to be described as an empirical polynomial in the form

$$y = Ax^2 + Bx + C \qquad \text{Equation 4.2}$$

The average A and B coefficients for the virgin loading line of the three tests on each the various granular materials are shown in Table 4.2. The coefficients are gradients of the stress stain curve and are therefore an indication of the system's stiffness. The stress is in *kPa* and the average represents 3 tests with a coefficient of variance (COV), A < 7% and B < 20%. The polynomial trendline fit was good with a correlation of R^2 > 0.98. The single and paired GB virgin loadings were not included as the low virgin loading stress level (15 *kPa*) resulted in less repeatable behaviour.

Table 4.2 Average polynomial coefficient for the virgin loading stress strain response of various materials and filling methods

Filling method	Coefficient	PET pellets	Black eyed beans	Black kidney beans
Ascending cone	*A*	2.6E+05	3.8E+05	9.0E+04
	B	3.0E+03	2.6E+03	5.3E+02
Rainfall	*A*	5.4E+05	5.9E+05	1.4E+05
	B	6.3E+03	7.7E+03	2.2E+03

The coefficient B represents the initial gradient when stresses are very low. Granular solids are often unpredictable at low stresses and this is reflected in high COV for B. The two filling methods produced very large differences in virgin loading gradient with the denser filling method having a higher gradient (stiffer system) as expected. The smallest gradient is seen in the ascending cone (loose) filling method of BKB. This is primarily due to the large a_r of the material which inhibits a naturally denser packing arrangement, especially when filled loosely. When filled using the rainfall filling method (dense), the PP and the BEB show similar stiffness gradients.

4.3.2 Lateral pressure ratio

The well established Janssen (1895) formula uses the equilibrium of a horizontal slice of the granular material to estimate pressures in deep silos. Janssen's lateral pressure ratio *K* describes the relationship between the average stresses acting on the finite dimension of a slice and the stresses that act on the walls of a silo. It is a widely used parameter for design in geotechnical engineering and almost all design codes use a Janssen-type pressure distribution to predict silo pressures (Wilms 1992; Rotter 2001; EN 1991-4 1995). Due to the inherent variability of granular materials, Eurocodes (1996) suggest altering the lateral pressure ratio by a conversion factor when designing silos and tanks.

Janssen assumed that the ratio between the average effective vertical stress σ_v' and the stress normal to the wall, σ_h' is a constant for a given bulk material stored in a silo. The lateral pressure ratio *K*, can be described as

$$K = \frac{\sigma_h'}{\sigma_v'} \qquad \text{Equation 4.3}$$

The experimental setup for the confined compression test restricted the measurement of pressures within the apparatus and therefore *K* is defined in this thesis using σ_h' as the average horizontal pressure in the sample (determined using strain measurements around the cylinder wall) and σ_v' as the average platen stresses (determined using the stresses on the top and bottom platens). The lateral pressure ratios for the various materials using the ascending cone and rainfall filling method are shown in Table 4.3.

Table 4.3 the lateral pressure ratio *K* for various granular materials and filling methods

Filling method	Ascending cone		Rainfall	
	AVG	COV	AVG	COV
Single glass beads	0.65	9.1%	0.64	9.2%
Paired glass beads	0.71	6.7%	0.66	7.8%
PET pellets	0.44	5.3%	0.33	0.6%
Black eyed beans	0.60	3.5%	0.46	17.1%
Black kidney beans	0.53	6.5%	0.45	3.7%

Each test was carried out 3 times for repeatability
AVG: average, COV: coefficient of variance

The lateral pressure ratio *K* depends on the material properties of the grain, moisture content, bulk density, packing arrangement and bedding structure of the grain formed during the filling process (Horabik and Rusinek 2002). It can be seen from Table 4.3 that for each granular material K is greater for systems with a looser filling than the denser equivalent. This suggests that for lower bulk densities, the horizontal pressures transferred from vertical stresses will be greater.

The single GB show a relatively minor difference in filling method. As the other parameters are kept constant during the test, this suggests that the packing arrangement is very similar. During filling, the single GB will roll and settle into a naturally dense packing arrangement, regardless of the filling method. The single and paired GB have a significantly larger difference in *K* as a result of different filling methods than the PP, BEB and the BKB. One possible explanation is the difference in bulk Poisson's ratio υ_b, which is directly linked to packing arrangements. The squatter experimental setup for the GB (see section 3.2.2.1) may have contributed to a higher υ_b, increasing *K*.

4.3.3 Bulk stiffness parameter

The bulk stiffness of a system is a useful method to describe and predict how solids will react under a variety of pressures. The bulk loading and unloading stiffness parameters are often used in geotechnics and are the gradients of the loading and unloading curves in the void ratio versus compression stress semi-logarithmic plot; also known as λ and κ respectively. The advantage of using a semi-log plot is that the unloading curve is straightened and a logarithmic trendline can be added to the loading and unloading lines. Whereas λ is a parameter dependent on the plastic properties of bulk system, κ is mainly dependent on the elastic properties (see section 2.3.1.1). Another advantage of using the bulk stiffness parameter to calibrate the DEM models is that they may be described using a single parameter.

To protect the integrity of the brittle glass beads a lower stress level was used (35 *kPa*) than the other granular materials which were compressed to 65 *kPa*. Each test was conducted three times for repeatability and each material was filled using the ascending cone (AC) and rainfall filling (RF) method. A summary of the salient results obtained from the confined compression test for the various granular materials are shown in Table 4.4.

Table 4.4 Bulk stiffness parameters and initial void ratios of various materials

Material	Filling method	e_0		Loading, λ		Unloading, κ	
		AVG	COV	AVG	COV	AVG	COV
Single glass beads [1]	AC	0.73	2.4%	3.7E-03	2.2%	2.9E-03	3.1%
	RF	0.66	5.2%	3.5E-03	2.6%	3.0E-03	2.5%
Paired glass beads [1]	AC	0.85	0.7%	4.3E-03	10.9%	2.6E-03	0.3%
	RF	0.71	0.8%	4.1E-03	11.6%	2.7E-02	3.3%
PET pellets [2]	AC	0.65	1.6%	8.5E-03	5.0%	2.2E-03	2.9%
	RF	0.49	3.5%	4.7E-03	4.3%	1.8E-03	1.7%
Black eyed beans [2]	AC	0.59	0.3%	7.5E-03	0.5%	1.9E-03	1.3%
	RF	0.46	6.2%	4.1E-03	4.5%	1.5E-03	2.3%
Black kidney beans [2]	AC	0.63	0.2%	1.7E-02	1.7%	3.3E-03	2.3%
	RF	0.53	0.9%	1.1E-02	1.8%	2.7E-03	1.9%

Compression stress level [1] 35 *kPa*, [2] 65 *kPa*
AVG: Average, COV: coefficient of variance, e_o: initial void ratio, AC: ascending cone, RF: rainfall, Sample size=3

4.3.4 Observations and discussion

The main observations that were made from the confined compression test results on the various granular materials are summarised below:

I. The bulk stiffness parameters λ and κ represent the loading and unloading gradient of a void ratio versus log-stress graph respectively and therefore, a lower gradient translate to a stiffer system. As expected, the general trend for the five different granular materials is a lower bulk stiffness gradient for a denser filling method (RF) than the respective looser filling method (AC).

II. Systems with higher initial void ratios e_0 will have higher bulk stiffness parameters and vice versa. Systems with greater void ratios and looser packing arrangements will be more susceptible to incurring larger system strains during compression than denser systems.

III. The bulk loading stiffness parameter λ for BKB is the highest amongst the five materials (i.e. softest system). This is in part due to the packing arrangement during filling. The BKB have the largest aspect ratio (a_r=2.20) of the five materials and naturally pack into a looser arrangement.

IV. The low COV for of the bulk stiffness parameters in all the tests (<5%), except for the loading of paired GB, highlights the repeatability of the experiment. The high COV seen in the paired GB can be explained by the rearrangement of the system during loading as a result of the significantly squatter experimental setup for the GB (see section 3.2.2.1) and the high a_r of the paired spheres (a_r=2.00), which lead to an unstable packing arrangement during filling.

V. The average initial void ratios e_0 for the single and paired GB systems was 30% higher than the average e_0 for other materials (0.74 and 0.56 respectively) and is a direct result of the greater boundary effects of the squatter experimental setup used for the GB.

VI. Although the rotating drum test did not produce significantly discriminating factors for the five different materials, it can be seen (Table 4.1) that the confined compression test produce a range bulk stiffness gradients (2E-2 to 4E-3). This highlights the importance of using several tests to calibrate the optimisation procedure. As described in Chapter 3, each experiment was chosen as the bulk response parameters were influence by

contrasting materials properties; the dynamic ϕ_r is primarily influenced by frictional forces, and the bulk stiffness parameters by the particles shear modulus.

VII. As described in Chapter 3, the bulk stiffnesses are influence by the stress level applied during confined compression. To preserve the integrity of the single and paired glass beads (GB) a maximum stress of 35 *kPa* was applied. This is reflected in the bulk stiffness parameters where κ for the GB (~3E-3) is relatively similar to the other materials, even though the particle shear modulus is much higher.

4.4 The influence of particle aspect ratio on the bulk response parameters

The various granular materials chosen for this study have contrasting material characteristics including the particle aspect ratio a_r, which is defined as the ratio of major to intermediate dimensions of the particle. An investigation into the effects of a_r on the dynamic ϕ_r and bulk loading λ and unloading κ parameters using the ascending cone (AC) and rainfall (RF) filling method was carried out. The results are plotted in Figure 4.3.

It should be noted that the magnitude of the single and paired GB results for the confined compression test should not be compared directly with the other materials as the experimental setup varied.

Excluding the single GB, it can be seen (Figure 4.3, a) that a_r has minimal influence on the dynamic ϕ_r. One would expect the dynamic ϕ_r to increase as a_r increases and the particle inter locking increases; however, the range tested in this thesis is relatively small (1.00-2.25) and therefore an accurate trend cannot be determined. The single GB have a dynamic ϕ_r 30% lower than the other materials. As mentioned previously, this is mainly due to the particles ability to roll and lack on inter-particle locking.

It can be seen from Figure 4.3 (b) and (c) that the bulk stiffness parameters λ and κ are significantly influenced the filling method as well as the a_r. The BKB have the largest a_r and the largest values of λ and κ which translates to a softer system. The greatest discrepancy between filling methods comes from loading the BKB, mainly due to the large a_r during loose filling (ascending cone) which will naturally inhibit denser formations.

The single and paired GB show negligible discrepancies between filling methods and minimal effects of a_r on the bulk stiffness parameters.

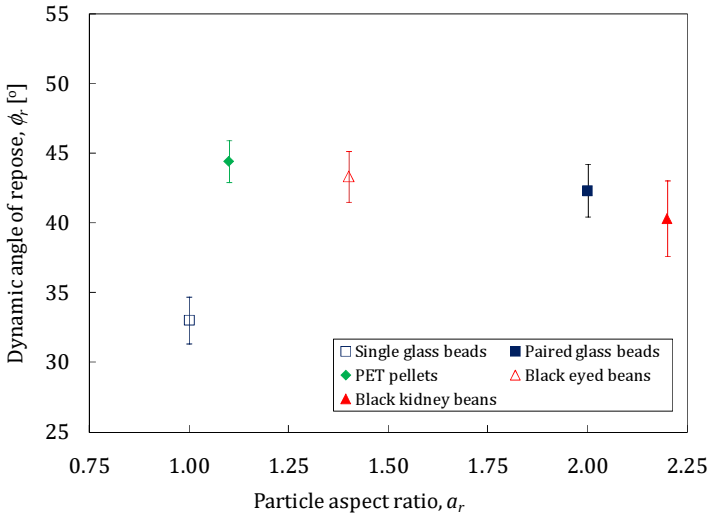

(a) Dynamic angle of repose at 7 *rpm*

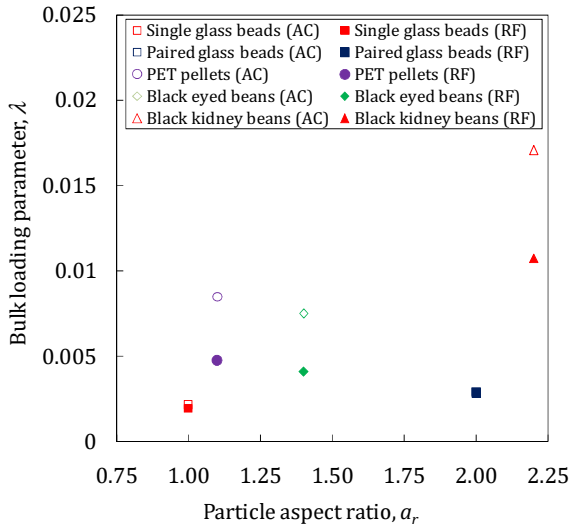

(b) Loading stiffness, λ

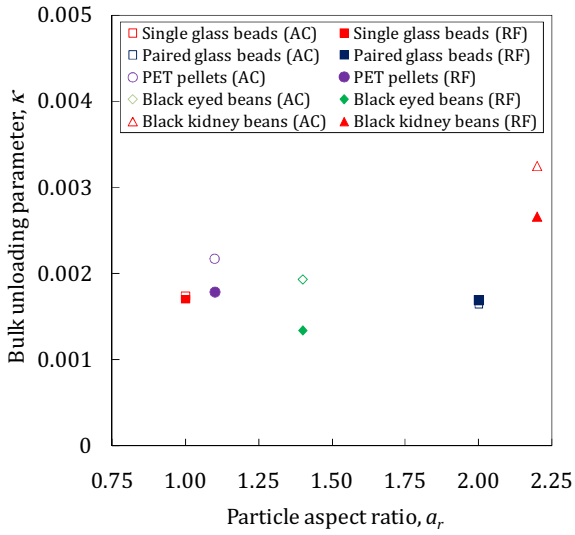

(c) Unloading stiffness, κ

Figure 4.3 The effect of particle aspect ratio on the dynamic angle of repose and bulk stiffness parameters using the ascending cone (AC) and rainfall (RF) filling method

4.5 Alternative device for calibrating DEM models

The particle packing structure in a bulk solid is generally understood to significantly influence its bulk behaviour (Chung 2006; Härtl 2008) and understanding the parameters that affects the system's packing arrangement and ultimately bulk properties is therefore essential. Chung (2006) investigated a dense filling method which involved rainfalling particle deposition through a sieve and Härtl (2008) investigated a loose filling method using an ascending cone filled with particles. An alternative device for calibrating DEM models was investigated by studying the effects of these two filling methods on the bulk properties of the various granular materials. Each filling method was carried out in two different containers; a control test using a 1 litre mould (BS 1377-4 1990) and a larger acrylic model silo with an internal diameter of 145 *mm* and the sample which had an average height of 340 *mm*. Silo filling bulk densities and initial void ratios of various materials using the two filling methods are shown in Table 4.5. The results for the control test produced similar results and can be found in Appendix A.

Table 4.5 Silo filling bulk densities and initial void ratios of various materials using two different filling methods

Material	Filling method	e_0	AVG ρ	COV
Single glass beads	Ascending cone	0.73	1475	1.0%
	Rainfall	0.66	1554	2.0%
Paired glass beads	Ascending cone	0.85	1375	0.2%
	Rainfall	0.71	1492	0.2%
PET pellets	Ascending cone	0.65	756	0.6%
	Rainfall	0.49	837	1.1%
Black eyed beans	Ascending cone	0.59	747	0.1%
	Rainfall	0.46	815	2.0%
Black kidney beans	Ascending cone	0.63	781	0.1%
	Rainfall	0.53	836	0.3%

AVG: Average, COV: coefficient of variance, e_o: initial void ratio, ρ: bulk density, Sample size=3

The very low coefficient of variance (<2%) highlights the tests' repeatability. As expected, for each granular material, e_0 is higher when filled with the ascending cone (loose method) than the rainfall (dense) method. As the solid density is consistent for each material,

denser filling methods will lead to a higher bulk density ρ. As mentioned previously, e_0 of the glass beads are higher due to the squatter experimental setup and greater boundary influence.

The difference in ρ between the two filling methods for each of the materials is less than 10%. As the difference is not significant, this suggests that the filling method is not a discriminating bulk response and it is therefore not suitable for calibrating the DEM models in the parametric optimisation and was therefore not used.

4.6 Summary

This chapter described and analysed the bulk experimental results obtained from two main devices using the five contrasting granular materials. The bulk responses that were measured to calibrate the DEM models were the dynamic angle of repose ϕ_r of granular materials in a drum rotating at 7 *rpm* and the bulk loading λ and unloading κ stiffness parameters determined using the confined compression test under a constant compression rate of 1 *mm*/*min*. Compression tests were carried out on systems filled using the ascending cone (looser) and rainfall (denser) filling method. The results for an alternative device for calibrating DEM models using silo filling were also included.

The general trend for all of the granular materials in the rotating drum device (less visible with paired GB) is an increase in dynamic ϕ_r as the drum rotational speed increases (Figure 4.1). The five different granular materials showed contrasting bulk responses including varying dynamic ϕ_r ranges and flow regime transitions speeds. The flow regime transition from slumping to avalanching occurred at a range of rotational speeds for various granular materials (2.5 to 11.5 *rpm*). The change in flow regime appeared to be influenced primarily by the particle aspect ratio a_r.

At lower rotational speeds, the paired GB displayed a significantly larger dynamic ϕ_r than the single GB (53% difference at 1 *rpm*). As angular velocities increase, the discrepancy reduces, demonstrating that individual particle properties may not have much influence at greater *rpm* and the flow regime is influenced primarily by the centrifugal forces and boundary conditions.

The two filling methods in the confined compression test produced significant differences in virgin loading gradient of the stress strain vs. curve. As expected, the denser filling method

had a higher gradient (stiffer system) than the looser filling method. The smallest gradient was seen in the ascending cone (loose) filling method of BKB. This statement is also true with regards to the bulk stiffness parameters, where the general trend for the five different granular materials is a lower bulk stiffness gradient for a denser filling method (rainfall filling) than the respective looser filling method (ascending cone). As expected, in all cases e_0 is higher when filled with the ascending cone (loose method) and as a consequence, the bulk density ρ is lower.

Silo filling with the ascending cone and rainfall filling methods did not produce a significant difference in ρ for the various granular materials and was therefore deemed unsuitable as a bulk response parameter to calibrate the DEM models in the parametric optimisation.

It can be seen from the results that the bulk behaviour of granular materials are complex and diverse in nature and predicting bulk responses numerically requires a deep understanding of the experimental devices and materials' properties.

Chapter 5

DEM parametric investigation on granular bulk behaviour

5.1 Introduction

The previous chapters have discussed the selection of the experimental devices, granular materials and bulk response parameters measurements used to calibrate the DEM models. This chapter will focus on the numerical DEM implementation used to simulate the bulk experiments as well as a parametric investigation of the DEM input parameters.

The DEM implementation will cover the rotating drum apparatus and the confined compression test and highlight any assumptions or simplifications that were made.

The optimisation procedure will use a matrix of simulations to optimise the DEM parameters. This matrix of simulations will provide the dataset necessary to establish optimised parameters using the calibration measurements acquired from the physical tests. The parametric investigation will focus on the other model parameters that are not optimised and are determined separately. Their influence on the dynamic angle of repose ϕ_r the bulk loading λ and unloading κ stiffnesses are analysed and discussed in the following chapter.

5.2 DEM Implementation

5.2.1 General

DEM is based on the use of an explicit numerical scheme in which the interactions between a finite number of particles are monitored contact by contact and the motion of the particles is modelled particle by particle. The widely used DEM with soft contact approach was used in this study. Specifically, the DEM code EDEM (DEM Solutions Ltd 2009) was used exclusively for the simulations mentioned in this thesis. The Hertz-Mindlin no-slip contact model with damping and a frictional slider in the tangential direction was adopted. Except where explicitly stated, a multiplier of 20% was applied to the computed critical time step for the simulations carried out. This value was chosen to achieve numerical stability without increasing the computational cost. It should be noted that the chosen critical time step varied with the optimisation procedure.

Besides the particle density, the particle shear modulus G and the Poisson's ratio υ have to be specified as well as interactions such as damping, rolling friction and sliding friction. The walls are treated as entirely rigid and cannot deform under an applied force.

Establishing an accurate particle shape representation was not a priority for the optimisation procedure and a generic particle consisting of two spheres with equal radii were used, except where explicitly stated. The aspect ratio, a_r (major/intermediate dimensions) varied according to the requirements in each simulation.

After setting the DEM input parameters, a method for generating the particles to replicate the physical packing arrangement as accurately as possible whilst not increasing the computational cost was required. There are two types of particle generation methods available in EDEM; static and dynamic. Static generation produces particles at a specified time and the simulation is paused during particle generation, whereas the dynamic generation produces particles over the duration of a simulation and the simulation continues as the particles are created. For the present study, the particles were generated in a dynamic factory. It is clear that neither the particle or boundary shape nor the exact particle deposition method can be modelled exactly and therefore justifiable assumptions need to be made.

This section will describe the DEM implementation of the two laboratory devices used for the optimisation procedure. The DEM parameters adopted for the various simulations may be found in Appendix B.

5.2.2 Rotating drum experiment

The rotating drum was modelled at full scale using a similar number of particles (as the experiment) to fill the drum. All of the simulations consisted of three stages;

1. Random particle generation stage within the stationary drum (t_{sim}:0 - 4s),
2. Drum acceleration stage (t_{sim}:4 - 5s), and
3. Constant drum speed stage (t_{sim}:5 -20s).

The dynamic angle of repose ϕ_r is determined using images taken from t_{sim}:10 - 20s, where the drum acceleration effects on the particles are assumed to be dissipated, and the rotating drum flow regime has stabilised.

5.2.3 Confined compression test

Initial confined compression simulations were modelled at full scale, using the experimental dimensions and number of particles. However following a parametric investigation on the dimensional scaling (section 5.4.1), the confined compression cylinder was scaled down to 60% of its original size for computational efficiency.

Two methods of filling were used for the confined compression experiments; a dense method (particles rainfalling through a sieve) and a loose method (using an ascending cone). In an effort to reproduce accurate experimental packing densities, several numerical methods were explored. Preliminary studies simulated the experimental filling methods accurately using a scale sieve (14 *mm* aperture) as shown in Figure 5.1. Simulating filling methods in this manner was computationally expensive and not essential to produce experimental packing arrangement.

(a) Side view

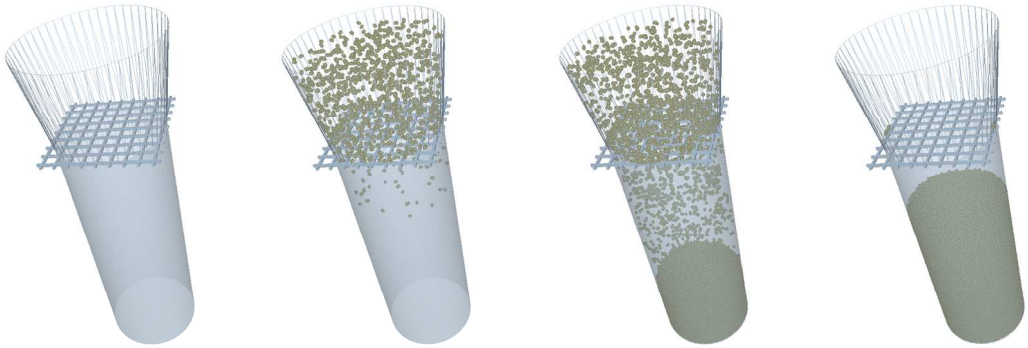

(b) Alternative angle

Figure 5.1 A sequence of images illustrating a preliminary study investigating the numerical rainfall filling of particles through a 14x14 *mm* sieve

Further investigations to produce packing densities similar to the physical test led to a method involving a parametric alteration. This method consisted of three stages;

1. Alter the particle-particle and particle-wall frictional parameters as well as the particle generation rate to achieve a target packing density.
2. Randomly generate the particles within the cylinder, which reduces the time they take to settle.
3. Restore the parameters to their original values and leave to settle

To produce a denser packing arrangement, a lower value of friction and a lower particle generation rate are needed and vice versa for a looser packing arrangement. The parameters to achieve a loose and dense packing arrangement can be found in Appendix B.

Unlike Chung's (2006) experimental setup of the confined compression test, the acrylic cylinder in this thesis was not supported at the base. Therefore, by applying a load from the top, the sample is in fact experiencing a two way compression from the top and bottom platens.

The boundaries and geometries in EDEM are rigid and do not allow for movement as a result of forces from particles. It was chosen to perform a two way compression on the sample by loading from the top and bottom at as shown in Figure 5.2.

(a) Unrestraint geometries (Experimental) (b) Restraint geometries (Numerical)

Figure 5.2 Simulating unrestraint geometries in DEM simulations

After the randomly generated particles have settled, the top layer of particles may be uneven. To flatten the surface, an initial pre-stressing load of 3.5 *kPa* was applied by lowering the top platen until the desired stress was achieved. This load corresponded to the experimental stress applied by the acrylic platen used to flatten the top surface in the physical test.

It is generally understood that the behaviour of granular solids at very low stresses can be highly variable and sensitive to the local particle packing structure (Härtl 2008; Chung 2006). For this reason, this study focuses on the behaviour at stresses greater than 5 *kPa* in the experiments as well as the numerical simulations.

All the confined compression simulations were conducted in a systematic manner and consisted of four stages;

1. Random particle generation within the cylinder (t_{sim}:0 - 4s),
2. Application of 3.5 *kPa* pre-stressing to level the top surface by lowering a top platen

3. Two way loading to the desired stress level
4. Two way unloading to 5 *kPa*

The starting condition of the confined compression test is the state after the pre-stressing has been applied and the analysis on the bulk stiffness is adjusted accordingly. In other words, the strain of the sample at this point is taken as 0%; however the vertical stress in the sample is still 3.5 *kPa*.

5.3 Investigation of non-optimised parameters

The optimisation in this thesis will focus on optimising three inter-particle parameters (coefficient of sliding friction, rolling friction and restitution) and the particle stiffness. The main reason for choosing inter-particle parameters was the scenario specific nature of the particle to wall interactions.

These four inter-particle parameters will be varied whilst the other parameters are each fixed at a constant value. A parametric investigation for each of the non-optimised parameters was carried out to determine the most suitable value to adopt. Their influence on the dynamic angle of repose ϕ_r and the bulk loading λ and unloading κ stiffnesses parameters were analysed and are discussed herein.

5.3.1 Reference simulation

To carry out a robust parametric study, a reference simulation was needed. The DEM implementation for the reference simulation was chosen as typical mid values, based on literature (Chung 2006; Härtl 2008; Dury et al. 1998) and lab experiments (see Chapter 3). The DEM implementation used for the reference simulation is presented in Table 5.1. Unless explicitly stated otherwise, these were the DEM parameters adopted in the parametric study simulations. In addition, the y-axis scale for each bulk response plot is consistent throughout the parametric study to aid visual comparison (e.g. 30° to 60° for the dynamic angle of repose).

Table 5.1 Reference simulation case for the parametric study

DEM Implementation	Value
PP, PW coefficient of sliding friction ($\mu_{pp},\ \mu_{pw}$)	0.30
PP, PW coefficient of restitution ($e_r,\ e_{r,pw}$)	0.50
PP, PW coefficient of rolling friction ($\mu_{r,pp},\ \mu_{r,pw}$)	0.04,0.00
Poisson's ratio, υ	0.30
Particle density, ρ_s [kg/m^3]	1200
Particle shear modulus, G [Pa]	1E7
Number of spheres in a particle	2
Aspect ratio, a_r	1.50
Sphere radius [mm]	3.3
Number of particles in drum	600
Scale of experimental drum	100%
Number of particles in confined compression cylinder	3100
Initial void ratio in confined compression cylinder	0.54
Scale of experimental confined compression test	60%
Compression speed of each plate [*mm/sec*]	1
Fixed % of Rayleigh time step	20%

PP: particle to particle, PW: particle to wall

5.3.2 Shape representation

Particle shape representation is an important aspect in DEM simulations. Creating a more accurate representation of the grain shapes such as agricultural grains requires many spheres per particle. It has been suggested (Chung 2006; Härtl 2008) that an accurate geometrical representation of a granular material does not necessarily lead to a more accurate prediction of the bulk behaviour and often a quite crude representation with a few spheres can produce satisfactory results, thereby reducing the computational time. Increasing the number of spheres per particle will drastically increase the computational effort which may not be essential. An example of increasing the accuracy in shape representation and resolution using an increasing number of spheres can be seen in Figure 5.3. However as the optimisation procedure was designed to be applicable to a wide range of granular material, increasing the shape

representation accuracy for a specific material does not make sense. Instead a generic shape was used to model the various granular materials in this thesis: two spheres with equal radii.

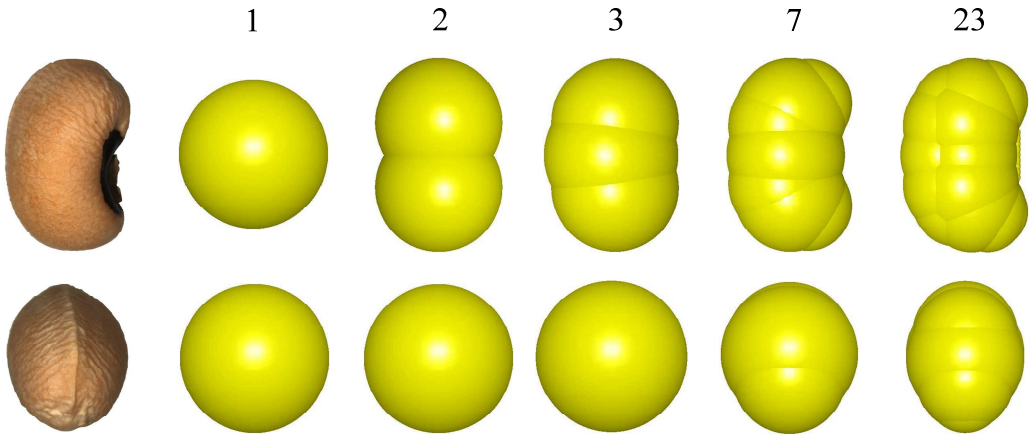

Figure 5.3 Shape representation of a black eyed bean using increasing number of spheres

5.3.3 Particle density

Altering the particle density ρ_s has two main effects in DEM simulations; first of all, if the volume of the particle remains constant, the mass of the particles will change and secondly the computational time will be affected. Changing the mass may affect systems where force calculations have a dominant influence and computational times are important when conducting numerous or large scale simulations.

What is important for this thesis is the effect ρ_s has on the bulk behaviour. Figure 5.4 illustrates the effect of changing ρ_s on the dynamic angle of repose ϕ_r. It can be seen that increasing the particle density from 120 to 12,000 kg/m^3 does not have a significant effect on the dynamic ϕ_r. At very high ρ_s, the dynamic ϕ_r decreases slightly (4%), possibly due to the increase in bulk weight affecting the rotational Froude number, *Fr*.

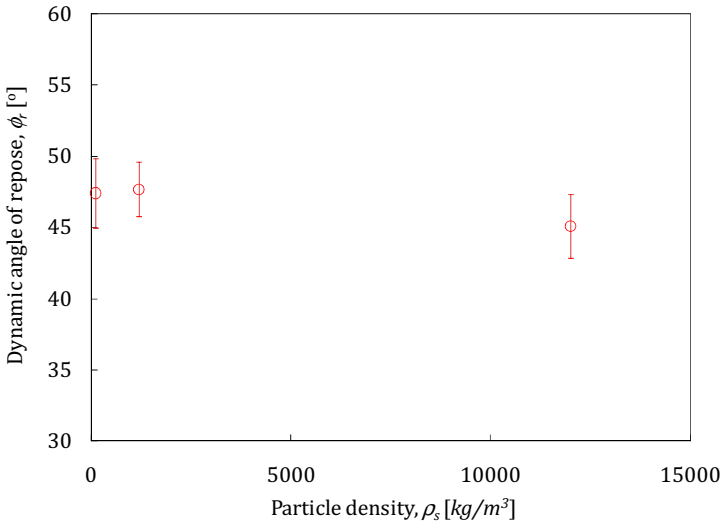

Figure 5.4 Effect of particle density on the dynamic angle of repose

Error bars represent ±1 standard deviation, sample size=10

Decreasing ρ_s will increase the computational time (see section 2.2.6). The change in computational time can be estimated using the Rayleigh time step R_T. Decreasing ρ_s by 100 will increase the computational time by 10.

As far as the confined compression simulations are concerned, changing the particle density will change the bulk weight of the particles and the initial pressure on the bottom platen. In other word, increasing ρ_s in the confined compression simulations will lead to a minor increase of the initial vertical stresses (the void ratio vs. log-stress plots will shift accordingly); however, as the bulk loading stiffnesses λ and κ are gradients, they are not expected to be influenced.

From a scientific standpoint and for analytic simplicity, a round value of 1000 kg/m^3 for the particle density was chosen for the numerical dataset.

5.3.4 Particle Poisson's ratio

The particle Poisson's ratio v is the ratio of transverse contraction strain to longitudinal extension strain in the direction of the stretching force. Figure 5.5 demonstrates the influence of v on the bulk stiffness parameters. It can be seen that as v increases, the loading and unloading

stiffness parameters decrease, which translates to a stiffening of the system. Increasing the Poisson's ratio from 0.1 to 0.45 will decrease λ and κ by 24% and 23% respectively.

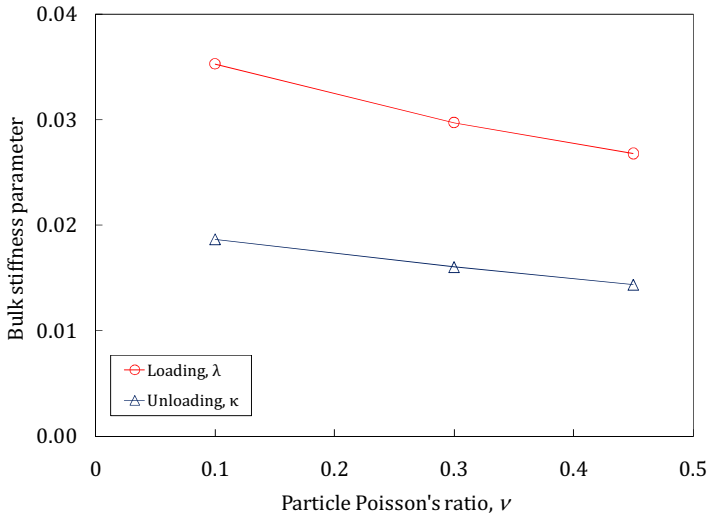

Figure 5.5 Influence of Poisson's ratio on bulk stiffness

Albeit a discriminating factor, ν is not a focus for this study and will not be optimised. A mid value between typical organic and inorganic solids was chosen for the fixed value. Agricultural materials have a Poisson's ratio around ν = 0.4 (Chung 2006) and glass beads have a Poisson's ratio of ν = 0.22 (Härtl 2008). Therefore, a Poisson's ratio of ν = 0.3 was chosen to be used in the numerical dataset simulations.

5.3.5 Particle to wall coefficient of sliding friction

The particle to wall coefficient of sliding friction μ_{pw} is very scenario specific and will vary depending on the properties of the contact surfaces and the particles involved. This parametric study investigated the effect of μ_{pw} on the bulk stiffness parameters and the dynamic angle of repose ϕ_r. In the confined compression test, the shear forces and mobilised friction along the wall were examined, and in the rotating drum the effect of varying the inner drum wall μ_{pw} versus the end plate μ_{pw} were investigated.

Typical values of μ_{pw} for the material used in this study against an acrylic surface range from 0.2 to 0.4 (Chung 2006; Härtl 2008), however a wider range was used in the parametric study.

Confined compression test

The effect of μ_{pw} on the numerical bulk stiffness parameters were investigated and produced the results shown in Figure 5.6. The general trend for λ and κ is a decrease in bulk stiffness gradient as μ_{pw} increases. This translates to a stiffening of the system. The frictional forces along the wall act to restrain the compression during loading and restrict rebounding during unloading. Therefore, increasing μ_{pw} contributes to a stiffening of the system.

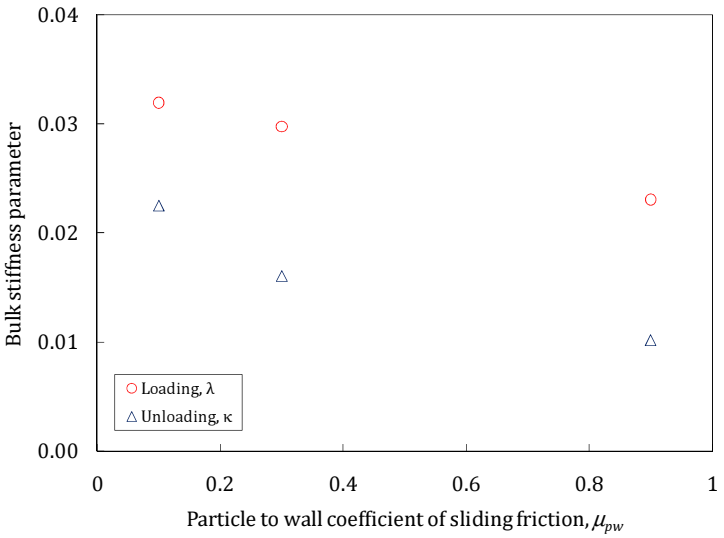

Figure 5.6 The effect of particle to wall coefficient of sliding friction μ_{pw} on the numerical bulk loading and unloading stiffness parameters

Frictional forces along the boundary wall

To better understand the influence of μ_{pw} on bulk behaviour, the frictional forces along the cylinder wall were examined in detail. The mobilised friction coefficient μ_{mob} is the ratio of shear force F_s to normal F_n force at each contact and is an indicator of proportion of frictional forces that exists at that contact. When $\mu_{pw} = \mu_{mob}$ the frictional forces is said to be fully

mobilised. The wall friction can be analysed using μ_{mob} of the particles against the cylinder wall at each contact point. The particle to wall shear forces acts in the opposite direction to the movement of the particles and theoretically, in a two way compression the intensity will decrease as it approaches the plane of equilibrium where the shear force is zero (Figure 5.7).

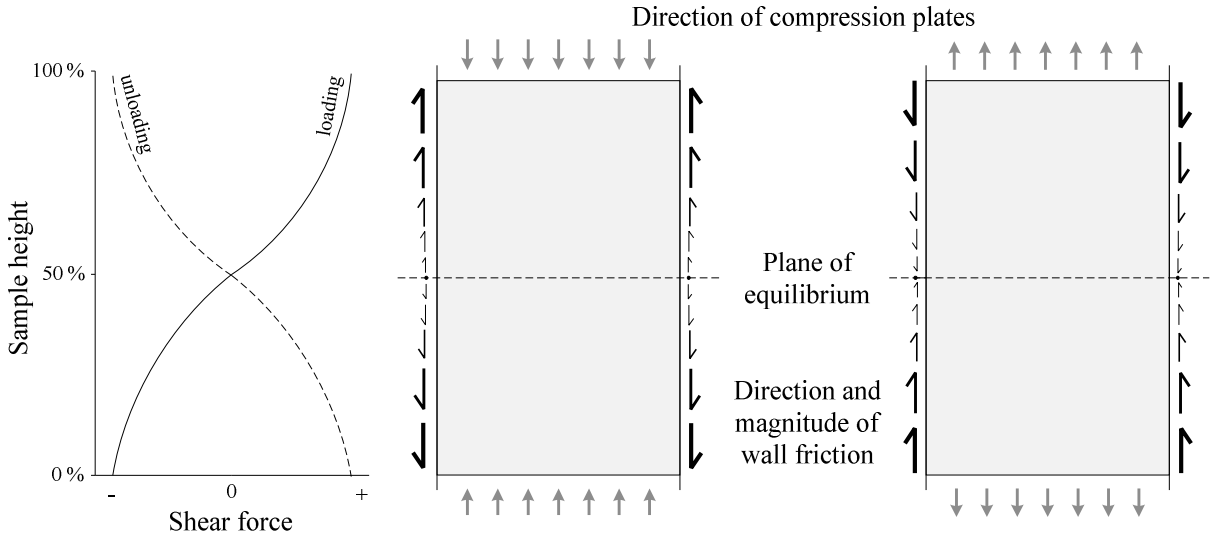

(a) Particle to wall shear forces (b) Loading (c) Unloading

Figure 5.7 Theoretical prediction for the direction and magnitude of particle to wall tangential forces during loading and unloading in confined compression

The total frictional force on the wall F_w can be written as

$$F_w = \int 2\pi R \,.\, \tau_w \, dh \qquad \text{Equation 5.1}$$

Where R is the radius of the cylinder, dh is the changed in height and τ_w is the wall shear stress. The mobilised frictional forces along the wall were examined for the two simulations referred to in Figure 5.6 where μ_{pw}= 0.1 and μ_{pw}= 0.9. The forces were examined at two specific time steps when the average platen vertical stress was at 30 *kPa* during loading and at 30 *kPa* during unloading. Assuming circumferential symmetry, μ_{mob} can be plotted against the contact height (as a percentage of total height) as shown in Figure 5.8 (a, b). Although the

mobilised friction is a coefficient, for illustrative purposes a negative value of μ_{mob} indicates upward shear forces in the z- direction.

From Figure 5.8, it can be seen that the magnitude of mobilised friction is greater when μ_{pw}= 0.9 than when μ_{pw}= 0.1. The plane of equilibrium where the shear forces are zero should theoretically be located around the mid-height of the sample if the sample is compressed at the same rate from both ends. However, it can be seen that this plane is found slightly above the mid-height of the sample (55-70% of sample height), with μ_{pw}= 0.1 showing a plane higher than μ_{pw}= 0.9. This is possibly due to the numerical setup used to simulate experiment. Experimentally, the compression stress is applied from a top platen (Instron machine) and as a result of the unrestrained cylinder, two-way compression of the sample occurs. Numerically this is replicated by moving the top and bottom platen together (for loading) and in opposite directions (for unloading). As a result of gravitational forces, the initial conditions before confined compression occurs are different near the top and bottom platens. The bottom platen experiences the additional stress due to the self weight of the sample, whereas the top platen only experiences the 3.5 *kPa* from the pre-stressing. The packing arrangement is also denser in the bottom half of the sample and the particles are less inclined to move during compression and vice versa for the top half.

Preliminary analyses of the scatter plots in Figure 5.8 (a, b) would suggest that many contacts have been fully mobilised. To reveal a potential trend in the numerical confined compression, averaging methods (moving averages) were used as shown in Figure 5.8 (c, d). In addition, a histogram of the mobilised friction was produced (Figure 5.9) to determine the frequency of the contacts that have been mobilised.

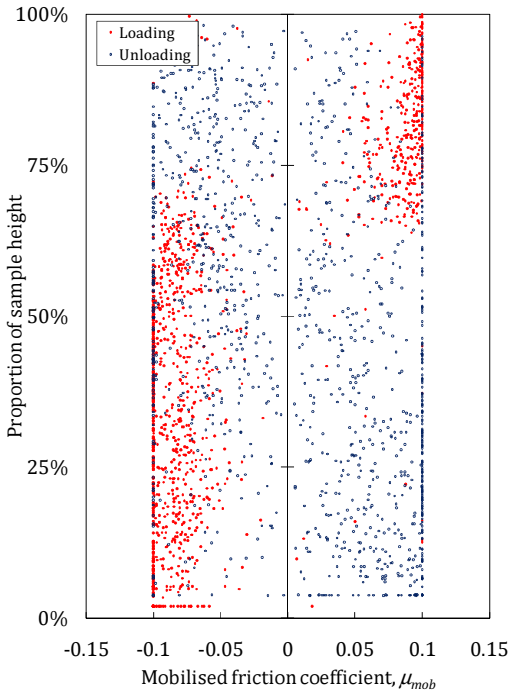

(a) Scatter plot, μ_{pw}= 0.1

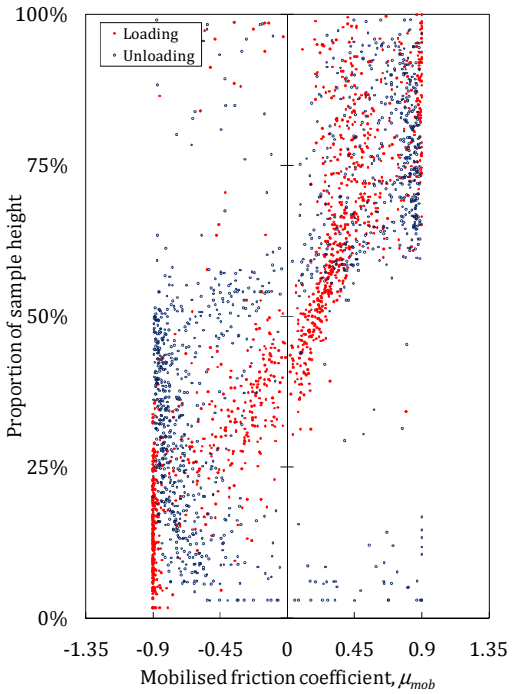

(b) Scatter plot, μ_{pw}= 0.9

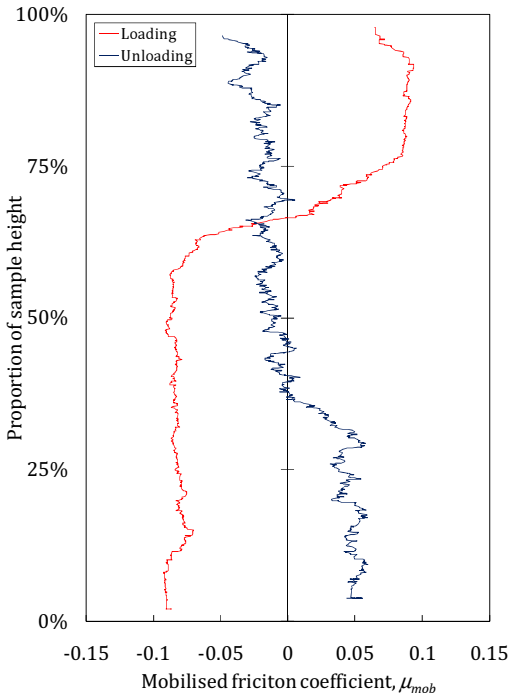

(c) Moving average, μ_{pw}= 0.1 (50 data points)

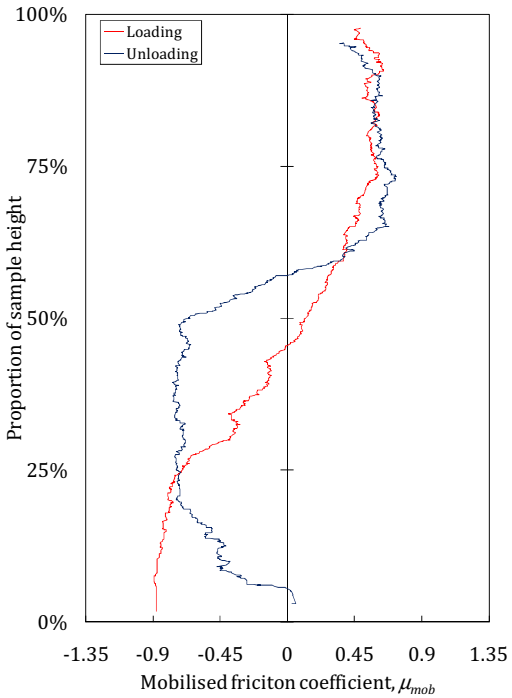

(d) Moving average, μ_{pw}= 0.9 (50 data points)

Figure 5.8 The particle to wall tangential forces along the cylinder wall during confined compression

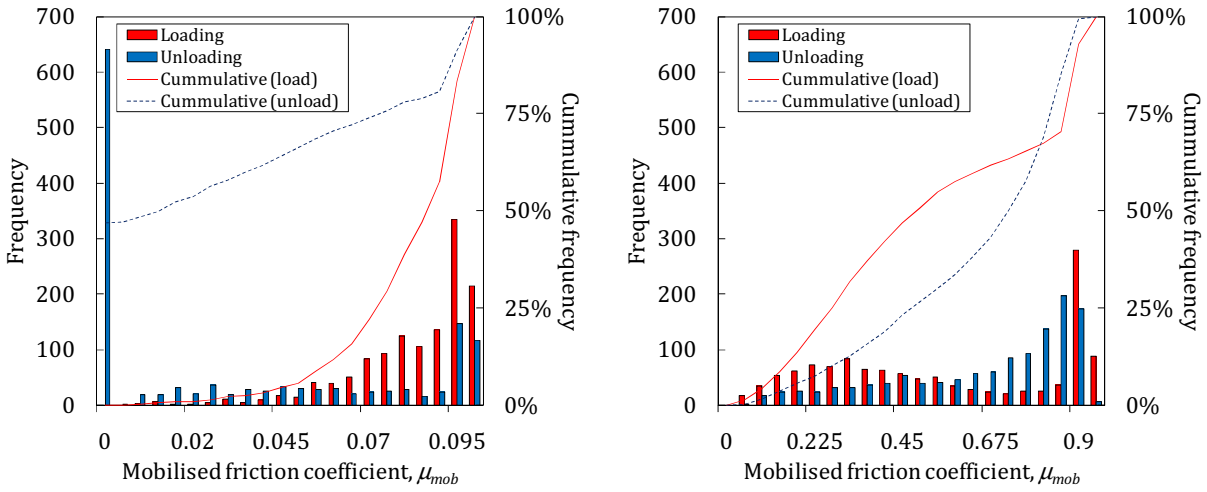

(a) μ_{pw}= 0.1 (b) μ_{pw}= 0.9

Figure 5.9 Frequency and cumulative frequency for the mobilised friction along the cylinder boundary

From Figure 5.9 we can see that when $\mu_{pw} = 0.1$, a majority of the shear force contacts during loading are either fully mobilised or close to full mobilisation. However, during unloading 50% of the contacts have little to no shear mobilisation. When $\mu_{pw} = 0.9$, the mobilised friction is more evenly distributed during loading and unloading.

The mobilised friction along the boundary wall when μ_{pw}= 0.1 (Figure 5.8, c) follows the theoretical trend as shown in Figure 5.7 (c) where shear forces are positive in the top half and negative in the bottom half for loading, and vice versa for unloading. Analysis conducted on the stiffness parameters showed that μ_{pw} had a greater influence on the bulk unloading stiffness κ than the bulk unloading stiffness λ and increasing μ_{pw} from 0.1 to 0.9 resulted in a 30% and 55% decrease in λ and κ respectively.

The loading trend when μ_{pw}= 0.9 (Figure 5.8, d) appear to follow theoretical predictions. In this case, μ_{mob} is greatest at the extremities which would suggest more movement near the compression plates. However the unloading trend displays irregular results, the reasons for which are not fully understood.

5.3.5.1 The effect of inner drum wall and end plate friction in the rotating drum

Dury et al. (1983) suggested that the dynamic ϕ_r near the end plates would be heavily influenced by the particle to wall coefficient of friction μ_{pw}. This forms the basis for this section of the parametric study.

With respect to the rotating drum device, the inner drum wall is the section lining the inside of the drum and the end plates are the circular plates on either side of the drum confining the granular materials (Figure 2.5). A parametric study was carried out to find the effect of altering the inner drum wall and the end plate friction μ_{pw} independently. Figure 5.10 illustrates the influence of the inner drum wall friction and the end plate friction on the dynamic ϕ_r. It can be seen that the dynamic ϕ_r is not significantly influenced by the inner drum wall μ_{pw}. This is because, as long as the rotational Froude number Fr is great enough and the $\mu_{pw} > \mu_{pw,c}$ (where $\mu_{pw,c}$ is defined by Mellmann (2001) as the critical particle to wall friction where slippage no longer occurs) so that the particles do not slip along the inner wall in a sliding, surging or slumping regime, the particles will be carried to the top of the granular material surface profile height. At this point, the particle's weight will cause it to roll down the surface profile regardless of the inner wall μ_{pw}. Therefore as long as the inner drum μ_{pw} is large enough to prevent particles slippage, μ_{pw} should have a minimal effect on the dynamic ϕ_r.

Figure 5.10 concurs with Dury et al.'s (1998) observation on the significant influence of μ_{pw} on the dynamic ϕ_r. Increasing the end plate μ_{pw} from 0.1 to 0.9 will increase the angle of repose by 40%.

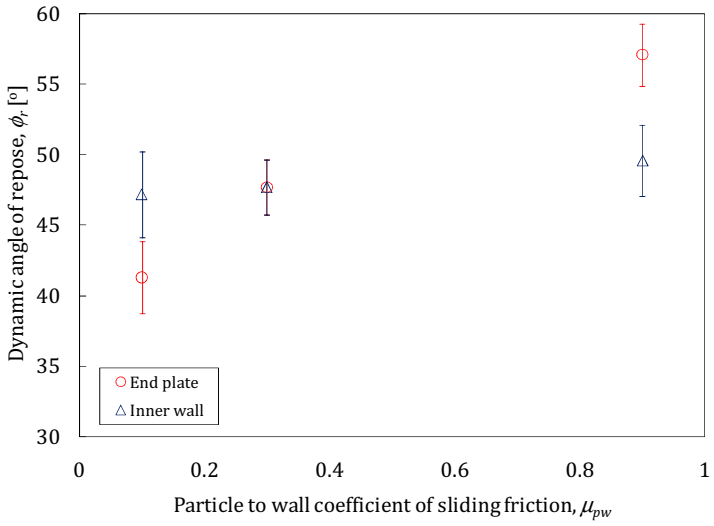

Figure 5.10 The influence of inner drum wall friction and end plate friction on the dynamic angle of repose at 7 *rpm*

Error bars represent ±1 standard deviation, sample size=10

The particle to wall coefficient of friction is relative to the material of the particle and the wall. Therefore, μ_{pw} is very problem specific and will depend on the system that is being simulated. In an effort to establish a systematic approach to this problem, it is proposed to perform a pre-optimisation to determine an appropriate value to fix μ_{pw} at. The proposed method is as follows:

1. Determine the experimental bulk particle to wall coefficient of friction $\mu_{pw,bulk}$ for the particle and wall materials of interest (Generally determined using the Jenike shear tester). There are various granular materials used in this thesis with varying $\mu_{pw,bulk}$, however, for the purposes of this study a value of $\mu_{pw,bulk}$=0.29 will be used. This represents an average value of the organic material ($\mu_{pw,bulk}$=0.34, Chong 2006) and glass beads ($\mu_{pw,bulk}$= 0.24, Härtl 2008) against an acrylic surface.

2. Following the determination of $\mu_{pw,bulk}$, infer the correct particle input parameter μ_{pw} that will produce the correct bulk behaviour. Härtl (2006) ran a series of numerical simulations to simulate the effects of increasing the μ_{pw} on $\mu_{pw,bulk}$ (using particles with an a_r = 1.50) to produce the graph shown in Figure 5.11.

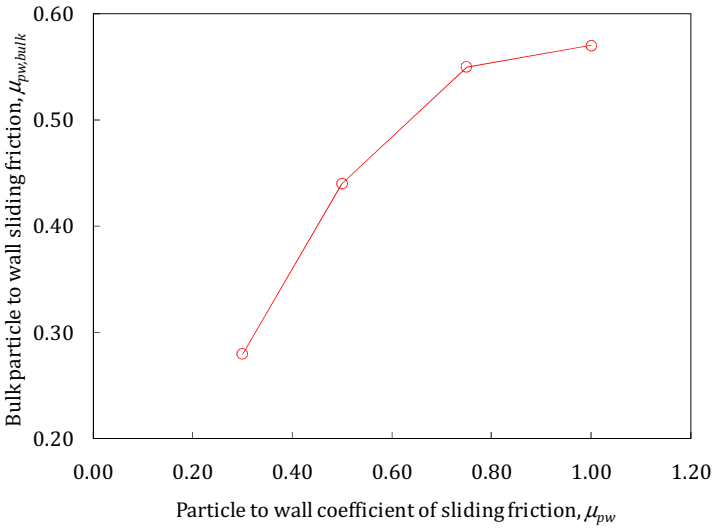

Figure 5.11 Effect of particle to wall sliding friction on the bulk particle to wall sliding friction using particle with 2 equal spheres with aspect ratio 1.50 as demonstrated by Härtl (2008)

3. To obtain a $\mu_{pw,bulk}$= 0.29, a μ_{pw}= 0.30 should be used and was the value chosen for this study.

For the purposes of this study, a particle to wall friction of μ_{pw}=0.3 will be used. Härtl (2008) has demonstrated DEM's ability to simulate bulk particle wall frictions at low values (i.e. a μ_{pw}= 0.3 will produce a $\mu_{pw,bulk}$=~0.3). However, for higher values of μ_{pw}, DEM will underestimate bulk behaviour of friction. A higher μ_{pw} may be needed to compensate because surfaces are not always perfectly flat as simulated in EDEM.

5.3.6 Coefficient of rolling friction

When a particle rolls along a surface, both the particle and the surface can deform to oppose this rolling motion. This is usually represented as a torque being applied to each of the bodies. The coefficient of rolling friction μ_r is a scalar value used to determine how much torque is required to be applied to an object of a given material at rest on a flat surface to put it into motion. Rolling friction in DEM simulations has been studied and reviewed in detail by Ai et al (2010) and summarised in 2.2.5.

The rolling friction model μ_r adopted in EDEM applies a torque to the contacting surfaces using Equation 5.2.

$$\tau_i = -\mu_r F_n R_i \omega_i \qquad \text{Equation 5.2}$$

where R_i the distance of the contact point from the center of mass and ω_i the unit angular velocity vector of the object at the contact point. The effect of the particle to wall coefficient of rolling friction $\mu_{r,pw}$ on the dynamic angle of repose ϕ_r was investigated and the results are shown in Figure 5.12. It can be seen that increasing $\mu_{r,pw}$ from 0 to 0.4 will increase the dynamic ϕ_r by 8%.

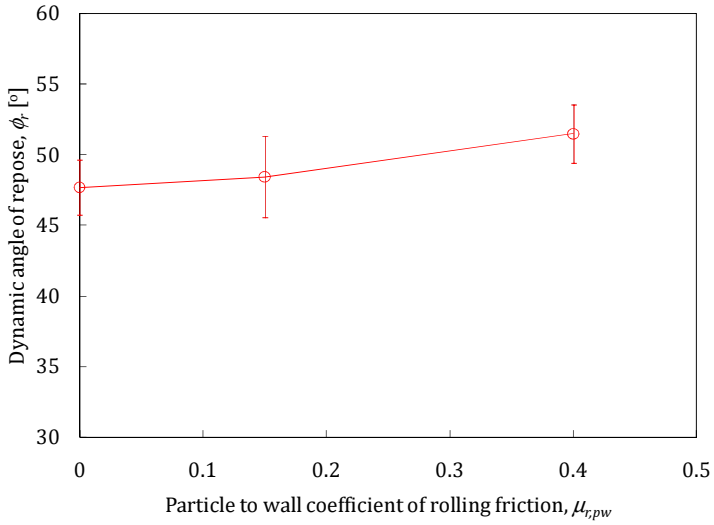

Figure 5.12 The influence of particle to wall coefficient of rolling friction on the dynamic angle of repose

Error bars represent ±1 standard deviation, sample size=10

The influence of $\mu_{r,pw}$ on the bulk stiffness parameters during confined compression is shown in Figure 5.13. The effect of increasing $\mu_{r,pw}$ from 0 to 0.4 will see a linear increase of λ and κ by 8% and 15% respectively. The increase in κ is almost double that of the λ increase. As with the particle to wall coefficient of sliding friction, the boundary effect plays a dominant role in the system's ability to rebound during unloading. Therefore, increasing the rolling friction will result in a stiffening of the system.

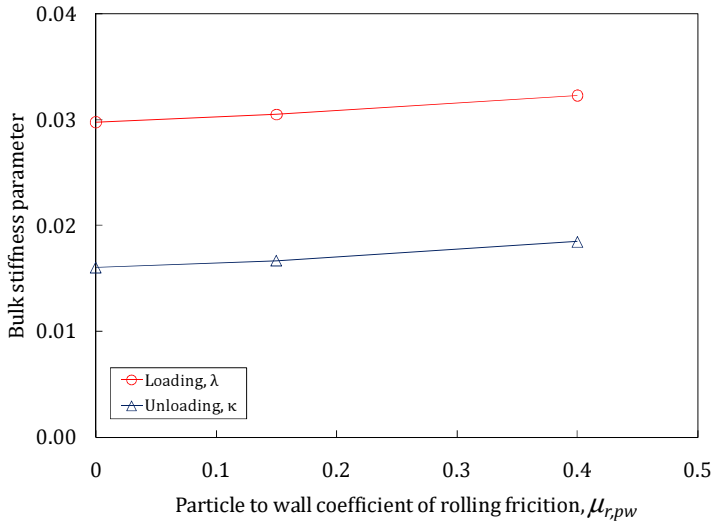

Figure 5.13 The influence of the particle to wall coefficient of rolling friction on the bulk loading and unloading stiffness during confined compression

The rolling friction model adopted in EDEM is a relatively simple one based on model A (Ai et al. 2010). For more information on the various models see section 2.2.5. It was chosen to exclude the particle to wall rolling friction $\mu_{r,pw}$ by setting the value to zero when conducting the numerical dataset simulations. However, the particle to particle rolling friction $\mu_{r,pp}$ will be optimised. Using this setup, the effect of including and excluding the rolling friction model from the simulation can be evaluated.

5.3.7 Vertical confined compression stress

The numerical effect of the average vertical compression stress σ_v on the bulk stiffness parameters was investigated. Three simulations were run using the reference simulation values (Table 5.1) with different maximum compression stress levels to produce the results shown in Figure 5.14.

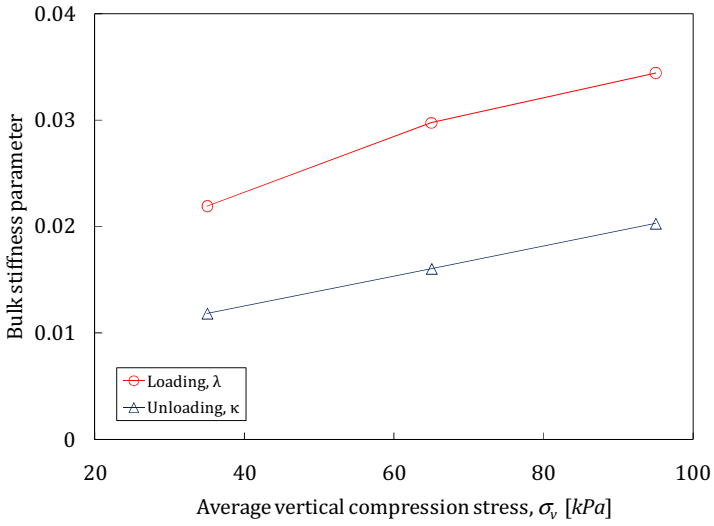

Figure 5.14 The influence of confined compression stress level on the bulk stiffness parameters

The bulk stiffness parameters are seen to increase with increasing maximum compression stress level. The numerical trend observed for κ conflict with the experiementally expected results. As κ is largely dependent on the systems elastic properties, the system's ability to rebound should not differ greatly with the unloading stress levels. This would manifest itself by parallel unloading lines for increasing vertical stress levels in the void ratio vs. log stress plots. However, plastic deformation at the points of contacts are ignored in the DEM program used in this study and is based on a Hertz-Mindlin non-linear elastic model (discusses further in section 5.5), which will result in a greater rebound during unloading.

5.3.8 Simulation time step

The Rayleigh time step, T_R is the time taken for a shear wave to propagate through a solid particle and may be described as

$$T_R = \pi r^2 \left(\frac{\rho}{G}\right)^{\frac{1}{2}} \Big/ (0.1631v + 0.8766) \qquad \text{Equation 5.3}$$

where r is the radius of the smallest particle in the system, ρ_s is the particle density, G the shear modulus and v the Poisson's ratio (see section 2.2.6 for more details). In the DEM

software EDEM, it is possible to fix the computational time step to remain constant throughout the simulation. This is often expressed a percentage of T_R. A lower percentage will produce more accurate results than an equivalent higher percentage, but will increase the computational time. Typically, 20% of T_R has been used (Chung 2006; Härtl 2008) as this was verified to be adequate for slow shearing densely packed systems.

The effect of the computational time step (as a percentage of T_R) on the dynamic ϕ_r (Figure 5.15, a) and the bulk stiffness parameters (Figure 5.15, b) was investigated. The plots reveal that increasing the fixed T_R from 5% to 50% produces a variance in results of 3%. The bulk stiffness parameters are also minimally influenced and produce a variance in results less than 2% for an increase in fixed T_R from 5% to 20%.

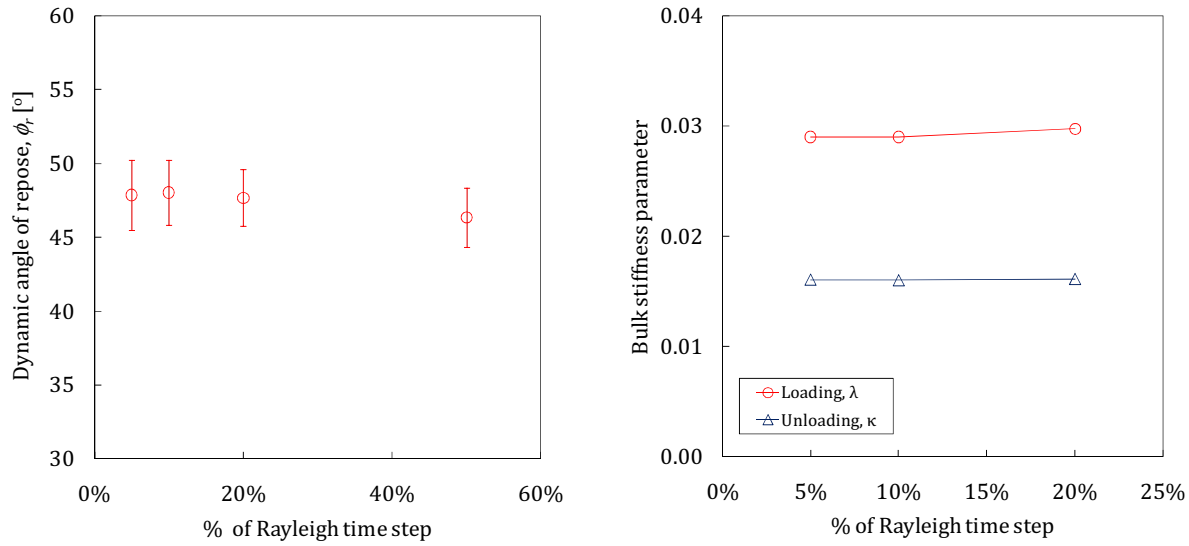

(a) Dynamic angle of repose

(b) Bulk stifness parameters

Figure 5.15 Influence of the percentage Rayleigh on the bulk response parameters

Error bars represent ±1 standard deviation, sample size=10

5.3.9 DEM sphere radius

Altering the particle sphere radius will invariably change the particle size and volume. The rotating drum setup uses a 40% fill volume to produce the optimum flow patterns to determine the dynamic ϕ_r. Increasing the particle radius will decrease the number of particles

needed to produce a 40% fill volume. This will in turn decrease the computational time. However, there are two main drawbacks to increasing the particle radius:

1. The number of particle along the surface profile decreases, which make the dynamic ϕ_r determination harder and more susceptible to fluctuations. This is illustrated in Figure 5.16.
2. The average number of particles between the end plates will decrease and the boundary effects will have a greater influence on the dynamic ϕ_r (Dury et al. 1998).

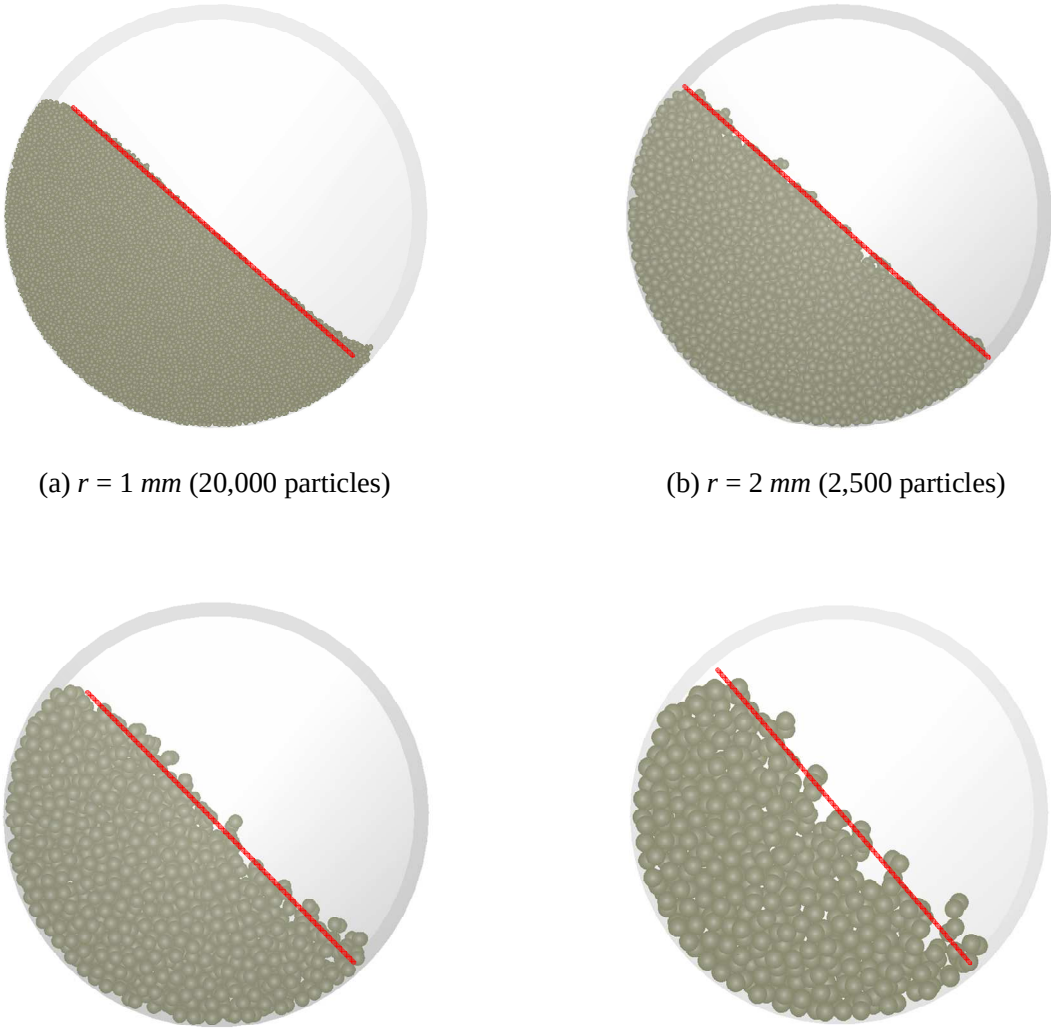

(a) r = 1 *mm* (20,000 particles)

(b) r = 2 *mm* (2,500 particles)

(c) r = 3 *mm* (750 particles)

(d) r = 4 *mm* (315 particles)

Figure 5.16 Dynamic angle of repose determination for increasing sphere radius

A parametric study was conducted to determine the effect of increasing the particle radius (decreasing the number of particles between end plates) on the dynamic ϕ_r. In addition, identical simulations were run replacing the drum end plates with periodic boundaries to simulate the mid section of a deep drum. The results are shown in Figure 5.17.

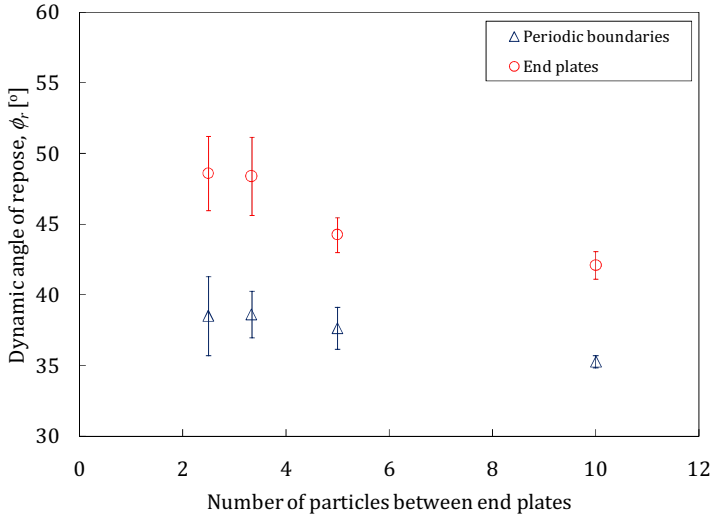

Figure 5.17 The effect of particle size on the angle of repose with and without periodic boundaries

Error bars represent ±1 standard deviation, sample size=10
length of particle based on the intermediate dimension

When end plates are present, the dynamic angle of repose, ϕ_r is significantly influenced by increasing the particle length/drum depth (reducing the particles radius), however when periodic boundaries are introduced the effect is much reduced. This highlights the influence of the end plate friction. When there are fewer particles between end plates (2 to 4), the difference in dynamic ϕ_r for simulation with end plates and with periodic boundaries is around 20%. This significant discrepancy highlights the need to fully understand the influence of the parameters on the simulation outcomes.

The standard deviation, represented by the error bar (based on 10 images) is larger when the number of particles between end plates is smaller. Again, this echoes the drawback of determining the dynamic ϕ_r using larger particles.

For the simulations with end plates, a tilting point may be observed between 3 and 5 particles between end plates. The optimisation procedure in this study focused on the inter-

particle parameters and to limit the boundary influence, four particles between the end plates should be a minimum. In light of this, a particle radius of 2.5 *mm* was eventually used in the numerical dataset simulations.

5.3.10 Particle aspect ratio

Granular materials are almost never perfectly spherical and shape representation using sphere based DEM code may be challenging. Using the multi-spherical method (Kremmer and Favier 2000; Favier et al. 2001; Matsushima 2004) it is possible to create a clump of spheres with varying sizes and positions which may be overlapped to create a desired shape. In this thesis, the particle aspect ratio a_r is defined as the ratio of major to intermediate dimensions. A parametric study was carried out to determine the effect of a_r using two equal spheres on the dynamic ϕ_r and the bulk stiffness parameters. To limit the number of variables, the particles consisted of 2 equal spheres with varying values of a_r between 1.00 and 2.00 as shown in Figure 5.18. Härtl (2008) highlighted the importance of a_r by comparing single (a_r= 1.00) and paired (a_r= 2.00) glass beads GB experimental and numerical results. He found that the inter-particle locking occurred considerably more in system with paired GB particle than in system with single GB.

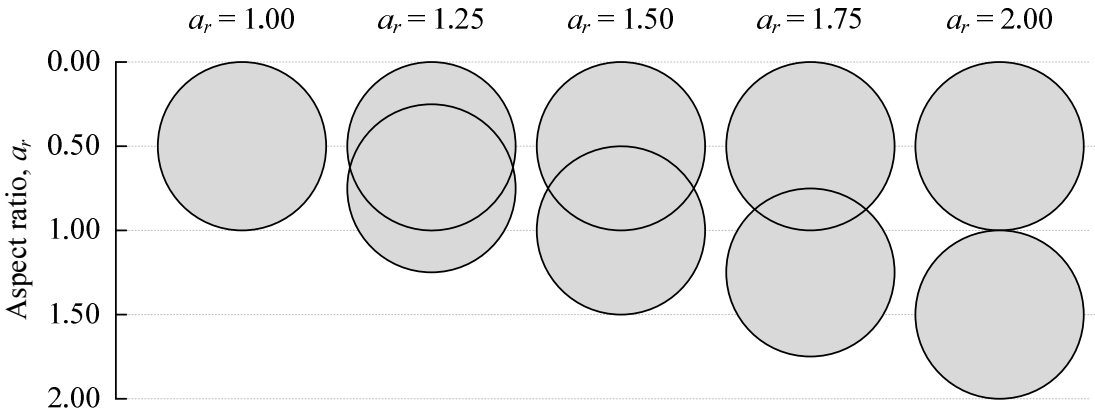

Figure 5.18 Range of aspect ratios a_r explored in the numerical simulations

The influence of a_r on the numerical dynamic ϕ_r is shown in Figure 5.19. The experimental results of the various granular materials used in this thesis are also plotted alongside the numerical results for comparison.

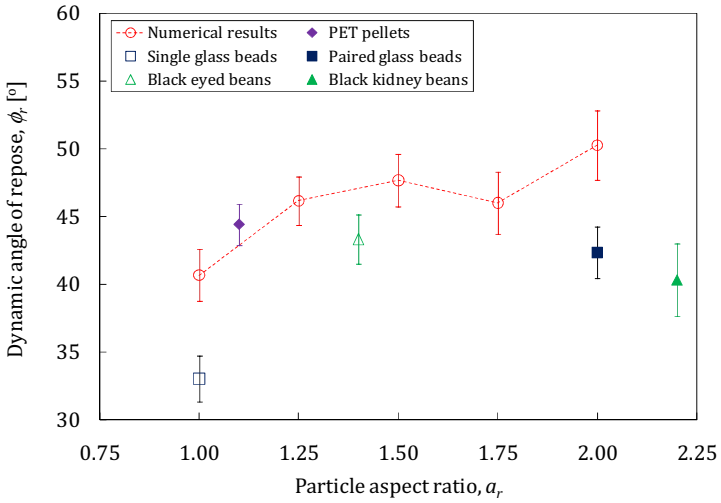

Figure 5.19 The influence of particle aspect ratio (using two equal spheres) on the numerical dynamic angle of repose compared with experimental results of various granular materials

Error bars represent ±1 standard deviation, sample size=10

As a_r increases, the general trend of the dynamic ϕ_r increases accordingly. Increasing a_r from 1.00 to 2.00 will see an increase in dynamic ϕ_r of 26%. All the DEM input parameters are fixed to the reference simulation values (Table 5.1), therefore the increase is a result of (a) the inter-particle locking and (b) the increase in boundary influence as the number of particles between end plates decreases (section 5.3.9).

Another important observation is the significant increase in dynamic ϕ_r (17%) when a_r is changed from 1.00 to 1.25. Spherical objects (a_r=1.00) have more degrees of freedom than non-spherical particles i.e. when placing single and paired GB on a flat surface, the single GB will be more inclined to roll. In the rotating drum, this translates to a lower dynamic ϕ_r as even the slightest non-shpericity (a_r=1.25) will reduce the particle's ability to move.

In general (excluding PET pellets), the numerical results tend to overestimate the experimental results for the dynamic ϕ_r. The experimental dynamic ϕ_r for the paired GB is significantly higher (29%) than the single GB, emphasising Härtl's (2008) findings. Although the

PET pellets have a low aspect ratio (a_r=1.10), the particle's angularity contributes inter locking forces.

In paired GB and numerical particles with a_r greater than 1.50, a pseudo friction is created by the indentation between the spheres. This pseudo friction is not present in the black eyed beans and black kidney beans, explaining the discrepancy in dynamic ϕ_r between black kidney beans and paired GB.

A similar parametric study was carried out on the confined compression simulations. The influence of the particle a_r on the bulk stiffness parameters was determined. As the particle shape varied, a new set of particles needed to be generated for each simulation and therefore, the packing arrangement varied. The results are shown on Figure 5.20 with the initial void ratio shown in the secondary axis (right).

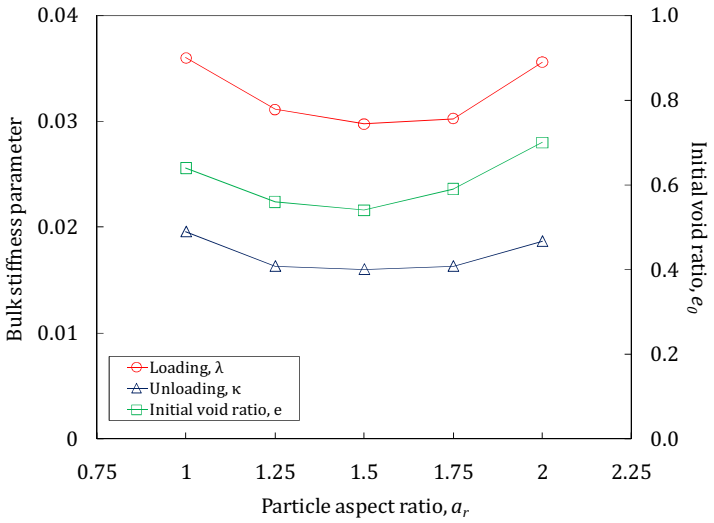

Figure 5.20 The influence of aspect ratio on the bulk stiffness parameters and initial void ratio in a confined compression simulation

It can be seen that the simulations with a_r= 1.00 and a_r= 2.00 have the highest bulk stiffness parameters (softest systems) compared to the other a_r, however, this coincides with the highest initial void ratio e_0. Taking into account e_0, the results would suggest that the particle a_r has a less effect on the bulk stiffness parameters than the plot would lead to believe.

Based on this parametric study, the most appropriate a_r to use in the optimisation procedure is a_r=1.20. This value was chosen to (a) satisfy the optimisation procedure's focus on

inter-particle properties by reducing the particle shape's influence on the bulk behaviour and (b) use a non-spherical particle to account for the non-shpericity observed in the various granular materials.

5.3.11 Effects of varying multiple parameter simultaneously

The parametric study discussed in this chapter investigated the effects of varying single parameters independently as this was the simplest method of determining and illustrating each DEM parameter's effect on the bulk behaviour. Certain parameters may have minimal influence on the bulk behaviour when varied independently but have significant influence when varied simultaneously. This was not accounted for in this section, however statistical analysis was carried out on the numerical dataset to establish the magnitude of multi parametric influence on the bulk response parameters (see section 6.4.4.1).

5.4 Numerical scaling of the experimental devices

Simulating full scale experimental systems can sometimes be unfeasible to compute. For example, a full scale confined compression experiment of single GB may contain thirty thousand particles, the experimental loading rate is 1 *mm*/*min* and the particle shear modulus *G* can exceed 1E10 *Pa*. All of these factors will significant increase the computational time. As far as the optimisation procedure is concerned, conducting a full factorial matrix of simulations at full scale could take months to compute. A scaling investigation was therefore carried out to determine the effects of scaling on the bulk response parameters.

The rotating drum experimental device was designed using dimensions that could be accurately simulated without the need for scaling. Therefore, this scaling analysis focused on the confined compression apparatus, more specifically the effects of scaling on the bulk stiffness parameters. Scaling was carried out on;

- The apparatus dimensions
- The particle shear modulus, *G*, and
- The sample compression rate.

5.4.1 Apparatus dimensional scaling

The apparatus dimension scaling study investigated the effect of scaling the system and therefore, number the particles (as the particles size remained constant) on the bulk stiffness parameters. Eventually the appropriate scaling was applied to the numerical dataset used in the optimisation procedure, therefore reducing the computational time. The error in results incurred from scaling will be used to correct the final data. A parallel study investigated the effect of wall friction during dimensional scaling by conducting identical simulations and reducing the particle to wall coefficient of sliding friction to zero.

5.4.1.1 DEM implementation and numerical setup

The experimental apparatus of the confined compression equipment has a height of 330 *mm* (based on the average sample height) and a diameter of 145 *mm* as described in section 3.2.2 and the DEM implementation used in this study is show in Table 5.2.

Table 5.2 DEM implementation of apparatus dimensions scaling investigation for confined compression

PP, PW coefficient of sliding friction ($\mu_{pp},\ \mu_{pw}$)	0.34
PP, PW coefficient of restitution ($e_r,\ e_{r,pw}$)	0.59
PP, PW coefficient of rolling friction ($\mu_{r,pp},\ \mu_{r,pw}$)	0.00
Poisson's ratio, υ	0.4
Particle density, ρ_s [kg/m^3]	1200
Particle shear modulus, G [Pa]	1E+7
Number of equal spheres in each particle	2
Sphere radius [*mm*]	3.3
Particle aspect ratio, a_r	1.50
Fixed time step in terms of Rayleigh time step	20%
Compression speed of each plate [*mm/sec*] [1]	0.5

[1] Two way compression
PP: particle to particle interaction, PW: particle to wall interaction

The size of the particles was kept constant throughout the scaling investigation. Two scaling methods were investigated; the first method investigated the effect of scaling the entire

cylinder proportionally by keeping the height to diameter (H/D) ratio constant. The original height to diameter ratio is 2.28 (330 *mm*/145 *mm*) and was compared to three smaller sizes. The second method investigated the effect of reducing the sample height whilst keeping the diameter constant at 145 *mm*. An illustrations of the various sizes used in this study is shown in Figure 5.21 with the run ID numbers circled for reference.

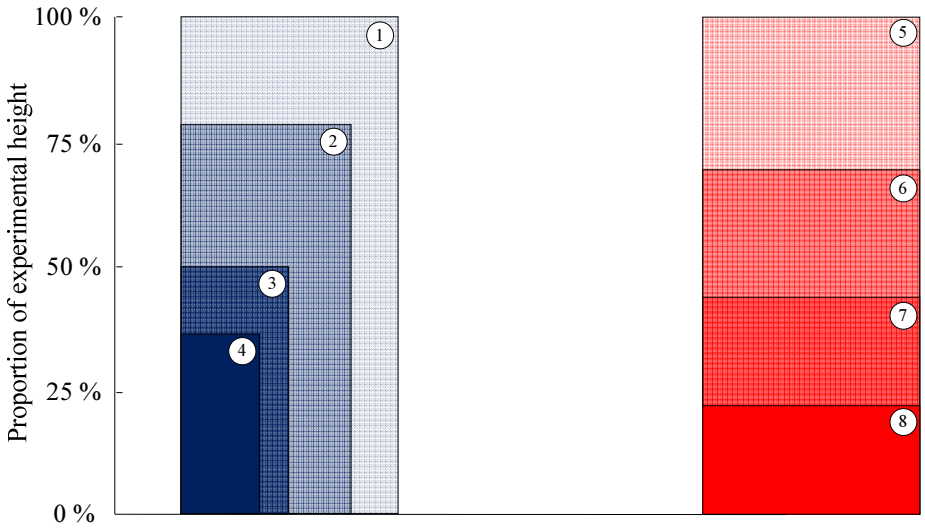

(a) Fixed height/diameter ratio (b) Fixed diameter

Figure 5.21 The various sizes used for the apparatus dimension scaling investigation of the confined compression equipment

The dimensions of the numerical systems and the salient values for the 8 runs are summarised in Table 5.3. Run 1 and 5 were identical runs but are named differently for analytical convenience, where run 1 refers to the fixed H/D and run 5 refers to the fixed D analysis.

Table 5.3 Summary of the numerical setup for the 8 runs used in the apparatus dimension scaling investigation

	Full scale	Fixed H/D ratio			Fixed D		
Run ID	1/5	2	3	4	6	7	8
Height [*mm*]	330	260	165	120	230	145	72.5
Diameter [*mm*]	145	114	72.5	52.6	145	145	145
H/D Ratio	2.28	2.28	2.28	2.28	1.59	1.00	0.50
Dimensional scaling factor, ξ	100%	79%	50%	36%	70%	44%	22%
Force required for 65 *kPa* [*N*]	1073	666	268	141	1073	1073	1073
Particles in system	14036	6793	1691	647	9781	6198	3184
Proportion of full scale	100%	48%	12%	5%	70%	44%	23%
Diameter /particles length [1]	18.8	14.8	9.4	6.8	18.8	18.8	18.8
Initial void ratio, e_0	0.58	0.60	0.65	0.71	0.58	0.60	0.64
Cylinder volume [mm^3]	5581	2742	696	273	3925	2512	1327
Cylinder surface area [cm^2]	1553	969	392	214	1083	693	366
% of original surface area	100%	62%	25%	14%	70%	45%	24%

H/D: height/diameter, height based on average sample height, D:diameter
[1] particle length based on average of major, intermediate and minor dimension

Loading stresses

The effect of scaling on the bulk stiffness parameters was the focus of this study. As λ and κ are dependent on the loading and unloading stress levels, it was important to (a) determine an appropriate stress level for the analysis and (b) keep the stress level constant throughout the analysis. As the diameter changes, the force required will change accordingly. The stress level chosen for this study was 65 *kPa* as this was the same used in the experiments.

Number of particles in the system

The main purpose of the scaling analysis is to reduce the computational time. One aspect of the simulation that greatly influences the computational time is the number of particles (and therefore spheres) in the system. Scaling the system down whilst keeping the particle size

constant will decrease the cylinder volume and therefore the number of particles that can reside in it. The particles in the various runs are shown in Table 5.3.

Void ratio

The bulk stiffness parameters are significantly influenced by the packing arrangement in the system, e.g. a densely packed system will exhibit greater bulk stiffness than an equivalent looser system with similar granular materials. Therefore, the initial packing arrangement and the initial void ratio of the system are important. Moreover, λ and κ are dependent on the initial and consequent change in void ratio. As described in section 3.2.3.1, the packing density and initial void ratio is dependent on various parameters including the filling method, cylinder dimensions and particle contact parameters. To perform a comparative study, it was essential to limit the amount of variables (e.g. height and diameter). Therefore, the particle DEM parameters and filling methods were kept constant for the 8 runs. In each test, a factory was placed just above the required sample height and the particles were generated dynamically in four seconds. The predicted sample height was based on the volume of the cylinder, volume of particles and the initial void ratio of the full scale experiment (Table 5.2). For example, in run 2 it was predicted that the number of particles needed to produce a sample height of 260 *mm* was 6800 particles. The particle generation rate was therefore 6800/4=1700 particle per second. After four seconds of generation, the sample was left to settle for one second before any particles above 260 *mm* were removed (in the case of run 2, seven particles were removed). Following the settlement, 10 *N* were applied from a top plate to level the sample and the height of this plate was used to determine the initial void ratio.

Particle to wall coefficient of sliding friction

A parallel study investigated the effects of the particle to wall friction μ_{pw} on κ and λ during scaling. This was accomplished by rerunning runs 2, 4, 6 and 8 with the wall friction removed (μ_{pw}= 0). The reruns were conducted using exported input decks from an equivalent simulation so that the particle packing arrangement and porosity would remain consistent.

5.4.1.2 Discussion and analysis

From Table 5.3 it can be seen that decreasing the apparatus by 64% whilst fixing the H/D ratio will reduce to number of particles by 95% (run 4). This is in part due to the packing arrangement that will become looser as the Diameter/particle length ratio decreases. However reducing the fixed D height by 78% (run 8) will only see the number of particle decrease by 77% as the Diameter/Particle length ratio remains constant.

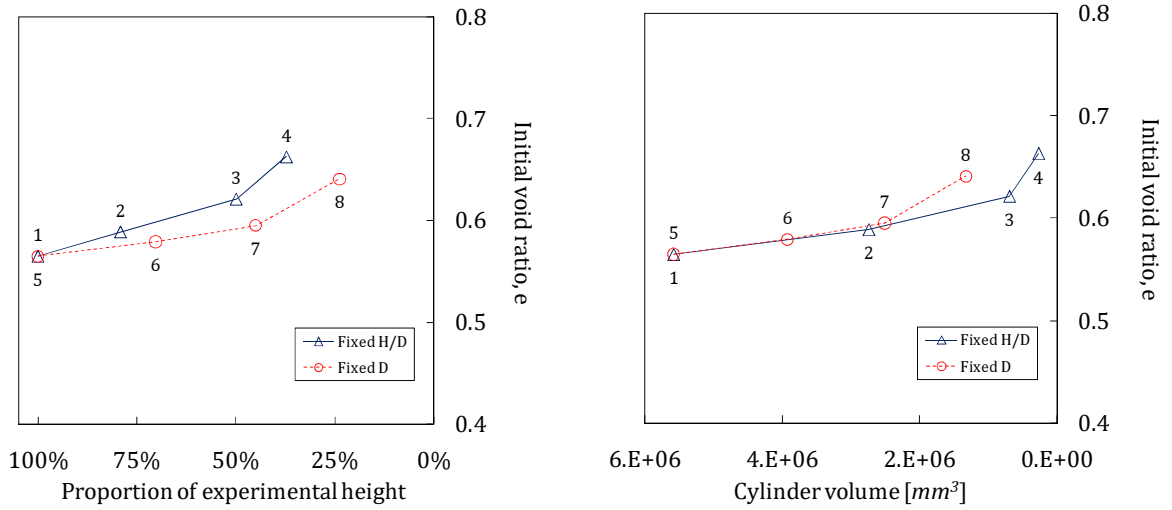

(a) (b)

Figure 5.22 The effects of scaling on the initial void ratio with respect to the (a) experimental height and the (b) cylinder volume

H/D: height/diameter, height based on average sample height, D:diameter, PW: particle to wall

Figure 5.22 (a) shows the variations in initial void ratio e_0 with respect to the dimensional scaling factor ξ for the 8 runs. It can be seen that as the system is scaled down, the void ratio increases (sample becomes looser) which is a natural phenomenon in response to the greater boundary effect. More specifically, this is due to the particle's ability to pack more densely against another layer of particle as opposed to being constraint by a boundary layer as shown in Figure 5.23. For similar reasons, the overall fixed diameter runs have a lower initial void ratio than the fixed H/D runs. Therefore by plotting the initial void ratio relative to the cylinder volume (Figure 5.22, b), the discrepancies between the two scaling methods are reduced.

(a) Particle to wall (b) Particle to particle

Figure 5.23 Illustration of the effect of boundaries on the packing arrangement

Figure 5.24 demonstrates the effects of scaling the confined compression system height on the bulk loading stiffness parameter λ.

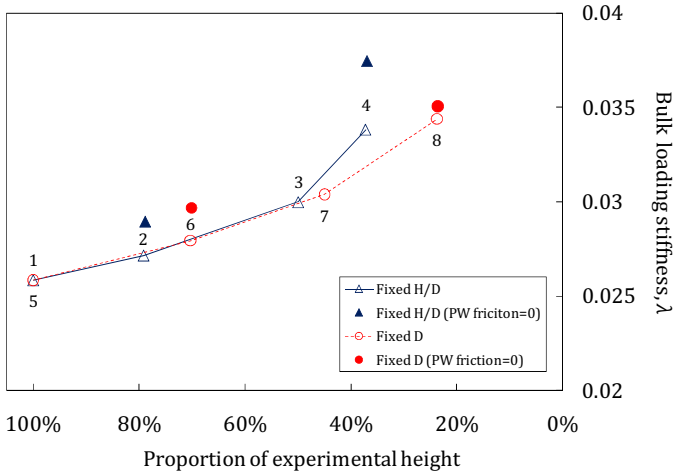

Figure 5.24 Confined compression sample height scaling influence on the bulk loading stiffness λ

H/D: height/diameter, height based on average sample height, D:diameter, PW: particle to wall

The general trend is an increase in λ as the sample height is scaled down; this translates to a softening of the system. This may be attributed in part to the increase in e_0 when the system is scaled down and therefore more voidage is available for compression. In addition, the system softening can be explained by the wall friction effect within the system. As explained in section 5.3.5, the particle to wall friction coefficient of friction μ_{pw} has a significant influence on the bulk stiffness of a system during confined compression. The particle to wall frictional forces act

in the opposite direction to the movement of the particles (by slippage) during compression and is proportional to the number of contacts along the wall. Therefore, the squatter samples will have less surface area for frictional forces to be mobilised and this will result in a softer system. Similarly, removing wall friction (μ_{pw}= 0) would make the system softer because the compression force is no longer absorbed through wall friction and more forces are transferred to particles and the sample will undergo greater compression strains.

At low scaling (ξ = 20% to 40%), the effects of wall friction are more noticeable in fixed H/D runs than fixed D runs. This is illustrated by the discrepancies in λ between runs 4 and 8 with and without wall friction (10% and 2% respectively). This may be explained by the surface area; although these two runs have similar ξ, run 8 has almost twice as much cylinder surface area and particles (Table 5.3).

It can be seen that scaling the system down to 50% of the original height produces a relatively linear increase of λ with a low slope and the results for the fixed H/D and fixed D scaling trends are very similar. Scaling beyond 50% produces an accelerated increase of λ and discrepancies between the two scaling methods

Figure 5.25 demonstrates the numerical effect of scaling the confined compression experimental height on the bulk unloading stiffness κ.

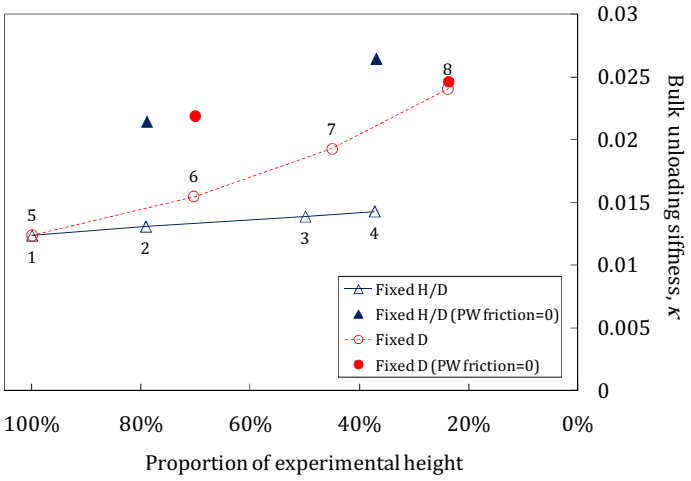

Figure 5.25 Confined compression sample height scaling influence on the bulk unloading stiffness, κ

H/D: height/diameter, height based on average sample height, D:diameter, PW: particle to wall

As the sample height decreases in the fixed D runs, the system becomes softer as κ increases. However, the fixed H/D scaling appears to be much less influenced by scaling. Reducing the scale down to 50% of the experimental height will increase κ by 10% and 50% for the fixed H/D and fixed D scaling respectively.

The particle to wall friction μ_{pw} plays a significant role in the unloading stiffness as it restricts the rebounding of the particles during unloading, i.e. removing the wall friction will cause the system to rebound more readily and will make the system softer (higher κ). This is highlighted by the discrepancies between runs with and without wall friction (specifically run 4). As mentioned previously, the cylinder surface area and particles in contact with the boundary surface will determine the magnitude of the discrepancies in runs with and without wall friction; as the scaling decreases, the surface area available for frictional forces decreases and eventually (run 8) the discrepancies in runs with and without wall friction becomes negligible. This is because a squat sample does not allow for wall friction to be mobilised as readily as larger scale systems where the influence of wall friction is reduced. It is for this reasons that Eurocode 1 (1996) encourages the use of a squat sample for K_0 testing.

Figure 5.26 illustrates the change in results incurred from numerical scaling on λ and κ relative to the full scale results. It can be seen that although λ is affected by the fixed H/D and fixed D scaling in a similar manner, the fixed D scaling affects κ significantly more than fixed H/D scaling. Any differences over 5% were considered significant and adjustments were factored into the results when used in the optimisation procedure.

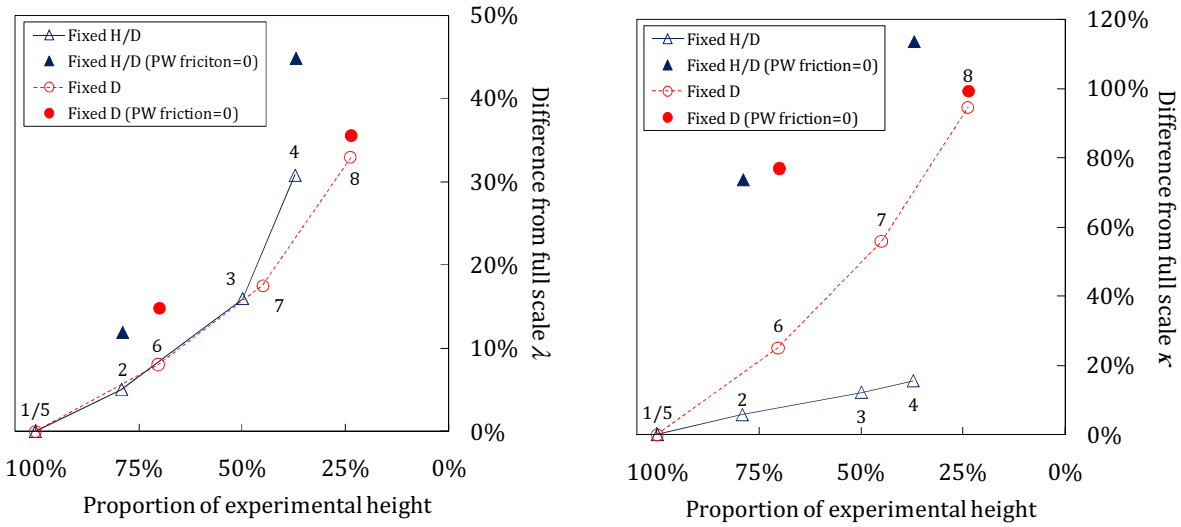

(a) Loading stiffness λ (b) Unloading stiffness κ

Figure 5.26 The change incurred from numerical scaling on the loading and unloading bulk stiffness of the confined compression test

H/D: height/diameter, height based on average sample height, D:diameter, PW: particle to wall

The following equations represent fitted trendlines to the curves in Figure 5.26, where ξ is the dimensional scaling factor with respect to experimental sample height, λ and κ are gradients with respect to void ratio and average compression stress in *kPa*.

Loading stiffness scaling influence

Fixed H/D: $\lambda = 0.803\xi^2 - 1.559\xi + 0.76$ (R^2=0.978) Equation 5.4

Fixed D: $\lambda = 0.416\xi^2 - 0.938\xi + 0.53$ (R^2 = 0.978) Equation 5.5

Unloading stiffness scaling influence

Fixed H/D: $\kappa = 0.242\xi + 0.244$ (R^2=0.998) Equation 5.6

Fixed D: $\kappa = 0.929\xi^2 - 2.38\xi + 1.45$ (R^2 = 0.999) Equation 5.7

As μ_{pw} has a significant influence on the bulk stiffness of the confined compression system, for parametric sensitivity robustness it should ideally be removed. Using a squatter

sample will minimise the effect of wall friction but add greater error to the results. However, particle to wall friction is a 'real' phenomenon and should not be ignored in the bulk sensitivity study.

Following the dimensional scaling investigation, the most appropriate and efficient scaling to be used in the numerical dataset was found to be ξ=60% of the experimental height. The relevant DEM implementation for a scaling of this magnitude is shown in Table 5.4.

Table 5.4 Relevant DEM implementation used in the numerical dataset simulation for a 60% scaling of the experimental height

Height [*mm*]	198
Diameter [*mm*]	87
H/D Ratio	2.28
Percentage of experimental height	60%
Particle in system	8800
Proportion of experimental particles	63%
Cylinder surface area [cm^2]	541
Percentage of experimental surface area	35%
λ increase due to scaling	12%
κ increase due to scaling	10%

It can be seen that scaling the system down to 60% of the experimental height will increase λ and κ by 12% and 10% respectively. Although the dimensional scaling study was carried out numerically, it will be assumed that the results and analysis are applicable to experimental dimensional scaling. Therefore, for the optimisation procedure, the change in bulk stiffness parameters as a result of scaling will be factored into the experimental results.

5.4.2 Numerical particle shear modulus scaling

The particle stiffness of granular materials may vary considerably. For example, Chung (2006) measured corn and glass beads to have a shear modulus of G = 1E7Pa and G = 1E10 Pa respectively. The computational time in numerical simulations is directly affected by the shear modulus (see section 2.2.6). Decreasing the shear modulus by 100 will decrease the computational time by 10. Chung (2006) reported that some DEM simulations results were not

sensitive to accurate G and could be scaled down by 1000 times to reduce the computational time significantly whilst maintaining a relatively high degree of accuracy data. However, as the particle stiffness is a dominant parameter in the bulk stiffness during confined compression, a parametric study is necessary. This parametric investigation will focus on the effect of scaling the particle shear modulus G on the bulk stiffness parameters.

Three parallel studies were conducted alongside the particle stiffness investigation: the first examined the effect of the particle aspect ratios a_r (Figure 5.18) using single (a_r= 1.00) and paired spheres (a_r= 2.00). The second investigated the elasto-plasticity of the system by monitoring the strain through three loading and unloading cycles at increasing stress levels. Finally, the effect of the compression stress level on the bulk stiffness parameters were monitored by analysing λ and κ at increasing stress levels.

5.4.2.1 DEM implementation and numerical setup

The sensitivity study DEM implementation was based on the confined compression of single and paired glass beads (GB) with a loose filling arrangement (see section 3.2.2). The sample was typically around 60 *mm* high. The DEM implementation used for this study can be found in appendix B. The squat setup was chosen to reduce the influence of wall friction and limit the variables affecting the analysis. The same DEM input file was used for all the single sphere simulations ensuring a consistent packing arrangement and e_0 throughout the study (the same method was applied to the paired sphere simulation). The input file was created by filling a cylinder (diameter 145 *mm*) with sufficient particles to create a 60 *mm* high sample (5000 single and 2500 paired spheres) using a mid-range stiffness of *G* = 1.7E8 *Pa*. Following the filling, the particle stiffness was altered to the desired value of *G* for each run and the system was left to settle. As the particle stiffness was altered, the numerical particle overlap altered accordingly. This either resulted in a sample slump (when *G* is reduced) or expansion (when *G* is increased) to satisfy Equation 2.2 and Equation 2.7. After the system had reached a state of equilibrium, 3.5 *kPa* of pre-stressing was added by a top platen to flatten the top surface (similar to the experiment). This is the initial condition for the confined compression analysis. The numerical compression speed used in this study was constant at a rate of 0.1 *mm*/*sec*. Five different shear moduli were used in this investigation ranging from 1E6 *Pa* to 1E10 *Pa* and all the other

parameters were kept constant. Each compression test was conducted in the same manner with three loading and three unloading cycles at increasing stress levels: 13.5, 23.5 and 33.5 *kPa*.

5.4.2.2 Discussion and analysis

The main observations made from the numerical particle stiffness investigation are summarised below:

Initial void ratio

As the particle shear modulus, *G* is altered the system either slumps or expands and the initial void ratio e_0 will therefore change. The effects of altering the particle shear modulus on e_o for single and paired spheres are shown in Figure 5.27.

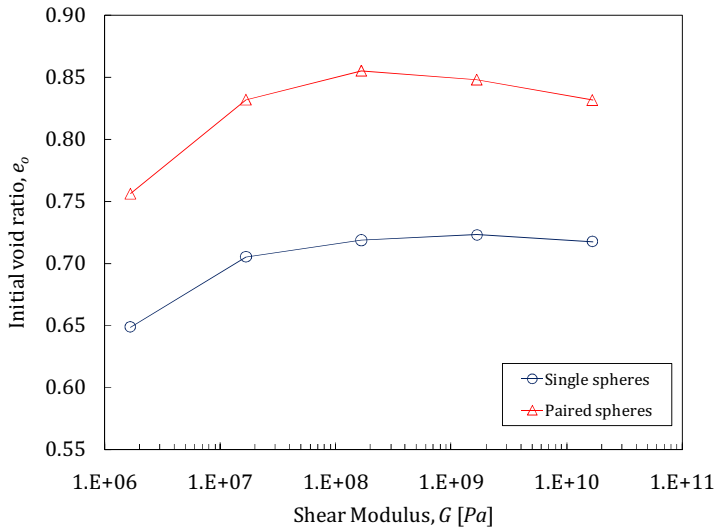

Figure 5.27 The effect of particle stiffness on the initial void ratio for single and paired spheres in a squat confined compression cylinder

Paired spheres have a consistently higher e_o than single spheres (15% higher). This is primarily due to the loose filling methods coupled with the single sphere's propensity to settling into a denser packing arrangement. The paired spheres, however, will be more restricted from denser packing.

For both single and paired spheres, the most significant increase in e_0 occurs between a *G*=1E6 *Pa* and *G*=1E8 *Pa*. This is a numerical phenomenon as a result of (a) the system's slump

due to the shear modulus reduction and increase in particle overlap and (b) as *G* is reduced, the top platen will need to be lowered further (relatively to higher *G*) to achieve the same pre-stressing of 3.5 *kPa*; the results is a decrease in e_0.

Between a *G*=1E8 *Pa* and *G*=1E10 *Pa*, e_o does not appear to be influenced significantly and in the case of the paired spheres, a minor decrease is observed (2%). A macroscopic study of the paired sphere simulation with a *G*=1E10 *Pa* showed that there was sample settling due to particle rearrangement as the pre-stressing occurred, which may have been a contributing factor.

Sample strain due to compression stresses

The influence of compression stress on the average vertical sample strains ε_v for single and paired spheres are shown in Figure 5.28.

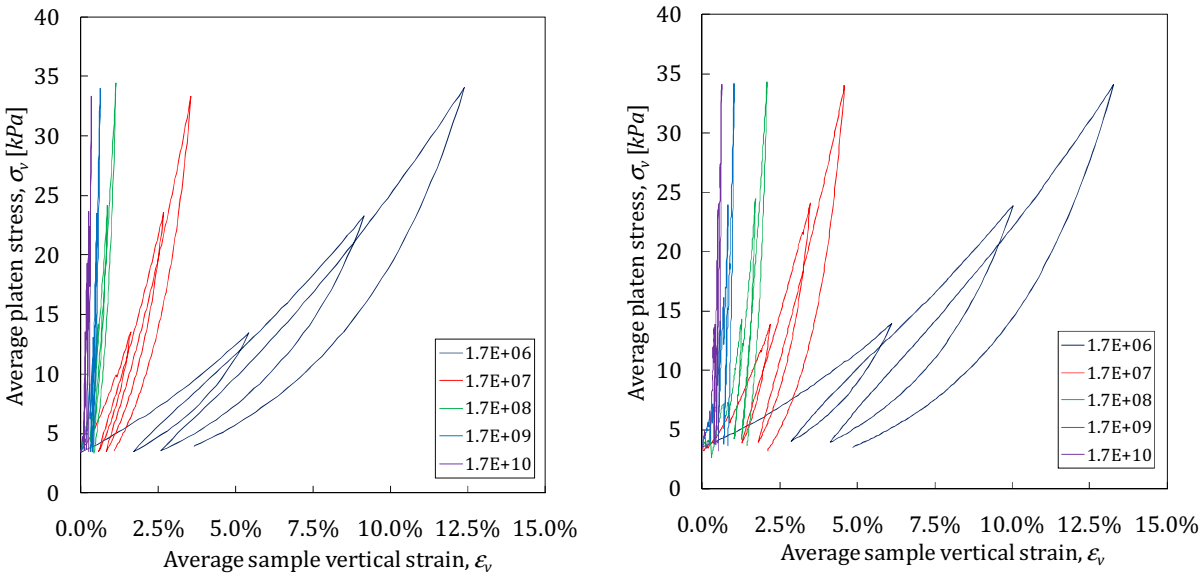

Figure 5.28 Average numerical vertical sample strains for (a) single and (b) paired spheres using varying particle shear moduli

In each ε_v increases proportionally to the increase in compression stress applied. This is illustrated by the peaks in the 1st, 2nd and 3rd loadings. For both particle sizes, a decreasing shear modulus incurs a larger ε_v from similar compression stresses. It can be seen, however, that the

difference in ε_v when *G*=1E6 *Pa* to *G*=1E8 *Pa* is considerably larger than from *G*=1E8 *Pa* to *G*=1E10 *Pa*.

The paired spheres show a greater ε_v than single spheres for matching particle *G*. The systems with paired spheres have greater e_0 (Figure 5.27) and are inclined to settle into a more unstable packing arrangement than single spheres. These phenomena may help to explain the higher ε_v found in systems with paired spheres. In addition, the DEM code adopted in the thesis (EDEM) does not include a plastic deformation model but only includes a non-linear elastic model. Therefore, any plasticity observed during loading and unloading is a direct result of particle rearrangement. The total plastic deformation can be quantified by observing ε_v on the final unloading. The final numerical sample strain of single and paired spheres for various shear moduli are shown in Table 5.5. It can be seen the plastic deformation observed for the paired spheres is typically double than that of the single spheres (excluding *G*=1E6).

Table 5.5 Final numerical sample average vertical strain of single and paired spheres for a range of particle shear modulus

Shear Modulus, G [*Pa*]	Single sphere	Paired sphere	% difference
1.67E+06	3.66%	4.87%	33%
1.67E+07	1.07%	2.10%	96%
1.67E+08	0.43%	0.84%	95%
1.67E+09	0.41%	0.82%	100%
1.67E+10	0.25%	0.51%	104%

Bulk stiffness parameters

The influence of *G* on the bulk stiffness parameters for single and paired spheres can be seen in Figure 5.29. The plots highlight the difference in λ and κ for various loading and unloading vertical stresses σ_v and are plotted on log-log scales.

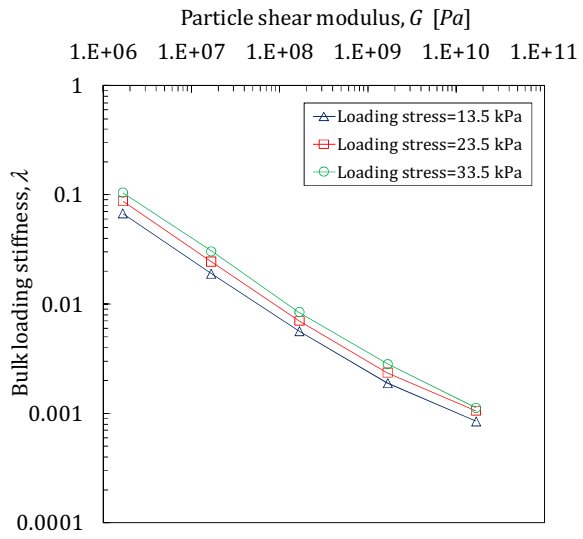

(a) Single spheres loading, λ

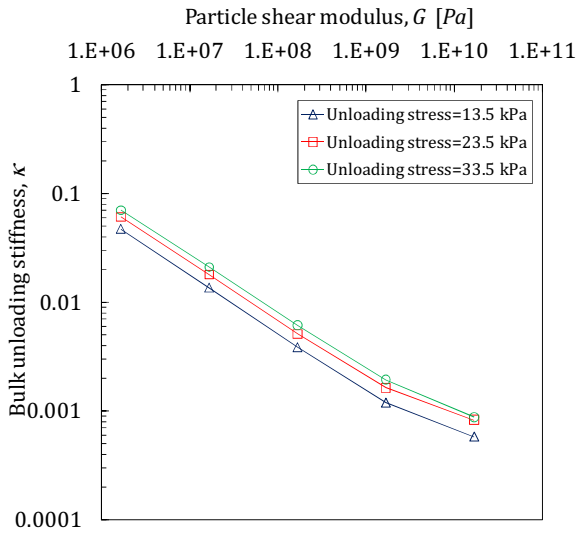

(b) Single spheres unloading, κ

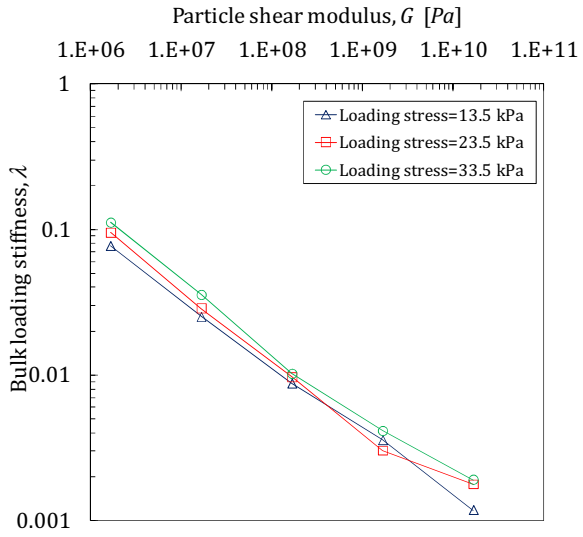

(c) Paired sphere loading, λ

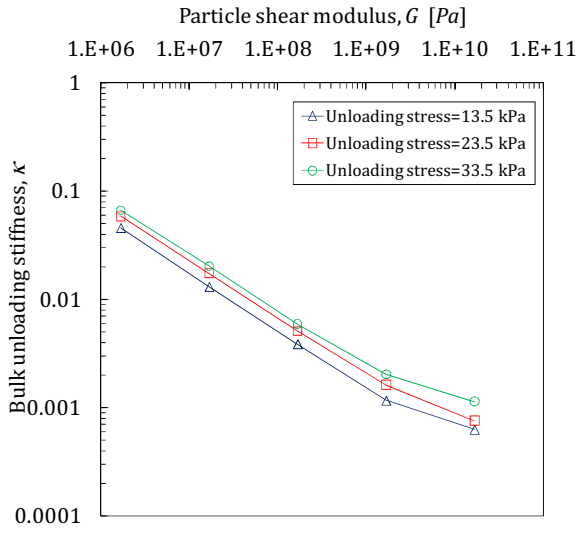

(d) Paired sphere unloading, κ

Figure 5.29 The influence of particle shear modulus G on the bulk loading λ and unloading κ stiffness parameters for single and paired spheres

As expected, the overall trend is a decrease in bulk stiffness gradient (a stiffening of the system) when G increases. In addition, the bulk stiffness gradients decrease as the compression stress increases. Therefore, at greater compression stresses, the system will behave in a stiffer manner. This is primarily due to the fact that compressing solids require more stress than

compressing voids. As compression occurs, the void ratio decreases and the stress requires to produce a greater strain increases exponentially. The bulk stiffness gradients when G = 1E10 Pa is higher than the overall trend would predict it to be. The reason for this is not fully understood and may be due to the role of contact friction.

The results for λ using paired sphere seen in Figure 5.29 (c) show intersecting trendlines from G=1E8 onwards, a phenomenon that does not occur in the other simulations. A macroscopic study of the paired sphere simulations showed that the system did not have a stable packing structure and the particles in the system would rearrange during compression. This is especially true at higher values of G. As λ is a function of the elastic and plastic behaviour of the system during compression, unstable systems will be more susceptible to particle rearrangement and λ may be influenced. This phenomenon does not occur during unloading as κ is a function of the elastic properties of the sample.

The linear relationship seen in the trend lines for the various conditions in the log-log plots in Figure 5.29 means that the bulk stiffness parameters may be expressed as

$$\lambda, \kappa = \frac{C}{G^n} \qquad \text{Equation 5.8}$$

Where G is the particle shear modulus in Pa, C and n are the constants which are derived from the best fit trendlines excluding the results obtained for runs using G=1E10, and the bulk stiffness gradient are relative to void ratio and compression stress in kPa. The values for C and n extracted from Figure 5.29 for the various conditions are shown in Table 5.6. These values will provide a reasonable indication for bulk stiffness gradients at various loading conditions.

Table 5.6 Constants for predicting the bulk stiffness parameters at various stress levels using Equation 5.8

	Single spheres		Paired spheres	
Loading stress, σ_v [kPa]	n	C	n	C
13.5	0.526	190.5	0.484	109.9
23.5	0.526	157.9	0.497	115.9
33.5	0.517	107.1	0.447	44.3
Unloading stress, σ_v [kPa]				
13.5	0.522	124.6	0.508	95.1
23.5	0.526	112.9	0.520	99.8
33.5	0.534	98.9	0.531	91.6

Adjusted simulation time

One final aspect to consider in the particle stiffness sensitivity study is the simulation time t_s (defined as the numerical time that has been simulated in the DEM simulation) to complete the loading and unloading cycles. This is not to be confused with the computational time t_c which is the real time taken to run the simulation. Although reducing *G* will decrease t_c, the average sample strain ε_v to achieve the desired compression stress will increase relative the higher values of *G*. In other word, decreasing *G* will create a softer system and the compression plates will need to travel further to achieve the desired stress compression stress levels. As the compression speed remains constant throughout the study, the computational time will increase.

For comparative purposes, simulation times were adjusted using a time factor. The time factor is the speed multiple relative to the value of *G* that results in the shortest t_c (in this study that is *G*=1E6 *Pa*). For example, when using single spheres t_s to perform a loading and unloading for *G*=1E6 *Pa* and *G*=1E8 *Pa* are 236 and 19 seconds respectively. However, it takes 10 times longer to compute a simulation where *G*=1E8 *Pa* than a similar simulation where *G*=1E6 *Pa* (see Equation 2.13); so the adjusted simulation time for *G*=1E8 *Pa* is 19x10=190 seconds. The adjusted simulation time, $t_{s,a}$ is a good indicator at the computational efficiency of the various simulations. The effect of varying the shear modulus *G* on $t_{s,a}$ is shown in Figure 5.30.

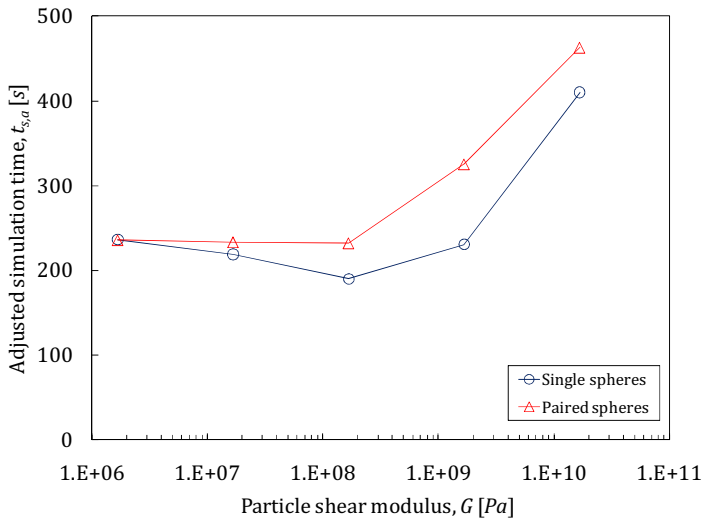

Figure 5.30 The effect of varying the shear modulus G on the adjusted simulation time

The results in Figure 5.30 demonstrate that running a simulation using G=1E6 Pa to G=1E8 Pa will have the same efficiency. So using a G closer to the experimental value will be more appropriate. However, changing the shear modulus from 1E8 Pa to 1E10 Pa will see a sharp increase in $t_{s,a}$. So if t_c is the priority (e.g. when running a large amount of simulations) limiting the shear modulus to 1E8 Pa would be advisable.

5.4.3 Confined compression plate rate scaling

The experimental compression rate of the Instron machine is 0.1 *mm/min* for the single and paired glass beads and 1 *mm/min* for the PET pellets, black eyed beans and black kidney beans. At these compression rates, a single test may take up to 5 minutes. Simulating these durations is unfeasible, especially when considering the amount of runs that need to be performed to create the numerical dataset used in the optimisation procedure. This study focused on the effect of varying the compression speed of the top and bottom plates on the bulk stiffness parameters. Three parallel studies were conducted alongside the compression rate investigation. The first examined the effects of using two varying a_r, using single and paired spheres. The second parallel study investigated the elasto-plasticity of the system by monitoring the sample strains during three loading and unloading cycles at increasing stresses. Finally, the effect of the

compression stress level on the bulk stiffness parameters were monitored using the loading and unloading gradients at increasing stresses.

DEM implementation

The DEM implementation and numerical setup was based on the experimental setup of the single and paired GB with loose filling. A loose filling arrangement was used for this study as it was deemed the most critical scenario for a compression rate investigation. The various compression rates examined in the study 0.1 (the experimental rate), 60, 320 and 720 *mm*/*min*. The sample was typically around 60 *mm* high and the DEM parameters used in the simulations can be found in Appendix B. As mentioned previously, the advantage of using a squat sample is that the influence of boundary friction is reduced.

Strain response due to compression

Figure 5.31 illustrates the effects of increasing the average platen vertical compression stress, σ_v on the average sample strain, ε_v at various compression rates.

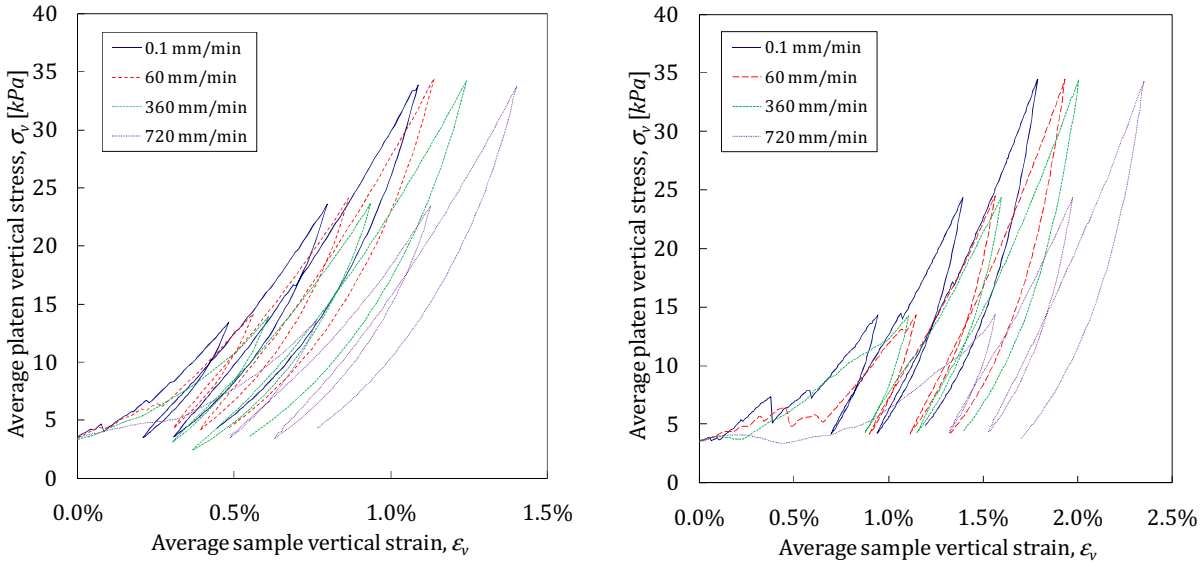

(a) Single spheres (b) Paired spheres

Figure 5.31 The effects of vertical stress due to various compression rates on the average sample strain

The stress-strain responses for single and paired spheres at increasing compression speeds show similar results. However, greater magnitudes of ε_v are observed in the paired

spheres than the single sphere simulations, possibly due to the looser arrangement and higher void ratio during filling for the paired spheres.

The behaviour of granular material under low pressures (~0-10 *kPa*) is significantly less repeatable for the single and paired spheres. This is highlighted by the shift in sample strain at lower stresses. However, at higher pressures the trendlines look very similar for each set of tests. It can be seen that the higher the compression rate, the greater the initial strain shift. For this reason, this study focused primarily on the granular behaviour at higher pressure (>10 *kPa*) which are less affected by this phenomenon. In addition, at lower compression speeds, the system has more time to adjust the confinement pressures, which may allows the particles to rearrange into more stable/stiffness arrangement.

Figure 5.32 demonstrates the effect of confined compression speed on the bulk stiffness parameters at various compression stress levels σ_v.

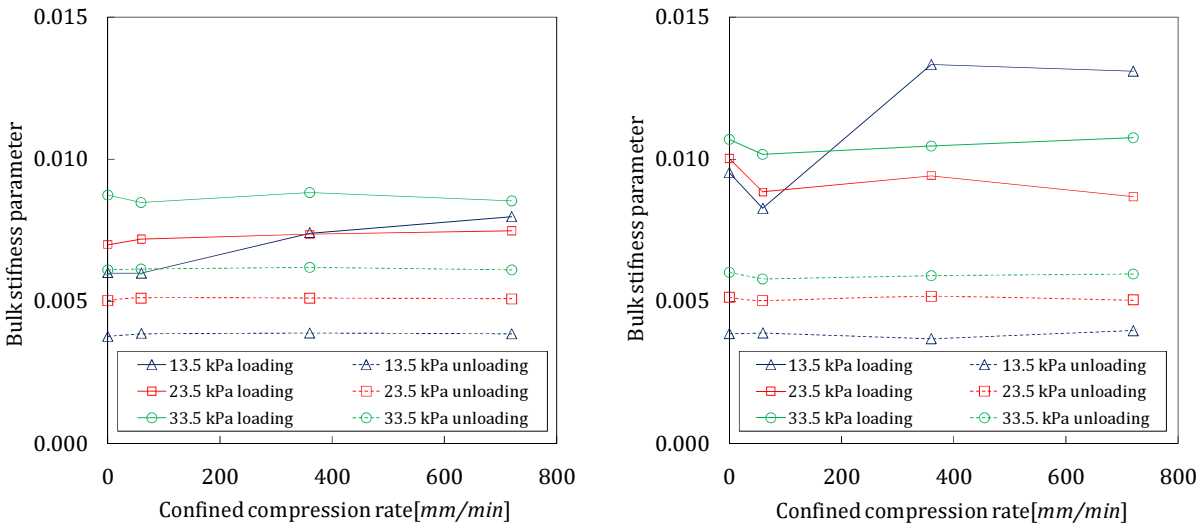

(a) Single spheres (b) Paired spheres

Figure 5.32 The effect of confined compression rate on the bulk stiffness parameters at various compression stress levels

Excluding the first loading to 13.5 *kPa*, all the trends display a similar pattern; as the σ_v level increases, the bulk stiffness parameters decrease (system stiffens). In general, the compression speed appears to have minimal influence on λ and κ.

It can be seen that the discrepancies between the single and paired spheres during loading and unloading are larger for λ than for κ. Therefore, it may be concluded that particle shape does not have a significant effect on κ.

The overall coefficient of variance of λ and κ for the various compression speeds is very low (~2%). For higher pressures (>10 *kPa*) it is not necessary to simulate at experimental speeds as the bulk stiffness parameters are not sensitive to compression rate. For very high compression rates (>1800 *mm*/*min*) a 20% Rayleigh time step may not sufficient.

5.5 Sources of error

Numerical stress strain anomalies

In certain confined compression simulations a numerical anomaly occurs during loading. An example is shown in Figure 5.33. From 0 to 30*kPa*, the sample exhibits typical exponential stiffening which is a behaviour seen in the experimental results. However, from 30 *kPa* onwards the graph suggests that smaller vertical stress increases are needed to produce greater strain; essentially the system is getting softer. This is of course a numerical anomaly.

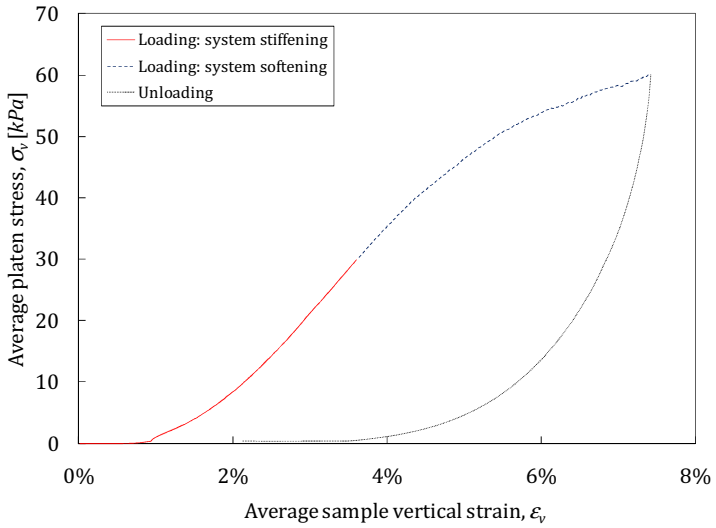

Figure 5.33 Numerical anomaly observed in certain confined compression simulations

After further analysis, it was established that this anomaly occurred as a result of large particle overlapping in the system. The main reasons for this include:

- Large value of fixed % of Rayleigh time step,
- At very large compressive forces, proportionally larger inter particle contact forces may make the particles more inclined to overlap
- In static or quasi-static systems with high values of rolling friction, large values of torque may cause particles to overlap
- If the shear modulus is alter from a low value to a relatively high value and the particles are confined, the system expansion may cause particles to overlap.

Throughout this study, any simulations where this phenomenon occurred were rerun to avoid erroneous results.

Lack of elasto-plastic model

Experimental and numerical analysis for confined compression revealed that some loading and unloading patterns are similar in the numerical and experimental data. These include the linear loading curve which increases with pressure and the crescent unloading curve with hysteretic loop on reloading. During the virgin loading, similar strains occur in both cases, however, there is one major mismatch between the two, caused by the lack of plasticity in the contact model used. This means that no plastic deformation occurs in the numerical simulation, resulting in excessive elastic rebound during unloading and further loading does not incur further deformation. In the experiment, further permanent deformation occurs during further loading cycles, which is absent from the current visco-elastic DEM contact model. During loading, the plastic deformation in granular solids is a result of two phenomena:

- The relative displacement of particles through rolling or sliding
- Plastic deformation of the particles at the points of contact

In DEM simulations, relative displacement occurs naturally. However, plastic deformation at the points of contact is often ignored in the numerical contact, including EDEM (DEM Solutions Ltd 2009), the DEM program used in this thesis, which is based on a Hertz-Mindlin non-linear elastic model. Therefore for soft agricultural grains, EDEM is expected to

underestimate the total plastic deformation of the system. Further research could investigate the introduction of an elasto-plastic contact model to address this anomaly. However, for the current study, this issue will not be addressed.

5.6 Summary

The parametric and scaling sensitivity analysis has produced some interesting and important results that will support the model calibration and ultimately, the optimisation procedure in this study. This section will summarise the main conclusions.

5.6.1 DEM input parameters

A thorough parametric investigation was conducted using DEM simulations to gain a deeper understanding of DEM input parameters influence on the bulk responses parameters. The key results are summarised below

I. Scaling the particle density, ρ_s has a minimal effect on the dynamic angle of repose, ϕ_r or bulk stiffness parameters, λ and κ. It will however, affect the computational time.

II. Scaling the particle Poisson's ratio, υ will affect the bulk stiffness parameters significantly. Increasing υ from 0.1 to 0.45 will stiffen λ and κ by 24% and 23% respectively.

III. The frictional forces along the wall will restrict confined compression during loading and prevent the system from rebounding during unloading. Therefore, increasing the particle to wall coefficient of friction μ_{pw} will contribute to stiffening the system; as μ_{pw} increases the bulk stiffness parameters significantly decrease.

IV. As long as the inner drum friction μ_{pw} is large enough to prevent particle slippage, μ_{pw} has a minimal effect on the dynamic ϕ_r. However, the drum end plate μ_{pw} has a significant effect on the dynamic ϕ_r. Increasing the end plate μ_{pw} from 0.1 to 0.9 will see a 40% increase in dynamic ϕ_r. A pre-optimisation procedure should be carried out as specified in section 5.3.5.1 to determine an appropriate value of μ_{pw} to use.

V. The particle to wall coefficient of rolling friction, $\mu_{r,pw}$ has a minimal effect on the dynamic ϕ_r. However, the boundary conditions contribute significantly to the bulk stiffness in confined compression and increasing $\mu_{r,pw}$ will decrease λ and κ.

VI. Fixing the time step to varying percentages of the Rayleigh time step, T_R has a minimal on the dynamic ϕ_r , λ and κ. It will however, affect the computational time. A minor variation is results is noticed when a fixed T_R of more than 10% is used.

VII. The dynamic ϕ_r is significantly influenced by increasing the number of particles between end plates (reducing the particle radius) when end plates are present. However, when periodic boundaries are introduced, the effect is reduced. When there are fewer particles between end plates (2 to 4), the difference in dynamic ϕ_r for simulations with end plates and with periodic boundaries is significant.

VIII. The standard deviation of the dynamic ϕ_r determination is greater when there are fewer particles along the surface profile (larger particles radii).

IX. The dynamic ϕ_r is significantly influenced by the particle aspect ratio, a_r. Increasing a_r from 1.00 to 2.00 will see an increase in dynamic ϕ_r of 26%. This is due to (a) the inter-particle locking and (b) the increase in boundary influence as the number of particles between end plates decreases. The majority of the increase happens when a_r is changed from 1.00 to 1.25 as even the slightest non-shpericity (a_r=1.25) will limit the particle's ability for movement.

X. Simulations where a_r=1.00 and a_r=2.00 have higher bulk stiffness parameters than particles with intermediate a_r (a_r=1.25, 1.50 and 1.75); however this was found to coincide with the higher initial void ratios, e_0. Ignoring the effects of e_0, the influence of a_r on the bulk stiffness parameters is greatly reduced.

5.6.2 Scaling sensitivity study

In an effort to maximise the computational efficiency, a scaling sensitivity study was performed on the confined compression simulations. This included the numerical scaling of the apparatus dimensions, particle shear modulus *G* and the confined compression plate speed. The key findings of the sensitivity study were:

XI. Scaling the confined compression cylinder dimensions down to 50% of the experimental height gives a relatively linear increase of λ with a low gradient. Similar results may be observed for fixed height/diameter and fixed diameter scaling. Scaling beyond 50% produces an accelerated increase of λ and discrepancies between the two scaling methods.

XII. For the fixed D scaling, κ increases as the sample height decreases. However, fixed H/D scaling appears to have much less influence on κ. Reducing the scale down to 50% of the experimental height will increase κ by 10% and 50% for the fixed H/D and fixed D respectively.

XIII. Paired spheres have a consistently higher e_o than single spheres for squatted setups. For both single and paired spheres, the most significant increase in e_o occurs between a particle shear modulus, *G*=1E6 *Pa* and *G*=1E8 *Pa*. Between *G*=1E8 *Pa* and *G*=1E10 *Pa*, e_o does not appear to be influenced.

XIV. As the vertical stress applied during confined compression increases, the average sample vertical strain ε_v increases. It was shown, however, that the difference in ε_v when *G*=1E6 *Pa* to *G*=1E8 *Pa* is considerable larger than from *G*=1E8 *Pa* to *G*=1E10 *Pa*. Paired spheres show greater ε_v than single spheres for matching *G*. The plastic deformation observed for the paired spheres is typically double that of the single spheres (excluding *G*=1E6) and as the DEM code does not include an elasto-plastic contact model, this is a direct result of particles rearrangement.

XV. Based on the adjusted simulation time $t_{s,a}$ analysis, the use of simulations where *G* is smaller than 1E8 *Pa* are the most computationally efficient.

XVI. As expected, an increase in *G*, will see the bulk stiffness parameters decrease (stiffening). However, changing *G* from 1E9 *Pa* to 1E10 *Pa* has a less effect on the bulk stiffness parameters.

XVII. A linear relationship between the compression stress and the bulk stiffness gradients means that bulk stiffness parameters may be predicted using Equation 5.8, where *G* is the particle shear modulus in *Pa*, *C* and *n* are the constants which are derived from the best fit trendlines (see Table 5.6).

$$\lambda, \kappa = \frac{C}{G^n}$$ Equation 5.8

XVIII. The overall coefficient of variance of λ and κ for compression speeds from 0.1 *mm/min* to 720 *mm/min* is low (~2%). Therefore, for higher pressures (>10 *kPa*), it is not necessary to simulate at experimental speeds as the bulk stiffness parameters are not sensitive to compression rate. For very high compression rates (>1800 *mm*/*min*) a 20% Rayleigh time step may not be sufficient.

Chapter 6

Development of DEM model parameter optimisation procedure

6.1 Introduction

A great majority of DEM simulations are not validated against experiments and the model parameters are often assumed and not measured; so the influence of the model parameters on the prediction outcomes can be rather obscure (Chung 2006; Härtl 2008). In certain cases, when measured particle properties are used, validation studies have shown discrepancies between the experimental bulk behaviour and DEM simulation. There is a gap in the literature on how DEM parameters should be determined to produce quantitative DEM predictions. The aim of this thesis is to develop a robust methodology to determine optimised parameters that will predict accurate bulk behaviour in DEM simulations. The previous chapters have described various aspects of the optimisation procedure, including the development of bulk experiments, material characterisation and DEM parameters sensitivity studies.

This chapter describes two separate attempts to develop an optimisation procedure by assembling the outcomes in the previous chapters in a series of steps.

6.1.1 A preliminary validation study using measured DEM parameters

A preliminary validation study was conducted to compare the numerical and experimental results of the single and paired glass beads (GB) using the dynamic angle of repose ϕ_r (Figure 6.1) as a bulk response parameter. The DEM parameters used for the numerical simulations were particle properties measured from the laboratory tests described in section 3.3. This investigation was conducted to highlight any discrepancies between numerical and experimental results when measured particle properties were used.

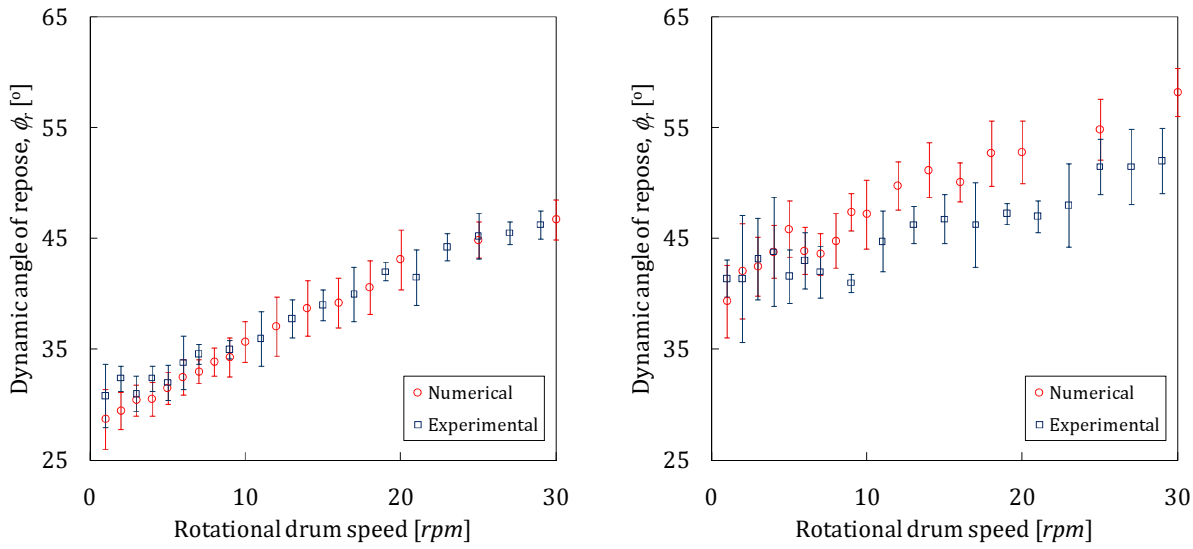

(a) Single glass beads (b) Paired glass beads

Figure 6.1 Numerical and experimental dynamic angle of repose comparison for single and paired glass beads in a rotating drum

Error bars represent ±1 standard deviation, sample size=10

It can be seen from Figure 6.1 that DEM predictions match the experimental results for single glass beads well for a full range of rotational drum speeds, with small discrepancies observed at lower *rpm*. However DEM predictions tend to overestimate the dynamic ϕ_r for

paired glass beads. The reason for the discrepancies are varied and include perfect numerical sphericity of particles that is not present in the experimental tests; this does however, highlight the need for a DEM parametric optimisation methodology that will systematically predict correct bulk behaviour.

6.1.2 DEM parameter optimisation methodology

The DEM parameters optimisation methodology developed for this study consists of three main steps:

1. Measure the experimental data that will be used to calibrate the DEM models;
2. Create the numerical dataset that will describe the influence of the DEM parameters;
3. Optimise the DEM parameters using step 1 and 2

A flow diagram of the optimisation procedure is shown in Figure 6.2. Steps 1 and 2 have been covered extensively in Chapters 2 to 4 and this chapter will focus on step 3.

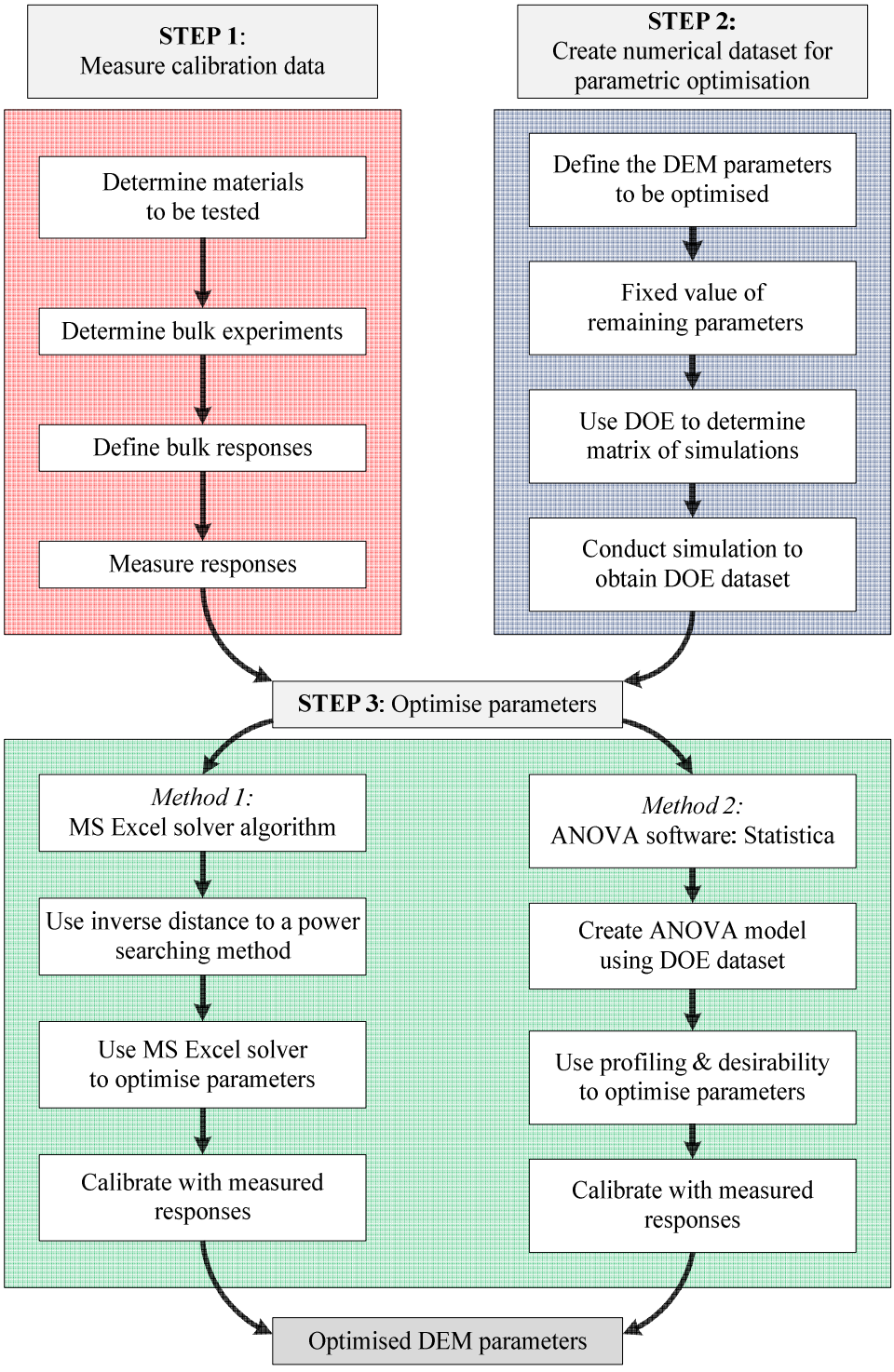

Figure 6.2 Flow diagram of the DEM parameter optimisation methodology

6.2 STEP 1: Measure the calibration data

The first step in the optimisation procedure is to acquire the data that will be used to calibrate the DEM model in the optimisation procedure. This can be achieved by:

1. Determining the material to be tested
2. Determining the bulk experiments to be used
3. Defining the bulk response parameters that will be measured from the experimental devices, and
4. Measuring the responses.

6.2.1 Determine the material to be tested

An appropriate sample of the material should be chosen to be used for calibrating the DEM models. When deciding which material to select, the granular materials that are predominately present in the industrial system which will eventually be modelled should be considered. In addition, it should be determined whether the material properties of the granular material used in the experiments are representative of those in the system that will eventually be modelled. For example, recently harvested grains may have higher water contents than laboratory samples. Higher waters contents will increase the moisture and mass of the grain and change bulk behaviour, especially in dynamic systems.

The optimisation procedure developed in this thesis was designed to be generic and applicable to a wide range of materials. To illustrate this, two organic and three inorganic materials were chosen. These were:

- Single glass beads (GB)
- Paired glass beads (GB)
- PET pellets (PP)
- Black eyed beans (BEB)
- Black kidney beans (BKB)

The single and paired GB were chosen as they are widely used in scientific research (Dury, Ristow et al. 1998; Chung 2006; Härtl 2008) and because their spherical shape makes numerical shape representation simpler. PP were chosen as an industrial material and is relatively

smaller in volume than the other materials. Finally, two organic materials with contrasting properties were chosen to illustrate agricultural handling scenarios; BEB and BKB. The BKB have a significantly larger aspect ratio a_r than the BEB but have a smoother surface. The various granular materials and their properties are described in section 3.3.

6.2.2 Determine the bulk experiments

The following step is to determine which bulk experiments will be used in the DEM model calibration. Choosing the appropriate bulk measurements to calibrate the DEM models is of paramount importance. When deciding which bulk experiment to use, the following should be considered:

- What industrial loading conditions does the granular material experience in the full scale system?
- Are the loading conditions in the bulk experiment representative of the industrial conditions?
- Will the bulk experiment produce repeatable bulk parameters that are relatively easily to measure?
- Will the bulk experiment produce sufficiently discriminating values from variations in material properties, so that the optimisation procedure is well posed to infer the DEM model parameters from these measurements?

Bearing these considerations in mind, the two laboratory devices chosen to be used in this thesis were: the rotating drum device and the confined compression test. These devices were chosen as they can produce bulk responses that are repeatable and easy to quantify, as well as produce discriminating results in numerical simulations when the DEM parameters are varied. The experimental devices are described in detail in section 3.2.

6.2.3 Define the bulk response parameters

Following the selection of the bulk experiments, the appropriate bulk response parameters to be measured must be defined. When deciding which bulk experiment to use, the following should be considered:

- Is the bulk response parameter highly repeatable and relatively easily to measure from the bulk experiment?
- What DEM parameter will eventually be optimised? For example, a response that is heavily influenced by the shear modulus *G* will produce a more accurately optimised value of *G*.
- Can more than one response be extracted from a single experiment?

The bulk response parameter chosen from the rotating drum device was the dynamic angle of repose, ϕ_r which is formed when the granular material is rotating at a speed of 7 *rpm*. The confined compression apparatus was used to determine the bulk stiffness of system by monitoring the change in void ratio from the stress applied during a loading and unloading cycle. The gradients of the loading and unloading curves λ and κ were the bulk response parameters used to calibrate the DEM models. The bulk response parameters are described in detail in section 3.2.

6.2.4 Measurement of bulk responses

Following the selection of the bulk response parameters, the experimental measurements should be acquired for each of the granular materials. A summary of the results for the materials and bulk response parameters used in this study are presented in Table 6.1.

The simulations that were employed to create the numerical dataset for the optimisation procedure used a scaled down system to reduce the computational time. However, the compression cylinder dimensional scaling investigation described in section 5.4.1 revealed that λ and κ are influenced by the scaling, therefore, the appropriate adjustments were applied to the bulk stiffness parameters when used to calibrate the DEM model.

Table 6.1 Summary of bulk experimental response parameters measurements used to calibrate the DEM models in the optimisation procedure

Material	Dynamic ϕ_r [°]		Confined compression bulk stiffness parameter					
	AVG	COV	Filling method	e_0	Loading λ		Unloading κ	
					AVG	COV	AVG	COV
Single glass beads	33.0	5.2%	AC	0.73	3.7E-03	2.2%	2.9E-03	3.1%
			RF	0.66	3.5E-03	2.6%	3.0E-03	2.5%
Paired glass beads	42.3	4.5%	AC	0.85	4.3E-03	10.9%	2.6E-03	2.7%
			RF	0.71	4.2E-03	11.6%	2.9E-03	3.3%
PET pellets	44.4	3.4%	AC	0.65	8.5E-03	5.0%	2.2E-03	2.9%
			RF	0.49	4.7E-03	4.3%	1.8E-03	1.7%
Black eyed beans	43.3	4.2%	AC	0.59	7.5E-03	0.5%	1.9E-03	1.3%
			RF	0.46	4.1E-03	4.5%	1.5E-03	2.3%
Black kidney beans	40.3	6.6%	AC	0.63	1.7E-02	1.7%	3.3E-03	2.3%
			RF	0.53	1.1E-02	1.8%	2.7E-03	1.9%

AVG: average, COV: coefficient of variance, AC: ascending cone, RF: rainfall filling, e_0: initial void ratio
Sample size for angle of repose=10, λ and κ=3
λ and κ are determined based on the change in void ratio due to applied vertical stress in *kPa*

6.3 STEP 2: Creating the numerical dataset for the parametric optimisation

The second step of the optimisation procedure is to create a numerical dataset that describes how the DEM parameters influence the numerical bulk response parameters. The creation of the dataset is achieved by:

1. Defining the DEM parameters to be optimised
2. Defining the values chosen for the remaining parameters
3. Using design of experiment (DOE) methods to determine the matrix of simulations to generate the numerical dataset
4. Conducting the simulations to create the dataset that will eventually be used in the parametric optimisation

6.3.1 Define DEM parameters to be optimised

Before defining which DEM parameters will be optimised, whether the parameter produces discriminating effects in the predicted bulk responses when varied and which parameters are important to the industrial systems that will eventually be modelled should be considered.

Determining which DEM input parameters will produce discriminating effects in bulk responses when varied, can be achieved through various methods. For the purposes of this study, this was achieved through parametric studies and knowledge from previous DEM studies. By altering individual and combinations of parameters, the bulk effects can be monitored and analysed. This method can be time intensive but assures a much deeper understanding of potential phenomena that can arise and their influence on the results. Other methods of identifying discriminating DEM parameters include sequential bifurcation which identifies important parameters whilst valuing parsimony (Bettonvil 1990; Bettonvil and Kleijnen 1997). In certain cases, a DEM parameter may have negligible effect on one bulk response but significant effects on another. In these cases, the DEM parameter should not be excluded.

When defining the bulk experiments and responses in step 1, the parameters that are important to the industrial systems that will eventually be modelled should be reviewed, so the parameters to optimise should ideally be known. For example, if the industrial scenario that will eventually be modelled is a granular compression system, a confined compression test would be a suitable bulk experiment to replicate the industrial loading conditions; and the bulk stiffness of the system under various loading conditions should be measured as a bulk response parameter. Furthermore, parametric studies have revealed that the particle shear modulus *G* significantly influences the bulk stiffness; therefore, *G* should be optimised.

As the particle to wall interactions are very specific to each industrial or scientific problem, the optimisation procedure focused on the inter-particle DEM parameters. In this study it was proposed to optimise the following four inter-particle mechanical properties;

- Particle to particle coefficient of sliding friction, μ_{pp}
- Particle to particle coefficient of restitution, e_r
- Particle to particle coefficient of rolling friction, $\mu_{r,pp}$
- Particle contact shear modulus, G

Preliminary studies revealed that e_r had minimal influence on dynamic angle of repose and the bulk stiffness parameters, primarily as the numerical systems modelled were quasi static and dominated by slow shearing. Therefore, e_r is included as an optimised parameter to illustrate the effect of including a non discriminating parameter.

6.3.2 Choosing values for the remaining parameters

After the selection of the optimised parameters, the values for the remaining parameters should be decided. In some instances, a parameter may produce discriminating effects but optimising it may not be desired. In this case an appropriate value must be chosen. For example, the particle to wall sliding friction μ_{pw} has a significant influence on the dynamic angle of repose ϕ_r, however as the thesis focused on inter-particle parameters, it will not be optimised. A systematic approach was proposed in section 5.3.5.1 using a pre-optimisation procedure to determine an appropriate value for μ_{pw}.

Although a DEM parameter does not produce discriminating effects in bulk responses when varied, it may still be of interest in the full scale models, and should therefore, not be ignored. For example, even though the particle mass has minimal effect on the dynamic ϕ_r, the optimised parameters may eventually be used in a system where force and momentum accuracy is required. In this case, the mass can either be fixed at the real value or scaled for the optimisation procedure and eventually changed back to the original value in the full scale simulation.

It has been suggested (Chung 2006;Härtl 2008) that an accurate geometrical representation of a granular material does not necessarily yield more accurate results, especially if the system modelled is static or quasi-static. Increasing the number of spheres to model a DEM particle will drastically increase the computational effort which may not be essential. The optimisation procedure was designed to be applicable to a wide range of granular material and a generic shape was used to model the various granular materials in this thesis.

Parametric scaling can be used to reduce the computational time but may affect the accuracy of the results. A cost-benefit analysis should be conducted to evaluate where the priorities lie and scale the parameters accordingly. The fixed values of the remaining parameters for this study are shown in Table 5.1. A detailed investigation describing the effects of parametric scaling on the bulk response parameters is presented in Chapter 5.

It is generally accepted that the bulk stiffness of a system is dependent on the initial porosity and packing condition of the system. It should be noted that when attempting to use the optimisation procedure for the confined compression test, the initial void ratio e_0 in the experiments should match the e_0 for the DEM runs in the dataset within 5%. Once the optimisation has been performed using the correct porosity, the optimised parameters may then be used for a range of void ratios.

Table 6.2 DEM implementation used in the simulations to create the numerical dataset

DEM Implementation	Value
PW coefficient of sliding friction, μ_{pw}	0.30
PW coefficient of restitution, $e_{r,pw}$	0.50
PW coefficient of rolling friction, $\mu_{r,pw}$	0.00
Poisson's ratio, υ	0.30
Particle density, ρ_s [kg/m^3]	1000
Number of equal spheres in a particle	2
Aspect ratio, a_r	1.20
Sphere radius [mm]	2.5
Number of particles in drum	1600
Scale of experimental drum	100%
Number of particles in confined compression cylinder	8800
Scale of experimental confined compression test	60%
Compression speed of each plate [mm/sec] [1]	3
Fixed % of Rayleigh time step	10%

PW: particle to wall interaction
[1] Two way compression

6.3.3 Use DOE to determine the matrix of simulation

Design of Experiment (DOE) is a methodical approach to investigate a system or process. Essentially a set of structured tests are carefully designed where the input variables are changed and the responses and effects of these changes on the pre-defined output are then assessed. DOE is an effective way to maximise the amount of information gained whilst reducing the amount of resources used. It is especially useful as it allows a judgment on the significance to the output of

input variable acting alone and allows for multiple variables acting in combination with one another.

The problem with conventional experimental methods of changing input parameter independently, then monitoring the magnitude of the response in each case (apart from the obvious time issue) is that various input parameters may rely on interaction or have interdependencies. In other words, some large responses may not occur when multiple input parameters are changed simultaneously. However, DOE plans for all possible dependencies in the first instance, and then prescribes exactly what data is needed to assess them. This is particularly useful as it will show whether the size of the response is based on a single or combination of input parameters. From this information, the exact length and size of the experiments are known before the testing begins.

Undertaking DOE procedure starts with identifying the input variables responses that are to be measured. For each input variable, a number of levels are defined that represent the range for which the effect of that variable is desired to be known.

The main goal in step 2 is to create a dataset that will describe how the DEM parameters affect the bulk responses. To determine the relationship between a single parameter and a bulk response is relatively simple: vary the parameter at desired levels between a predetermined low and high value and measure the response to produce a response curve. These low and high values are chosen based on a reasonable range for each parameter. The response curve can then be used to predict what value of DEM parameter is required to produce the desired bulk response. When the number of DEM parameters and bulk responses increases, the number of simulations required to produce all the possible combinations and permutations increases exponentially. For example, with 5 DEM parameters, each with 4 levels and 2 bulk responses, $2 \times 4^5 = 2048$ simulations would be required to produce the full matrix of simulations. For linear response curves, 2 levels are sufficient to describe the curve (low and high), however, Figure 6.3 illustrates the oversimplification in results when using 2 levels to describe a non-linear response curve. Non-linear response curves are typically seen in granular solids and a minimum of 3 levels are required (low, mid and high) to describe them adequately. Figure 6.3 (a) shows an example where 2 levels will underestimate the bulk response between the low and high values. In the case of Figure 6.3 (b), using 2 levels would show a minimal influence of the DEM

parameters on the bulk responses, however, 3 levels would reveal a very different response curve.

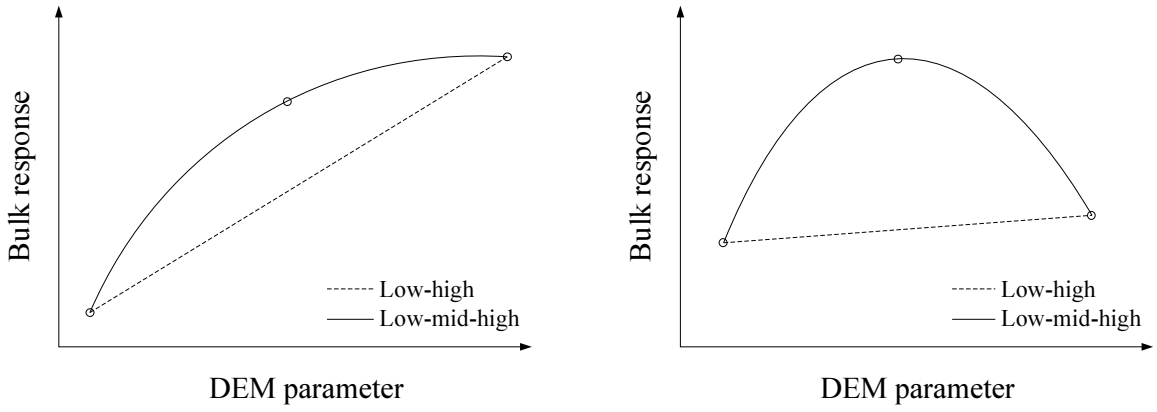

Example (a) Example (b)

Figure 6.3 A description of a non-linear response curve using 2 and 3 levels.

Running a full matrix of simulations with 3 levels is time intensive. For example, in this study, 4 DEM parameters with 3 levels using 3 bulk responses (NB: the bulk loading and unloading stiffness are extracted from the same confined compression test) were chosen, this would require $2 \times 3^4 = 162$ simulations. DOE can be used to reduce the number of simulations (and resolution of the dataset) and still produce a useful dataset using factorial design. The statistical package Statistica v9.0 (StatSoft 2009) was used for the experimental design in this study, more specifically, the $3^{(k-p)}$ Box-Behnken factorial design. The Box-Behnken design develops highly fractionalised designs to screen the maximum number of main effects in the least number of experimental runs (Box and Behnken 1960; Box and Draper 1987; Plackett and Burman 1946). These designs do not follow a simple design generating algorithm, but are constructed by combining two-level factorial design with incomplete block designs, and have complex confounding of interactions. The general mechanism of generating fractional factorial designs with 3 levels starts with a full factorial design, and then uses the interactions of the full design to construct new factors by making their factor levels identical to those for the respective interaction terms. An interaction effect may occurs when a relation between (at least) two variables is modified by (at least one) other variable. This ensures that the design remains balanced and minimises confounding between the main effects and lower-level interactions.

Using Box-Behnken factorial design, $2 \times 3^{4-1} = 54+2$ simulations were required to produce the numerical dataset. The two additional simulations are centre points run using all mid values, to account for any response curves that are similar to Figure 6.3 (b). The main advantage of adding extra centre points is that you can estimate pure error without having to replicate the entire design, while keeping the design balanced. This allows you to perform significance tests for all of the effects in the design and do a goodness of fit test. The mid level value does not necessarily have to be the geometric mid value between the high and low. To increase the accuracy of the dataset and subsequently the optimisation procedure, choosing a mid value that will produce 50% of the bulk response increase from low to high should be used. For example, from Figure 6.3 (b) we can see that increasing the DEM parameters by 40% will increase the bulk response by 50%; therefore, the DEM parameter mid value should be 40% of the DEM parameter range.

Based on the parametric study in Chapter 5, the low, mid and high values used in the DOE were chosen to be the values listed in Table 6.3. It should be noted that the optimisation procedure requires the same low, mid and high values to be consistent for all the bulk response parameters. For further details on performing experimental design using Statistica, refer to Appendix C.

Table 6.3 Low, mid and high levels used in the design of experiments (DOE) to produce the numerical dataset for the optimisation procedure

DEM input parameter	Low	Mid	High
PP sliding friction, μ_{pp}	0.1	0.3	0.6
PP restitution, e_r	0.1	0.5	0.9
PP rolling friction, $\mu_{r,pp}$	0.00	0.04	0.10
Particle shear modulus, G $[Pa]$	1E+6	1E+7	1E+9

6.3.4 Conduct simulation to obtain DOE dataset

After the partial factorial matrix of simulations has been determined, the various simulations were conducted to obtain the numerical bulk responses. With factorial experimental design, there may be a considerable number of runs and manually starting each simulation can be very time consuming and inefficient. The DEM software used in this thesis EDEM (DEM

Solutions Ltd 2009) allows simulations to be run in batch mode from its console. The input decks for each simulation must be set up before and EDEM's console will carry out the processing with the user specified parameters. For further information on EDEM batch mode console processing flags, refer to Appendix C.

The DEM input parameters that were not being optimised have been previously chosen (section 6.3.2) and these remained constant throughout the DOE. To ensure this, identical input files (except for the optimised parameters) were used. The rotating drum simulations were simpler to model and conducted as specified in section 5.2.2. However, the confined compression simulations posed a problem as the bulk stiffness parameters are sensitive to packing arrangement. Therefore, to establish a robust comparative analysis, a consistent packing arrangement for the confined compression simulations was necessary. A single file containing generated particles was used as the starting point of each confined compression simulation using the implementation method described in section 5.2.3 to establish an e_o similar to experimental values. The particles were generated using a mid shear modulus value of G=1E7 *Pa*. As G is one of the parameters to be optimised, it will invariably change and alter voidage in the system (see section 5.4.2.2 for more information). For example, reducing the shear modulus to 1E6 *Pa* will cause the particles in the confined compression cylinder to slump and vice versa. One possible solution to avoid the change in system volume is by removing gravity in the simulations as Chung (2006) implemented in his benchmark tests. The contact forces between the particles are based on the weight of the particles (ρg), and reducing the gravity to zero will essentially make the particles weightless. Changing the G with no gravity will therefore not cause the system to slump or expand to a new equilibrium. For the purposes of this thesis, the weight of the particles on the confined compression bottom platen was important for analysis and gravity was therefore left at 9.81 m/s^2.

It was found that the difference between the average numerical and experimental initial void ratio was 5.4% (0.53 and 0.56 respectively) and the coefficient of variance between the initial void ratios in the DOE dataset was 4.9 %. These differences were deemed satisfactory for the purposes of this study.

After all the simulations had been conducted, the bulk response parameters were extracted to produce the DOE dataset shown in Table 6.4 (see Appendix C for more details).

Table 6.4 Partial factorial dataset used for in the optimisation procedure

Run	DEM input parameters				Bulk response parameters		
	G	e_r	μ_{pp}	$\mu_{r,pp}$	ϕ_r	λ	κ
1	1E+06	0.1	0.1	0.00	31.1	1.34E-01	8.62E-02
2	1E+09	0.1	0.1	0.04	36.3	4.43E-03	1.29E-03
3	1E+07	0.1	0.1	0.10	38.9	5.84E-02	2.73E-02
4	1E+09	0.1	0.3	0.00	36.7	3.26E-03	1.37E-03
5	1E+07	0.1	0.3	0.04	43.4	6.77E-02	2.30E-02
6	1E+06	0.1	0.3	0.10	48.4	1.30E-01	9.60E-02
7	1E+07	0.1	0.6	0.00	38.7	6.92E-02	2.44E-02
8	1E+06	0.1	0.6	0.04	44.6	1.29E-01	9.74E-02
9	1E+09	0.1	0.6	0.10	49.0	2.72E-03	1.66E-03
10	1E+09	0.5	0.1	0.00	30.6	3.02E-03	1.42E-03
11	1E+07	0.5	0.1	0.04	35.8	2.83E-02	1.57E-02
12	1E+06	0.5	0.1	0.10	36.6	1.75E-01	7.71E-02
13	1E+07	0.5	0.3	0.00	37.7	2.45E-02	1.51E-02
14	1E+06	0.5	0.3	0.04	41.3	8.72E-02	4.83E-02
15	1E+09	0.5	0.3	0.10	48.7	5.76E-03	1.24E-03
16	1E+06	0.5	0.6	0.00	37.7	7.90E-02	5.97E-02
17	1E+09	0.5	0.6	0.04	43.7	4.10E-03	1.39E-03
18	1E+07	0.5	0.6	0.10	51.9	2.43E-02	1.79E-02
19	1E+07	0.9	0.1	0.00	30.6	2.70E-02	1.55E-02
20	1E+06	0.9	0.1	0.04	32.7	9.92E-02	5.14E-02
21	1E+09	0.9	0.1	0.10	36.1	4.33E-03	1.21E-03
22	1E+06	0.9	0.3	0.00	35.1	8.67E-02	4.84E-02
23	1E+09	0.9	0.3	0.04	42.7	3.65E-03	1.34E-03
24	1E+07	0.9	0.3	0.10	48.9	2.55E-02	1.53E-02
25	1E+09	0.9	0.6	0.00	40.0	2.75E-03	1.57E-03
26	1E+07	0.9	0.6	0.04	43.4	2.40E-02	1.76E-02
27	1E+06	0.9	0.6	0.10	50.9	8.02E-02	6.03E-02
28	1E+07	0.5	0.3	0.04	42.6	2.54E-02	1.51E-02

G:particle shear modulus, e_r: coefficient of restitution, μ_{pp}:particle to particle coefficient of sliding friction, $\mu_{r,pp}$: particle to particle coefficient of rolling friction, ϕ_r: dynamic angle of repose, λ:bulk loading stiffness, κ:bulk unloading stiffness

6.4 STEP 3: Parametric optimisation

After the creation of the numerical dataset and the measurement of the experimental calibration data, the final step is to determine the optimised DEM parameters (independent variables) that will produce a best match with the set of measured bulk response parameters for a real bulk solid. Searching or optimisation techniques can be used to find the optimised parameters and thereby produce a model that has been calibrated with experimental results. To conduct a comparative study, two searching techniques were used; the first is a simple method based on Microsoft Excel's Solver algorithm and the second is a robust method that involves the use of the commercial statistical analysis program Statistica.

This section will start by introducing the concept of optimisation followed by a comparative study of the two parametric optimisation methods.

6.4.1 Concept of optimisation

This section will discuss the concept of optimisation in the context of this study. A vector X_i is the set of DEM input parameters to be optimised, for example the coefficient of sliding friction, particle shear modulus, contact restitution, etc.

$$[X_i] = \begin{bmatrix} X_1 \\ X_2 \\ X_3 \end{bmatrix} \qquad \text{Equation 6.1}$$

A set of bulk calibration experiments should be conducted in which several bulk measurements are made to be used for the inverse solution and optimisation procedure. In this study, the rotating drum and the confined compression tests were used to measure the dynamic angle of repose ϕ_r and the bulk stiffness parameters. The vector B_i contains these measured bulk responses:

$$[B_i] = \begin{bmatrix} B_1 \\ B_2 \\ B_3 \end{bmatrix} \qquad \text{Equation 6.2}$$

A matrix of DEM simulations are conducted covering the appropriate range of values for the DEM input parameters X_i. The results of these simulations produce a series of response surfaces describing how the DEM parameters X_i influences the selected bulk responses. So we can express each predicted bulk response as a function of the DEM input parameters.

Assembled in matrix form, we get the vector of predicted bulk responses C_i, given by

$$[C_i] = [M][X_i] \quad \text{Equation 6.3}$$

Several methods such as multiple linear regression can be used to establish the matrix $[M]$. Multiple linear regression may not work as well where the parameters do not have linear relationship with the bulk response parameters. Other possible solutions include the use of a generalised additive model in the form of

$$y = sum(f_i x_i) \quad \text{Equation 6.4}$$

where f_i is an unspecified non-parametric function to be determined from either known causal relationships or estimated using a scatter plot smoother technique. This allows the function f_i to pick up possible non-linearities in the effects of DEM input parameters X_i.

An optimisation/searching technique is needed to find the optimum set of vector X_i, so as to minimise the differences between measured and predicted bulk response parameters. This may be given by the least squares error estimation between the predicted responses C_i and measured responses B_i, as given by the objective function

$$T = \sqrt{([B_i] - [C_i])^2} \quad \text{Equation 6.5}$$

The main purpose of the optimisation procedure is therefore to find the optimum X_i by minimising T.

6.4.2 A study of bulk friction as an example of optimisation

A simple regression procedure may be used to establish predictive correlations between bulk and particle properties. Härtl (2008) proposed an optimisation procedure to establish the influence of particle to particle sliding friction μ_{pp} on bulk internal friction $\mu_{pp,bulk}$ for particles with different aspect ratios a_r. For each a_r, a total of fourteen DEM simulations were carried out on a 143 *mm* diameter shear cell with a constant normal load of 25 *kPa*. Using these numerical results, a curve was fitted to the data points based on the Equation 6.6. Error minimisation techniques were used on the equations coefficients *A*, *B* and *C* to produce the trendline Equation 6.7.

$$y = \left(\frac{Ax + B}{x + C}\right) \qquad \text{Equation 6.6}$$

$$\mu_{pp,bulk} = \frac{(2.94 \cdot a_r - 2.09) \cdot \mu_{pp} + (0.33 \cdot a_r - 0.28)}{\mu_{pp} + (1.08 \cdot a_r - 0.82)} \qquad \text{Equation 6.7}$$

Superimposing Equation 6.7 over the numerical results produces the plot in Figure 6.4. It may be seen that this simple equation provides a good description of how the particle aspect ratio a_r and particle contact friction μ_{pp} combine to influence the resulting bulk internal friction, $\mu_{pp,bulk}$ in a densely packed granular assembly. At lower ranges of μ_{pp} (0.1-1.0) the trendline matches the numerical $\mu_{pp,bulk}$ closely, however at larger values of μ_{pp} discrepancies start to arise.

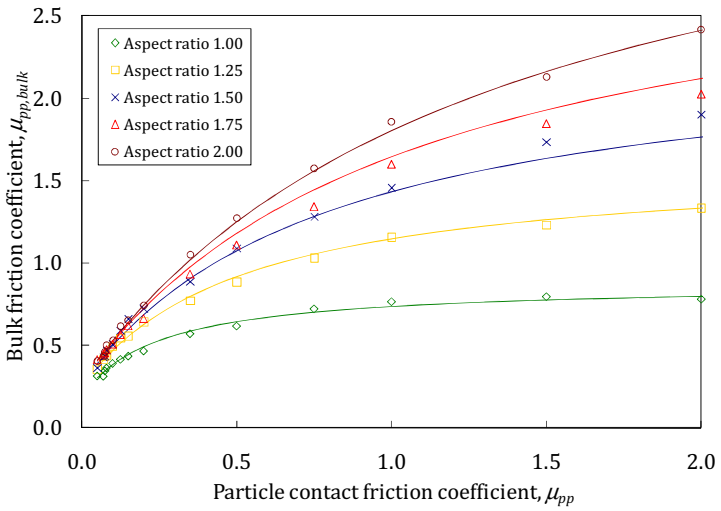

Figure 6.4 The influence of inter particle friction on the bulk friction for particles with different aspect ratios (after Härtl 2008)

This simple parametric optimisation is a useful and effective manner to illustrate the potential of optimisation techniques to calibrate DEM models for agricultural grains. However, as granular behaviour is complex in nature, optimising individual parameter independently may lead to oversimplifications. This section attempts to explore and establish the relationships for multiple parameters using two methods.

6.4.3 Development of model parameters optimisation techniques

Two optimisation techniques were attempted. The first is a simple method based on the Microsoft Excel Solver algorithm. The second is a more robust method that involves the use of the statistical analysis program Statistica (StatSoft 2009).

6.4.3.1 Method 1: Microsoft Excel Solver algorithm

The first method uses the inverse distance interpolation on a response surface represented by a set of multivariate scattered data points given by the numerical dataset and the Microsoft Excel Solver (MES) searching algorithm.

An Excel spreadsheet was developed to set out the optimisation procedure to evaluate the DEM input parameters required to produce the desired bulk responses. The searching technique adopted in this model was the inverse distance to a power method, where the influence of the

dataset on the optimised parameters is inversely proportional to the distance, given the following equations.

$$u(x) = \frac{\sum w(x)u}{\sum w(x)} \quad \text{Equation 6.8}$$

$$w(x) = \frac{1}{D(x)^p} \quad \text{Equation 6.9}$$

$$D = \sqrt{(x_2 - x_1)^2 + (y_2 - y_1)^2 + \cdots + (z_2 - \mathrm{z}_1)^2} \quad \text{Equation 6.10}$$

where u is the interpolated value, w is the weighting factor, p adjusts the sensitivity of the weighting, x is the given value, and D is the distance from x. An illustration of the inverse distance in a two dimensional plane is shown in Figure 6.5, where u_2 will have more influence on the x than u_3 but less than u_1.

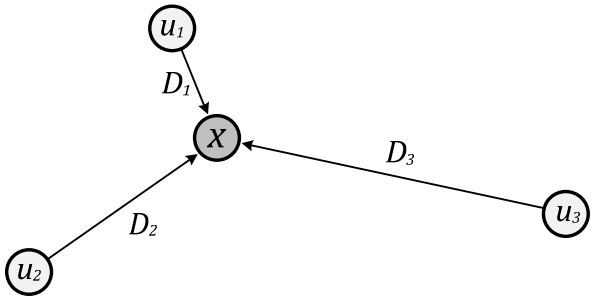

Figure 6.5 Illustration of inverse distance method used in the parametric optimisation

The graphical user interface (GUI) designed for the MES method is shown in Figure 6.6.

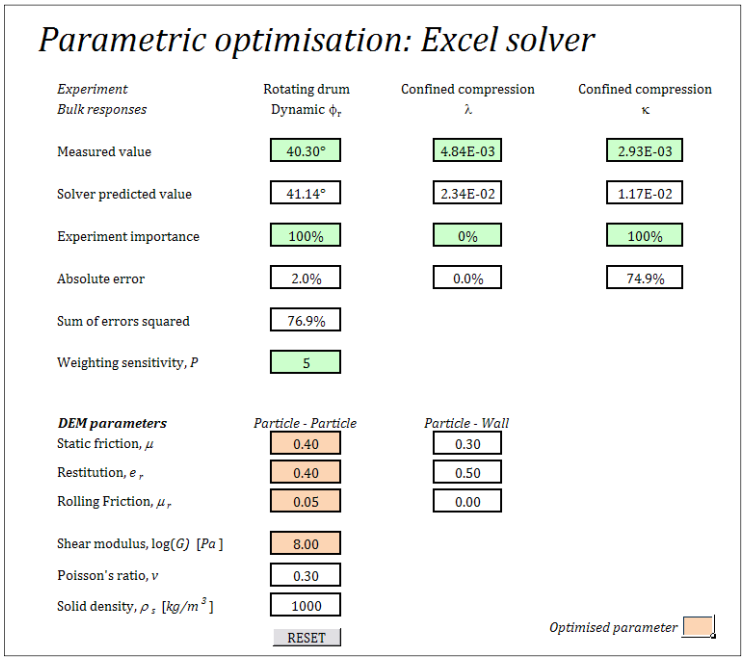

Figure 6.6 Graphical user interface designed for the Microsft Excel Solver method

The explanations of the terms found in the GUI are as follows:

- *Experiment* is the bulk experimental device used
- *Bulk response* is the response parameter measured from the experiment that will be used to calibrate the DEM model in the optimisation procedure
- *Measured value* is the experimental value measured from the bulk test.
- *Solver predicted value* is the bulk response parameter that the optimised set of parameters will predict using the inverse distance method.
- *Experiment desirability* can be incorporated into the optimised parameters if an experiment is of greater importance. This is achieved by increasing the experiment desirability which is directly linked to the 'error squared'.
- *Error squared* is the difference between the *Measured value* and *Solver predicted value* with the *Experimental desirability* factor applied
- *Sum of errors squared* is the total sum of errors squared from each of the bulk responses.

- *Weighting sensitivity p* is used to calibrate the sensitivity of the inverse distance method using Equation 6.9.
- *Optimised parameters* are the input parameters determined by the solver that will produce the smallest *sum of errors squared* value.
- *Reset* will return the optimised parameters back to mid range values.

Solver optimisation implementation

A sensitivity study on the effects of the various options and parameters of the MES algorithm on the optimised parameters are presented in Appendix C. From the results of the parametric sensitivity study, it was established that:

- The initial starting values of the optimised parameters are important. As a forward derivative method was used for searching (see section 2.7.1.4), using extreme range values as the starting value may point the searching algorithm in the wrong direction. Using mid range values as the starting point is therefore advised.
- Due to the low resolution of the numerical dataset (reduced factorial), optimising using 3 bulk responses without creating an ANOVA model occasionally returned irregular outcomes. It was therefore chosen to optimise the parameters based on two response parameters; the dynamic angle of repose ϕ_r and the unloading parameter κ.
- Another drawback of the reduced factorial dataset is the increased distances between data points. To increase the influence of each dataset point, a weighing factor p=5 was used. Further research could investigate the expansion of the dataset by generating additional points based on the original data.

The Excel Solver implementation of the optimisation procedure can be found in Table 6.5. For further information on the various options and their significance see Appendix C.

Table 6.5 Excel Solver option implementation for the optimisation procedure

Option	*value*
Max time [*sec*]	32000
Iterations	32000
Precision	1E-06
Tolerance	1%
Convergence	0.0001
Estimates	Quadratic
Derivatives	Forward
Search algorithm	Newton

6.4.4 Method 2: ANOVA software, Statistica

The second parametric optimisation method used the statistical software Statistica. This software was chosen as it included a design of experiment (DOE) and experiment analysis section. The parametric optimisation using Statistica was carried out in two parts; first an ANOVA model was created based on the numerical dataset and second, the optimised parameters were determined using profiling and desirability.

6.4.4.1 Creating the ANOVA Model used in the optimisation procedure

Analysis of variance (ANOVA) is used to test for significant differences between means by comparing variances. More specifically, by partitioning the total variation into different sources, it is possible to compare the variance due to the between-groups variability with the variance due to the within-group variability.

The determination of the optimised parameters will depend on the ANOVA model used, and an appropriate model should be determined which will characterise the bulk responses most accurately. The following section describes various considerations to account for when creating the ANOVA model

Data transformation

The various DEM parameters (independent variables) may have contrasting ranges of data. For example, the coefficient of sliding friction ranges from 0.1 to 0.6 whereas the particle shear modulus *G* ranges from 1E6 *Pa* to 1E9 *Pa*. Although Statistica uses standardisation techniques to limit the influences of range, the greater range of *G* values may influence the ANOVA model and create a bias in the optimisation. In these cases, a transformation may be required.

The simplest method of managing the contrast is by applying a transformation function to the data, run the optimisation procedure and then apply the inverse of the transformation function to the results as shown in Figure 6.7. In this example, the transformation function was $log_{10}(x)$ to change to range of shear modulus from 1E6-1E9 *to* 6-10.

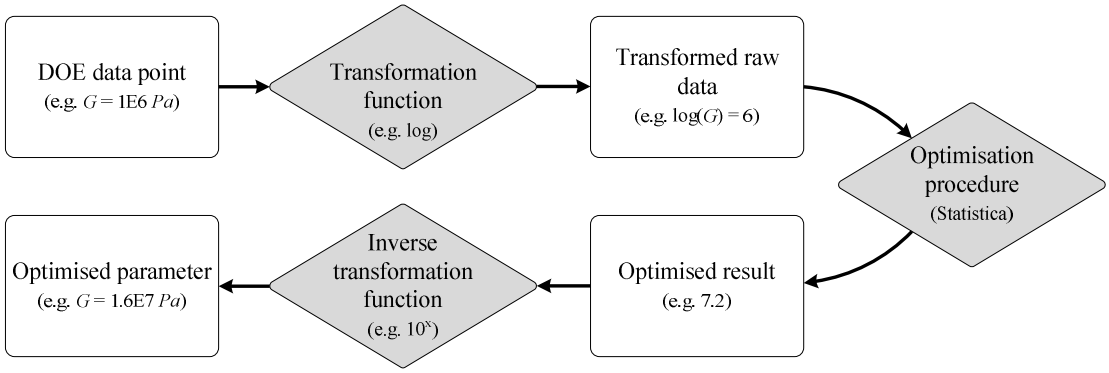

Figure 6.7 Flow chart of the data transformation procedure

In certain cases a polynomial equation may not be accurate enough to describe a response curve, in which case, other transformation may be used, including generalised linear models (GLM) (McCulloch and Nelder 1983). GLM generalises regression by establishing a relationship between a linear model and response variables using a transformation function. The advantage of using a linear model would mean that the response curve could be described using 2 data points (high and low), the disadvantage being the additional complexity included in the optimisation procedure. The majority of the responses curves in this study can accurately be described using second order polynomials and therefore GLM methods were not explored.

ANOVA model and regression coefficients

Once the data has been transformed, a multiple regression is performed on the dataset to determine the regression coefficient for the various parameters. These are computed for the various bulk response parameters to determine a model with one set of regression coefficient applicable to all the bulk response parameters. Any non-linearity of the response curves is accounted for by including linear (L) and quadratic (Q) coefficient for each parameter. When the quadratic coefficient is close to zero, the response curve is linear, and the quadratic coefficient should be ignored from the model. The coefficient of determination R^2 is an indication of the correlation of an ANOVA model with the dataset ranging from 0 to 1, where 1 is a perfect correlation in which predictions based on the model will be more accurate. To achieve a R^2 value close to 1, several methods may be used. These include:

- *Ignoring some effects*: some parameters may have minimal effect on the bulk response parameters (e.g. quadratic coefficient of the restitution coefficient on the dynamic repose angle ϕ_r as seen in Figure 6.8, a) and may be ignored from the model to increase the R^2 value. It should be noted that some parameters may have minimal influence on one bulk response but significant influence on another. In this case, ignoring the parameter will decrease the correlation for that bulk response parameter. In the present study, however, no effects were ignored.
- *Two*-way *interaction*: In some instances, individual parameters independently may have less effect on bulk responses than the interaction of the two. Park and Ahn (2004) investigated the use of two-way interactions in design of experiments in addition to simply considering the main factors individually and found an increase in accuracy to predict optimised parameters. In this study, it was found that including a linear coefficient two-way interaction of the parameters increased the correlation and was therefore included.

Pareto chart analysis

Pareto principle states that in many events, a majority of the effects are a result of a minority of the causes. In the context of the optimisation procedure, a few DEM input parameters will be responsible for a majority of the changes in bulk response parameters. A Pareto chart of effects can be plotted in Statistica and shows the effect estimates sorted by their

absolute size. The Pareto chart is useful for reviewing a large number of factors and is an effective manner of quickly determining the main effects that influence the system. Figure 6.8 shows the Pareto chart of effects using standardised effect estimates for the various bulk responses. The statistical significance parameter α_s was set to 5% (highlighted in the Pareto charts by the red dotted line) to indicate any effects that were deemed statistically insignificant. However, due to the inherent variability of granular materials, a α_s between 5% and 10% is acceptable.

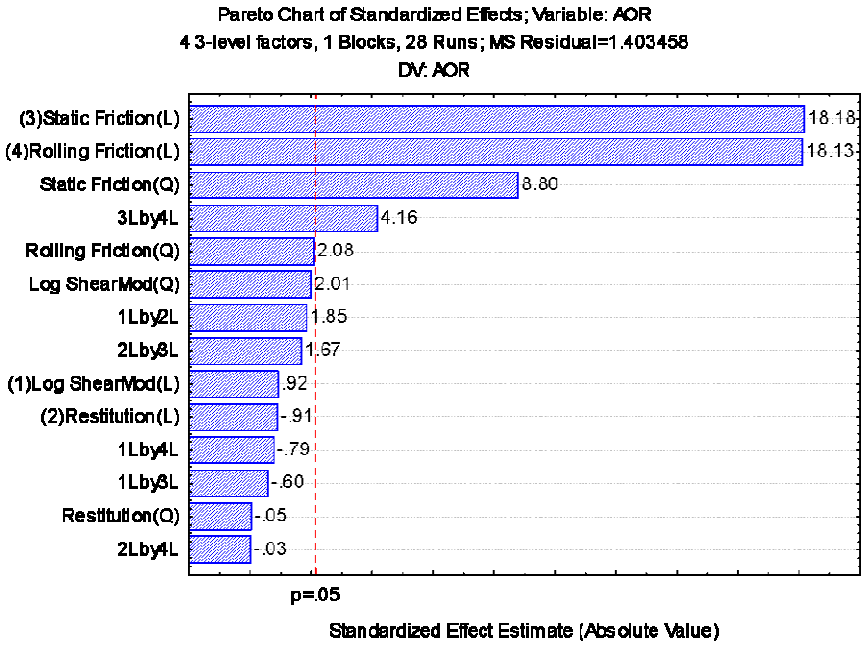

(a) Dynamic angle of repose (R^2 = 0.98)

Figure 6.8 Pareto chart of effects using standardised effects estimates for the various bulk response parameters using the numerical dataset (determined using Statistica)

(L):linear coefficient, (Q):quadratic coefficient, xLbyxL:two way interaction between linear coefficients

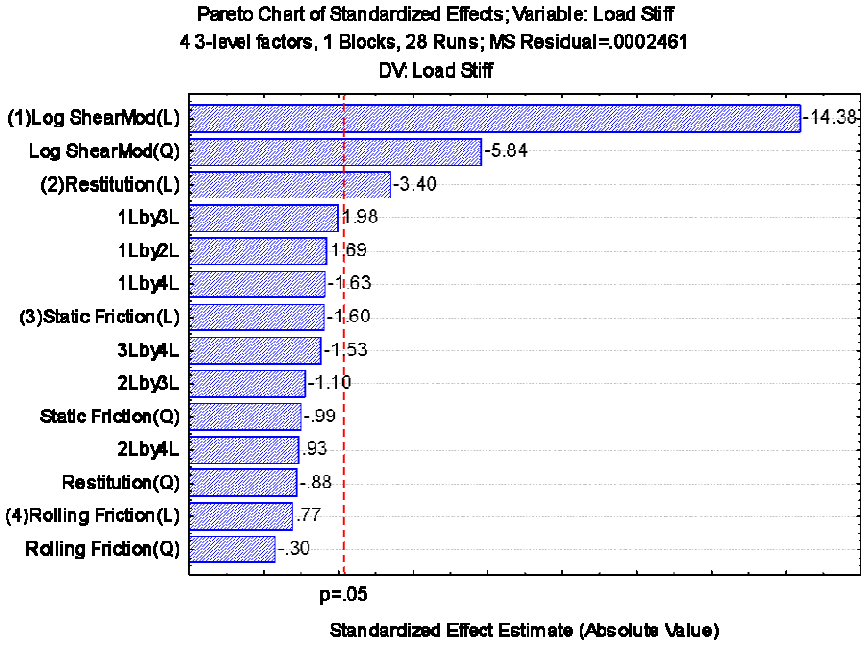

(b) loading stiffness parameter, λ (R^2 = 0.95)

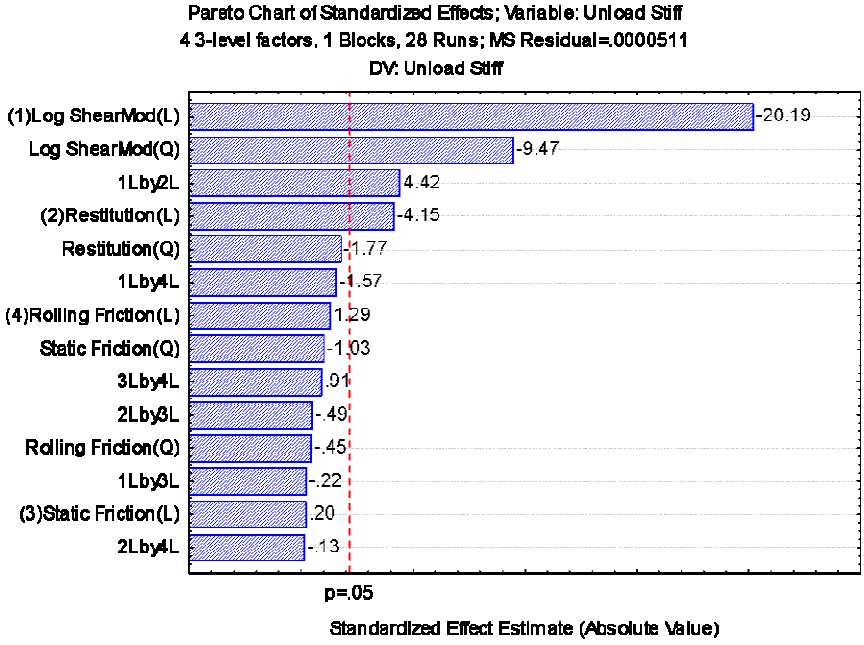

(c) Unloading stiffness parameters, κ (R^2 = 0.97)

Figure 6.8 Pareto chart of effects using standardised effects estimates for the various bulk response parameters using the numerical dataset (determined using Statistica)

(L):linear coefficient, (Q):quadratic coefficient, xLbyxL:two way interaction between linear coefficients

As expected, (Figure 6.8, a) shows that the significant effect on the dynamic ϕ_r comes from the linear and quadratic coefficients of the static μ_{pp} and rolling $\mu_{r,pp}$ friction, where the linear coefficient have significantly more influence than the quadratic coefficients. The Pareto chart of effects also highlights the significant influence of the two-way interaction between μ_{pp} and $\mu_{r,pp}$. In addition, the particle shear modulus *G* and the coefficient of restitution e_r have minimal influence on the dynamic ϕ_r.

As expected, the bulk stiffness parameters λ and κ are predominantly influenced by the particle shear modulus *G* (linear and quadratic coefficients). Surprisingly, the linear coefficient of e_r has an influence on λ and κ. As the system is quasi-static and e_r was not expected to play a significant role, so this is not easily explicable. The damping ratio β_d is directly influenced by e_r (Equation 2.11) when particles are in movement. One possible explanation would suggest that there is particle movement during the loading and unloading of the sample. In addition, μ_{pp} and $\mu_{r,pp}$ appear to have minimal effect on the bulk stiffness parameters. Although, it should be noted that as these are standardised effects, μ_{pp} and $\mu_{r,pp}$ may have effects on the bulk parameters but are proportionally smaller compared to *G*.

6.4.4.2 Parametric optimisation using predicted response and response desirability

Following the creation of the ANOVA model, profiling using the *response desirability* function in Statistica is used to obtain the optimised parameters. Response and desirability profiling allows the inspection of the response surface produced by fitting the observed responses using a model based on levels of the DEM parameters. The profiler will enable the inspection of the predicted values for the bulk response parameters at different combinations of levels of the DEM parameters, specifying the desirability function for each of the bulk responses and searching for the levels of the DEM parameters that produce the closest match with the measured bulk response parameters. The experimentally measured values of the bulk responses (Dynamic ϕ_r, λ and κ) are used to calibrate the response surface. The desirability function can be used to constrain some of the parameters in the optimisation, so that the optimisation procedure does not return unrealistic values (for example $\mu_{pp} < 0$).

Statistica optimisation implementation

A parametric sensitivity analysis on the effects of the various options available in the *Profiling and Desirability* function was first conducted on a set of fabricated results to determine to most appropriate setup to use for the optimisation procedure and is presented in Appendix C. From the sensitivity study results, it was determined that:

- There are two main searching methods in Statistica, the *general function optimisation* and *optimum desirability at exact grid points*. As the *general function optimisation* does not constrain the optimised values at exact points (which were not necessary for the purposes of this thesis) the computational time will decrease and profiling curve will be less restricted, therefore this method was used. The searching algorithm used to determine the optimised parameters is based on the simplex method of function optimization (O'Neill 1971; Nelder and Mead 1965) which uses a nonlinear estimation algorithm that does not rely on the computation or estimation of the derivatives of the loss function. Instead, at each iteration the function will be evaluated at m+1 points in the m dimensional parameter space.
- The searching method is not confined to exact grid points, therefore, a reasonable *number of steps* (data points along the profile surface) should be chosen. A total of 20 steps were used in this study.
- Statistica allows for up to three "inflection points" in the *desirability function* for predicted values of the bulk responses. Using the *s&t curvature* parameters, a value for the exponent of the desirability function may be specified, representing the curvature in the desirability function between the low and medium inflection points of the function and between the medium and high inflection points of the function respectively (Figure 6.9, c). It was determined that using a desirability of 1 for the central inflection point produced more accurate results (Figure 6.9, a) and narrowing the range of the inflection point constrained the optimisation and lead to greater errors (Figure 6.9, b). In addition, the *s&t curvature* parameters showed negligible effect on the results (Figure 6.9, c). Therefore the range of the inflection points matched the range of the dataset and the *s&t curvature* was left to a default value of 1.

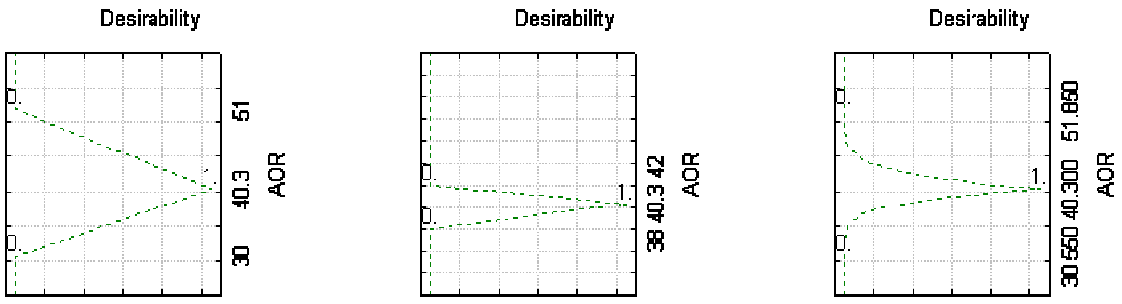

(a) Central inflection point (b) Reduced range (c) *s*&*t* parameters = 5

Figure 6.9 Illustration of the desirability function in Statistica for the dynamic angle of repose

- Finally, the current levels of the predictor variables for the prediction profile compound graph can be set using the *Set factor at* option. These can either be set to the *mean value*, *user specified* or *at optimum value*. The last option will determine the optimum value that will suit the other option's criteria. The *at optimum value* was found to produce the most accurate answers with regards to the optimisation procedure as this option did not constrain the searching method.

6.5 Optimised DEM parameters

Following the creation of the ANOVA model based on the numerical dataset, the *profiling and desirability* function in Statistica was used to determine a set of optimised parameters for each granular material based on their experimental measurements.

6.5.1 Results and discussion

The optimised parameters for the single and paired GB, PP, BEB and BKB can be found in Table 6.6 and Table 6.7 using the Microsoft Excel Solver (MES) and Statistica method respectively.

Due to the resolution of the partial factorial numerical dataset, the optimisation of the parameters using the MES method was carried out excluding the bulk loading stiffness λ. It can be seen from Table 6.6 the error between the experimental results and the solver predicted results are minimal in most cases (<1%) excluding single GB. The reason for this is because the dynamic ϕ_r (33^o) lies in the lower ranges of the dataset, and the other materials (cases 3-10) lie within the middle of the dataset. This highlights the searching method's difficulty when optimising values around the extremities of the dataset range. In addition, the sliding friction, μ_{pp} in many of the cases is at the extreme low or high (0.1 or 0.6). This is due to the MES computational technique which uses iterative numerical methods that involve "plugging in" trial values, Excel Solver performs analyses of the responses and their rates of change as the parameters are varied, to guide the selection of new trial values, until the responses approaches the desired value or a defined constraint is met, for example $0.1<\mu_{pp}<0.6$ (see section 2.7.1.4). As μ_{pp} has significant influence on the dynamic ϕ_r, the Solver will monitor a greater response when altering this parameter and therefore focus on this parameter. It can be seen that many of the optimised parameters are similar to the levels of the data set (e.g. μ_{pp}= 0.1, 0.3, 0.6). This is because of the numerical dataset resolution combined with the high weighting factor, p.

For almost all the granular materials, excluding the BEB (case 7-8), this optimisation procedure does not discriminate between the loose and dense filling methods. This is primarily because the filling method affects λ which is not taken into account in the optimisation, and the unloading parameter κ is similar for the two filling methods.

Table 6.6 Parametric optimisation using Excel Solver for various granular materials and filling methods

Case	1	2	3	4	5	6	7	8	9	10
Experimental results										
Material	Single GB	Single GB	Paired GB	Paired GB	PP	PP	BEB	BEB	BKB	BKB
AVG dynamic ϕ_r	33.0	33.0	42.3	42.3	44.4	44.4	43.3	43.3	40.3	40.3
Filling method	AC	RF	AC	RF	AC	RF	AC	RF	AC	RF
AVG Unloading stiffness, κ [1]	3.2E-03	3.3E-03	2.9E-03	3.2E-03	2.4E-03	2.0E-03	2.1E-03	1.7E-03	3.6E-03	2.9E-03
Optimised parameters										
Shear modulus, G [Pa]	1.9E+08	1.9E+08	2.0E+08	1.9E+08	2.4E+08	2.6E+08	2.6E+08	3.2E+08	1.8E+08	2.0E+08
Coeff of restitution, e_r	0.15	0.18	0.36	0.29	0.11	0.21	0.10	0.40	0.33	0.28
Coeff of sliding friction, μ_{pp}	0.10	0.10	0.59	0.60	0.60	0.60	0.60	0.60	0.26	0.28
Coeff of rolling friction, $\mu_{r,pp}$	0.00	0.00	0.10	0.08	0.10	0.10	0.10	0.10	0.03	0.02
Predicted bulk response										
Dynamic ϕ_r	39.16	39.2	42.3	42.3	42.8	43.01	43.16	43.2	40.3	40.3
Error	18.7%	18.8%	0.0%	0.0%	-3.6%	-3.1%	-0.3%	-0.2%	0.0%	0.0%
Unloading stiffness, κ	3.2E-03	3.3E-03	2.9E-03	3.2E-03	2.4E-03	2.1E-03	2.1E-03	1.7E-03	3.6E-03	2.9E-03
Error	-0.1%	0.1%	-0.1%	0.0%	0.1%	8.3%	-0.1%	-0.2%	0.1%	0.1%

[1] Bulk stiffness parameters have been adjusted to account for scaling
AVG: average, GB: glass beads, PP: PET pellets, BEB: black eyed bean, BKB: Black kidney beans, AC: ascending cone filling, RF: rainfall filling
Error represent the % difference between the experimental and predicted bulk response parameter

Table 6.7 Parametric optimisation using Statistica for various granular materials and filling methods

Case	1	2	3	4	5	6	7	8	9	10
Experimental results										
Material	Single GB	Single GB	Paired GB	Paired GB	PP	PP	BEB	BEB	BKB	BKB
AVG dynamic ϕ_r	33.0	33.0	42.3	42.3	44.4	44.4	43.3	43.3	40.3	40.3
Filling method	AC	RF	AC	RF	AC	RF	AC	RF	AC	RF
AVG loading stiffness, λ [1]	4.1E-03	3.9E-03	4.8E-03	4.6E-03	9.5E-03	5.3E-03	8.4E-03	4.6E-03	1.9E-02	1.2E-02
AVG Unloading stiffness, κ [1]	3.2E-03	3.3E-03	2.9E-03	3.2E-03	2.4E-03	2.0E-03	2.1E-03	1.7E-03	3.6E-03	2.9E-03
Optimised parameters										
Shear modulus, G [Pa]	1.9E+07	4.5E+07	2.5E+07	2.2E+07	5.6E+07	7.0E+07	6.9E+07	7.3E+07	2.4E+07	3.9E+07
Coef. of restitution, e_r	0.87	0.27	0.37	0.41	0.10	0.10	0.10	0.10	0.33	0.22
Coef. of sliding friction, μ_{pp}	0.15	0.10	0.32	0.32	0.31	0.28	0.25	0.25	0.42	0.27
Coef. of rolling friction, $\mu_{r,pp}$	0.00	0.00	0.03	0.03	0.05	0.05	0.05	0.05	0.00	0.02
Predicted bulk response										
Dynamic ϕ_r	33	33	42.3	42.3	44.4	44.4	43.3	43.3	40.3	40.3
Error	0.0%	0.0%	0.0%	0.0%	0.0%	0.0%	0.0%	0.0%	0.0%	0.0%
loading stiffness, λ	8.9E-02	1.3E-01	1.4E-02	1.5E-02	1.4E-02	1.2E-01	1.3E-02	1.2E-02	1.9E-02	1.5E-02
Error	2074%	3155%	199%	215%	43%	2234%	55%	168%	0%	28%
Unloading stiffness, κ	3.2E-03	3.3E-03	2.9E-03	3.2E-03	2.4E-03	2.0E-03	2.1E-03	1.7E-03	4.3E-03	2.9E-03
Error	-0.1%	0.1%	-0.1%	-0.1%	0.1%	0.1%	-0.2%	-0.2%	20.3%	0.2%

[1] Bulk stiffness parameters have been adjusted to account for dimensional scaling
AVG: average, GB: glass beads, PP: PET pellets, BEB: black eyed bean, BKB: Black kidney beans, AC: ascending cone filling, RF: rainfall filling
Error represent the % difference between the experimental and predicted bulk response parameter

The optimisation using Statistica, optimised the DEM parameters based on the dynamic ϕ_r, λ and κ. From Table 6.7 it may be observed that the errors between the experimental bulk responses and the Statistica predicted bulk response parameters are negligible with respect to the dynamic ϕ_r and κ (<1%); however they are significant for λ (0-3000%). This can be attributed to two main reasons; the experimental values of λ lies at the extremity of the dataset (illustrated in Figure 6.10), and secondly, the lack of plasticity in the DEM contact model makes matching up λ difficult, which involves plastic deformation at particle contacts (see section 2.2.2.2). When the value of the experimental parameters lies near the extremities of the DOE dataset, the inflection points in the desirability curve lie close to each other and profiling may be more prone to irregular results.

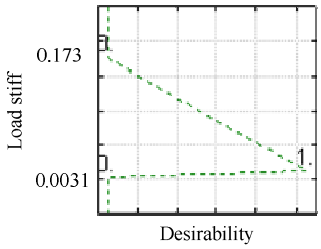

Figure 6.10 Typical Desirability plot for the unloading stiffness, λ using the DOE dataset

In addition, the lack of plasticity in the contact model results in the λ component of the numerical dataset having a trend dictated by the particle relative motion and contact elasticity (influenced primarily by the particle shear modulus *G*) but not the contact plasticity. The parameter κ, however, is dictated by the system's ability to rebound under unloading. Essentially, *G* is optimised using two bulk response parameters with contrasting trends. In addition, the Pareto chart of effects reveals that *G* has a greater influence on κ than on λ and is why the optimisation favours κ (lower experimental to predicted error) than λ. In the case of the black kidney beans filled with the ascending cone (case 9), the profiling favours λ over κ (0% to 20% error respectively) as the value lies within the mid range of the dataset and a better correlation can be achieved.

From the Pareto chart of effects (Figure 6.8) we can see two distinct sets of effects; the dynamic repose angle ϕ_r influenced primarily by the frictional parameters (μ_{pp} and $\mu_{r,pp}$) and

the bulk stiffness, λ and κ influenced primarily by the particles shear modulus *G*, which is reflected in the optimised parameters. In most cases, (excluding the black kidney beans) the optimised parameters for different filling methods have similar values of μ_{pp} and $\mu_{r,pp}$, as calibration measurement of the dynamic ϕ_r is the same. The optimised parameters differ only in *G*, related to bulk stiffness which is influenced by the filling methods. As *G* was shown to have a minimal effect on the dynamic ϕ_r, it is assumed that the numerical predictions of the dynamic ϕ_r will be similar for a pair of optimised parameters from a granular material (e.g. cases 7 and 8 will produce similar predictions of the dynamic ϕ_r).

6.5.2 Limitations and sources of errors

The two optimisation methods have shown useful results and predictions of bulk behaviour in granular systems. When applying these methods, several limitations and sources of errors should be considered.

6.5.2.1 MS Excel Solver

The MES method has been shown to be a simple and efficient method of parametric optimisation, however, several limitations of this method include:

- The use of design of experiment (DOE) methods has the advantage of reducing the number of experiments to conduct; however the resolution of the data will decrease accordingly. For inverse distance methods, an appropriate scatter of data points is essential. When the number of DEM parameters and bulk response parameters are low, a full factorial matrix of simulations should be conducted. One possible solution could investigate the expansion of the dataset by generating additional data points based on the original data using interpolations method. This will increase the accuracy of the searching method.
- MES performs analyses of the responses and their rates of change, since the parameters are varied, to guide the selection until the responses approach the desired values or a defined constraint is met. However, parameters are optimised one at a time and focus is placed on parameters with the greatest influence, which may in some cases have negative influences. The error can be reduced by increasing the resolution of the dataset.

- Due to numerical dataset resolution, the parametric optimisation using more than 2 bulk response parameters produced irregular behaviour. To account for the low resolution, the weighting factor *p* was increased to 5. In this case, the optimised parameters will be biased towards the exact dataset values.

6.5.2.2 Statistica

The Statistica based parametric optimisation method was shown to be a robust and stable method; however, several limitations of this method include:

- One possible limitation of the ANOVA model in Statistica is that a single model is used to describe the response surface for each bulk response parameter; therefore compromises and biases are made. The model may have a good correlation with one bulk response but not another. The model used in this chapter did in fact have a good match for all of the bulk responses ($R^2 > 0.95$), however in situations where this is not the case, a separate ANOVA model for each response may be necessary and adjustments to the optimisation may need to be carried out accordingly.
- Basing assumptions solely on statistical analysis may be misleading, as the ANOVA results may be specific to the numerical simulations and not transferable to full scale systems. Sequential bifurcation and Pareto analysis determines which parameters have statistically significant influence on the bulk response parameters using the numerical dataset, however, it does not take into account any unpredictable behaviour or errors that arise due to numerical phenomenon. Although time consuming, parametric investigation are useful to form a deeper understanding of what influences the bulk behaviour and why.

6.5.2.3 General limitations

Some general limitations to the methodology include:

- Additional bulk response parameters may be relatively easily added to the numerical dataset by running a set of simulations using the same combination of parameters as the previous DOE (e.g. Table 6.4). However, the addition of extra DEM parameters requires an entirely new DOE dataset to be created.

- For both optimisation methods, the range of the dataset is crucial. The experimental value used to calibrate the models should lie in the mid range of the numerical dataset. For example, this study aimed to develop a generic optimisation procedure for a range of granular materials and therefore used particle shear modulus range from 1E6-1E9 *Pa*. However, this range should be adjusted to suit the type of material tested; for example, glass beads should use a range of G = 1E8-1E10 *Pa*.

6.6 Summary

This chapter has described the development of a DEM model parameter optimisation methodology. The procedure consists of three steps;

1. The measurements of the data that will be used to calibrate the DEM models;
2. The creation of the numerical dataset that will describe how the DEM parameters influence the bulk behaviour;
3. The optimisation of the DEM parameters using the results from Step 1 and 2

To conduct a comparative study, two searching methods were used in the optimisation procedure; the first was a simple method based on Microsoft Excel's Solver algorithm coupled with an inverse distance weighing. The second was a robust method which involved the use of the statistical analysis program Statistica. It was shown that the Excel Solver algorithm required less time to determine the optimised parameters, but was limited by the resolution of the numerical dataset and could only perform an accurate parametric optimisation based on two bulk response parameters (dynamic ϕ_r and κ). Alternatively, Statistica was able to produce a set of DEM parameters that were optimised using the three bulk responses. In addition, recommendations and considerations for each step have been proposed.

Chapter 7

Verification and validation of the model calibration methodology

7.1 Introduction

Chapter 6 provided a detailed description and analysis of the DEM model parameter optimisation methodology. Experimental bulk responses were measured and used to calibrate DEM models based on numerical dataset. The result was a set of optimised DEM parameters that were expected to predict the bulk responses for various granular materials. However, a verification and validation is required to determine the robustness of the optimisation procedure.

This chapter will verify and validate the set of optimised parameters for black eyed bean (BEB). A verification was conducted by simulating the two calibration experiments using the optimised parameters and comparing them with the experiments. In addition, a validation was performed by predicting the bulk response in a large scale system. The optimised parameters determined with the Statistica and Microsoft Excel Solver algorithm for different filling methods can be found in Table 7.1.

Table 7.1 Optimised parameters of black eyed beans used in the verification and validation study

Optimised parameters	Case 1	Case 2	Case 3	Case 4
Optimisation algorithm	Solver	Solver	Statistica	Statistica
Filling method	AC	RF	AC	RF
Shear modulus, G [Pa]	2.6E+08	3.2E+08	6.9E+07	7.3E+07
Coefficient of restitution, e_r	0.10	0.40	0.10	0.10
Coefficient of sliding friction, μ_{pp}	0.60	0.60	0.25	0.25
Coefficient of rolling friction, $\mu_{r,pp}$	0.10	0.10	0.05	0.05

AC: ascending cone, RF: rainfall

7.2 Optimised DEM parameter verification

The first step in the verification and validation study is to verify whether the optimised parameters do in fact produce the bulk responses predicted by the optimisation procedure and how closely they match the measured experimental results. This was achieved by rerunning the calibration experiments using the optimised parameters. To establish a robust comparison, the DEM implementation remained consistent with the numerical dataset, except for the optimised parameters.

7.2.1 Results and analysis

The discrepancies between the measure experimental and the numerical bulk responses using the four sets of optimised parameters are shown in Table 7.2.

Table 7.2 Comparison between measured bulk responses and numerical bulk responses of simulations using the optimised parameters

Optimised parameters	Case 1	Case 2	Case 3	Case 4
Optimisation algorithm	Solver	Solver	Statistica	Statistica
Filling method	AC	RF	AC	RF
Dynamic angle of repose, ϕ_r				
Experimental [1]	43.3	43.3	43.3	43.3
Verification	49.1	48.8	43.1	43.4
Error	-11.8%	-11.2%	0.6%	-0.3%
Loading stiffness, λ				
Experimental	8.4E-03	4.6E-03	8.4E-03	4.6E-03
Verification	7.9E-03	9.0E-03	4.4E-03	9.8E-03
Error	6%	-49%	92%	-53%
Unloading stiffness, κ				
Experimental [1]	2.1E-03	1.7E-03	2.1E-03	1.7E-03
Verification	2.8E-03	2.6E-03	1.4E-03	4.9E-03
Error	-24%	-36%	47%	-66%

[1] Experimental bulk stiffness parameters have been adjusted to account for scaling (see section 5.4.1)
AC: ascending cone filling, RF: rainfall filling

It can be seen that the optimised parameters determined using the Solver algorithm in Cases 1 and 2 overestimate the dynamic ϕ_r by 5.8° (11%), however the parameters determined using Statistica agree with the dynamic ϕ_r well (<1%). The parametric study described in Chapter 6 revealed that the dynamic ϕ_r was primarily influenced by the inter-particle coefficient of sliding μ_{pp} and rolling $\mu_{r,pp}$ friction. Each pair of cases with respect to the optimisation algorithm has similar results for μ_{pp} and $\mu_{r,pp}$, it would therefore be expect to produce similar dynamic ϕ_r. This is shown in the small differences (<1%) between Cases 1-2 and 3-4.

The verification of the bulk loading λ and unloading κ stiffness parameters show larger discrepancies from experimental values, with errors ranging from 6% (λ for Case 1) to 92% (λ for Case 2). The optimised parameters that match the experimental values of λ and κ the closest is Case 1, using the solver algorithm with the ascending cone filling method.

In Chapter 6, the difficulty for the optimisation algorithm to find optimal parameters which lie near the extremities of DOE range was highlighted (see section 1.1). For example, the DOE range for the particle shear modulus *G* was 1E6 to 1E9 *Pa*. The searching algorithm determined that the optimised parameter lies near 1E9 *Pa* (using the experimental results for calibration), therefore, it will be more prone to error. This phenomenon is highlighted in the verification stage by the greater accuracy seen in the models predicting the dynamic ϕ_r (which lay in the middle of the DOE range) compared to λ and κ (which lied at the extremities of the DOE range).

7.3 Validation study using a large scale experiment

Although the verification stage has highlighted some discrepancies between the laboratory measured bulk response parameters and those obtained using the optimised parameters, predicting correct bulk behaviour in larger and more complex systems is the main goal of this study. The following section will describe a validation study using one set of optimised parameters in a large scale system by predicting the response of a shallow footing penetration on a bed of BEB.

7.3.1 Experimental setup

When selecting the large scale validation experiment, quantitative data of the bulk responses are needed to compare with numerical results. Extracting usable data from industrial equipment may often be difficult as they were not developed for this purpose. The experiment chosen for the validation was an existing setup in the University of Edinburgh laboratories which consisted of a rigid footing penetration test in a thin slice as shown in Figure 7.1. The experimental setup restricted the lateral movement of particles and therefore could be considered a quasi two dimensional planar model representing a section of a strip footing. This experiment was chosen as it satisfies numerous criteria, including;

- Laboratory setup facilitated quantitative bulk response data extraction
- The penetration test is well defined (BS 1377-4 1990)
- Bearing capacities of footings are well defined (Terzaghi 1943)
- The granular loading conditions replicate some aspects of the bulk experimental devices used for calibrating the DEM models (granular compression and inter-particle properties in a thin slice)
- The loading conditions are representative of granular handling scenarios in agricultural equipment (compression and penetration of machinery in granular material).

The experimental setup consisted of an acrylic container (1000x600x30 *mm*), penetrated using a 150x25x30 *mm* footing. The footing was driven by an Instron machine at a constant rate of 20 *mm*/*min* and constant logging rate of 1 *Hz*. The Instron was also used to determine the force the footing (it is assumed that the force applied to the footing F_T is equal to the force applied by the footing). The experimental tests were carried out on the BEB and the container was filled using the rainfall filling method from the top of the container. This filling method was used as it produced more repeatable results than the ascending cone filling method. This is because the ascending cone method created an unstable packing arrangement that was more susceptible to collapsing and rearrangement during penetration. Three tests were conducted to check for repeatability.

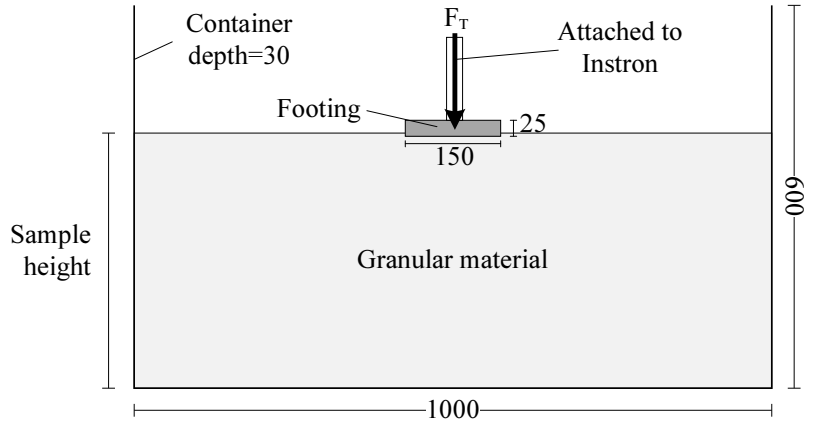

Figure 7.1 Experimental setup of the footing penetration validation test

(All dimensions in *mm*)

A sequence of images demonstrating the rigid footing test on BEB at various penetration depths are shown in Figure 7.2.

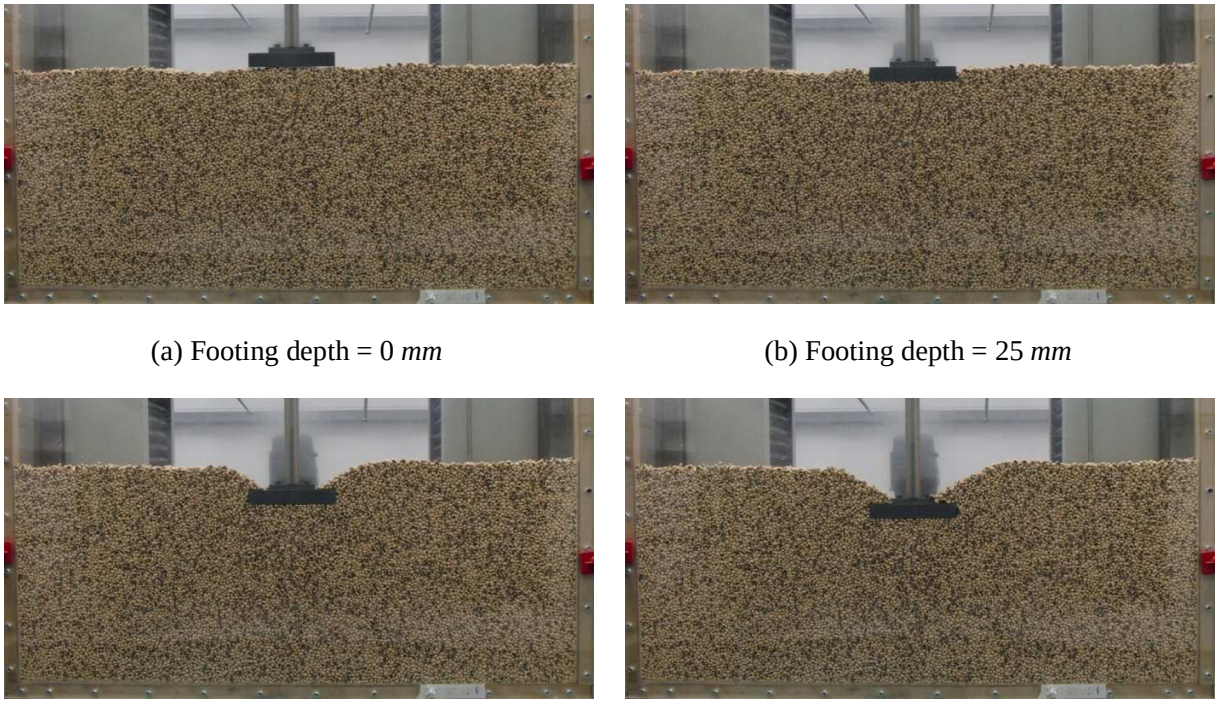

(a) Footing depth = 0 *mm* (b) Footing depth = 25 *mm*

(c) Footing depth = 75 *mm* (d) Footing depth = 100 *mm*

Figure 7.2 Sequence of images of the rigid footing penetration test using black eyed bean at various penetration depths

7.3.1.1 Vertical stresses along the base of the footing

The experimental loading resistance σ_v on the rigid footing due to penetration is shown in Figure 7.3. As the depth of penetration $\leq$ breath of the footing, the footing may be considered shallow.

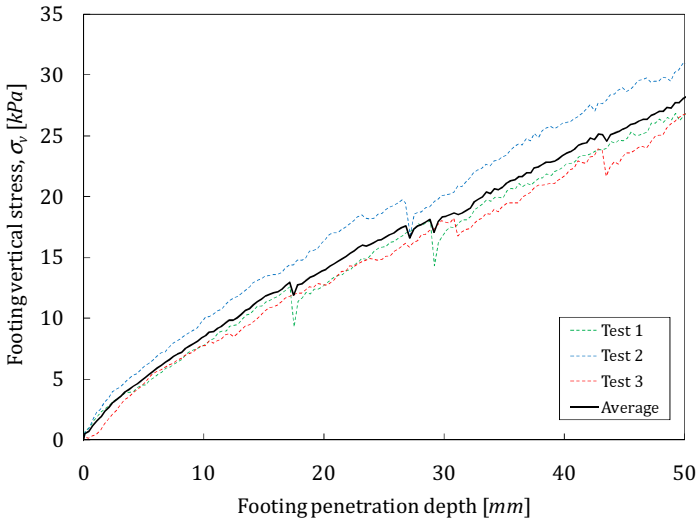

Figure 7.3 Experimental loading resistance results of a rigid footing during penetration

Three tests were conducted to check for repeatability. It can be seen that the footing penetration test is repeatable and therefore, an average line was determined by averaging the stresses for the three tests at similar penetration depths. This average line was used to represent the experimental results in the numerical footing parametric study described in section 7.3.2.1.

The ultimate bearing capacity q_u for a strip footing can be expressed as (Terzaghi 1943)

$$q_u = cN_c + \gamma D N_q + 0.5\gamma B N_\gamma \qquad \text{Equation 7.1}$$

where c and γ are the apparent cohesion and bulk unit weight of the granular material, D and B are the depth and breadth of the footing and N_c, N_q and N_γ are bearing capacity factors respectively. The cohesion in the granular materials is assumed to be negligible ($c = 0$) and γ, N_q, B and N_γ are constants, therefore q_u is proportional to D. This is highlighted by the constant increase in vertical footing stress as the depth of penetration increases (Figure 7.3).

It should be noted that Equation 7.1 is used for plane strain calculations and the experimental setup restricted particles from moving laterally. Therefore, the boundary effects such as wall friction are expected to contribute to the bulk stiffness of the system.

7.3.2 Numerical setup

7.3.2.1 Numerical footing penetration parametric study

Before simulating the footing penetration experiment using the optimised parameters, a study was conducted to determine to influence of various parameters on the bulk responses. The numerical setup adopted for the study used the exact dimensions of the experiment container and footing; however, to reduce the computational time, periodic boundaries were used to reduce the simulated section of the container. The container was narrowed down to 400 *mm* in length as shown in Figure 7.4. A macroscopic investigation of the simulation revealed that there was no major particle movement across the periodic boundary. The DEM implementation of the parameters were based on the optimised parameters of case 4 (to match the experimental filling method) and the parameters used to create the DOE dataset in Chapter 6 to give the parameters shown in Table 7.3. Simulating the physical penetration rate of was numerically unfeasible; therefore a loading rate of 1,200 *mm*/*min* was used. Furthermore, 20% of the Rayleigh time step was used in the study as opposed to the 10% used in the DOE dataset.

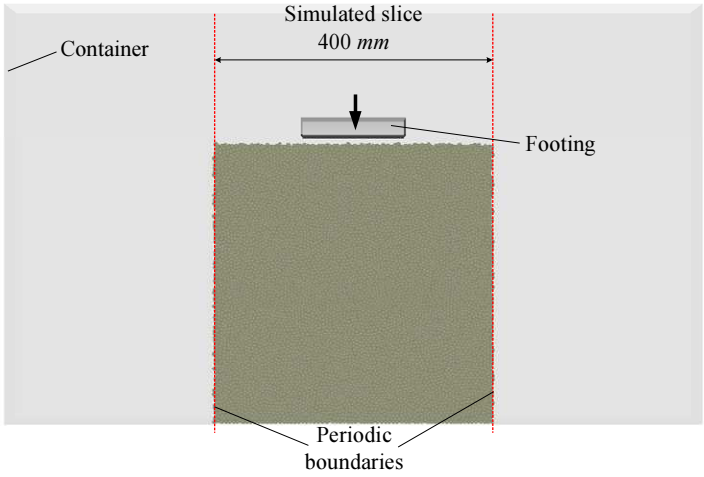

Figure 7.4 Numerical setup illustrating the footing penetration test simulated container slice using periodic boundaries

In an effort to match the initial void ratios e_0 of the experiment, a parametric alteration was carried out similar to the one used to create the numerical dataset (see section 5.2). The

inter-particle and boundary frictional parameters were reduced during the filling stage and returned to optimised values before starting the penetration.

Various parameters were varied independently from a reference case for the parametric study. The reference case DEM implementation used in the footing experiment parametric study for the filling stage and footing penetration can be found in Table 7.3.

Table 7.3 Reference case DEM implementation used in the footing experiment parametric study

Parameters	Filling stage	Footing penetration
Shear modulus, G [Pa]	7.3E+07	7.3E+07
PP, PW Coefficient of restitution ($e_r,\ e_{r,pw}$)	0.10, 0.10	0.10, 0.50
PP, PW Coefficient of sliding friction ($\mu_{pp},\ \mu_{pw}$)	0.10, 0.10	0.25, 0.30
PP, PW Coefficient of rolling friction ($\mu_{r,pp},\ \mu_{r,pw}$)	0.00, 0.00	0.05, 0.00

PP: particle to particle, PW: particle to wall

Six separate runs were simulated using variations of the reference case:

Run 1 (e_0=0.56) used the reference case DEM implementation from Table 7.1 including the parametric alteration during the filling stage to match the experimental e_0.

Run 2 (e_0=0.70) used the reference case DEM implementation from Table 7.1 however no parametric alteration occurred during filling stage. The result of higher inter-particle and boundary frictions was a higher e_0.

Run 3 (e_0=0.56) investigated the footing penetration rate by reducing the reference case speed by ten times to 2 *mm/sec*. The DEM implementation was identical to Run 1 excluding the footing rate.

Run 4 (e_0=0.54) investigated boundary influence by increasing the thickness of the container from 30 to 40 *mm* and resulted in a lower e_0. The DEM implementation was identical to Run 1 excluding the container depth.

Run 5 (e_0=0.56) studied the effect of the container wall sliding friction on the system by reducing the particle to wall friction to zero. The DEM implementation was identical to Run 1 excluding the particle to wall sliding friction coefficient.

Run 6 (e_0=0.56) simulated 600 *mm* of the container length (with periodic boundaries) to determine the influence of scaling the simulated container slice length on the results. The DEM implementation was identical to Run 1 excluding the simulated container length.

The numerical loading resistance experienced by the footing during penetration for the 6 runs is compared with the experimental results in Figure 7.5.

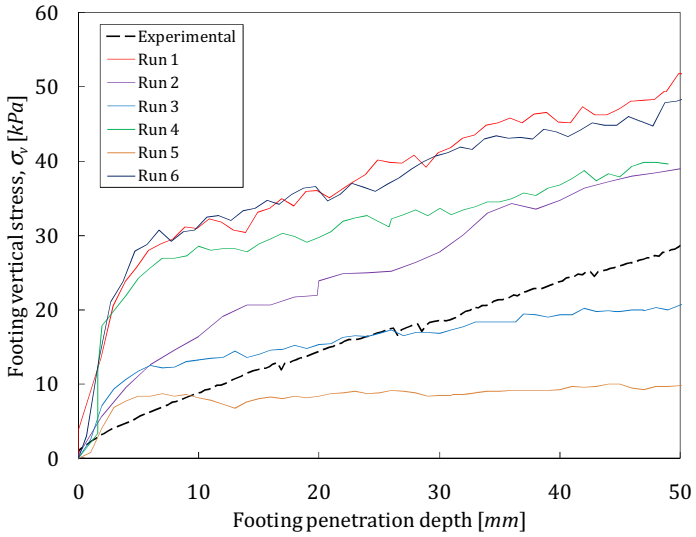

Figure 7.5 The numerical loading resistance experienced by the footing during penetration for the 6 runs used in the parametric study compared with the experimental results

It can be seen that each run response (less obvious in the averaged experimental results) is bilinear and composed of an initial stiffness and a hardening phase as illustrated in Figure 7.6 (using run 6). For this analysis, the point of intersection is defined as the ultimate bearing capacity q_u.

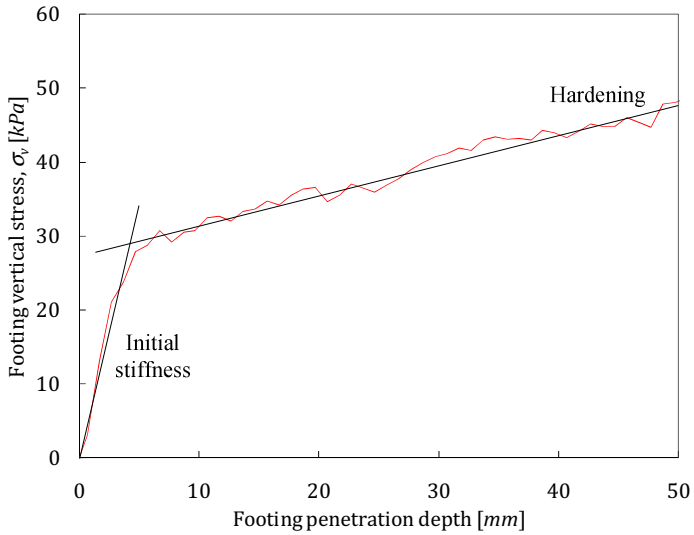

Figure 7.6 Illustration of the footing penetration bilinear response curve

As the container boundary was expected to play a significant role in the stiffness of the systems, the total vertical force of the footing base, container base and container shear force during the footing penetration were analysed. The results are shown in Figure 7.7.

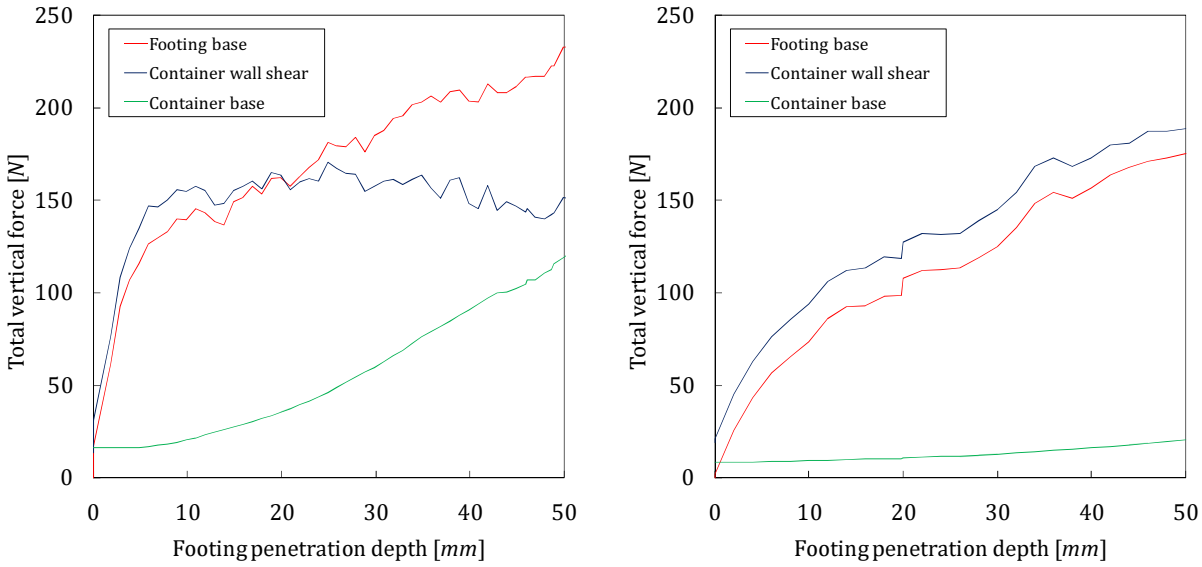

(a) Run 1 (b) Run 2

Figure 7.7 Total vertical force on the footing base, container base and container shear force during the penetration in the various runs of the footing pametric study

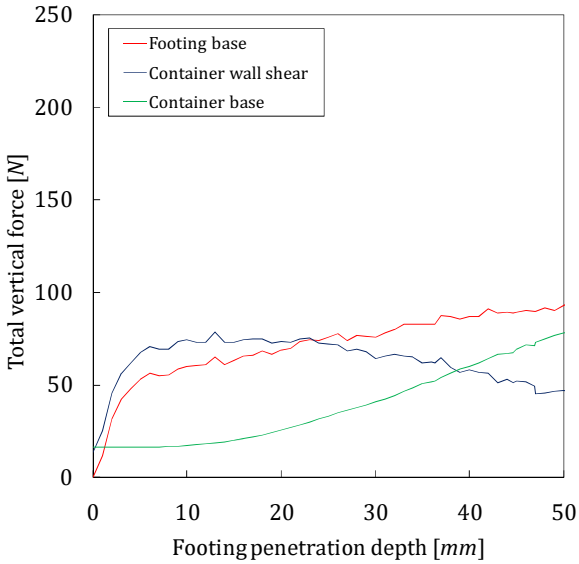

(c) Run 3

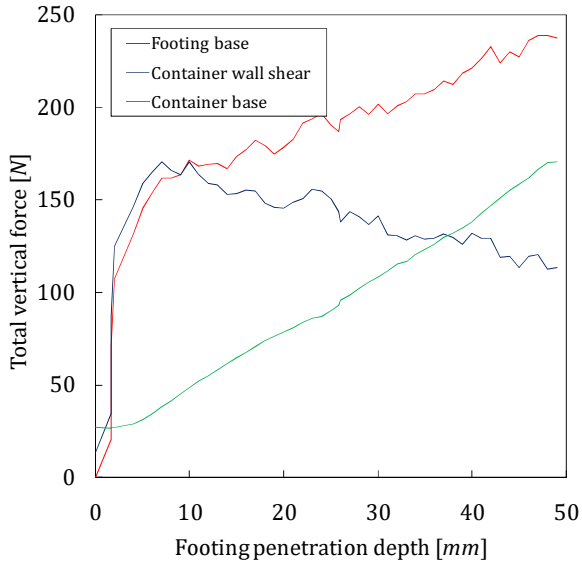

(d) Run 4

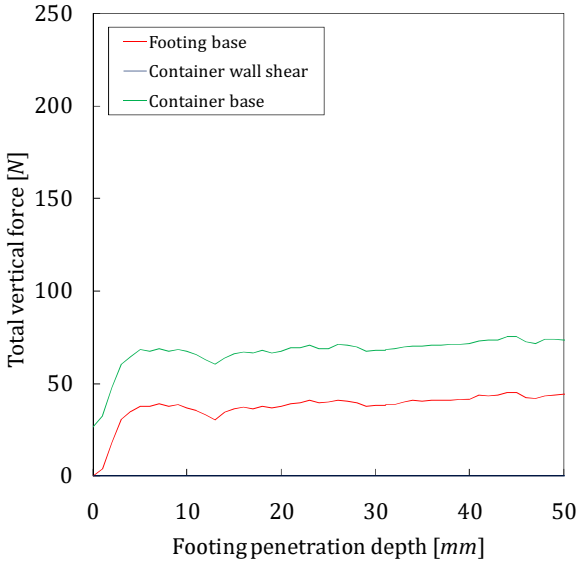

(e) Run 5

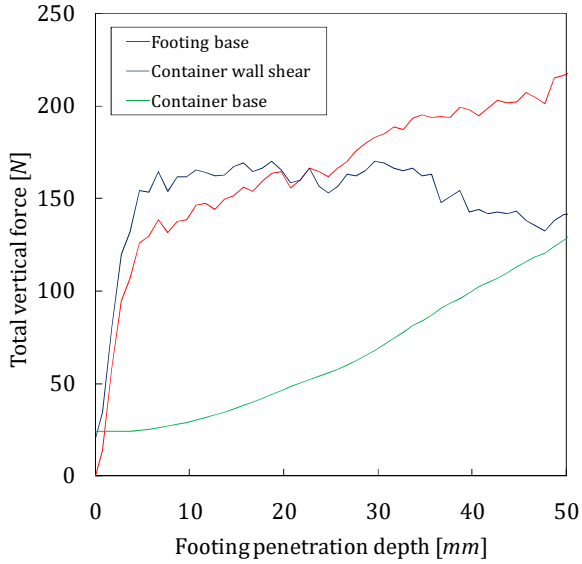

(f) Run 6

Figure 7.7 Total vertical force on the footing base, container base and container shear force during the penetration in the various runs of the footing pametric study

The initial forces seen in the container wall shear and base are a result of the particle weight. The total weight of the particles is typically 3000 g, therefore $\pm$ 30 N are distributed to the container wall and base.

7.3.2.2 Analysis and discussion

Experimental results

The magnitude of q_u is significantly smaller than the numerical results of the reference run (Run 1) and reached at a lower footing penetration. However, the gradient of the initial stiffness and hardening phase are similar to Run 1.

Run 1: Reference run

The ultimate bearing capacity is reached at a depth of 5 *mm* where q_u = 30 *kPa*. The initial stiffness gradient is considerably steeper than the hardening phase. A look at the shear forces along the wall and the vertical forces along the base (Figure 7.7) shows that a majority of the footing stresses are transferred to the container wall during the initial loading. As the footing penetration depth increases, the forces absorbed in the wall decrease and a greater proportion is transferred to the container base.

Run 2: No parametric alteration during filling

The higher wall friction during filling led to a higher e_0 than the reference case. The result is softer system illustrated by the lower gradient of the initial stiffness. The magnitude and depth of q_u is not as clearly defined as the Run 1, however, the gradient of the hardening phase is similar.

Figure 7.7 (b) reveals that a very small proportion of the footing stresses are transferred to the container base during penetration.

Run 3: Footing penetration rate

Reducing the penetration rate from 20 to 2 *mm/sec* reduces the magnitude of q_u by 60%. The hardening phase gradient is lower than in Run 1, exhibiting a softer system. However, the initial stiffness gradient and depth q_u are similar.

Although the magnitudes are proportionally smaller, Figure 7.7 (c) shows that the proportion of footing stresses that are transferred to the wall and container base are similar to Run 1.

Run 4: Container depth

Increasing the container depth from 30 to 40 *mm* was expected to reduce the boundary effect. The initial stiffness gradient and magnitude of q_u is similar to Run 1, however, the hardening phase displays a softer system. Figure 7.7 (d) shows that as after q_u is reached, the proportion of stresses transferred to the base of the container increases sharply. Increasing the depth of the container has reduced arching of the particles and force transfer to the container wall.

Run 5: No wall friction

When the particle to wall sliding friction is set to zero, the influence of the boundaries is highlighted. The initial stiffness gradient and magnitude of q_u is significantly lower than Run 1. The hardening phase gradient is almost negligible with increasing footing penetration depth. With no wall friction, the stress applied by the footing is entirely transferred to the base of the container (Figure 7.7, e).

Run 6: Container length scaling

Increasing the simulated length of the container from 400 to 600 *mm* was found to have minimal influence on the initial stiffness and the magnitude of q_u. However, the hardening phase displays a softer system (smaller gradient).

7.3.2.3 Validation simulation

It was decided to conduct the validation study on one set of optimised parameters. The set that was assumed to produce the best results (based on the verification in section 0) were the optimised parameters of BEB with the rainfall filling method determined using Statistica (case 4 Table 7.1). Following the footing parametric study in section 7.3.2.1 it was decided to use the following setup for the validation simulation:

- The numerical particle used in the optimisation procedure consisted of 2 overlapping equal spheres with an aspect ratio of 1.20. The space between the spheres is a pseudo-void which is not present in the granular material; therefore matching the experimental porosity may create a denser system. The numerical setup focused on

matching the filling conditions and packing arrangement rather than e_0 and no parametric alteration was conducted during the filling stage.

- The optimisation procedure simulations were designed to be applicable to a wide range of granular materials and used a particle to wall sliding friction coefficient μ_{pw} = 0.3. Once the optimised parameters have been determined, an appropriate value of μ_{pw} should be used in further simulations which is representative of the material being simulated. A value of μ_{pw} = 0.13 was chosen based on the laboratory tests results for black eyed beans (table Table 3.6) and the method described in section 5.3.5.
- The simulate container slice length did not appear to influence the results and a 400 *mm* slice was therefore used.

The main discrepancies between the numerical and experimental setups are highlighted in Table 7.4.

Table 7.4 Numerical and experimental footing penetration test setup discrepancies

	Experimental	Numerical
Footing loading rate [*mm*/*min*]	20	1200
Number of particles in container	43600 [1]	33406 [2]
Average particle length/ container depth [3]	4.3	5.6
Aspect ratio of particle, a_r	1.40	1.20
Initial void ratio, e_0	0.52 [4]	0.66
Average sample height [*mm*]	396	395

[1] Estimated using sample and average particle weight
[2] Using particles in a 400 *mm* slice
[3] Average particle length based on average of major, intermediate and minor dimensions
[4] Average of three tests

7.3.3 Results and analysis

The numerical results of the validation simulation using the optimised parameters of BEB are compared with the experimental results in Figure 7.8 and the forces found on the footing base, container wall and container base during penetration are show in Figure 7.9.

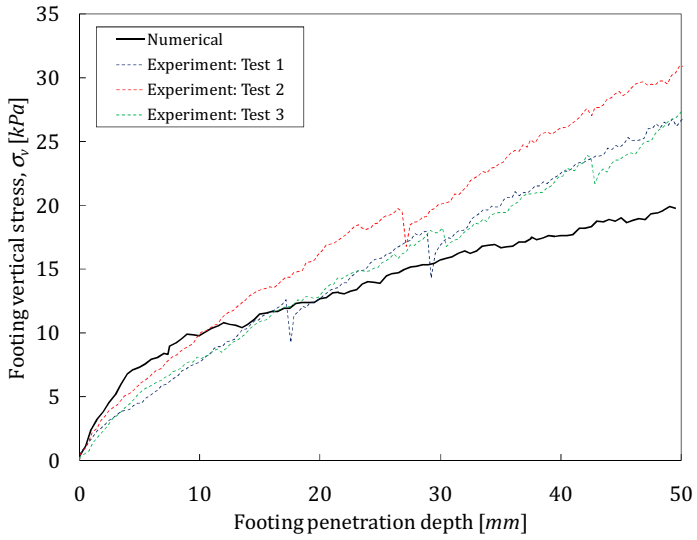

Figure 7.8 Comparison between experimental results and numerical simuations results using the optimised parameters of black eyed beans of the loading resistance of a footing penetration test

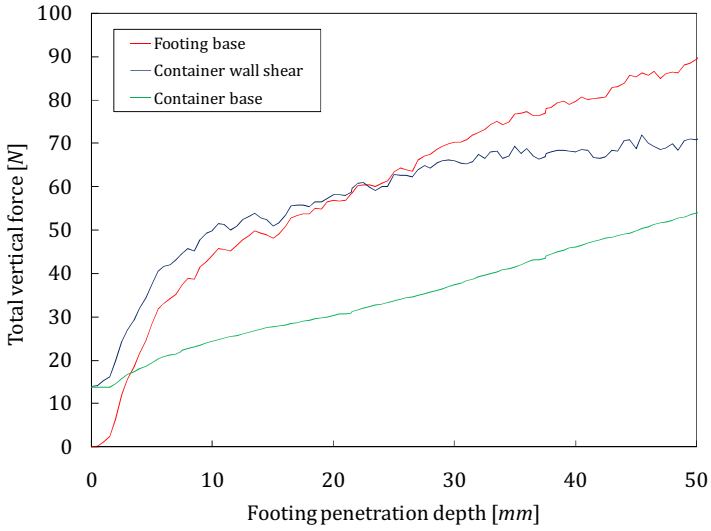

Figure 7.9 Total vertical force on the footing base, container base and container shear force during the footing penetration using the optimised parameters of black eyed beans

From Figure 7.8 it can be seen that the DEM simulations using the optimised parameters of BEB predicts loading resistance on the footing during penetration with an acceptable degree of accuracy for industrial application. The vertical stress is underestimated by 10% at a penetration depth of 30 *mm*. It can be seen that the numerical simulations overestimated the initial stiffness gradient and underestimated the hardening phase. The numerical results match the experimental results reasonably for a depth of 0 to 25 *mm*. As the hardening phase gradient differs between the numerical and experimental results, increasing the penetration depth further than 25 *mm* will increase the error proportionally. One possible explanation for the discrepancy in hardening phase gradient is the difference between the numerical and experimental particle size and therefore the average number of particles across the depth of the container will change (Table 7.4). Fewer particles across the container depth will increase particle arching and particle to wall frictional forces, and stiffen the system. This is illustrated by the higher number of particles across the container depth and lower hardening phase gradient in the numerical simulations. Based on the parametric study described in section 7.3.2.1, simulating the penetration test with matching particle size is expected to increase the gradient of the numerical hardening curves and match the experimental results more accurately. At initial penetration depths (<5 *mm*) a majority of the vertical forces applied by the footing are transferred to the container wall as shown in Figure 7.9. As the depth increases, the proportion of forces transferred to the container base increases accordingly and the boundary effect is reduced.

The compressive forces experienced by the particles within the system of the validation simulation at increasing penetration depths are illustrated in Figure 7.10. It can be seen that the numerical results display qualitative bulk behaviour similar to the classical concept for failure mechanism of shallow strip footings (Hansen et al. 1969; Terzaghi 1943), where the failure of plastic zone consists of:

- A triangular zone beneath the footing, pushed down as a block
- Radial shear zones
- Passive shear zones beyond the radial shear zones.

Qualitative discrepancies between the numerical and experimental results were observed in the magnitude of the particle piles formed above the footing edges as a result of penetration. Numerically, the piles are larger than in the experiment.

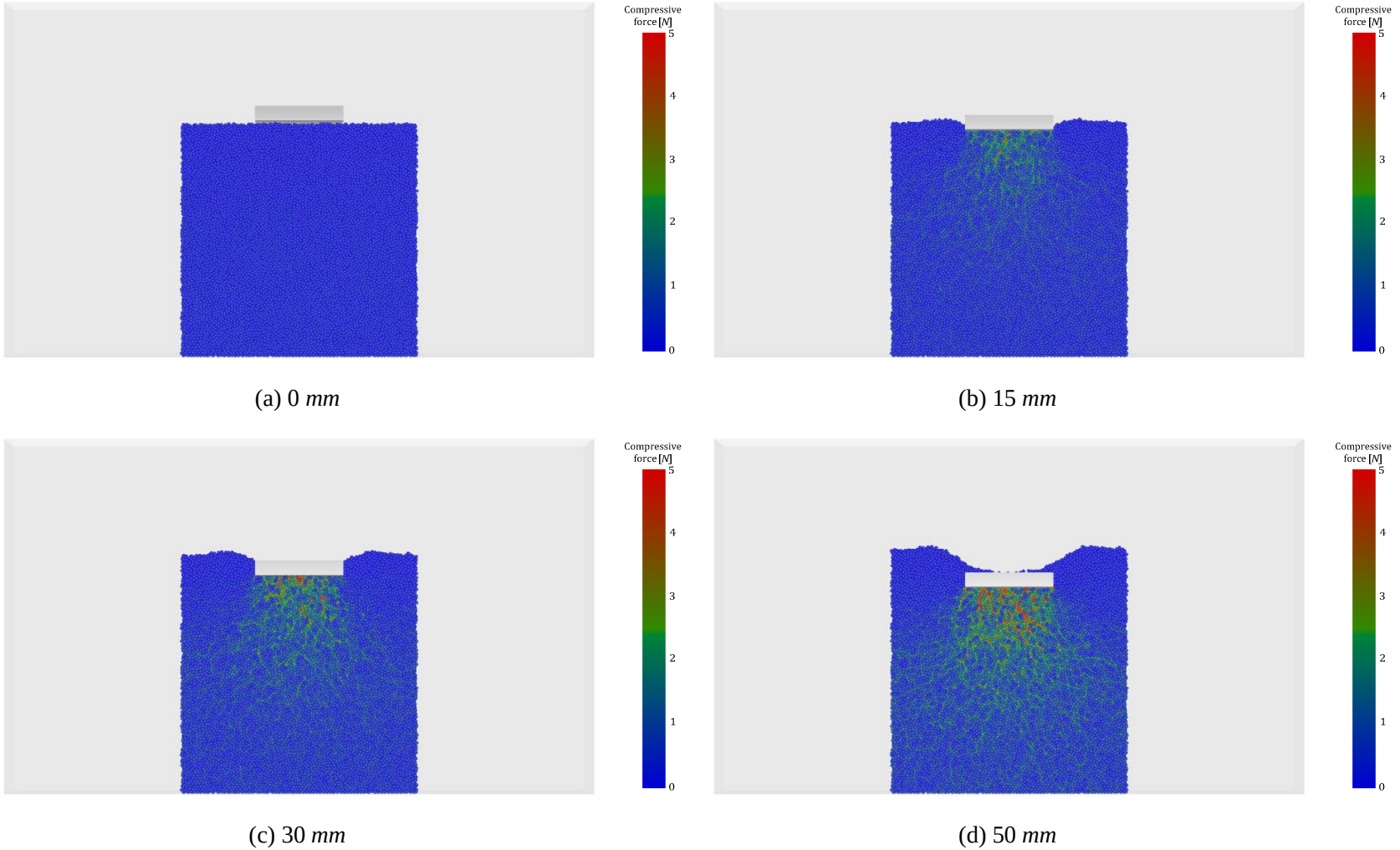

(a) 0 *mm*

(b) 15 *mm*

(c) 30 *mm*

(d) 50 *mm*

Figure 7.10 Illustration of the inter particle compressive force due to footing penetration for the validation simulation using the optimised parameters of black eyed beans at increasing depths

7.4 Summary and conclusions

A verification and validation of the optimised parameters for BEB determined using the parametric optimisation methodology described in Chapter 6 was presented in this chapter. The optimised parameters were verified by simulating the calibration experiments and one set of parameters was validated in a large scale system.

The verification of the optimised parameters revealed that running simulations using input parameters determined with the Solver algorithm overestimated the experimental dynamic ϕ_r by 11%, however, the parameters determined using Statistica agree with the dynamic ϕ_r well (<1%). The optimised DEM parameters had greater difficulties to produce results similar to the experimental bulk stiffness parameters. The optimised parameters that matched the measured values of λ and κ the closest was Case 1, using the solver algorithm with the ascending cone filling method.

The optimised parameters of BEB determined with Statistica were used in a validation study. A shallow rigid footing penetration test was chosen as the large scale experiment for the study and the experimental results were shown to be repeatable. DEM simulations predicted vertical stresses on the footing during penetration to an acceptable degree of accuracy for industrial application up to 30 *mm* where the loading resistance was underestimated by 10%. The numerical simulations overestimated the initial stiffness gradient and underestimated the hardening phase; however the smaller numerical particle size may have led to a softer system as a result of reduced boundary effects. In addition, the simulation predicted accurate vertical stresses at penetration depth between 5 and 25 *mm*.

The verification and validation has demonstrated the potential of the parametric optimisation to predict qualitative and quantitative bulk responses in large scale simulations with a degree of accuracy suitable for industrial applications.

Chapter 8

Conclusions and recommendations for further research

The research in this thesis was carried out to study the experimental and the DEM predicted bulk behaviour of granular materials to develop a methodology for calibrating DEM models using bulk physical tests. This chapter summarises the conclusions determined throughout the thesis and suggests recommendations of relevant topics for further research.

8.1 General conclusions

8.1.1 Granular material properties

A detailed understanding of a granular system is crucial when attempting to model it, whether it is on a micro (particle) or macro (bulk) scale. One aspect that is particularly important is correctly identifying the granular material properties which may either be physical (properties that can be determined without altering its shape or density) or mechanical (properties that reveal its elastic and plastic behaviour when a force is applied). The optimisation procedure developed

to calibrate DEM models described in this thesis was developed to be applicable to a wide range of materials and therefore a contrasting set of granular materials were chosen. The five granular materials tested in this study were:

1. Single glass beads (GB)
2. Paired glass beads (GB)
3. Polyethylene terephthalate pellets (PP)
4. Black eyed beans (BEB)
5. Black kidney beans (BKB)

It is important to distinguish between particle and bulk properties, whether referring to physical or mechanical properties. It has been demonstrated in Chapter 3 that measured individual particle properties are different from measured bulk properties as additional forces such as those arising from particle interlocking are not accounted for in individual particle measurements.

8.1.2 Experimental bulk behaviour using rotating drums and confined compression tests

Bulk physical tests and their bulk responses were used to calibrate the DEM models in the optimisation methodology. Two laboratory devices were chosen to be used in this study; the rotating drum and the confined compression test. These devices were chosen as they are devices that can produce bulk responses that are repeatable and easy to quantify, as well as generate discriminating results in numerical simulations when the DEM input parameters are varied.

The bulk response determined from the rotating drum device was the dynamic angle of repose ϕ_r. formed when granular material in a 40% filled drum is rotating at a speed of 7 *rpm*. The confined compression apparatus was used to determine the bulk stiffness of a system by monitoring the change in void ratio from the stress applied during one loading and unloading cycle. The gradients of the loading λ and unloading κ curve were the two bulk response parameters were extracted from the confined compression test. Compression tests were carried out on systems filled using an ascending cone (looser) and rainfall (denser) filling method. The key results of the bulk physical experiments can be summarised as follows:

I. The general trend for all of the granular materials (less visible with paired GB) is an increase in dynamic ϕ_r as the drum rotational speed increases.

II. The five different granular materials showed contrasting bulk responses including varying dynamic ϕ_r ranges and flow transition speeds. The flow regime transition (from slumping to avalanching) appears to be influenced by two main parameters: the particle aspect ratio a_r (defined as the major to intermediate dimension ratio) and the particle sliding friction.

III. At lower rotational speeds, the paired GB displayed a significantly larger dynamic ϕ_r than the single GB. As the angular velocity was increased, the discrepancy reduced suggesting that individual particle properties have smaller influence at greater *rpm* and the flow regimes are influenced primarily by the centrifugal forces and boundary conditions.

IV. The two filling methods in the confined compression test produced significant differences in virgin loading gradient of the stress-strain curve. As expected, the denser filling method had a higher gradient (stiffer system) than the looser filling method.

V. For the same filling method, the five different materials produced a range of bulk stiffnesses. The softest system was observed in the ascending cone filling of BKB which coincided with the highest a_r of the five materials.

VI. The single GB showed minimal differences in bulk stiffness parameters between the two filling methods, which was attributed to a sphere's natural ability to roll into a dense packing arrangement regardless of filling method.

8.1.3 Parametric investigation and scaling sensitivity study

8.1.3.1 DEM input parameters

A parametric investigation was conducted on DEM simulations to gain a deeper understanding into the influence of the input parameters on the bulk behaviour. The main conclusions are:

I. Scaling the particle density ρ_s and using 5%-20% of the Rayleigh time step T_R was found to have a minimal effect on the dynamic ϕ_r and the bulk stiffness parameters. However, the computational time was affected.

II. As long as the inner drum friction μ_{pw} is large enough to prevent particle slippage, μ_{pw} was also found to have a minimal effect on the dynamic ϕ_r. However, the drum end plate μ_{pw} has a significant effect on the dynamic ϕ_r. Scaling the particle Poisson's ratio υ was found to affect the bulk stiffness parameters significantly, as one would expect.

III. The dynamic ϕ_r was shown to be significantly influenced by increasing the number of particles between end plates (reducing the particle radius) when end plates are present. However, when periodic boundaries are introduced, the effect is significantly reduced.

IV. The particle a_r was observed to significantly influence the dynamic ϕ_r due to the particle interlocking and the increase in boundary influence as the number of particles between end plates decreases.

V. The frictional forces along the wall will restrain confined compression during loading and prevent the system from rebounding during unloading. Therefore increasing μ_{pw} will contribute to a stiffening of the system; as μ_{pw} increases, the bulk stiffness parameters λ and κ decrease significantly (indicating increasing stiffness).

VI. Simulations with particle a_r=1.00 and a_r=2.00 have higher bulk stiffness parameters than particles with intermediate a_r values; however, this was found to coincide with a higher initial void ratio e_0. Taking into account e_0, the effect of a_r is reduced.

8.1.3.2 Numerical scaling sensitivity study

In an effort to maximise the computational efficiency, a scaling sensitivity study was performed on the confined compression simulations. This included a numerical scaling of the apparatus dimensions, the particles shear modulus, *G* and the confined compression plate rate. The key findings of the sensitivity study are:

I. Two methods of dimensional scaling were examined, fixing the height/diameter (H/D) ratio and fixing the diameter (D) of the confined compression cylinder. Scaling the cylinder down to 50% of the experimental height produced a relatively linear increase of λ with a low gradient for both fixed H/D and fixed D scaling. Scaling beyond 50% produced an accelerated increase of λ and an increasing discrepancy between the two scaling methods.

II. For the fixed D scaling, κ increased (system became softer) as the sample height decreased. However, the fixed H/D scaling appears to have much less influence on κ. Reducing the scale down to 50% of the experimental height will increase κ by 10% and 50% for the fixed H/D and fixed D respectively.

III. The particle shear modulus *G* was investigated on both single and paired sphere (two equal spheres, a_r=2.00) particles. It was shown that the change in volumetric strain ε_v from *G*=1E6 *Pa* to *G*=1E8 *Pa* was considerably larger than from *G*=1E8 *Pa* to *G*=1E10 *Pa*. Paired spheres showed a greater ε_v than single spheres for matching value of *G*.

IV. As *G* increased, the bulk stiffness parameters decreased (stiffening). However, it was found that changing *G* from 1E9 *Pa* to 1E10 *Pa* has a smaller effect on the bulk stiffness parameters.

V. The experimental compression plate speed was 0.1 *mm/min*, which was numerically unfeasible. A range of compression plate speeds from 0.1 *mm/min* to 720 *mm/min* were simulated to determine the effect of the compression speed on the bulk stiffness parameters and the difference was found to be negligible. It was concluded that simulating the relatively slow experimental compression speed is unnecessary as the bulk stiffness parameters are not sensitive to the compression rate.

8.1.4 Parametric optimisation methodology

The thesis proposed a DEM model parameter optimisation procedure which consisted of three steps:

1. The measurement of the physical experimental data that was used to calibrate the DEM models;
2. The creation of the numerical dataset that was used to describe how the DEM parameters influence the bulk behaviour;
3. The optimisation of the DEM parameters using the results from Step 1 and 2

The measurement of the bulk response parameters used to calibrate the DEM models was conducted on the rotating drum and confined compression test (Step 1).

The numerical dataset describing how the DEM input parameters influence the numerical bulk responses was created by simulating the bulk physical tests, varying the DEM parameters and monitoring the effect of the input parameters on the numerical dynamic ϕ_r, λ and κ. The design of experiments (DOE) method was used to determine a reduced factorial numerical dataset (Step 2).

Two techniques were used in the optimisation procedure (Step 3); the first was a simple method based on Microsoft Excel's Solver algorithm coupled with a weighted inverse distance method. The second was a robust method which involved the use of the statistical analysis program Statistica. It was shown that the Excel Solver algorithm required less time to determine the optimised parameters, but was limited by the DOE dataset resolution and could only perform an optimisation based on two bulk responses (dynamic ϕ_r and κ) in the present setup.

Before using the *profiling and desirability* function in Statistica, the creation of an ANOVA model based on the numerical dataset was required. The profiling was then able to produce a set of optimised DEM parameters based on the three bulk responses parameters.

Finally, a verification and validation of the methodology was presented using the optimised parameters of BEB. The optimised parameters were verified by rerunning simulations using the same system as the numerical dataset and validated by predicting the response of a shallow footing penetration on a bed of BEB.

The verification of the optimised parameters revealed that running simulations using input parameters determined with the Solver algorithm overestimated the experimental dynamic

ϕ_r by 11%, however, the parameters determined using Statistica agree with the dynamic ϕ_r well (<1%). The optimised DEM parameters had greater difficulties to produce results similar to the experimental λ and κ.

The experimental results of the validation study were shown to be repeatable with the ultimate bearing capacity q_u reached at a penetration of ±6 *mm*. The numerical simulation overestimated the initial stiffness gradient and underestimated the hardening phase, however, the smaller numerical particle size may have led to a softer system as a result of reduced boundary effects. DEM simulations predicted vertical stresses on the footing during penetration to an acceptable degree of accuracy for industrial applications up to a penetration depth of 30 *mm* where the vertical stress was underestimated by 10% demonstrating the potential of the optimisation procedure to predict bulk responses in large scale systems using optimised DEM parameters.

8.2 Suggestions for further research

The thesis has presented a detailed study on the calibration of DEM models using bulk physical tests. Several areas that are worthy of further research include:

8.2.1 Physical experiments and bulk responses

I. The end plate friction of the rotating drum was shown to significantly influence the dynamic ϕ_r, especially in drums with less than 4 particles between endplates. To reduce the boundary effect of the endplates, a deeper rotating drum should be developed. For computational efficiency, the deeper drum could then be simulated using periodic boundaries.

II. Preliminary investigations used Particle Image Velocimetry (PIV) techniques to identify velocity flow patterns and magnitudes in the transverse plane of a rotating drum. Although PIV methods seemed promising, it was decided to focus on a single bulk response parameter from the rotating drum. Future research could investigate the use of PIV technique as a method of capturing bulk responses to calibrate DEM models.

8.2.2 Numerical simulations

I. There is one major mismatch between the numerical and experimental results caused by the lack of plasticity in the contact model used (Hertz-Mindlin no slip). This means that no plastic deformation occurred in the numerical simulation, resulting in excessive elastic rebound during unloading. In the experiment, further permanent deformation occurs during further loading cycles, which is absent from the current visco-elastic DEM contact model. An elasto-plastic contact model needs to be implemented in the EDEM code to address this anomaly.

II. Although BEB and the PP produce the same experimental dynamic ϕ_r at 7 *rpm* (~43°), this angle is a result of different flow patterns and regimes; the BEB exhibited an avalanching regime whereas the PP produce an S-shape from a cascading regime. The parametric optimisation did not focus on reproducing accurate flow patterns numerically and as a result, no distinction was made between the two materials with regards to the dynamic ϕ_r. Further research could focus on reproducing accurate flow regimes by describing the flow regime in terms of particle bed length, active and passive regions thicknesses, bed turnover time and filling degree.

8.2.3 Parametric optimisation procedure

I. The parametric study presented in this thesis illustrated the methodology using four DEM parameters and three bulk responses. Increasing the number of DEM parameters and bulk responses will in turn increase the number of simulations required to build the numerical dataset, however, a higher degree of detail will be included in the numerical model. The profiling in Statistica (StatSoft 2009) allows up to ten independent (DEM parameters) and ten dependent (bulk responses) to be analysed simultaneously. Several suggestions for further parameters to optimise are listed below.

    a. The packing arrangement of particles has been shown to significantly influence the bulk behaviour, specifically with regards to bulk stiffness in the confined compression tests. In the thesis, this was accounted for by keeping the porosity of the system constant where possible. Further research could include the initial void ratio and packing arrangement as optimised parameters.

b. Because the systems described in this thesis are mainly static or slow shearing, accurate shape representation was not essential as the optimisation procedure incorporated adjustments to the parameters to account for any discrepancies. For systems with greater movement and/or greater particle to geometry interaction, it would be sensible to include shape representation as one the parameter to be optimised.

c. This study focused on the optimisation of inter-particle parameters primarily due to the inherent scenario specific nature of the particle-wall parameters. Further research should include particle to wall parameters as optimised parameters.

II. Statistica uses the predicting and profiling to determine a set of optimised parameters that will produce the highest desirability base on a predefined ANOVA model. It has been shown that various input parameters influence the bulk responses with varying degrees. Therefore, different combinations of parameter values could potentially produce the same bulk response. Further research should investigate the range of combinations that are possible and what influence this has in full scale industrial scenarios.

III. The optimisation searching algorithm using Microsoft Excel Solver coupled with a weighted inverse distance used a partial factorial DOE to populate the dataset. Further research could investigate an expansion of the dataset by generating additional data points based on the original data using interpolations method which would increase the accuracy of the searching method.

Chapter 9

References

3D Scanners Ltd (1998) *ModelMaker-User Manual*.

Adrian, R. J. (2005) Twenty years of particle image velocimetry. *Experiments in Fluids* **39,** 159-169.

Afzalinia, S. and Roberge, M. (2007) Physical and mechanical properties of selected forage materials. *Canadian Biosystems engineering* **49,** 2.

Ai, J. (2010) Particle scale and bulk scale investigation of granular piles and silos. Edinburgh, University of Edinburgh. PhD.

Ai, J., Chen, J. F., Ooi, J. Y. and Rotter, J. M. (2010) Assessment of Rolling Resistance Models in Discrete Element Simulation.

Anandarajah, K., Hargrave, G. K. and Halliwell, N. A. (2006) Digital Particle Image Velocimetry: Partial Image Error (PIE). *Journal of Physics: Conference Series* **45,** 174-185.

ASABE (2008) Method of Determining and Expressing Fineness of Feed Materials by Sieving. *American Society of Agricultural Engineers*.

ASAE (1998) Compression test of food materials of convex shape. *ASAE Standards*, 500-504.

Bansal, R. K., Walker, J. T., Gardisser, D. R. and Grift, T. E. (1998) Validating FLUENT for the flow of granular materials in aerial speaders. *American Society of Agricultural Engineers* **41,** 29-35.

Barker, D. B. and Fourney, M. E. (1977) Measuring fluid velocities with speckle patterns. *Optics Letters* **1,** 135-137.

Beer, F. P. and Johnson, E. R. (1976) *Mechanics for engineers; static and dynamics*, New York, MacGraw-Hill.

Bell, T. (2005) Challenges in the scale-up of particulate processes: an industrial perspective. *Powder Technology* **150,** 60-71.

Bettonvil, B. (1990) *Detection of important factors by sequential bifurcation*, Tilburg University Press.

Bettonvil, B. and Kleijnen, J. P. C. (1997) Searching for important factors in simulation models with many factors: sequential bifurcation. *European Journal of Operational Research* **96,** 180-194.

Beverloo, W. A., Leniger, H. A. and Van De Velde, J. (1961) The flow of granular solids through orifices. *Chemical Engineering Science* **15,** 260-269.

Boateng, A. A. and Barr, P. V. (1997) Granular flow behaviour in the transverse plane of a partially filled rotating cylinder. *Journal of Engineering and Applied Science* **330,** 233-249.

Bonamy, D., Daviaud, F. and Laurent, L. (2002) Experimental study of granular surface flows via a fast camera: A continuous description. *Physics of Fluids* **14,** 1666.

Box, G. E. P. and Behnken, D. W. (1960) Some new three level designs for the study of quantitative variables. *Technometrics* **2,** 455-475.

Box, G. E. P. and Draper, N. R. (1987) *Empirical model-building and response surfaces*, Wiley New York.

Box, G. E. P. and Wilson, K. B. (1951) On the experimental attainment of optimum conditions. *Journal of the Royal Statistical Society. Series B (Methodological)* **13,** 145.

Box, J. M. (1965) New method for constraint optimisation and a comparison with other methods. *Computer Journal* **8,** 42-52.

Brilliantov, N. V. and Pöschel, T. (1998) Rolling friction of a viscous sphere on a hard plane. *EPL (Europhysics Letters)* **42,** 511–516.

BS 1377-4 (1990) Soils for civil engineering purposes – part 4: compaction.

Buick, J. M., Chavez-Sagarnaga, J., Zhong, Z., Ooi, J. Y., Campbell, D. M. and Greated, C. A. (2005) Investigation of silo honking: slip-stick excitation and wall vibration. *Journal of engineering mechanics* **131**(3)**,** 299-307.

Chen, J. F. (2002) Load-Bearing Capacity of Masonry Arch Bridges Strengthened with Fibre Reinforced Polymer Composites. *Advances in Structural Engineering* **5,** 37-44.

Chou, H.-T. and Lee, C. F. (2009) Cross-sectional and axial flow characteristics of dry granular material in rotating drums. *Granular Matter* **11,** 13-32.

Chung, Y. C. (2006) Discrete element modelling and experimental validation of a granular solid subject to different loading conditions. Edinburgh, University of Edinburgh. PhD.

Chung, Y. C. and Ooi, J. Y. (2006) Confined Compression and Rod Penetration of a Dense Granular Medium: Discrete Element Modelling and Validation. *Modern Trends in Geomechanics* **106,** 223-239.

Chung, Y. C. and Ooi, J. Y. (2008) Influence of Discrete Element Model Parameters on Bulk Behavior of a Granular Solid under Confined Compression. *Particulate Science and Technology: An International Journal* **26,** 83-96.

Connor, W. S. and Young, S. (1961) *Fractional factorial designs for experiments with factors at two and three levels*, US Dept. of Commerce, National Bureau of Standards; for sale by the superintendent of documents, USGPO, Washington.

Craig, R. F. (2004) *Craig's soil mechanics*, Taylor and Francis.

Cundall, P. A. (1971) A computer model for simulating progressive, large-scale movements in blocky rock systems. *Proc. Symp. Int. Soc. Rock Mech*.

Cundall, P. A. and Strack, O. D. L. (1979) A discrete numerical model for granular assemblies. *Geotechniques.* Storming Media.

Das Gupta, S., Khakhar, D. V. and Bhatia, S. K. (1991) Axial transport of granular solids in horizontal rotating cylinders. Part 1: Theory. *Powder Technology* **67,** 145-151.

Del Castillo, E., Montgomery, D. C. and McCarville, D. R. (1996) Modified desirability functions for multiple response optimization. *Journal of Quality Technology* **28,** 337-345.

DEM Solutions Ltd (2009) *EDEM User Maual*, DEM Solutions.

Derringer, G. and Suich, R. (1980) Simultaneous optimization of several response variables. *Journal of quality technology* **12,** 214-219.

Ding, Y. L., Forster, R. N., Seville, J. P. K. and Parker, D. J. (2001a) Scaling relationships for rotating drums. *Chemical Engineering Science* **56,** 3737-3750.

Ding, Y. L., Forster, R. N., Seville, J. P. K. and Parker, D. J. (2002) Granular motion in rotating drums: bed turnover time and slumping-rolling transition. *Powder Technology* **124,** 18-27.

Ding, Y. L., Seville, J. P. K., Forster, R. N. and Parker, D. J. (2001b) Solids motion in rolling mode rotating drums operated at low to medium rotational speeds. *Chemical Engineering Science* **56,** 1769-1780.

Dudderar, T. D. and Simpkins, P. G. (1977) Laser speckle photography in a fluid medium. *Nature Publishing Group* **270,** 45-47.

Dupont (2009) www.dupont.com. Wilmington, Delaware, United States.

Dury, C. M., Ristow, G. H., Moss, J. L. and Nakagawa, M. (1998) Boundary effects on the angle of repose in rotating cylinders. *Physical Review E* **57,** 4491-4497.

Elperin, T. and Vikhansky, A. (1998) Granular flow in a rotating cylindrical drum. *Europhysics Letters (EPL)* **42,** 619-624.

EN 1991-4 (1995) Eurocode 1: Basis of Design and actions on structures. Part 4; Actions in silos and tanks.

ENV, D. (1991) Basis of design and actions on structures. *Europhys. Lett*.

Favier, J. F., Abbaspour-Fard, M. H. and Kremmer, M. (2001) Modeling nonspherical particles using multisphere discrete elements. *Journal of Engineering Mechanics* **127,** 971-977.

Ferreira, M. M. C., Ferreira, W. C. J. and Kowalski, B. R. (1996) Rank determination and analysis of non-linear processes by global linearizing transformation. *Journal of Chemometrics* **10,** 11-30.

Fylstra, D., Lasdon, L., Watson, J. and Waren, A. (1998) Design and use of the Microsoft Excel Solver. *Interfaces***,** 29-55.

Ginsberg, J. H. and Genin, J. (1984) *Dynamics*, New York, John Wiley and Sons, Inc.

Giunta, A. A., Wojtkiewicz Jr, S. F. and Eldred, M. S. (2003) Overview of modern design of experiments methods for computational simulations. *AIAA* **649,** 6-9.

Golden Software Inc (2002) Surfer v8.0. Golden, Colorado, USA.

Govender, I., McBride, A. T. and Powell, M. (2004) Improved experimental tracking techniques for validating discrete element method simulations of tumbling mills. *Experimental Mechanics* **44,** 593-607.

Grift, T. E., Walker, J. T. and Hofstee, J. W. (1996) Aerodynamic properties of individual fertilizer particles. *Work* **40,** 13-20.

Grousson, R. and Mallick, S. (1977) Study of flow pattern in a fluid by scattered laser light. *Applied Optics* **16,** 2334-2336.

Gu, Z., Lu, L. and Ai, L. (2009) Impact energy loss from particle surface roughness in particulate systems. *Europhysics Letters* **87,** 14003.

Hansen, B., Christensen, N. J. and Karafiath, L. L. (1969) Discussion of theoretical bearing capacity of very shallow footings. *J. Soil Mech. Fdns. Div., ASCE* **95,** 1568-1572.

Harrington, E. C. (1965) The desirability function. *Industrial Quality Control* **21,** 494-498.

Härtl, J. (2008) A study of granular solids in silos with and without an insert. Edinburgh, The University of Edinburgh. PhD.

Härtl, J. and Ooi, J. Y. (2008) Experiments and simulations of direct shear tests: porosity, contact friction and bulk friction. *Granular Matter* **10,** 263-271.

Henein, H., Brimacombe, J. K. and Watkinson, A. P. (1983) Experimental study of transverse bed motion in rotary kilns. *Metallurgical and Materials Transactions B* **14,** 191-205.

Hertz, H. R., Jones, W. C., Jones, D. E., Wheeler, B. I. and Schott, G. A. (1896) *Miscellaneous papers*, Macmillan.

Himmelblau, D. M. (1972) *Applied Nonlinear programming*, McGraw-Hill.

Horabik, J. and Rusinek, R. (2002) Pressure ratio of cereal grains determined in a uniaxial compression test. *International Agrophysics* **16,** 23–28.

IChE (1989) Standard shear testing technique for particulate solids using Jenike Shear cell. IChE/EFChE joint publication.

Instron (2009) www.instron.com. Norwood, MA, US.

Itasca (2003) *PCF3D User Manual*, Minneapolis, USA, Itasca Consulting Group Inc.

Iwashita, K. and Oda, M. (2000) Micro-deformation mechanism of shear banding process based on modified distinct element method. *Powder Technology* **109,** 192-205.

Janoyan, K. D. and Yu, X. (2005) Direct Shear Testing of Rocks. **6,** 1-15.

Janssen, H. J. (1895) Versuche ueber Getreidedrack in Silozellen. *Versuche über Getreidedruck in Silozellen* **39,** 1045-1049.

Jester, W. and Klik, A. (2005) Soil surface roughness measurement—methods, applicability, and surface representation. *Catena* **64,** 174-192.

Jiang, M. J., Yu, H.-S. and Harris, D. (2005) A novel discrete model for granular material incorporating rolling resistance. *Computers and Geotechnics* **32,** 340-357.

Johnson, K. L. (1987) *Contact mechanics*, Cambridge University press.

Khakhar, D. V., McCarthy, J. J. and Ottino, J. M. (1997) Radial segregation of granular mixtures in rotating cylinders. *Physics of Fluids* **9,** 3600.

Kim, T., Hampton, J. G., Opara, L. U., Hardacre, A. K. and Mackay, B. R. (2002) Effects of maize grain size, shape and hardness on drying rate and the occurrence of stress cracks. *Journal of the Science of Food and Agriculture* **82,** 1232-1239.

Kleijnen, J. P. C. (2005) An overview of the design and analysis of simulation experiments for sensitivity analysis. *European Journal of Operational Research* **164,** 287-300.

Kleijnen, J. P. C. (2008a) *Design and analysis of simulation experiments*, Springer Verlag.

Kleijnen, J. P. C. (2008b) Design of experiments: overview. *Proceedings of the 40th Conference on Winter Simulation.* Winter Simulation Conference.

Kleijnen, J. P. C. (2008c) Response surface methodology for constrained simulation optimization: an overview. *Simulation Modelling Practice and Theory* **16,** 5064.

Kosma, A. and Cunningham, H. (1962) Tables for calculating the compressive surface stresses and deflections in the contact of two solid elastic bodies where principal plans of curvature do not coincide. *Journal of Industrial Mathematics, Detroit, MI* **12,** 31-40.

Kremmer, M. and Favier, J. F. (2000) Coupling discrete element and rigid body dynamics. *ASAE Paper No. 003077 3077, St. Joseph, Michigan* **1,** 971-980.

Kremmer, M. and Favier, J. F. (2001) A method for representing boundaries in discrete element modelling - Part I: Geometry and contact detection. *International Journal for Numerical Methods in Engineering* **51,** 1407-1421.

Kuo, H. P., Shih, P. Y. and Hsu, R. C. (2006) Coupled axial-radial segregation in rotating drums with high fill levels. *AIChE journal* **52,** 2422-2427.

Lambe, T. W. and Whitman, R. V. (2008) *Soil mechanics SI version*, Wiley India Pvt. Ltd.

Landry, J. W., Grest, G. S., Silbert, L. E. and Plimpton, S. J. (2003) Confined granular packings: Structure, stress, and forces. *Physical Review E* **67,** 41303.

Laurent, B. F. C., Bridgwater, J. and Parker, D. J. (2002) Convection and segregation in a horizontal mixer. *Powder technology* **123,** 9-18.

Li, J., Langston, P. A., Webb, C. and Dyakowski, T. (2004) Flow of sphero-disc particles in rectangular hoppers - a DEM and experimental comparison in 3D. *Chemical Engineering Science* **59,** 5917-5929.

Li, Y., Xu, Y. and Thornton, C. (2005) A comparison of discrete element simulations and experiments for sandpiles composed of spherical particles. *Powder Technology* **160,** 219-228.

Lim, S.-Y., Davidson, J. F., Forster, R. N., Parker, D. J., Scott, D. M. and Seville, J. P. K. (2003) Avalanching of granular material in a horizontal slowly rotating cylinder: PEPT studies. *Powder Technology* **138,** 25-30.

Liu, L., Wong, Y. S. and Lee, B. H. K. (2002) Non-linear aeroelastic analysis using the point transformation method, Part 1: Freeplay model. *Journal of Sound and Vibration* **253,** 447-469.

Lois, G., Lemaitre, A. and Carlson, J. (2004) Granular Temperature in Shear Granular Flows. *APS Meeting Abstracts.*

Lorenz, A., Tuozzolo, C. and Louge, M. Y. (1997) Measurements of impact properties of small, nearly spherical particles. *Experimental mechanics* **37,** 292-298.

Lukaszuk, J., Stasiak, M., Rusinek, R. and Horabik, J. (2001) Effect of moisture content on the angle of internal friction of cereal grain. *Acta Agrophysica* **46,** 105-113.

Masroor, S. A., Zachary, L. W. and Lohnes, R. A. (1987) A test apparatus for determining elastic constants of bulk solids. *SEM Spring Conference on Experimental Mechanics, Houston, TX, USA.*

Matsushima, T. (2004) 3-D image-based discrete element modeling for irregular-shaped grains. *Symposium, 2nd International PFC, Kyoto.* A. A. Balkema Publishers.

Matsushima, T. and Saomoto, H. (2002) Discrete element modeling for irregularly-shaped sand grains. *Proc. NUMGE2002: Numerical Methods in Geotechnical Engineering***,** 239–246.

Matsushima, T., Saomoto, H., Matsumoto, M., Toda, K. and Yamada, Y. (2003) Discrete element simulation of an assembly of irregularly-shaped grains: Quantitative comparison with experiments. *ASCE Engineering Mechanics Conference, Seattle, USA.*

McBride, A. T., Govender, I., Powell, M. and Cloete, T. (2004) Contributions to the experimental validation of the discrete element method applied to tumbling mills. *Engineering Computations* **21,** 119-136.

McCulloch, C. E. and Nelder, J. A. (1983) *Generalized Linear Models*, Chapman and Hall.

McLean, R. A. and Anderson, V. L. (1984) *Applied Fractional Factorial Designs*, Marcel Dekker, New York.

Mellmann, J. (2001) The transverse motion of solids in rotating cylinders; forms of motion and transition behavior. *Powder Technology* **118,** 251-270.

Mendeley (2008) Getting Started with Mendeley. *Mendeley Desktop.* London, Mendeley Ltd.

Metcalfe, G., Shinbrot, T., McCarthy, J. J. and Ottino, J. M. (1995) Avalanche mixing of granular solids. *Nature* **374,** 39-41.

Microsoft Office (2007) Microsoft Excel. Redmond, Washington, United States.

Mindlin, R. D. and Deresiewicz, H. (1953) Elastic Spheres in Contact Under Varying Oblique Forces. *ASME Journal of Applied Mechanics* **20,** 327-344.

Mishra, B. K. (2003a) A review of computer simulation of tumbling mills by the discrete element method: Part I - contact mechanics. *International Journal of Mineral Processing* **71,** 73-93.

Mishra, B. K. (2003b) A review of computer simulation of tumbling mills by the discrete element method: Part II - Practical applications. *International Journal of Mineral Processing* **71,** 95-112.

Molenda, M., Horabik, J., Ross, I. J. and Montross, M. D. (2002) Friction of wheat: grain-on-grain and on corrugated steel. *Transactions of the ASAE* **45,** 415-420.

Molenda, M., Thompson, S. A. and Ross, I. J. (2000) Friction of Wheat on Corrugated and Smooth Galvanized Steel Surfaces. *Journal of Agricultural Engineering Research* **77,** 209-219.

Munjiza, A. (2004) *The combined finite-discrete element method,* Sussex, England, John Wiley and Sons Inc.

Muthuswamy, M. and Tordesillas, A. (2006) How do interparticle contact friction, packing density and degree of polydispersity affect force propagation in particulate assemblies? *Journal of Statistical Mechanics: Theory and Experiment* **2006,** 9003-9003.

Myers, R. H. and Montgomery, D. C. (1971) *Response surface methodology*, Allyn and Bacon Boston.

Myers, R. H., Montgomery, D. C. and Anderson-Cook, C. M. (2009) *Response surface methodology: process and product optimization using designed experiments*, Wiley.

Nakagawa, M., Altobelli, S. A., Caprihan, A. and Fukushima, E. (1997) NMRI study: axial migration of radially segregated core of granular mixtures in a horizontal rotating cylinder. *Chemical Engineering Science* **52,** 4423-4428.

Nakagawa, M., Altobelli, S. A., Caprihan, A., Fukushima, E. and Jeong, E.-K. (1993) Non-invasive measurements of granular flows by magnetic resonance imaging. *Experiments in Fluids* **16,** 54-60.

Nedderman, R. M. (1992) *Statics and kinematics of granular materials*, Cambridge, Cambridge Univ Pr.

Nelder, J. and Mead, R. (1965) A simplex algorithm for function minimization. *The Computer Journal*. **7,** 308-313.

Ning, Z. and Ghadiri, M. (1996) Incorporation of Rayleigh damping into TRUBAL and determination of the critical time step.

O'Neill, R. (1971) Function minimization using a simplex procedure. *Journal of the Royal Statistical Society, Series C (Applied Statistics)*, **20,** 338-345.

O'Sullivan, C. and Bray, J. D. (2004) Selecting a suitable time step for discrete element simulations that use the central difference time integration scheme. *Engineering Computations* **21,** 278-303.

O'Sullivan, C., Bray, J. D. and Riemer, M. (2004a) Examination of the response of regularly packed specimens of spherical particles using physical tests and discrete element simulations. *Journal of engineering mechanics* **130,** 1140.

O'Sullivan, C., Cui, L. and Bray, J. D. (2004b) Three-dimensional discrete element simulations of direct shear tests. *Numerical Modeling in Micromechanics Via Particle Methods-2004: Proceedings of the 2nd International PFC Symposium, Kyoto, Japan, 28-29 October 2004.* Taylor and Francis.

Odagi, K., Tanaka, T. and Yamane, K. (2002) DEM simulation of compression test of particles. *Proceedings of World Congress on Particle Technology.*

Ooi, J. Y. (1990) Bulk solid behaviour and silo wall pressures. School of Civil and Mining Engineering. Sydney, University of Sydney. PhD.

Ooi, J. Y., Hardy, M. S. A. and Wood, G. S. (2005) *Soil Mechanics Databook.*

Ooi, J. Y., Pham, L. and Rotter, J. M. (1990) Systematic and random features of measured pressures on full-scale silo walls. *Engineering Structures* **12,** 74-87.

Orpe, A. and Khakhar, D. V. (2001) Scaling relations for granular flow in quasi-two-dimensional rotating cylinders. *Physical Review E* **64,** 31302.

Park, K. and Ahn, J. (2004) Design of experiment considering two-way interactions and its application to injection molding processes with numerical analysis. *Journal of Materials Processing Technology* **146,** 221-227.

Plackett, R. L. and Burman, J. P. (1946) The design of optimum multifactorial experiments. *Biometrika* **33,** 305.

Powell, M. and McBride, A. T. (2004) A three-dimensional analysis of media motion and grinding regions in mills. *Minerals Engineering* **17,** 1099-1109.

Prasad, A. K. (2000) Particle image velocimetry. *Current Science* **79,** 51-60.

Rao, S. J., Bhatia, S. K. and Khakhar, D. V. (1991) Axial transport of granular solids in rotating cylinders. Part 2. Experiments in a non-flow system. *Powder Technology* **67,** 153-162.

Renouf, M., Bonamy, D., Dubois, F. and Alart, P. (2005) Numerical simulation of two-dimensional steady granular flows in rotating drum: On surface flow rheology. *Physics of Fluids* **17,** 103303.

Ristow, G. H. (1996) Dynamics of granular materials in a rotating drum. *Europhysics Letters (EPL)* **34,** 263-268.

Ristow, G. H. (1998) Flow properties of granular materials in three-dimensional geometries. *Habilitation, Philipps-Universitat Marburg*.

Rotter, J. M. (2001) *Guide for the economic design of circular metal silos*, Taylor and Francis.

Rotter, J. M., Holst, J. M. F. G., Ooi, J. Y. and Sanad, A. M. (1998) Silo Pressure Predictions Using Discrete-Element and Finite-Element Analyses. *Philosophical Transactions: Mathematical, Physical and Engineering Sciences* **356,** 2685-2712

Rotter, J. M., Pham, L. and Neilsen, J. (1986) On the specification of loads for the structural design of bins and silos. *Second International Conference on Bulk Materials Storage, Handling and Transportation: 1986; Preprints of Papers.* Institution of Engineers, Australia.

Rutgers, R. (1965) Longitudinal mixing of granular material flowing through a rotating cylinder: Part I. Descriptive and theoretical. *Chemical Engineering Science* **20,** 1079-1087.

Sakaguchi, H., Ozaki, E. and Igarashi, T. (1993) Plugging of the flow of granular materials during the discharge from a silo. *International Journal of Modern Physics B* **7,** 1949-1963.

Santomaso, A. C., Ding, Y. L., Lickiss, J. R. and York, D. W. (2003) Investigation of the granular behaviour in a rotating drum operated over a wide range of rotational speed. *Science* **81,** 936-945.

Schwedes, J. (2003) Review on testers for measuring flow properties of bulk solids. *Granular Matter* **5,** 1-43.

Sepulveda, N., Krstulovic, G. and Rica, S. (2005) Scaling laws in granular continuous avalanches in a rotating drum. *Physica A: Statistical Mechanics and its Applications* **356,** 178-183.

Shelef, L. and Mohsenin, N. N. (1969) Effect of moisture content on mechanical properties of shelled corn. *Cereal Chemistry* **46,** 242-253.

Sherritt, R. G., Chaouki, J., Mehrotra, A. K. and Behie, L. A. (2003) Axial dispersion in the three-dimensional mixing of particles in a rotating drum reactor. *Chemical Engineering Science* **58,** 401-415.

StatSoft (2009) Statistica. 9.0 ed. Tulsa, OK, USA, StatSoft, Inc.

Sukumaran, B. and Ashmawy, A. K. (2001) Quantitative characterisation of the geometry of discrete particles. *Géotechnique* **51,** 619-627.

Swisher, J. R., Hyden, P. D., Jacobson, S. H. and Schruben, L. W. (2000) A Survey Of Simulation Optimization Techniques And Procedures. *Proceedings of the 2000 Winter Simulation Conference***,** 119-128.

Taberlet, N. and Richard, P. (2006) Diffusion of a granular pulse in a rotating drum. **73,** 1-6.

Taberlet, N., Richard, P. and Hinch, J. E. (2006) S shape of a granular pile in a rotating drum. *Physical Review E* **73,** 50301.

Taguchi, G. (1987) *System of experimental design*, Unipub New York.

Terzaghi, K. (1943) *Theoretical soil mechanics*, Wiley New York.

Thompson, S. A. and Ross, I. J. (1983) Compressibility and frictional coefficient of wheat. *Transactions of the ASAE* **26,** 1171-1176.

Tijskens, E., Ramon, H. and De Baerdemaeker, J. (2003) Discrete element modelling for process simulation in agriculture. *Journal of Sound and Vibration* **266,** 493-514.

Timoshenko, S. P. and Goodier, J. N. (1970) *Theory of elasticity*, New York, McGraw-Hill.

Tsuji, Y., Kawaguchi, T. and Tanaka, T. (1993) Discrete particle simulation of two-dimensional fluidized bed. *Powder Technology* **77,** 79-87.

Tsuji, Y., Tanaka, T. and Ishida, T. (1992) Lagrangian numerical simulation of plug flow of cohesionless particles in a horizontal pipe. *Powder technology* **71,** 239250.

Uysal, İ. and Güvenir, H. A. (1999) An overview of regression techniques for knowledge discovery. *The Knowledge Engineering Review* **14,** 319-340.

Van Puyvelde, D. R. (2006) Comparison of discrete elemental modelling to experimental data regarding mixing of solids in the transverse direction of a rotating kiln. *Chemical Engineering Science* **61,** 4462-4465.

Vu-Quoc, L. and Zhang, X. (1999a) An accurate and efficient tangential force-displacement model for elastic frictional contact in particle-flow simulations. *Mechanics of Materials* **31,** 235-269.

Vu-Quoc, L. and Zhang, X. (1999b) An elastoplastic contact force-displacement model in the normal direction: displacement-driven version. *Proceedings: Mathematical, Physical and Engineering Sciences* **455,** 4013-4044.

Vu-Quoc, L., Zhang, X. and Lesburg, L. (2000) A Normal Force-Displacement Model for Contacting Spheres Accounting for Plastic Deformation: Force-Driven Formulation. *Journal of Applied Mechanics* **67,** 363.

Walton, O. R. (1984) Motion of single frictional granules on rotating drum cylinders and cones. *Laser Program Annual Repose, Lawrence Livermore National Laboratory Report* **84,** 7.12-7.17.

Walton, O. R. (1994) Effects of interparticle friction and particle shape on dynamic angles of repose via particle-dynamics simulation. *Mechanical and Statistical Physics of Particulate Materials.* California.

Walton, O. R. and Braun, R. L. (1993) Simulation of rotary drum and repose tests for friction spheres and rigid clusters. *Workshop on flow particulates and fluids*.

Wang, L., Park, J. and Fu, Y. (2007a) Representation of real particles for DEM simulation using X-ray tomography. **21,** 338-346.

Wang, L., Park, J. and Fu, Y. (2007b) Representation of real particles for DEM simulation using X-ray tomography. *Construction and Building Materials* **21,** 338-346.

Westerweel, J. (1997) Fundamentals of digital particle image velocimetry. *Measurement Science and Technology* **8,** 1379-1392.

Wilms, H. (1992) Criteria for evaluation of silo design codes. *ZKG International, Edition B* **45,** 110-114.

Wu, C. F. J. and Hamada, M. (2000) *Experiments: planning, analysis, and parameter design optimization*, Wiley New York.

Xu, Y. and Yung, K. L. (2003) The effect of inertial normal force on the rolling friction of a soft sphere on a hard plane. *EPL (Europhysics Letters)* **61,** 620.

Yang, C. S., Kao, S. P., Lee, F. B. and Hung, P. S. (2004) Twelve different interpolation methods: A case study of Surfer 8.0. *Proceedings of the XXth ISPRS Congress.*

Yang, R. Y., Yu, A. B., McElroy, L. and Bao, J. (2008) Numerical simulation of particle dynamics in different flow regimes in a rotating drum. *Powder Technology* **188,** 170-177.

Yang, R. Y., Zou, R. P. and Yu, A. B. (2003) Microdynamic analysis of particle flow in a horizontal rotating drum. *Powder Technology* **130,** 138-146.

Zhang, X. and Vu-Quoc, L. (2000) Simulation of chute flow of soybeans using an improved tangential force-displacement model. *Mechanics of Materials* **32,** 115-129.

Zhang, X., Yao, Q., Li, S. Q., Zhao, X. L. and Liu, G. Q. (2006) Characterization of cascading granular flow in a quasi-two-dimensional rotating drum. *2006 AIChE Spring National Meeting - 5th World Congress on Particle Technology*.

Zhou, Y., Wright, B., Yang, R. Y., Xu, B. and Yu, A. (1999) Rolling friction in the dynamic simulation of sandpile formation. *Physica A: Statistical Mechanics and its Applications* **269,** 536-553.

Zhou, Y. C., Yu, A. B., Stewart, R. L. and Bridgwater, J. (2004) Microdynamic analysis of the particle flow in a cylindrical bladed mixer. *Chemical Engineering Science* **59,** 1343-1364.

Zhu, H. and Yu, A. B. (2002) Averaging method of granular materials. *Physical Review E* **66,** 1-10.

Zhu, H. P. and Yu, A. B. (2004) Steady-state granular flow in a three-dimensional cylindrical hopper with flat bottom: microscopic analysis. *Journal of Physics D: Applied Physics* **37,** 1497.

Zuriguel, I., Gray, J. M. N. T., Peixinho, J. and Mullin, T. (2006) Pattern selection by a granular wave in a rotating drum. *Physical Review E* **73,** 71-74.

Appendix A

A.1 Jenike bulk friction experiments

The shearing response for various granular materials obtained from Jenike bulk friction experiments are show in Figure A.1. The experiment was carried out using a Jenike shear cell with a diameter of 143 *mm* and the upper shear ring was displaced at a nominal rate ~1 *mm*/*min* in all tests. Two different experiments were conducted; the first used two shearing rings to determine the bulk internal friction $\mu_{pp,bulk}$, the second used one shear ring on an acrylic surface to determine the bulk particle to wall friction $\mu_{pw,bulk}$.

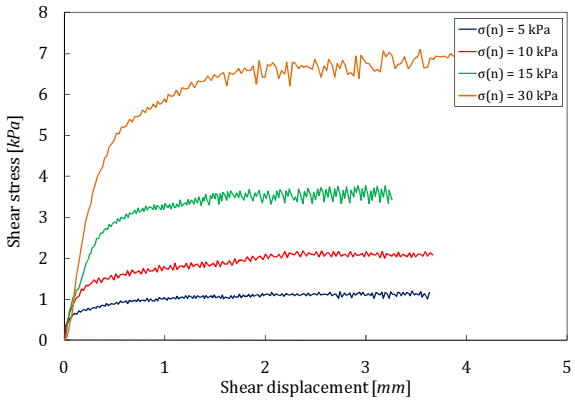

(a) Single glass beads, wall friction

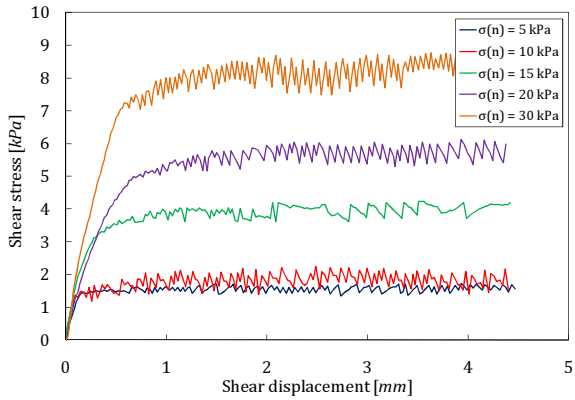

(b) Paired glass beads, wall friction

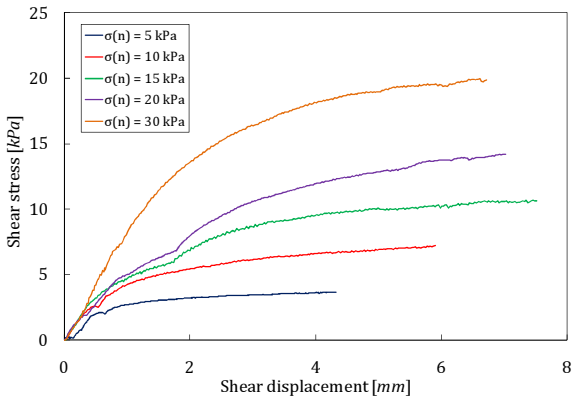

(c) PET pellets, internal friction

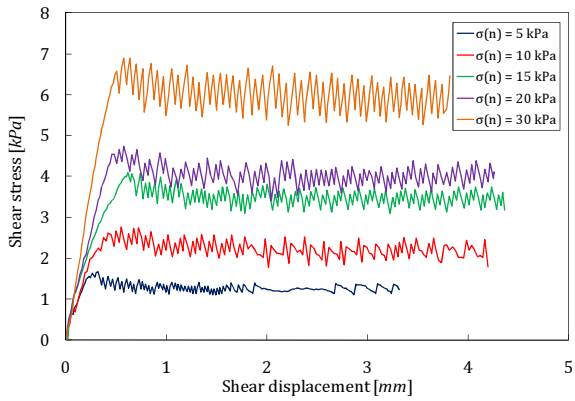

(d) PET pellets, wall friction

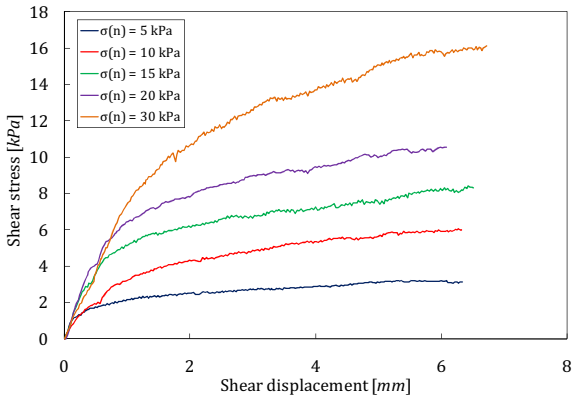

(e) Black eyed beans, internal friciton

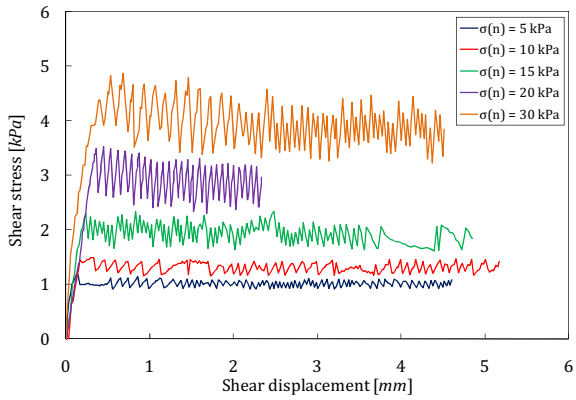

(f) Black eyed beans, wall friciton

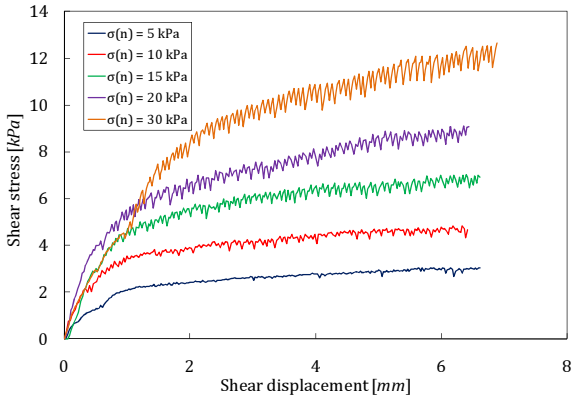

(g) Black kidney beans, internal friciton

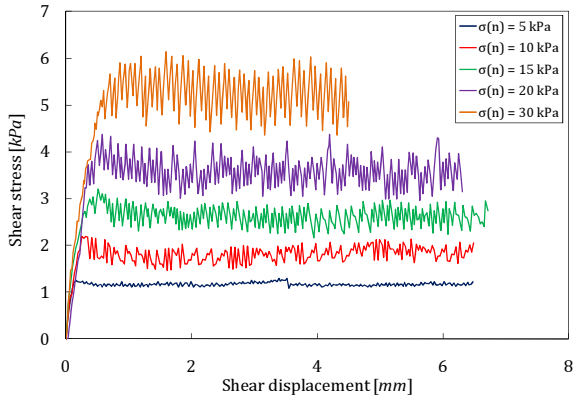

(h) Black kidney beans, wall friciton

Figure A.1 Shearing response for various granular materials obtained from Jenike bulk friction experiments

A.2 Absorption of normal forces in a Jenike shear cell through wall friction

The normal stress used to determine the coefficient of friction in the Jenike shear cell experiments is based on the total load applied to the top of the sample. It is generally assumed that the entire load is transferred to the plane of shear. However, this may lead to overestimation of the normal loads as some of the load will be absorbed through wall friction along the inside of the shear ring. An equation for the actual stress at the shear plane is derived below. Assume the typical setup of the Jenike shear tester shown in Figure A.2.

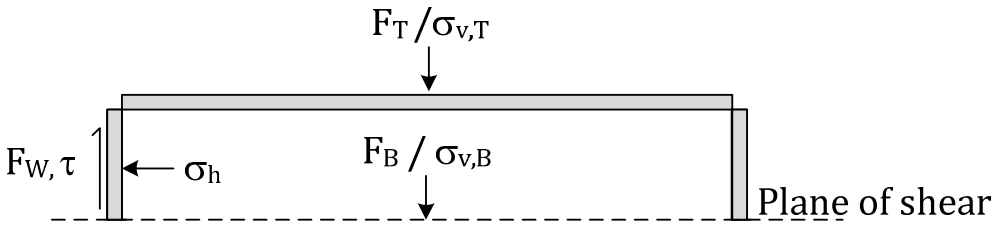

Figure A.2 Typical setup of a Jenike shear tester

$$\sigma_h = K\sigma_v \quad \text{Equation A.1}$$

$$\tau = \mu\sigma_h = \mu K\sigma_{v,T} \quad \text{Equation A.2}$$

$$F_W = 2\pi RH.\tau = 2\pi RH.\mu K\sigma_{v,T} \quad \text{Equation A.3}$$

$$F_T = \sigma_{v,T} \cdot \pi R^2 \quad \text{Equation A.4}$$

$$F_B = F_T - F_W = \sigma_{v,T} \cdot \pi R^2 - 2\pi RH.\mu K\sigma_{v,T} \quad \text{Equation A.5}$$

$$F_B = \sigma_{v,T} \cdot \pi[R^2 - 2RH.\mu K] \quad \text{Equation A.6}$$

$$\sigma_{v,B} = \frac{F_B}{\pi R^2} \quad \text{Equation A.7}$$

$$\sigma_{v,B} = \sigma_{v,T} - \left[1 - \frac{2H \cdot \mu_{pp} \cdot K}{R}\right] \quad \text{Equation A.8}$$

A.3 Dynamic angle of repose for glass beads over a wide range of rotational speeds

The influence of rotational speed on the dynamic angle of repose for single and paired glass beads in a rotating drum is shown in Figure A.3. This covers a wider range of rotational speeds than was used in the thesis.

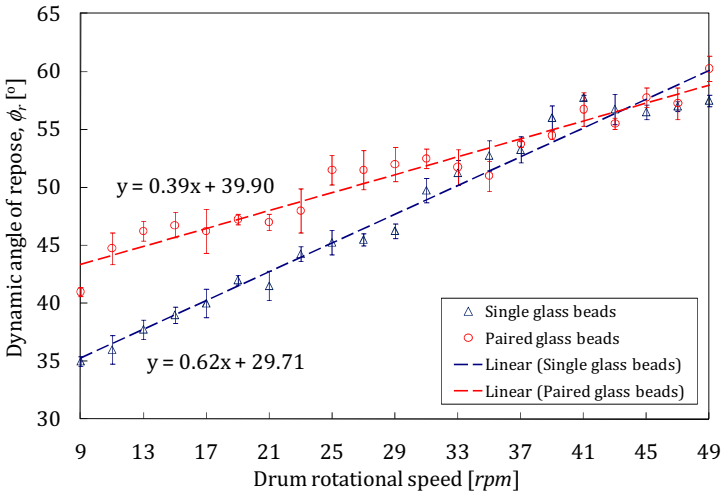

Figure A.3 The influence of rotational speed on the dynamic angle of repose using single and paired glass beads for a wide range of speeds

Each data point is an average of 10 images and the error bar represents the standard deviation

A.4 Control test for bulk densities using a 1 litre mould

The bulk densities and initial void ratios of the various materials were measured using two filling methods; an ascending cone (loose) and vibrating plate (dense) method. Each test was carried out three times for repeatability. A control test was carried out using a British Standard Institute 1 litre compaction mould (BS 1377-4 1990). The results are shown in Table A.1. See section 3.2.3.1 for more details.

Table A.1 Control test for bulk density measurements of granular material using a 1 litre compaction mould (BS 1377-4 1990)

Material	Filling method	e_0	AVG ρ	COV
PET pellets	Ascending cone	0.67	747	0.8%
	Vibrating plate	0.53	815	1.0%
Black eyed beans	Ascending cone	0.62	732	0.8%
	Vibrating plate	0.53	777	0.8%
Black kidney beans	Ascending cone	0.66	769	0.9%
	Vibrating plate	0.56	819	0.1%

AVG: Average, COV: coefficient of variance, e_o: initial void ratio, ρ: bulk density, Sample size=3

Appendix B

B.1 DEM implementation for numerical simulations

The DEM implementation for the numerical simulations conducted in this study have been highlighted and described in the main body the thesis, unless specified otherwise. The remaining DEM input parameters are listed in Table B.1. These parameters were used for the numerical particle stiffness and confined compression speed sensitivity investigations (see section 5.4). These input parameters are based primarily on the measured particle properties of Chung (2006) and Härtl (2008).

Table B.1 DEM implementation of numerical simulations used in the optimisation procedure

PP, PW coefficient of static friction ($\mu_{pp},\ \mu_{pw}$)	0.34
PP, PW coefficient of restitution ($e_r,\ e_{r,pw}$)	0.59
PP, PW coefficient of rolling friction ($\mu_{r,pp},\ \mu_{r,pw}$)	0.00
Poisson's Ratio	0.4
Particle Density [kg/m^3]	1200
Sphere radius [mm]	3
Fixed % of Rayleigh time step	20%

B.2 Producing dense and loose packing arrangements in DEM simulations

To achieve a denser or looser packing arrangement in DEM simulations, parametric alteration may be necessary. This may be achieved using the method highlighted in section 5.2 and the DEM input parameters listed in Table B.2.

Table B.2 DEM implementation used to artificially alter the packing arrranegement of simualtions

DEM Parameter	Original	Filling method	
		Loose	Dense
Particle-particle coefficient of friction	0.20	1.00	0.01
Particle-wall coefficient of friction	0.24	1.00	0.01
Particle generation rate [*particles/sec*]	1000	5000	250

Appendix C

C.1 Available batch mode console flags found in EDEM

The DEM software used in this thesis EDEM (DEM Solutions Ltd 2009) allows simulations to be run in batch mode from a console. The input decks for each simulation must be set up before and after which the console will carry out the processing based on the user specified parameter. The possible console processing flags for EDEM's batch mode as shown in Table C.1.

Table C.1 Console processing flags for EDEM's batch mode

Processing Options	Console Flags
Total Simulation run time	*-r*
Write out interval	*-w*
Grid cell size	*-g*
Time step	*-t*
Number of Processors	*-p*

Example of the batch mode command lines to run input files *a*, *b* and *c* for *20* seconds at *0.1* second write out, using a grid size cell of *2*, a time step of *0.00806* and *8* processors is shown below

```
c:
cd "c:\Program Files\DEM Solutions\EDEM v2.0.0\bin"
edem.exe -console -i "C:\EDEM_runs\a.dem" -r 20 -w 0.1 -g 2 -t 0.00806 -p 8
edem.exe -console -i "C:\EDEM_runs \b.dem" -r 20 -w 0.1 -g 2 -t 0.00806 -p 8
edem.exe -console -i "C:\EDEM_runs \c.dem" -r 20 -w 0.1 -g 2 -t 0.00806 -p 8
```

C.2 DOE Dataset

The complete set of results for the reduced factorial design of experiment (DOE) dataset used in the thesis is presented Table C.2.

Table C.2 DOE numerical dataset used in the parametric optimisaiton

Run	DEM input parameters				Dynamic ϕ_r		Bulk stiffness parameter		
	G	e_r	μ_{pp}	$\mu_{r,pp}$	AVG	COV	e_0	λ	κ
1	1E+06	0.1	0.1	0.00	31.1	3.5%	0.48	1.3E-01	8.6E-02
2	1E+09	0.1	0.1	0.04	36.3	3.5%	0.55	4.4E-03	1.3E-03
3	1E+07	0.1	0.1	0.10	38.9	5.5%	0.53	5.8E-02	2.7E-02
4	1E+09	0.1	0.3	0.00	36.7	2.2%	0.56	3.3E-03	1.4E-03
5	1E+07	0.1	0.3	0.04	43.4	4.0%	0.54	6.8E-02	2.3E-02
6	1E+06	0.1	0.3	0.10	48.4	3.2%	0.48	1.3E-01	9.6E-02
7	1E+07	0.1	0.6	0.00	38.7	3.2%	0.54	6.9E-02	2.4E-02
8	1E+06	0.1	0.6	0.04	44.6	3.5%	0.50	1.3E-01	9.7E-02
9	1E+09	0.1	0.6	0.10	49.0	1.9%	0.56	2.7E-03	1.7E-03
10	1E+09	0.5	0.1	0.00	30.6	2.4%	0.55	3.0E-03	1.4E-03
11	1E+07	0.5	0.1	0.04	35.8	3.4%	0.53	2.8E-02	1.6E-02
12	1E+06	0.5	0.1	0.10	36.6	3.0%	0.49	1.7E-01	7.7E-02
13	1E+07	0.5	0.3	0.00	37.7	4.2%	0.54	2.4E-02	1.5E-02
14	1E+06	0.5	0.3	0.04	41.3	4.2%	0.51	8.7E-02	4.8E-02
15	1E+09	0.5	0.3	0.10	48.7	2.7%	0.56	5.8E-03	1.2E-03
16	1E+06	0.5	0.6	0.00	37.7	2.1%	0.51	7.9E-02	6.0E-02
17	1E+09	0.5	0.6	0.04	43.7	3.7%	0.57	4.1E-03	1.4E-03
18	1E+07	0.5	0.6	0.10	51.9	3.2%	0.55	2.4E-02	1.8E-02
19	1E+07	0.9	0.1	0.00	30.6	2.8%	0.53	2.7E-02	1.5E-02
20	1E+06	0.9	0.1	0.04	32.7	4.3%	0.50	9.9E-02	5.1E-02
21	1E+09	0.9	0.1	0.10	36.1	3.2%	0.55	4.3E-03	1.2E-03
22	1E+06	0.9	0.3	0.00	35.1	3.8%	0.50	8.7E-02	4.8E-02
23	1E+09	0.9	0.3	0.04	42.7	3.7%	0.56	3.7E-03	1.3E-03
24	1E+07	0.9	0.3	0.10	48.9	5.5%	0.54	2.6E-02	1.5E-02
25	1E+09	0.9	0.6	0.00	40.0	2.1%	0.56	2.8E-03	1.6E-03
26	1E+07	0.9	0.6	0.04	43.4	3.0%	0.55	2.4E-02	1.8E-02
27	1E+06	0.9	0.6	0.10	50.9	5.7%	0.51	8.0E-02	6.0E-02

C.3 Parametric investigation on Microsoft Excel's solver algorithm coupled with a weighted inverse distance method

This parametric study investigated the effect of the various options in the Microsoft Excel solver on the optimised parameters. In each case, the calibration data used in each run was:

- Dynamic ϕ_r = 40
- Bulk loading stiffness, λ = 0.009
- Bulk loading stiffness, κ = 0.002
- Weighting sensitivity p = 1

The description of the various runs are as follows

Reset: The starting values of each run

1. Optimise Dynamic ϕ_r only
2. Optimise λ only
3. Optimise κ only
4. Optimise Dynamic ϕ_r and λ
5. Optimise Dynamic ϕ_r and κ
6. Optimise λ and κ
7. Optimise Dynamic ϕ_r, λ and κ
8. Rerun run 1
9. Run 1, with p=10
10. Run 2, with p=10
11. Run 3, with p =10
12. Run 4, with p =10
13. Run 5, with p =10
14. Run 6, with p =10
15. Run 7, with p =10
16. Run 1 with low starting values
17. Run 1 with high starting values
18. Run 16, with p =10
19. Run 17, with p =10
20. Experimental desirability, Dynamic ϕ_r=100%, λ=50% and κ=10%

Table C.3 Optimised parameter results obtained from the parametric study conducted using the Microsoft Excel Solver algorithm

Run	RESET	1	2	3	4	5	6	7	8	9	10
PP static friction, μ_{pp}	0.40	0.11	0.31	0.30	0.20	0.10	0.30	0.30	0.11	0.20	0.40
PP restitution, e_r	0.40	0.42	0.50	0.50	0.50	0.50	0.50	0.50	0.42	0.38	0.44
PP rolling friction, $\mu_{r,pp}$	0.05	0.00	0.10	0.10	0.05	0.00	0.10	0.10	0.00	0.00	0.05
Particle Stiffness, G [Pa]	8.00	8.71	9.00	9.00	9.00	9.00	9.00	9.00	8.71	8.04	8.10
Sum of Error	169.9%	0.0%	0.0%	0.0%	42.6%	28.3%	31.2%	47.9%	0.0%	0.0%	0.0%

Run	RESET	11	12	13	14	15	16	17	18	19	20
PP static friction, μ_{pp}	0.40	0.60	0.22	0.28	0.20	0.18	0.12	0.60	0.20	0.55	0.24
PP restitution, e_r	0.40	0.15	0.43	0.26	0.10	0.51	0.13	0.90	0.13	0.88	0.36
PP rolling friction, $\mu_{r,pp}$	0.05	0.03	0.01	0.00	0.10	0.10	0.03	0.00	0.06	0.10	0.00
Particle Stiffness, G [Pa]	8.00	8.21	8.10	8.19	8.12	8.10	6.24	9.00	6.25	8.85	8.11
Sum of Error	169.9%	0.0%	0.0%	0.0%	46.3%	50.7%	0.0%	0.0%	0.0%	0.0%	4.9%

C.4 Microsoft Excel Solver options

Various parameters are available in the Microsoft Excel Solver (MES) package. A graphical user interface is shown in Figure C.1. The chosen input values used for in the optimisation procedure described in Chapter 6 are listed and explained below.

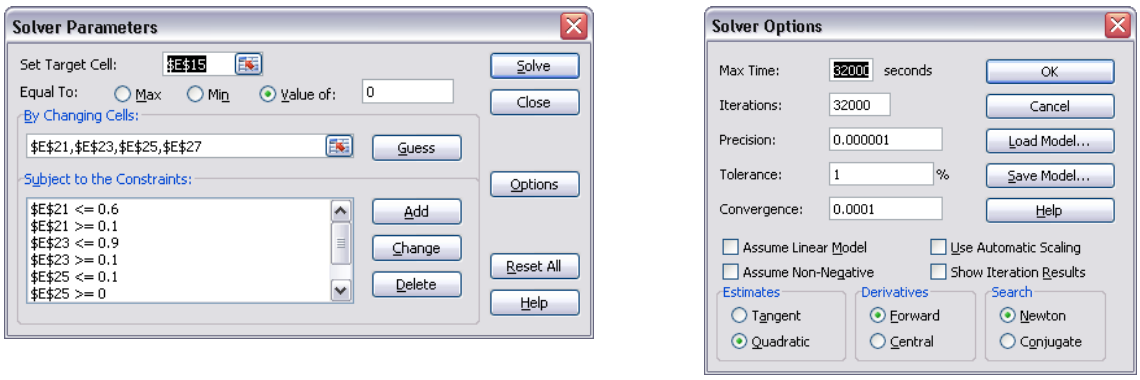

Figure C.1 Graphical user interface for Microsoft Excel Solver options windows

- *Max time*: is how long Solver should work on the problem.
- *Iterations*: is the number of iterations solver will go through during the optimisation.
- *Precision*: is how precise Solver should be working on a possible solution against the constraints.
- *Tolerance*: is how precise Solver should be on meeting integer constraints.
- *Convergence*: lets Solver know when to quit looking for a better solution
- *Assume Linear Model*: lets Solver know that a linear model is being used, making the solution time faster.
- *Assume Non-negative*: lets Solver know variables are >= 0
- *Show Iteration Results*: lets Solver know to pause between iterations.
- *Use Automatic Scaling*: lets Solver know variables are of different magnitudes.
- *Estimates*: Choose Tangent or Quadratic extrapolations; use Quadratic for non-linear optimisation models.
- *Derivatives*: provides clues as to how the adjustable cells should be varied.
- *Search*: allows the choice of the algorithm for Solver to use to find the optimal solution.

C.5 Parametric investigation on the *Profiling and Desirability* tab in Statistica

A parametric study was conducted on to determine the sensitivity of the various options and parameters when using the Profiling and Desirability and $3^{(k-p)}$ *and Box-Behnken Design* tab in Statistica v9.0.

$3^{(k-p)}$ *and Box-Behnken* designs will generate and analyse designs with 3-level factors. In the analysis, the main effects and interactions can be partitioned into linear and quadratic components.

Introduction

Using STATISTICA for the optimisation of the DEM input parameters involved the use of the *Response Desirability Profiling* (RDP) function that can be found under the *Prediction and Profiling* tab. The program option path in Statistica to get to the *response desirability profiling* tab is shown in Figure C.2.

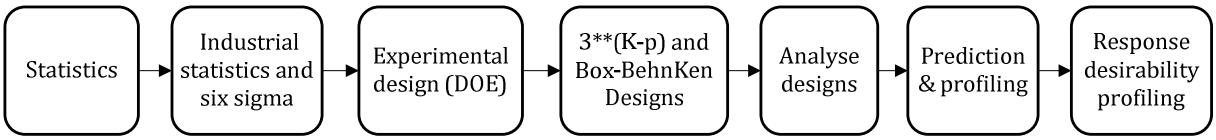

Figure C.2 Program option path in Statistica v9.0

Images of the *Response desirability profiling* option window is shown in Figure C.3 where key options highlighted with circled letters.

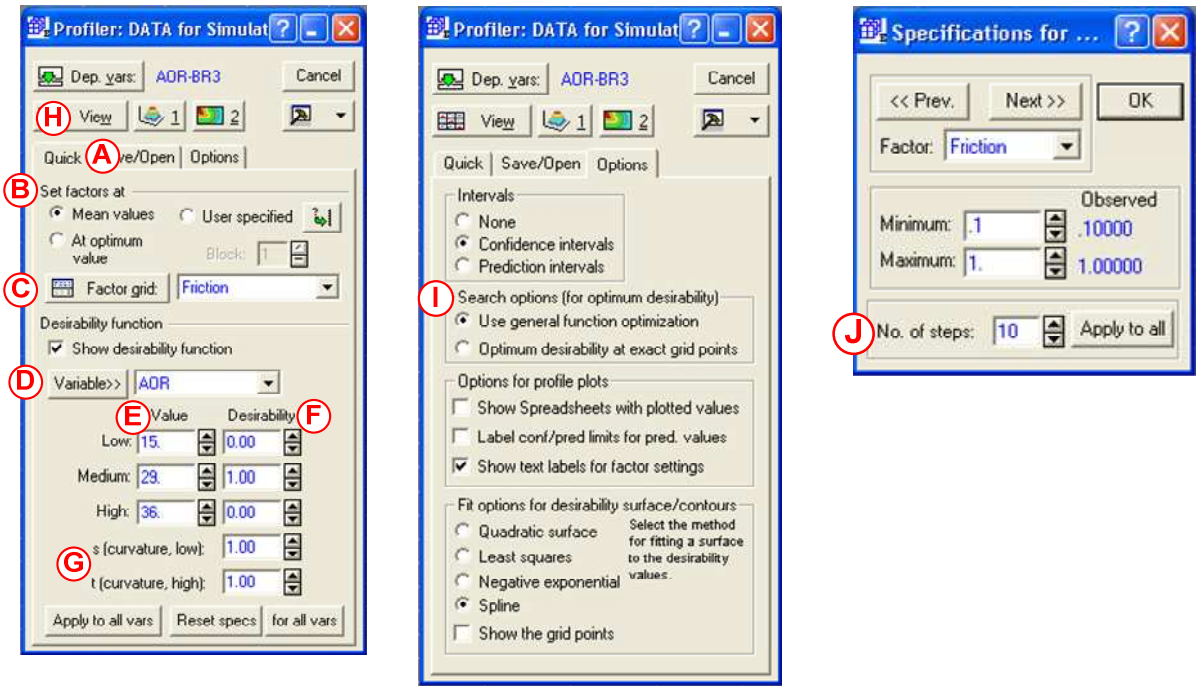

(a) Quick tab (b) Options tab (c) Factor grid

Figure C.3 Various profiler windows

Fictitious data

A set of fictitious data was created with three input parameters and three bulk response parameters. This data was manufactured using predetermined trends to see if the optimisation procedure could detect these. Introducing the raw data into Statistica gave rise to several problems that were subsequently addressed as highlighted in later on. The final set of data that was used in the sensitivity study is shown in Table C.4.

Table C.4 Transformed fictitious raw data used in the sensitivity analysis

Run	Input Parameters			Bulk responses		
	Friction	Log stiffness	Restitution	AOR	UNLD Stiff	BR3
1	0.1	6.22	0.1	15	20000	100
2	0.1	6.22	0.5	16	19000	500
3	0.1	6.22	0.9	17	18000	900
4	0.1	8.22	0.1	17	15000	150
5	0.1	8.22	0.5	18	14000	550
6	0.1	8.22	0.9	19	13000	950
7	0.1	10.22	0.1	19	10000	200
8	0.1	10.22	0.5	20	9000	600
9	0.1	10.22	0.9	21	8000	1000
10	0.5	6.22	0.1	25	19500	110
11	0.5	6.22	0.5	26	18500	510
12	0.5	6.22	0.9	27	17500	910
13	0.5	8.22	0.1	27	14500	160
14	0.5	8.22	0.5	28	13500	560
15	0.5	8.22	0.9	29	12500	960
16	0.5	10.22	0.1	29	9500	210
17	0.5	10.22	0.5	30	8500	610
18	0.5	10.22	0.9	31	7500	1010
19	1.0	6.22	0.1	30	19000	120
20	1.0	6.22	0.5	31	18000	520
21	1.0	6.22	0.9	32	17000	920
22	1.0	8.22	0.1	32	14000	170
23	1.0	8.22	0.5	33	13000	570
24	1.0	8.22	0.9	34	12000	970
25	1.0	10.22	0.1	34	9000	220
26	1.0	10.22	0.5	35	8000	620
27	1.0	10.22	0.9	36	7000	1020

Uniform Low/Mid/High input parameter values for each Bulk Experiment

The analysis method used in Statistica v9.0 is the Select 3**(K-p) and Box-Behnken designs which is a 3-level factorial analysis. The input parameter values chosen for the bulk experiments should remain consistent for each bulk response. For example frictional values of 0.1/0.5/1.0 are chosen for the Low/Mid/High in the confined compression experiment, the same values for should be used for the angle of repose experiment.

C.6 Option sensitivity analysis

The following section will investigated the various options available in the profiler tab and their influence on the optimised parameters.

Reference case

A reference case was setup to evaluate the parametric influence. The implementation values for the reference case can be seen in Table C.5. It can be seen that the target values (b) have been achieved.

Table C.5 Reference case implementation values

(a) Profiler TAB Options

Profiler Tab			Figure C.4 legend
Quick tab	Set factor at	At optimum value	B
	factor grid (number of steps)	10	J
	s'	1	G
	t'	1	G
Option tab	Intervals	Confidence intervals	
	Search option	use general function	I
	fit option for desirability	spline	
Target Value in bold	Desirability (LOW/MID/HIGH)	(0.0,1.0,0.0)	F
	AOR	15/**29**/36	E
	UNLD Stiff	7000/**11000**/20000	E
	BR3	100/***560***/1020	E

(b) Results of the optimisation procedure

Bulk response	AOR	29
	UNLD Stiff	11000
	BR3	700
Input Parameters	Friction	0.49
	log (Stiffness)	9.11
	Restitution	0.62
Desirability achieved	0.99	

Search Options for optimum desirability (Figure C.3: I)

There are two main search options: *use general function optimisation* (GFO) and *optimum desirability at exact grid points* (ODEG). The GFO option (the simplex method of function optimisation) is generally faster, however the default method is ODEG, except when the number of predicted values that must be computed to perform the exhaustive grid search exceeds 200,000. In this case GFO becomes the default options. The ODEG option will perform exhaustive searches for the optimum desirability at every grid point. Using the GFO instead of the ODEG will produce a set of bulk responses that are closer to the target value as well as a

desirability closer to 1 whereas the ODEG will focus around the user-defined grid points and may therefore not be as accurate as well as be very time consuming. Examples of the two search methods for optimum desirability are shown in.

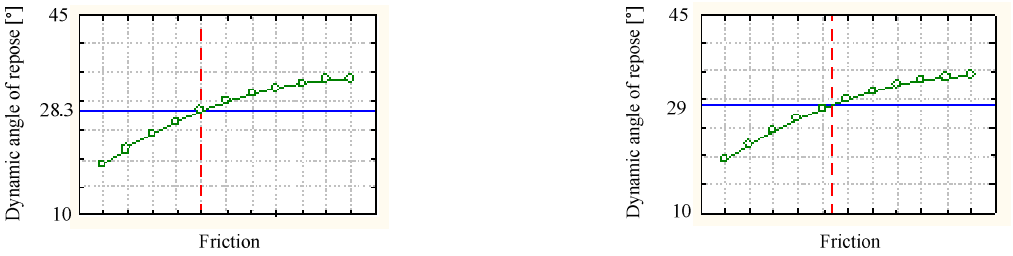

(a) Optimum desirability at exact points (b) Use general function optimisation

Figure C.4 Various search methods avaiable in Statistica v9.0

Factor Grid - Number of steps (Figure C.3 : J)

Enter the no. of steps to specify the number of intervals to apply to the required variable. 3 and 10 step intervals are show in Figure C.5. When using the GFO search method, the number of steps was shown to have minimal effect on the results. However, when using the ***optimum desirability at exact points*** search methods will constraint the search method. In this case, increasing the number of steps will give a greater accuracy.

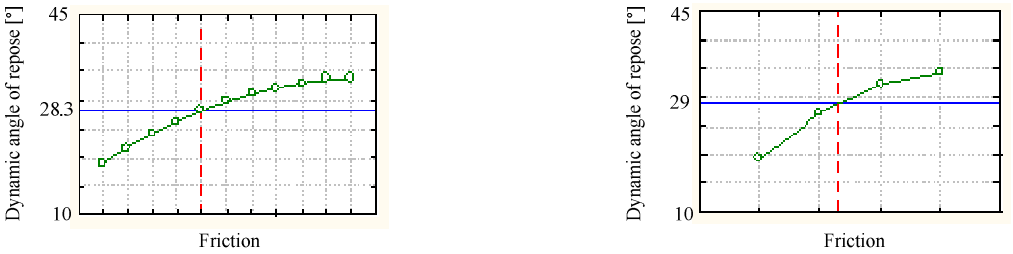

(a) 10 Step interval (b) 3 Step intervals

Figure C.5 Varying number of intervals

Desirability Function (Figure C.3 : D)

When the *Show desirability function* check box is set, desirability function specifications may be entered for the dependent variable displayed in the *Variable* box. These specifications

will determine the desirability function values corresponding to predicted values on the dependent variable.

The various fields for the Desirability function settings and their sensitivity are described below.

Values and desirability (Figure C.3 : E,F)

STATISTICA allows for up to three "inflection points" in the desirability function for predicted values for each dependent variable. As a default the Low and High are set as the lowest and highest values from the raw data and the Medium is the mean. However these can be changed to suit needs. Desirability values (from 0.0 for undesirable to 1.0 for very desirable) can be specified for the corresponding inflection points of the desirability function for each of the dependent variables. So, for the optimisation procedure, the target value (e.g. angle of repose = 29°) has the highest desirability. Several combinations of the values and desirability were carried out as shown in Table C.6.

Table C.6 Various value and desirability combinations for the Bulk response: Angle of repose target values are in Bold

			Low	Mid	High	Error TARGET value
Reference	Description	Value	15	**29**	36	
		Desire	0.0	1.0	0.0	0.00%
1	Narrow range	Value	26.1	**29**	31.9	
		Desire	0.0	1.0	0.0	-1.40%
2	Desire=0.5	Value	15	**29**	36	
		Desire	0.0	0.5	0.0	0.00%
3	Desire plateau	Value	15	26.1	**29**	
		Desire	0.0	0.5	1.0	0.00%
4	High Target	Value	15	**35**	36	
		Desire	0.0	1.0	0.0	-8.57%
5	Low target	Value	15	**18**	36	
		Desire	0.0	1.0	0.0	-8.57%

It can be seen that narrowing the ***values*** range (Table C.6: 1) will constrain Statistica v9.0 and lead to errors. Reducing the Target value desirability from 1.0 to 0.5 (Table C.6: 2) will not

affect the results as long the target desirability has the highest value. Making the target value the HIGH instead of the Mid inflection point will not affect the results greatly.

When the target values are near the extremities of the data range (Table C.6: 4,5) Statistica v9.0 has a little more trouble to determine the optimised parameters.

s&t curvature (Figure C.3 : G)

The desirability of responses need not decrease (or increase) linearly between inflection points in the desirability function. Assuming that an intermediate response is most desirable, a curvature can be added to the desirability between inflection points by changing to values of ***s and t*** (values from 0 to 50 can be used). The effect of varying *s&t* on the desirability function are shown in Figure C.6.

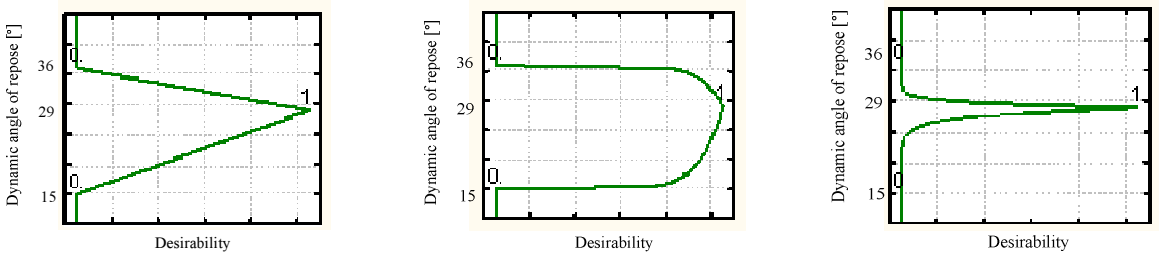

(a) s/t = 1 (b) s/t = 0.1 (c) s/t = 10

Figure C.6 The effect of varying s&t on desirability

The *s&t* did not influence the optimised results greatly. Decreasing the *s&t* value (Figure C.6: b) will allow the searching technique more freedom and may introduce a slight error in the optimised results.

Altering the *s&t* values may be useful if there is a "critical region" close to a desired, Mid response on a dependent variable beyond which the desirability of the response at first drops off very quickly, but drops off less quickly as the departure from the "targeted" value becomes greater.

Set factor at (Figure C.3 : C)

The current levels of the predictor variables for the prediction profile compound graph can be set with this the *Set factor at* option. This can either be set to the ***mean values*** (e.g. if the

restitution parameter ranges from 0.1 to 0.9, the restitution will be fixed at 0.5) or ***user specified*** or ***at optimum value***. This last option will determine the optimum value that will suit the other option's criteria.

The ***at optimum value*** was found to produce the most accurate answers for the optimisation procedure as this option did not constrain Statistica optimisation method.

Optimisation procedure with a known result

This final sensitivity analysis was a quantitative verification. This was done by using the bulk response from 2 runs of the raw data (Table C.7) to see how accurate the Statistica predictions were.

Table C.7 Quantitative verification of Statistica results

Run	Fric.	Stiff.	Rest.	AOR	UNLD STIF	BR3
9	0.1	10.22	0.9	21	8000	1000
Statistica	0.1	10.22	0.9	21	8000	1000
14	0.5	8.22	0.5	28	13500	560
Statistica	0.5	8.22	0.5	28	13500	560

The results and profiling output graphs of the sensitivity analysis can be found in sections C.8 and C.9 respectively.

C.7 Statistica v9.0 option sensitivity analysis data

	Run	REFERENCE CASE	1	2	3	4
	Description	**Target value**	**Search method**	**Factor Grid 5 steps**	**change desire to 0.5**	**Set factor at**
	Profiler Tab					
	Quick tab					
	Set factor at	At optimum value				**mean values**
	factor grid (number of steps)	10		**4**		
	s'	1				
	t'	1				
	Option Tab					
	Intervals	Confidence intervals				
	Search option	use general function	**use general function**			
	fit option for desirability	spline				
	Target Value in bold					
	Desirability (LOW/MID/HIGH)	(0.0,1.0,0.0)			**(0.0,0.5,0.0)**	
	AOR	15/29/36				
	UNLD Stiff	7000/11000/20000				
	BR3	100/560/1020				
	Results of optimisation procedure					
	AOR	29	28.24	29	29	28.593
	Error from TRAGET value	0.00%	-2.62%	0.00%	0.00%	-1.40%
	UNLD Stiff	11000	11346	11000	11000	13462
	Error from TRAGET value	0.00%	3.15%	0.00%	0.00%	22.38%
	BR3	700	659	700	700	560.75
	Error from TRAGET value	0.00%	-5.86%	0.00%	0.00%	-19.89%
	INPUT VALUES					
	Friciton	0.4919	0.46	0.4918	0.4918	0.5333
	Error from TRAGET value	0.00%	-6.49%	-0.02%	-0.02%	8.42%
	Stiffness (log)	9.1064	9.02	9.1064	9.1064	8.22
	Error from TRAGET value	0.00%	-0.95%	0.00%	0.00%	-9.73%
	Restitution	0.61807	0.58	0.61807	0.61807	0.5
	Error from TRAGET value	0.00%	-6.16%	0.00%	0.00%	-19.10%
	Desirability achieved	0.9999	0.9463	0.9999	0.5000	0.8152

	Run	REFERENCE CASE	5	6	7	8
	Description	**Target value**	**arrow Desire range±10%**	**Increasing Desire**	**High taget values**	**Low Target values**
	Profiler Tab					
Quick tab	Set factor at	At optimum value				
	factor grid (number of steps)	10				
	s'	1				
	t'	1				
Option tab	Intervals	Confidence intervals				
	Search option	use general function				
	fit option for desirability	spline				
Target Value in red	Desirability (LOW/MID/HIGH)	(0.0,1.0,0.0)		**0.0,0.5,1.0**		
	AOR	15/29/36	**26.1/29/31.9**	**15/26.1/29**	**15/35/36**	**15/18/36**
	UNLD Stiff	7000/11000/20000	**9900/11000/12100**	**7000/9900/11000**	**7000/19000/20000**	**7000/9000/20000**
	BR3	100/560/1020	**630/700/770**	**100/630/700**	**100/950/1020**	**100/400/1020**
Results of optimisation procedure	AOR	29	28.593	29	32	32
	Error from TRAGET value	0.00%	-1.40%	0.00%	-8.57%	-8.57%
	UNLD Stiff	11000	13462	11000	17000	17000
	Error from TRAGET value	0.00%	22.38%	0.00%	-10.53%	-10.53%
	BR3	700	560.75	700	920	920
	Error from TRAGET value	0.00%	-19.89%	0.00%	-3.16%	-3.16%
	INPUT VALUES					
	Friciton	0.4919	0.5333	0.4919	0.9999	1
	Error from TRAGET value	0.00%	8.42%	0.00%		
	Stiffness (log)	9.1064	8.22	9.1064	6.22	6.22
	Error from TRAGET value	0.00%	-9.73%	0.00%		
	Restitution	0.61807	0.5	0.61807	0.9	0.9
	Error from TRAGET value	0.00%	-19.10%	0.00%		
	Desirability achieved	0.9999	0.0000	1.0000	0.8808	0.2138

	Run	REFERENCE CASE	9	10	11	12	13
	Description	**Target value**	**Mixed High/Low target**	**Target value = run 9**	**Target value = run 14**	**Low s'/t'**	**High s'/t'**
	Profiler Tab						
Quick tab	Set factor at	At optimum value					
	factor grid (number of steps)	10					
	s'	1				0.1	10
	t'	1				0.1	10
Option tab	Intervals	Confidence intervals					
	Search option	use general function					
	fit option for desirability	spline					
Target Value in red	Desirability (LOW/MID/HIGH)	(0.0,1.0,0.0)					
	AOR	15/29/36	**15/30/36**	**15/21/36**	**15/28/36**		
	UNLD Stiff	7000/11000/20000	**7000/9000/20000**	**7000/8000/20000**	**7000/13500/20000**		
	BR3	100/560/1020	**100/750/1020**	**100/1000/1020**	**100/560/1020**		

Results of optimisation procedure	AOR	29	32	21	28	29	29
	Error from TRAGET value	0.00%	-8.57%	0.00%	0.00%	0.00%	0.00%
	UNLD Stiff	11000	17000	8000	13500	11000	11000
	Error from TRAGET value	0.00%	-10.53%	0.00%	0.00%	0.00%	0.00%
	BR3	700	920	1000	560	699.99	700
	Error from TRAGET value	0.00%	-3.16%	0.00%	0.00%	0.00%	0.00%
	INPUT VALUES						
	Friciton	0.4919	1	0.1	0.5	0.49018	0.49016
	Error from TRAGET value	0.00%		0.00%	0.00%	-0.35%	-0.35%
	Stiffness (log)	9.1064	6.22	10.22	8.22	9.1064	9.1064
	Error from TRAGET value	0.00%		0.00%	0.00%	0.00%	0.00%
	Restitution	0.61807	0.9	0.9	0.5	0.61806	0.61806
	Error from TRAGET value	0.00%		0.00%	0.00%	0.00%	0.00%
	Desirability achieved	0.9999	0.4323	1.0000	0.9999	1.0000	0.9999

C.8 Output graphs for the Statistica v9.0 sensitivity analysis

The profiling and desirability plots obtained from Statistica for the various cases studied in the parametric sensitivity study discussed in section C.6 are shown in Figure C.7.

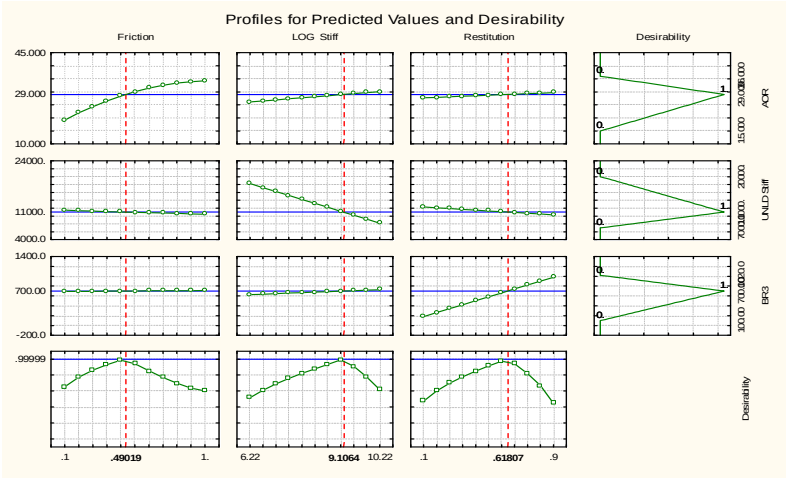

Reference case

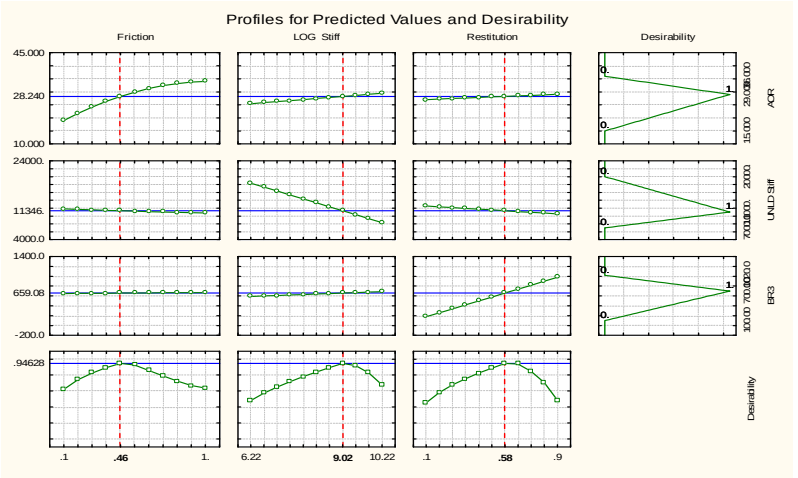

Case 1

Figure C.7 Profiling and desirability plots obtained from Statistica for the various cases studied in the parametric sensitivity study

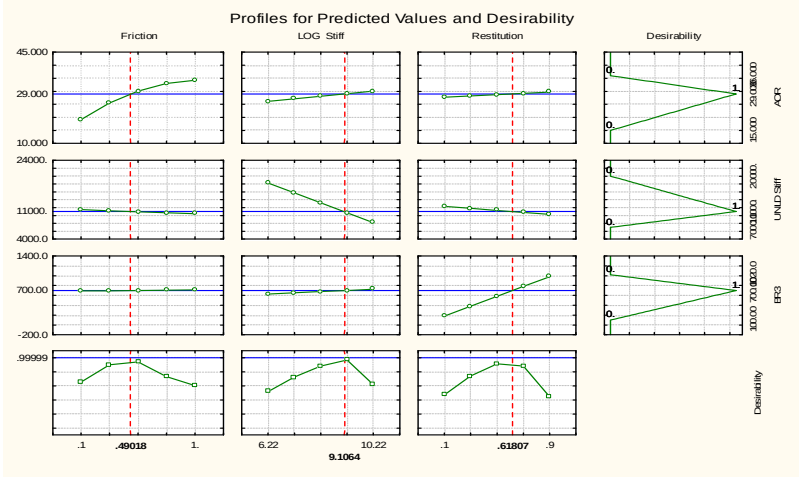

Case 2

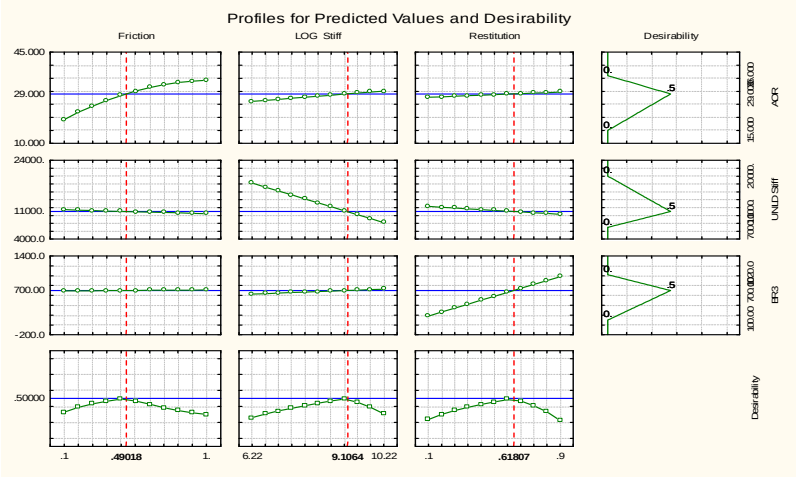

Case 3

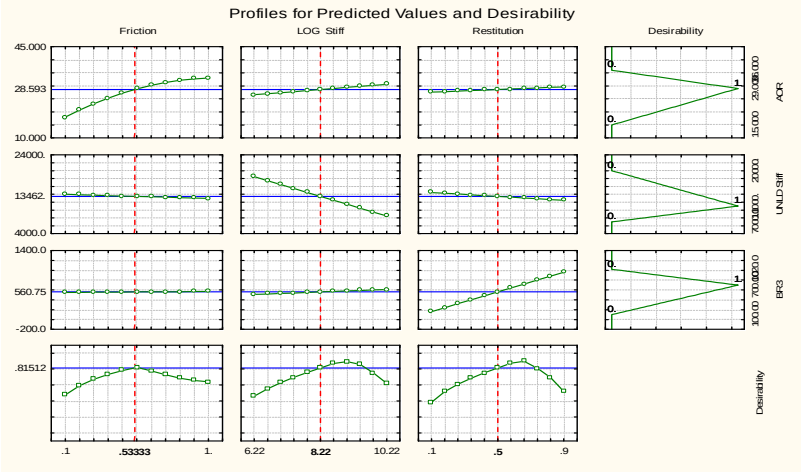

Case 4

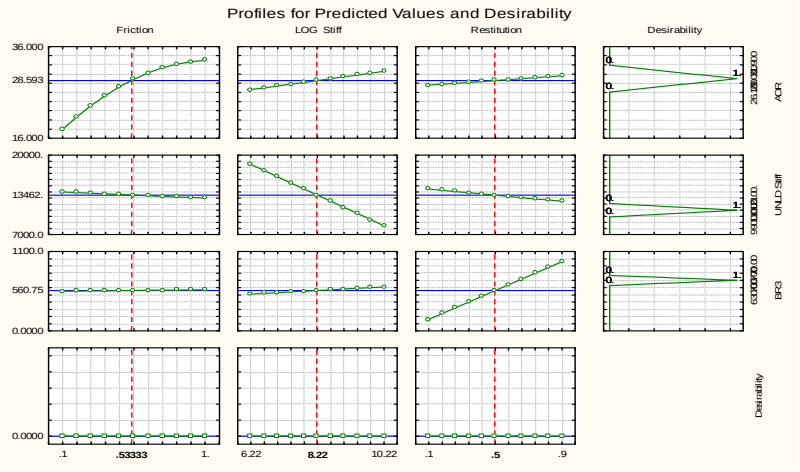

Case 5

Figure C.7 Profiling and desirability plots obtained from Statistica for the various cases studied in the parametric sensitivity study

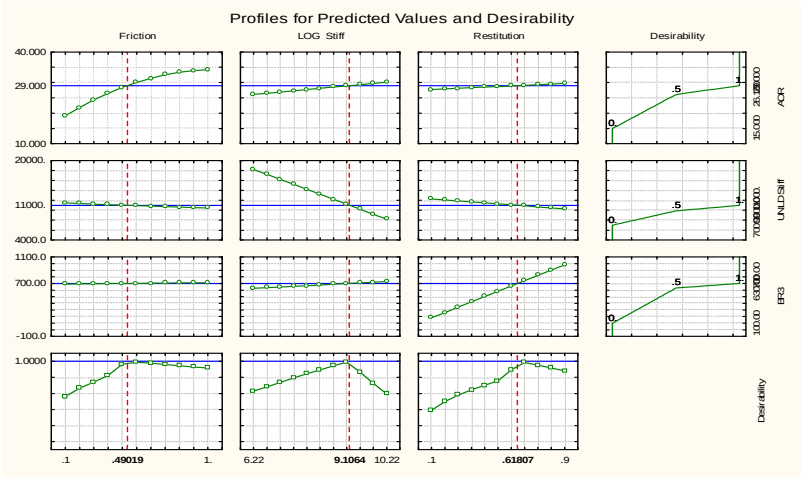

Case 6

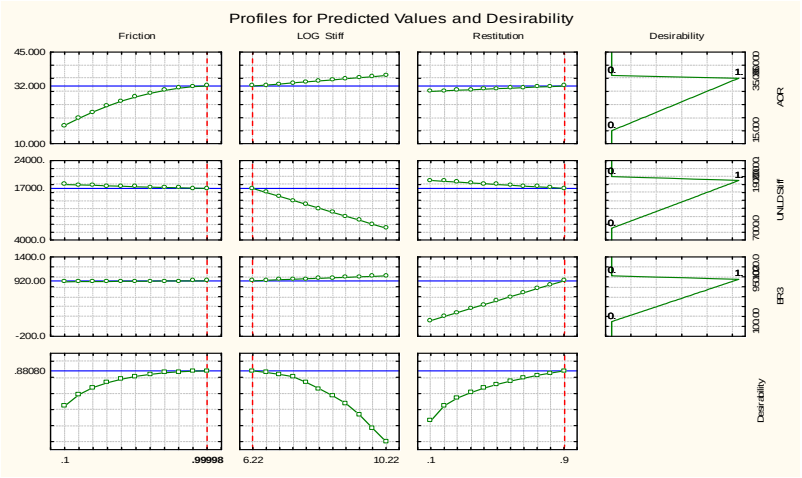

Case 7

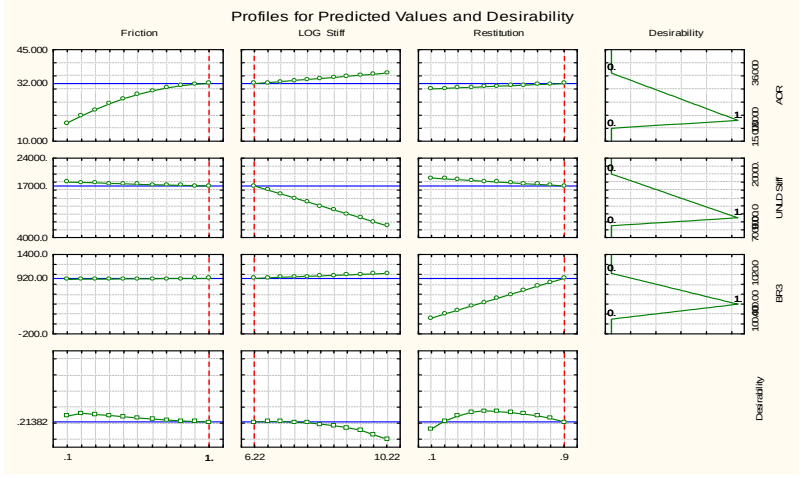

Case 8

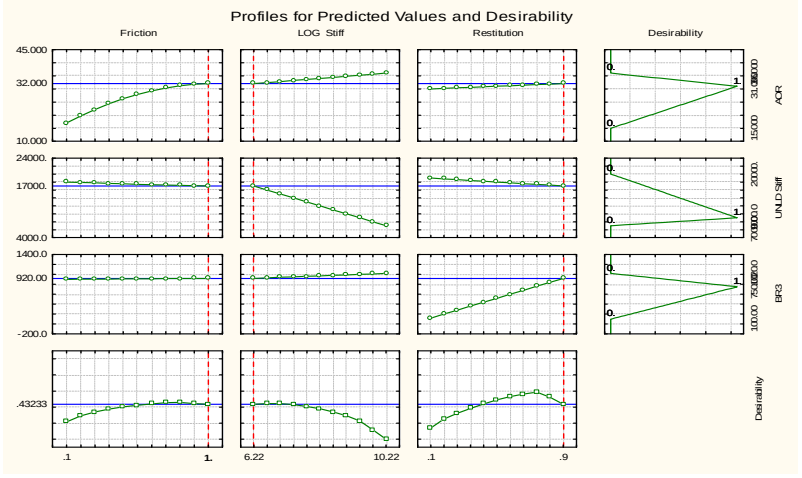

Case 9

Figure C.7 Profiling and desirability plots obtained from Statistica for the various cases studied in the parametric sensitivity study

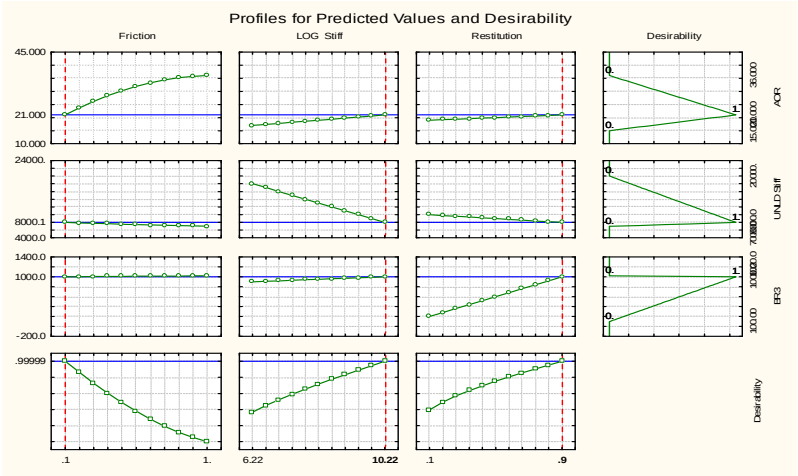

Case 10

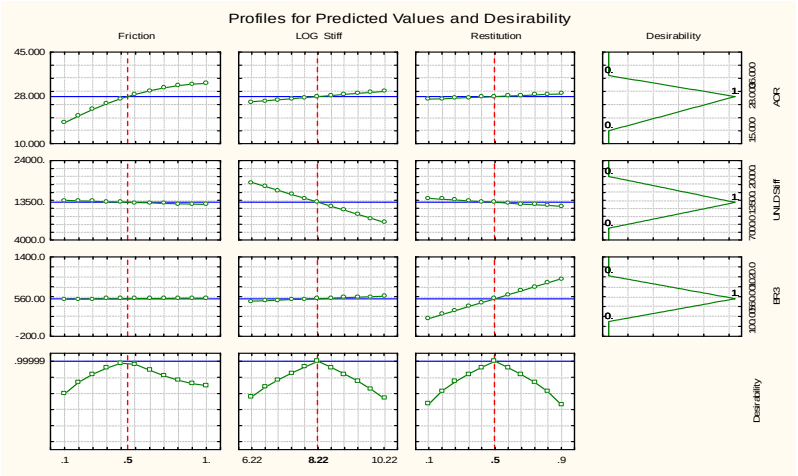

Case 11

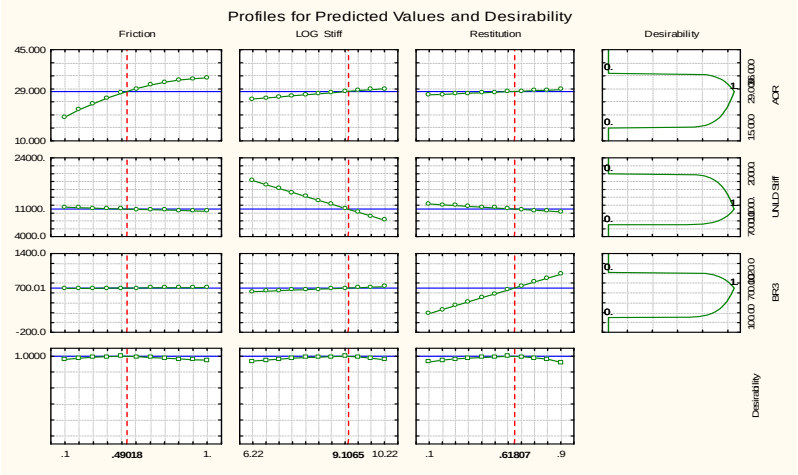

Case 12

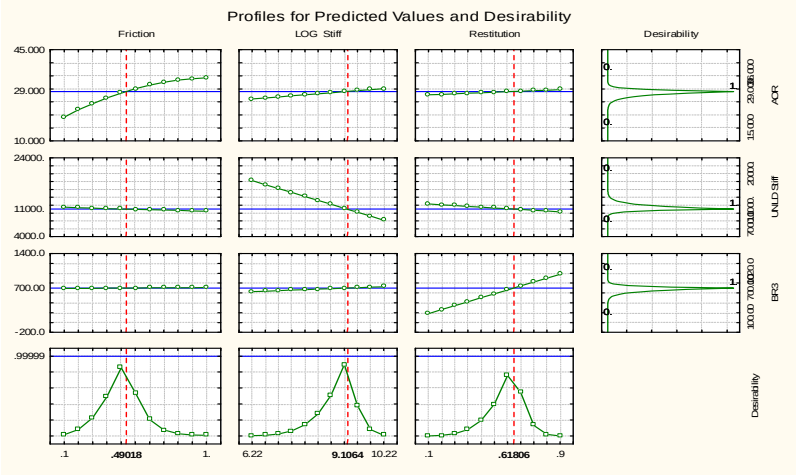

Case 13

Figure C.7 Profiling and desirability plots obtained from Statistica for the various cases studied in the parametric sensitivity study

C.9 Parametric optimisation procedure profiling and desirability plots

Using the profiling and desirability function in Statistica, the parametric optimisation was carried out for the single and paired glass beads (GB), PET pellets (PP), black eyed beans (BEB) and black kidney beans (BKB). Each granular material filled into the confined compression cylinder using either the ascending cone (AC) or the rainfall filling (RF) method. The profiling and desirability output plots from Statistica for the parametric optimisation are shown in Figure C.8. A total of ten cases were as described in Table C.8.

Table C.8 Parametric optimisation cases used in the thesis

Case	Material	Filling method
1	Single glass beads	Ascending cone
2	Single glass beads	Rain fall
3	Paired glass beads	Ascending cone
4	Paired glass beads	Rain fall
5	PET pellets	Ascending cone
6	PET pellets	Rain fall
7	Black eyed beans	Ascending cone
8	Black eyed beans	Rain fall
9	Black kidney beans	Ascending cone
10	Black kidney beans	Rain fall

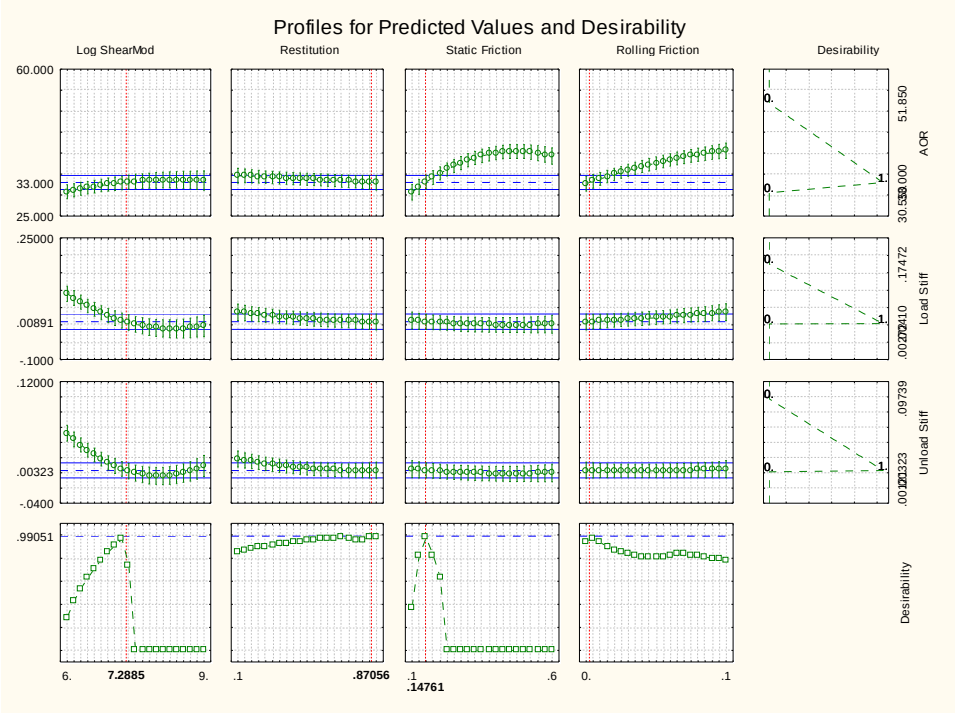

Case 1: single GB (AC)

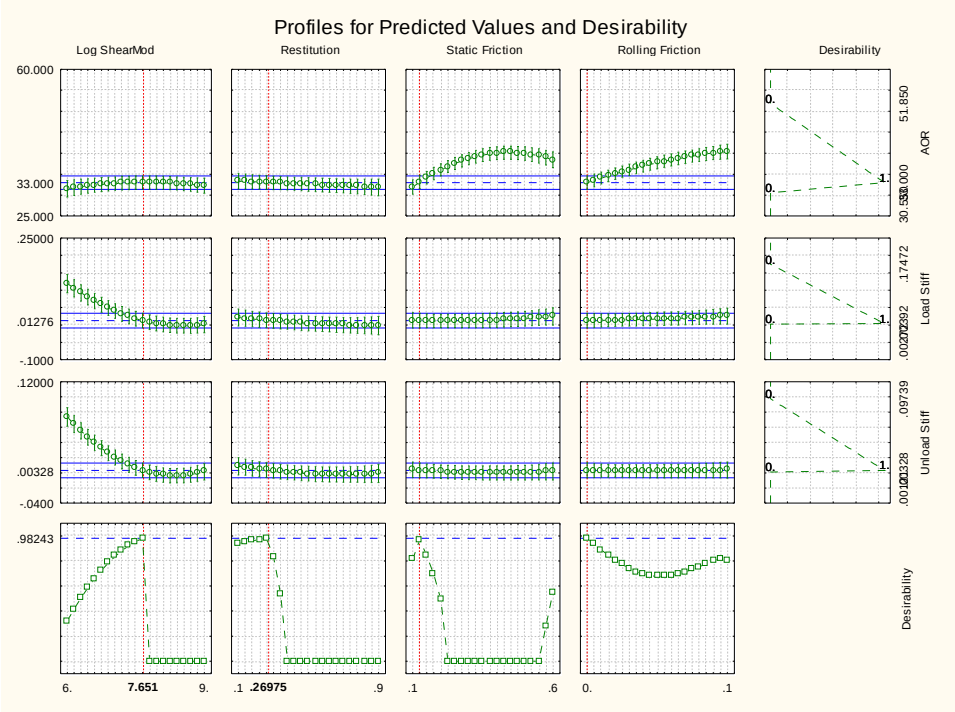

Case 2: single GB (RF)

Figure C.8 The profiling and desirability output plots from Statistica for the parametric optimsation

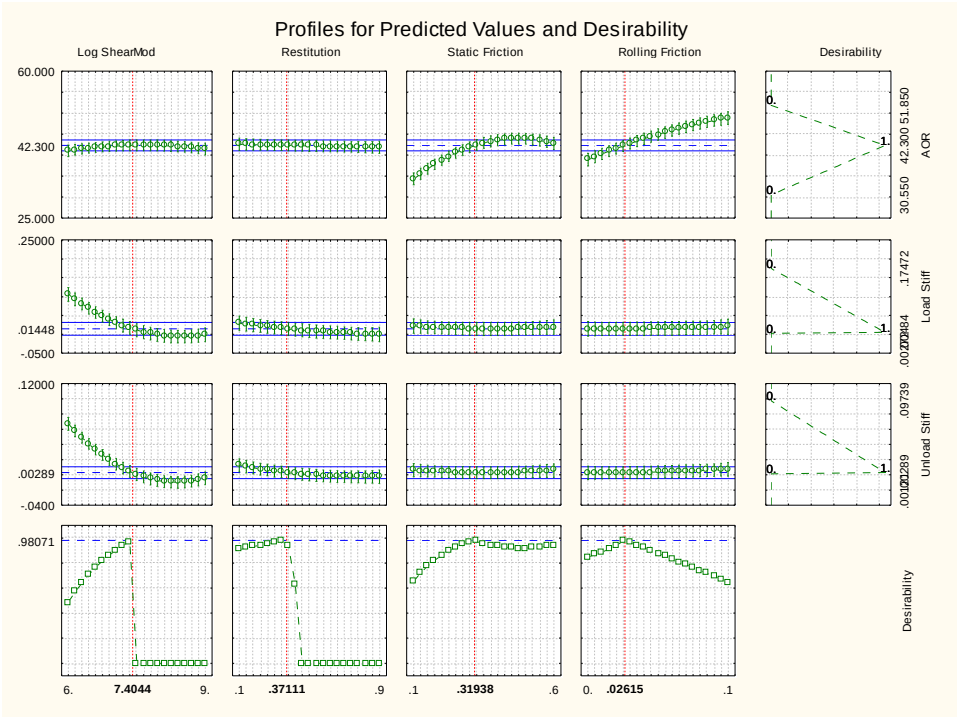

Case 3: Paired GB (AC)

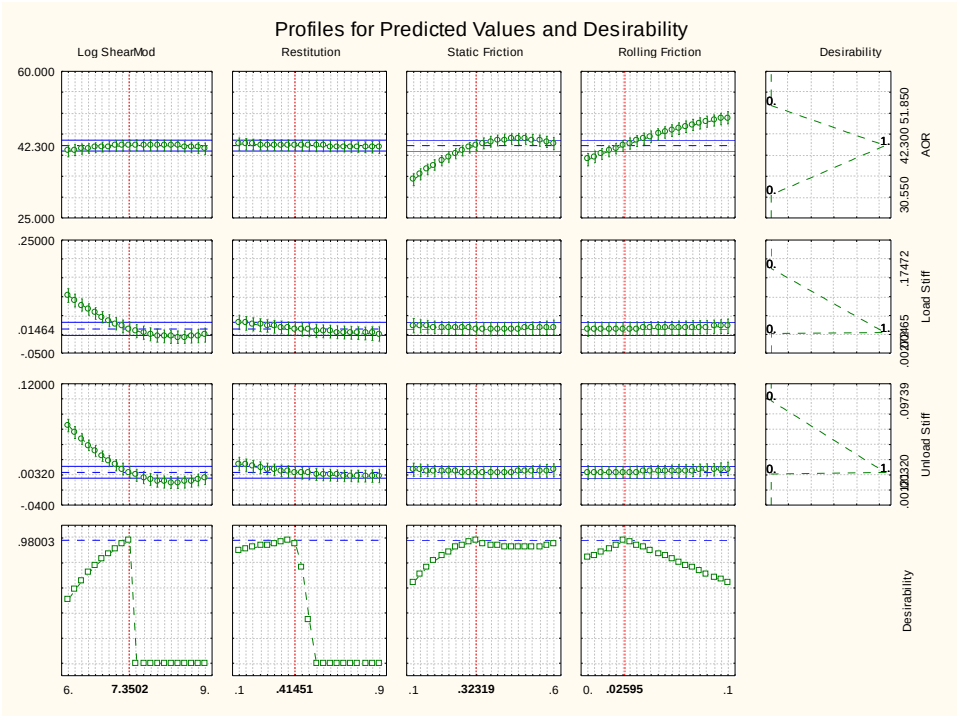

Case 4: Paired GB (RF)

Figure C.8 The profiling and desirability output plots from Statistica for the parametric optimsation

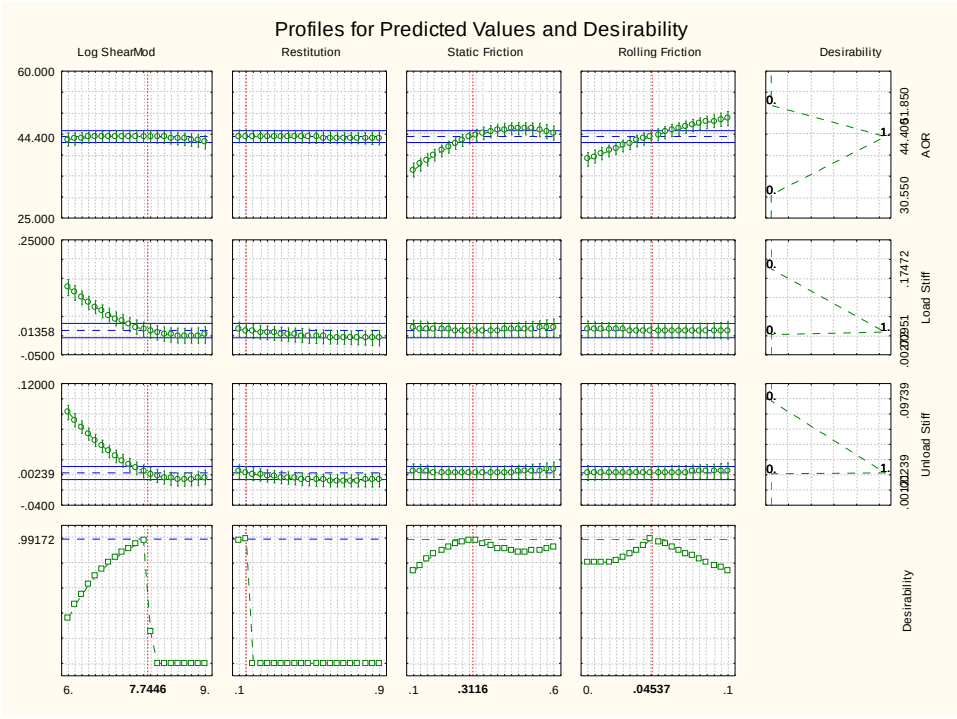

Case 5: PP (AC)

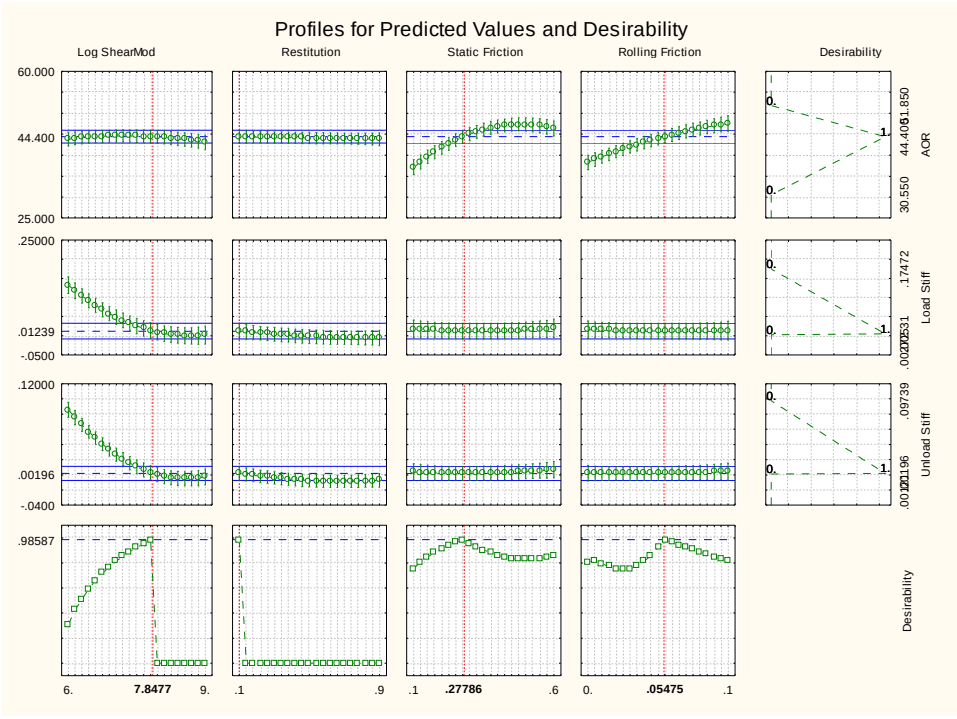

Case 6: PP (RF)

Figure C.8 The profiling and desirability output plots from Statistica for the parametric optimsation

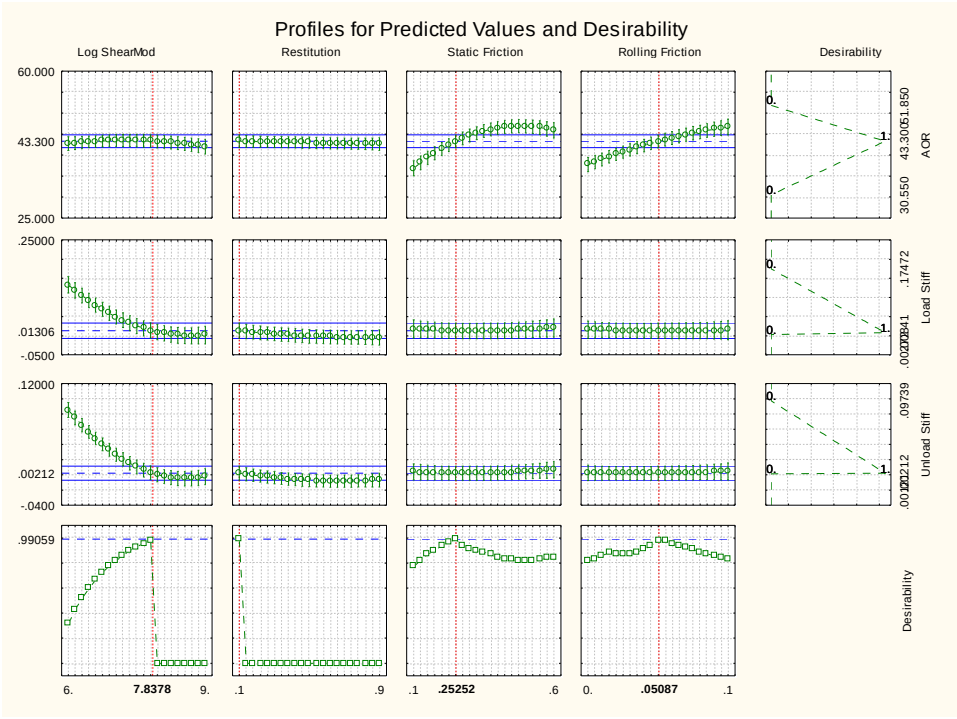

Case 7: BEB (AC)

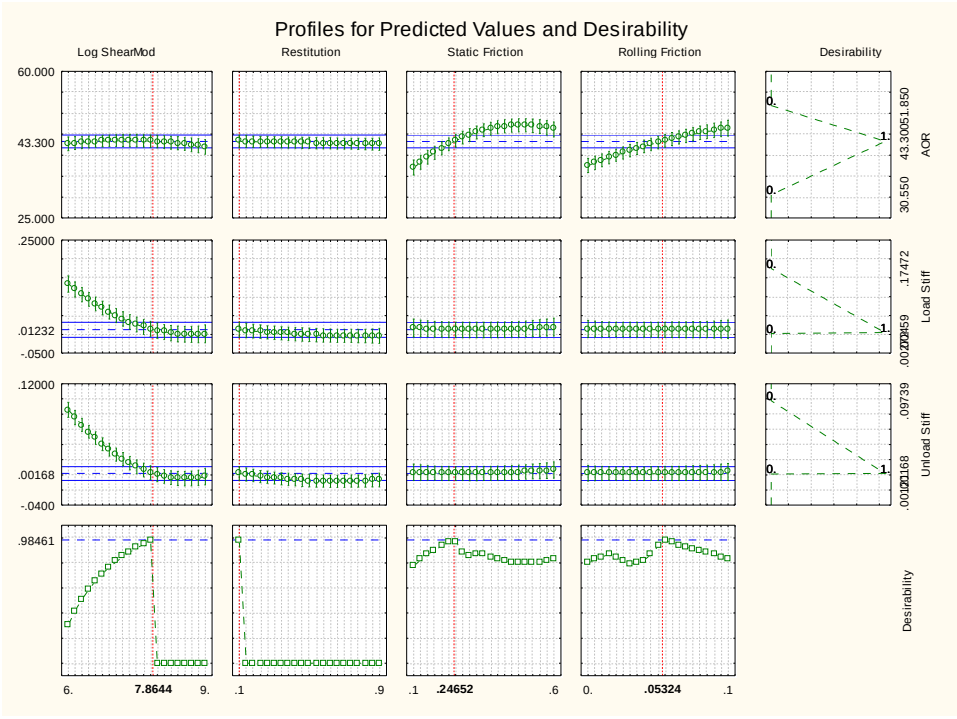

Case 8: BEB, RF

Figure C.8 The profiling and desirability output plots from Statistica for the parametric optimsation

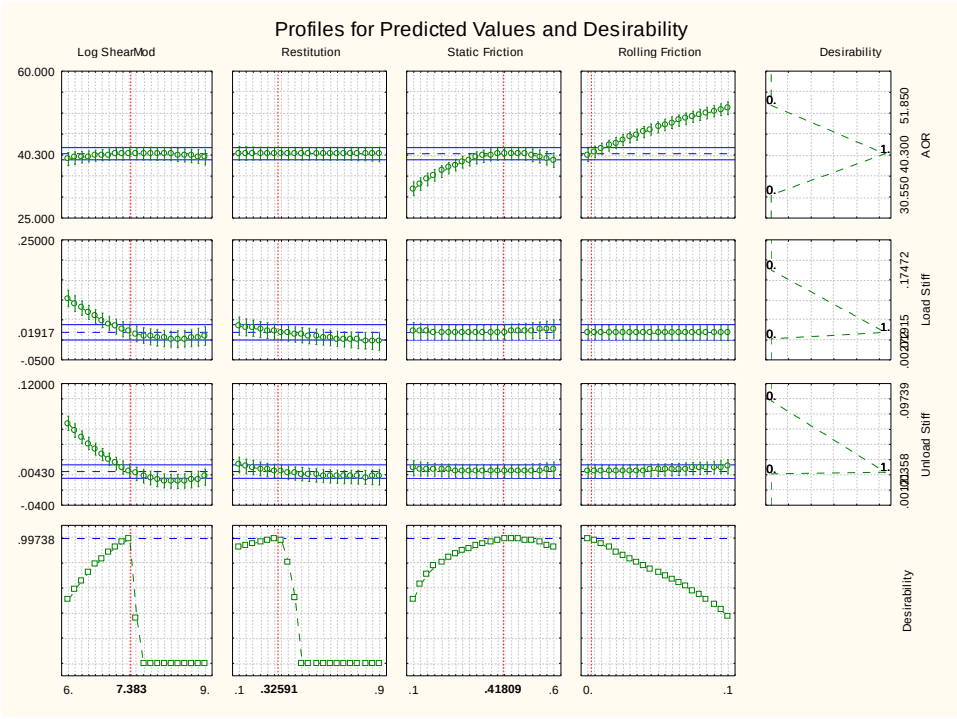

Case 9: BKB, AC

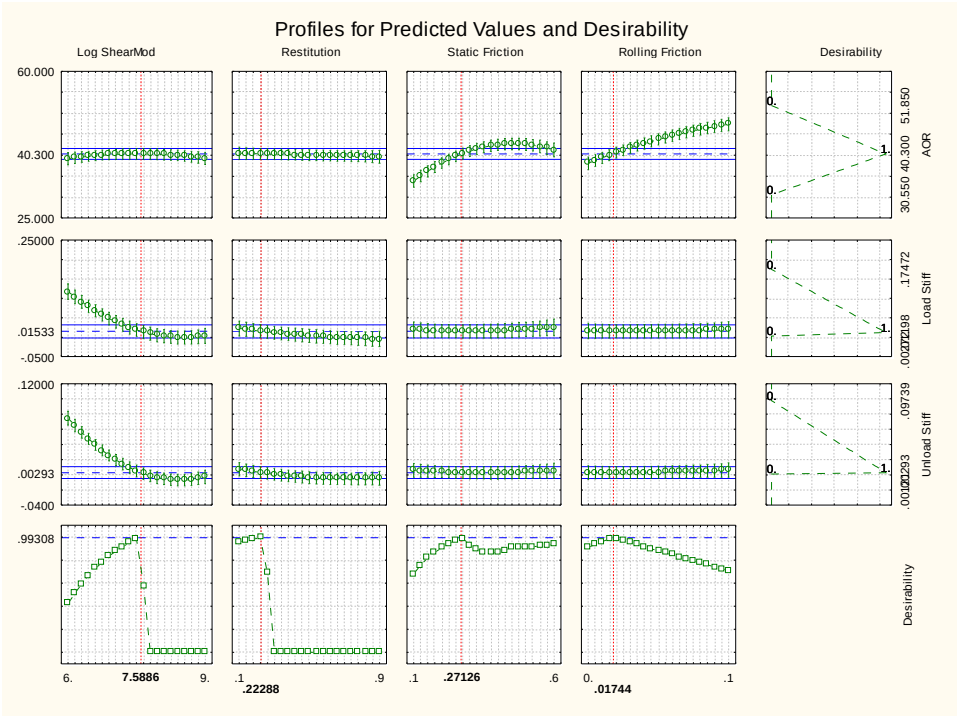

Case 10: BKB (RF)

Figure C.8 The profiling and desirability output plots from Statistica for the parametric optimsation

Appendix D

D.1 Rotating drum dynamic angle of repose verification

Rotating drum simulations were run using the optimised parameters of black eyed beans at 7 *rpm* for the verification described in section 0. 10 images were extracted from each simulation at various time steps. The dynamic angle of repose was then manually estimated to determine an average dynamic angle of repose as shown in Figure D.1.

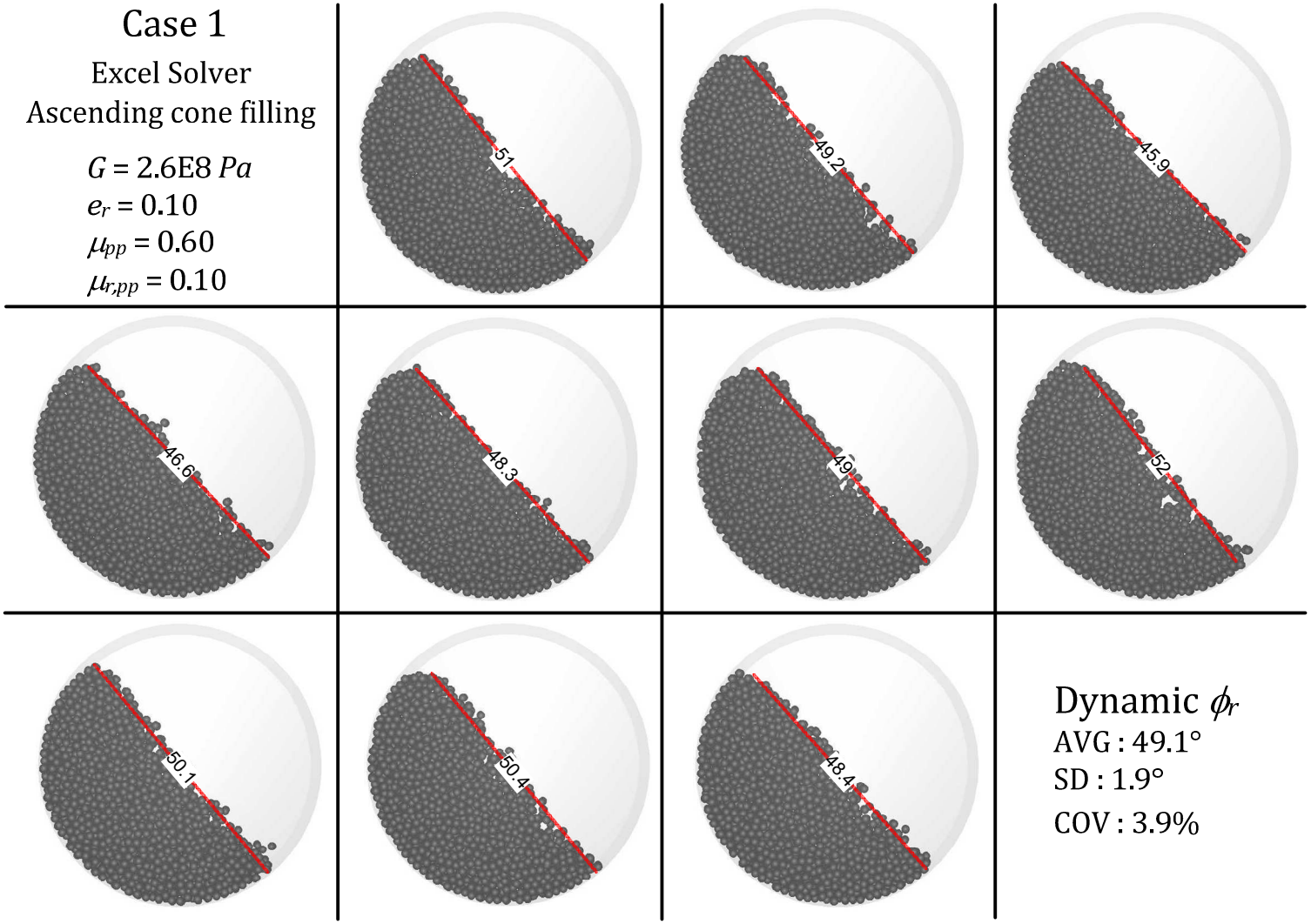

Figure D.1 Dynamic angle of repose determination for the verfification of the optimised parameters using black eyed beans

AVG: Average, SD: standard deviation, COV: coefficient of variance

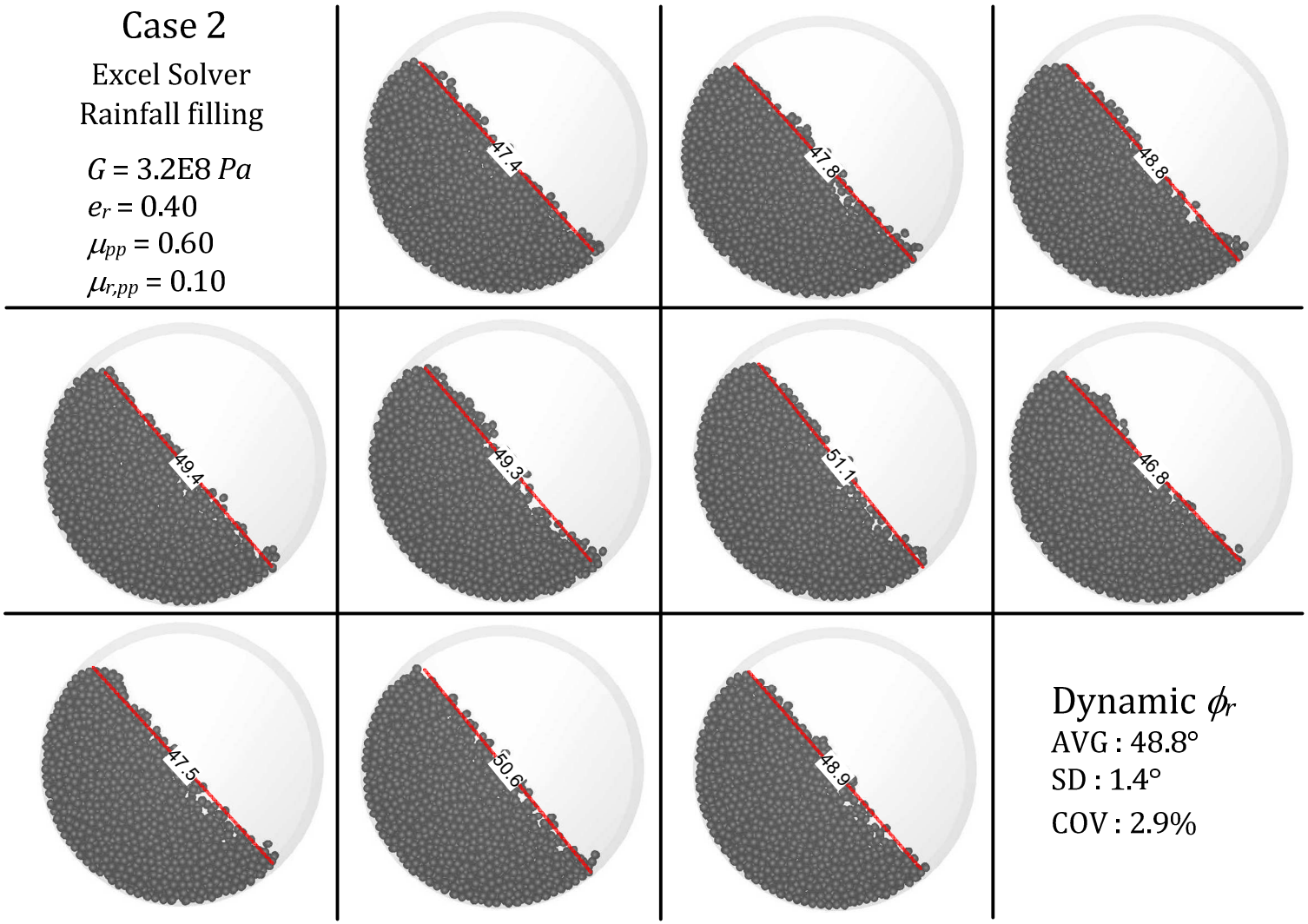

Figure D.1 Dynamic angle of repose determination for the verfification of the optimised parameters using black eyed beans

AVG: Average, SD: standard deviation, COV: coefficient of variance

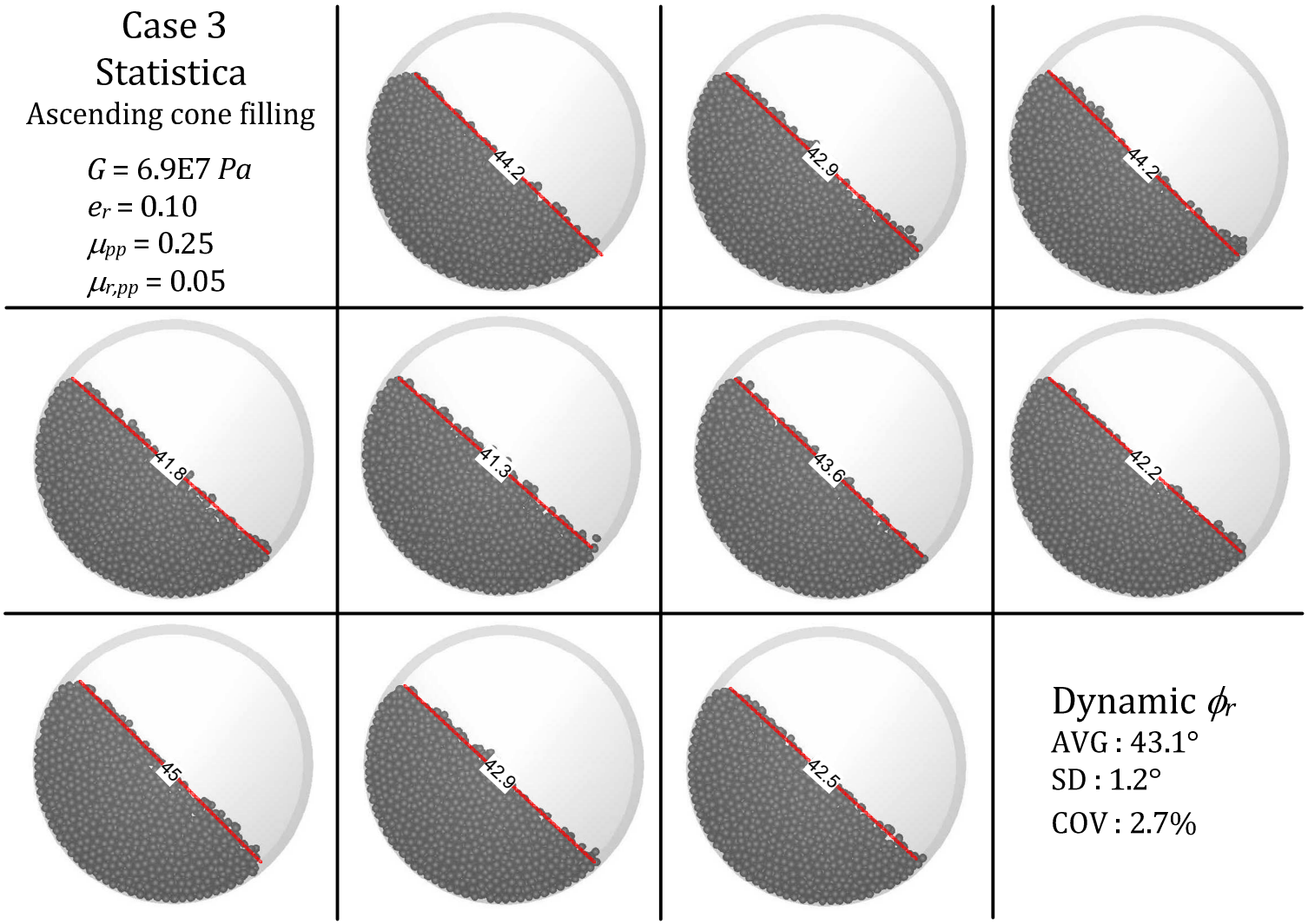

Figure D.1 Dynamic angle of repose determination for the verfification of the optimised parameters using black eyed beans

AVG: Average, SD: standard deviation, COV: coefficient of variance

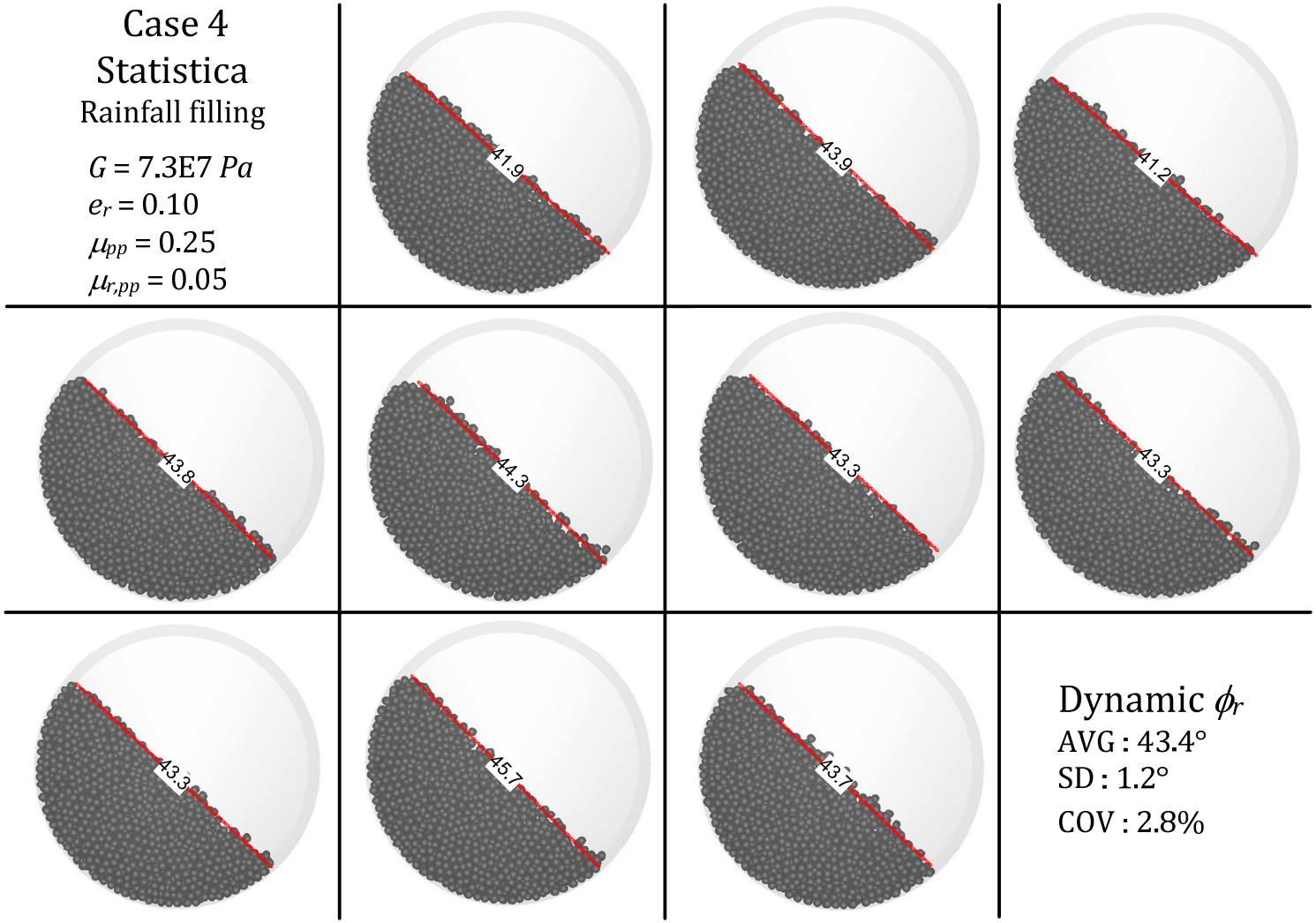

Figure D.1 Dynamic angle of repose determination for the verfification of the optimised parameters using black eyed beans

AVG: Average, SD: standard deviation, COV: coefficient of variance